

Lecture Notes on Machine Learning Methods in Geosciences

Gerard T. Schuster with Labs by Yuqing Chen, Zongcai Feng,
Zhaolun Liu, and Shihang Feng

January 20, 2019

Contents

Preface	vii
Abbreviations	ix
1 Introduction to Machine Learning in the Geosciences	1
1.1 Introduction	1
1.2 Three Classes of Machine Learning	5
1.2.1 Supervised Learning	5
1.2.2 Unsupervised Learning	9
1.2.3 Reinforcement Learning	9
1.3 Summary	10
2 Data Prediction by Least Squares Inversion	11
2.1 Least Squares Inversion	11
2.1.1 Overdetermined, Inconsistent, and Ill-conditioned Equations	12
2.1.2 Least Squares Solution	12
2.1.3 Regularized Least Squares Solution	17
2.1.4 Gradient of ϵ	20
2.1.5 Preconditioning	24
2.1.6 Overfitting Data	25
2.1.7 Inclusion of Bias Factor	29
2.2 Steepest Descent Optimization	29
2.3 Summary	31
2.4 Exercises	32
2.5 Appendix: Exact Step Length	34
3 Non-Linear Gradient Optimization	35
3.1 Non-linear Gradient Optimization	35
3.2 Rigorous Derivation of the Newton Formula	38
3.3 MATLAB Examples of Newton's Method	40
3.3.1 Inexact Newton Method	42
3.4 Multiscale Optimization	42
3.5 Diagram for Matrix-Vector Multiplication	43
3.6 Summary	47
3.7 Exercises	48

4	Introduction to Neural Networks	53
4.1	Neural Networks	53
4.1.1	Single-node Neural Network	56
4.1.2	One-node Neural Network with Cross-Entropy Objective Function	60
4.1.3	Two-node Neural Network	62
4.1.4	Multiple-node and Multiple-layer Neural Network	64
4.2	Multinomial Classifiers	65
4.3	ReLu Activation Function	66
4.4	Summary	67
4.5	Exercises	67
5	Multilayer Neural Networks	71
5.1	Introduction	71
5.2	Feed-forward Operation	71
5.3	Back-propagation Operation	72
5.3.1	Formula for $\partial\epsilon/\partial w_{ij}^{[N]}$	72
5.3.2	Formula for $\partial\epsilon/\partial w_{ij}^{[N-1]}$	73
5.3.3	Formula for $\partial\epsilon/\partial w_{ij}^{[N-2]}$	74
5.4	MATLAB Code	75
5.5	Numerical Examples	78
5.6	Summary	81
5.7	Exercises	81
5.8	Computational Labs	81
5.9	Appendix: Vectorized Steepest Descent Formula for Neural Networks	81
6	Convolutional Neural Networks	83
6.1	Introduction	83
6.2	Building Blocks of CNN	86
6.2.1	Convolution Layer	86
6.2.2	Activation Functions	89
6.2.3	Feature Maps	90
6.2.4	Pooling Layer	91
6.2.5	Fully-Connected Layer	93
6.2.6	Soft-Max Layer	93
6.2.7	Loss Function	93
6.2.8	Dropout Regularization	93
6.2.9	DropConnect Regularization	96
6.2.10	Local Response Normalization(LRN) Regularization	96
6.2.11	Mini-Batch	97
6.2.12	Step Length	98
6.3	Architectures of CNN	99
6.3.1	AlexNet	100
6.3.2	ZFNet	100
6.3.3	VGGNet	100
6.3.4	GoogleNet	102

6.3.5	ResNet	102
6.4	Deep Learning Software and Youtube Classes	104
6.5	Seismic Fault Interpretation by CNN	105
6.6	Summary	108
6.7	Exercises	109
7	Machine Learning Methods Applied to Geoscience Problems	111
7.1	Interpretation of Seismic Images by ML	111
7.2	Detection of Salt Body Boundaries by CNN	112
7.2.1	CNN Architecture	115
7.2.2	Monoparameter CNN	115
7.2.3	Monoparameter CNN	115
7.3	Detecting Rock Cracks by CNN	117
8	Recurrent Neural Networks	123
8.1	Theory of Recurrent Neural Networks	123
8.1.1	What can RNN's Do?	124
8.2	Training RNNs	125
9	Wave Equation Inversion and Neural Networks	127
9.1	Introduction	127
9.2	Theory for Wave Equation Inversion of Skeletonized Data	129
9.2.1	Feature Extraction	131
9.3	Conclusions	131
10	Neural Network Least Squares Migration	133
10.1	Sparse Least Squares Migration	133
10.2	Neural Network LSM	134
10.3	Numerical Results	136
10.4	Summary	136
10.5	Appendix	141
11	Sparse Inversion=Neural Networks	143
11.1	Introduction	143
11.2	Theory of Sparse Least Squares Migration	144
11.2.1	Least Squares Migration	144
11.2.2	Sparse Least Squares Migration	145
11.2.3	Single-Layer Sparse LSM	145
11.2.4	Multilayer Sparse LSM	147
11.3	Discussion	147
11.4	Appendix: Migration Green's Function	148
11.5	Appendix: Softmax2 Function	149

12 Support Vector Machines	151
12.1 Introduction	151
12.1.1 SVM Applications	152
12.2 Linear SVM Theory	154
12.3 Nonlinear SVM	156
12.4 Primal and Dual Solutions	158
12.5 Kernel Methods	160
12.6 Numerical Examples	164
12.6.1 MATLAB Codes	172
12.7 Multiclass SVM	173
12.8 Soft-Margin SVM	174
12.9 Practical Issues for Implementing SVM	175
12.9.1 Scaling	175
12.9.2 Data Augmentation	175
12.10 Summary	176
12.11 Exercises	176
12.12 Computational Labs	176
12.13 Appendix: Defining the Dual Problem with a Lagrangian	177
12.13.1 Simple Example of a Dual Solution	179
12.14 Appendix: Karush-Kuhn-Tucker Conditions	182
12.15 Appendix: Diffraction Stack Migration	182
12.15.1 Dip Angles, Coherency and Amplitudes of a Migration Image	184
13 Clustering Algorithms	187
13.1 Introduction	187
13.2 Theory of K-means Clustering	190
13.3 Information Weighted Clustering	191
13.3.1 Elbow Method for Determining the Number of Clusters	192
13.4 Numerical Examples	194
13.4.1 Picking Stacking Velocities by K-means Cluster Analysis	194
13.5 Summary	200
13.6 Exercises	202
14 Principal Component Analysis	205
14.1 Introduction	205
14.2 Theory of Principal Component Analysis	207
14.2.1 Simple Example	208
14.2.2 Filtering the PCA Components	210
14.2.3 Clustering the PCA Components	211
15 Sparse Coding	213
16 Generative Adversarial Networks	215
17 Compressive Sensing and Neural Networks	217

Preface

There are many definitions of *machine learning* (ML), but my favorite is from Stanford University (<https://www.techemergence.com/what-is-machine-learning/>).

Machine learning is the science of getting computers to act without being explicitly programmed.

This definition doesn't mean we don't have to write the programs, it means that the ML algorithms can learn from data without relying on rules-based programming. More generally, ML belongs to the larger class of artificial intelligence algorithms (see Figure 1), but the one that is attracting the most interest is that of deep learning with convolutional neural networks.

Machine Learning (ML) uses different algorithms to extract information from raw data. This book presents many of the basic geoscience ML algorithms, which can be classified into three categories: supervised learning, unsupervised learning, and reinforcement learning. Our main focus is on the theory and practice of supervised learning methods in geosciences, with an emphasis on neural networks and their applications to processing seismic data. This book is largely derived from my ML lecture notes taught at KAUST, where *Pattern Recognition and Machine Learning* by Bishop is a primary source of reference materials.

Case histories are used to demonstrate the practical use of ML in solving geoscience problems in seismic data processing. These problems include velocity analysis, demultiple, noise reduction in seismic data and migration images, and some interpretation examples. MATLAB labs are integrated throughout the text to deepen the reader's understanding of the concepts and their implementation. Such exercises are introduced early and geophysical applications are presented in almost every chapter. The reader who diligently goes through the chapters and labs will have a thorough grounding in some of the fundamental ML methods used in geosciences. The last chapter makes some connections between ML and compressive sensing, an exciting recent development partly pioneered by Michael Elad.

Acknowledgments

The author wishes to thank the support provided by the sponsors of the CSIM consortium. Strong support was also provided by King Abdullah University of Science and Technology who financially supported me while writing the final chapters.

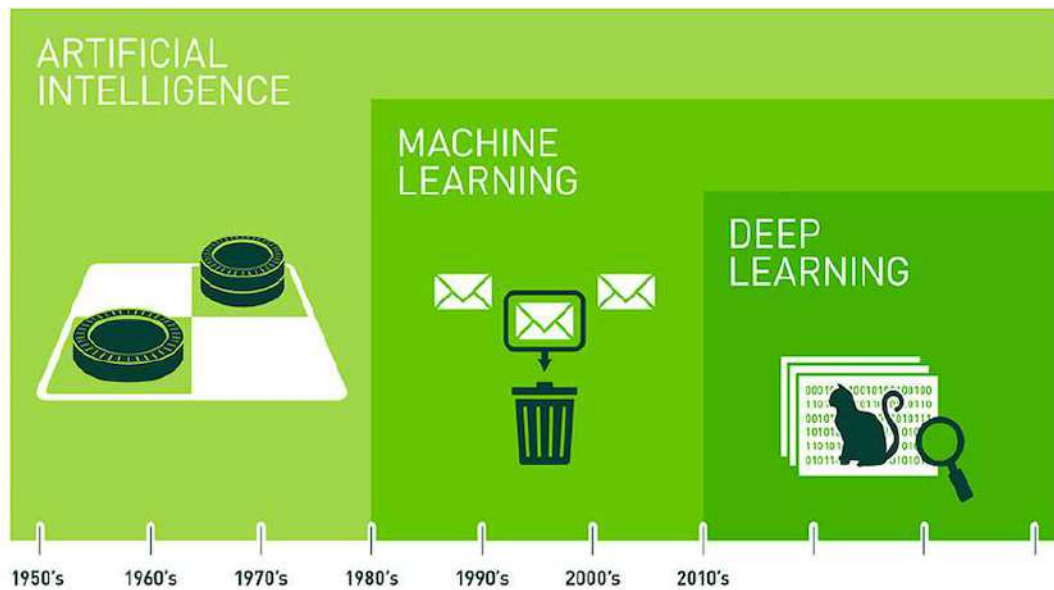


Figure 1: Evolution of different classes of Artificial Intelligence. According to <https://www.techemergence.com/the-difference-between-artificial-intelligence-and-machine-learning/the-difference>, artificial intelligence involves a machine doing something that only a human would be able to do. Source is Nvidia.

Abbreviations

- ABC - Absorbing boundary condition
- ADCIG - Angle-domain common image gather
- CAG - Common angle gather
- CG - Conjugate gradient
- CIG - Common image gather
- CMG - Common midpoint gather
- CNN - Convolutional neural network
- COG - Common offset gather
- CSG - Common shot gather
- DM - Diffraction-stack migration
- FD - Finite difference
- FCN - Fully connected neural network
- FWI - Full waveform inversion
- GOM - Gulf of Mexico
- KM - Kirchhoff migration
- LSM - Least squares migration
- LSRTM - Least squares reverse time migration
- MD - Migration deconvolution
- ML - Machine learning
- MVA - Migration velocity analysis
- NN - Neural network
- NMO - Normal moveout

- PDE - Partial differential equation
- PSTM - Prestack time migration
- QN - Quasi-Newton
- RNN - Recurrent neural network
- RTM - Reverse time migration
- SD - Steepest descent
- SPD - Symmetric positive definite
- SSP - Surface seismic profile
- QP - Quadratic programming
- VSP - Vertical seismic profile
- ZO - Zero offset
- WT - Wave equation travelttime tomography
- WTW - Wave equation travelttime and waveform tomography

Chapter 1

Introduction to Machine Learning in the Geosciences

The chapter provides a partial overview of machine learning methods and summarizes their historical development.

1.1 Introduction

Machine learning (ML) was generally defined by Arthur Samuel in 1950s as the following:

[Machine learning is the] field of study that gives computers the ability to learn without being explicitly programmed.

At that time the term *machine learning* was not in use, but this definition applies to the ML field today. Some researchers use the phrase "deep learning", but this typically refers to convolutional neural networks with many layers (Goodfellow et al., 2016).

Over the last 75 years machine learning has undergone several metamorphisms. From the 1940s to early 1960s, cybernetics defined (Wiener, 1948) as "the scientific study of control and communication in the animal and the machine", was the hot research topic related to ML (see blue curve Figure 1.1) and is now used in a rather loose way to imply "control of any system using technology." (Wikipedia). That is, it is the scientific study of how humans, animals and machines control and communicate with each other. It was partly inspired in the early 1940s by the discovery of a biological model for theories of learning (McCulloch and Pitts, 1943; Hebb, 1949).

The neuron-function model of the brain was recast as a mathematical algorithm known as the perceptron introduced by Rosenblatt (1958). In its simplest form the i^{th} input signal x_i to a neuron is related to the output y by

$$y = \sigma\left(\sum_i w_i x_i + b\right), \quad (1.1)$$

where w_i is the weight to the input x_i , b is a bias term and $\sigma(z) = 1/(1 + e^{-z})$ is the sigmoid function shown in Figure 1.2. In the original perceptron, the *activation* function

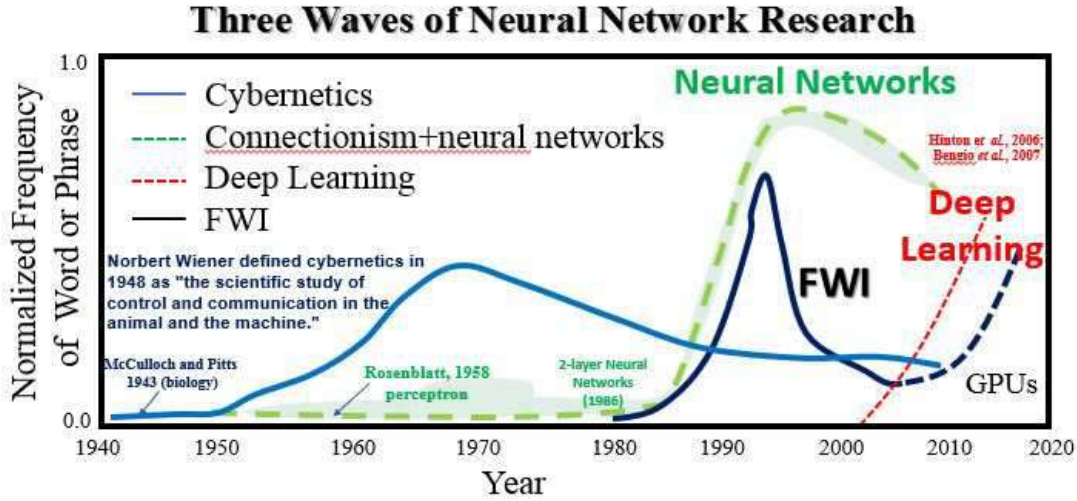


Figure 1.1: Two of the three historical waves of artificial neural nets research, as measured by the normalized frequency of the phrases cybernetics and connectionism or neural networks according to Google Books (Goodfellow et al., 2016). The third wave, deep learning, is schematically described by a rapid rise and does not correspond to the actual word count. For geophysicists, the schematic curve for FWI shows its rise, fall, and rebirth in the exploration community.

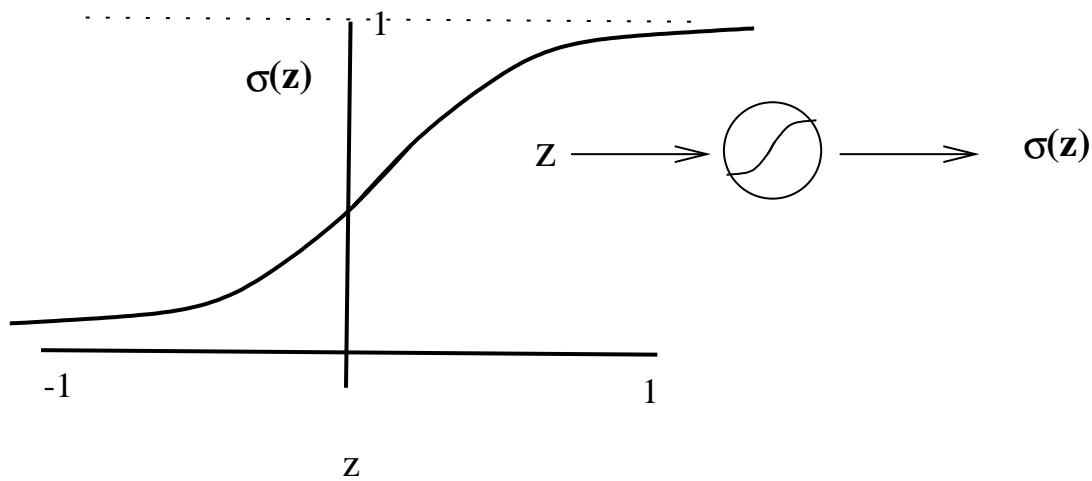


Figure 1.2: Sigmoid function plotted against its argument and its system diagram to the right.



Figure 1.3: Mark 1 computer for image recognition. The photograph on the left shows how the inputs were obtained using a simple camera system in which an input scene, in this case a printed character, was illuminated by powerful lights, and an image focussed onto a 20×20 array of cadmium sulphide photocells, giving a primitive 400 pixel image. The perceptron also had a patch board, shown in the middle photograph, which allowed different configurations of input features to be tried. Often these were wired up at random to demonstrate the ability of the perceptron to learn without the need for precise wiring, in contrast to a modern digital computer. The photograph on the right shows one of the racks of adaptive weights. Each weight was implemented using a rotary variable resistor, also called a potentiometer, driven by an electric motor thereby allowing the value of the weight to be adjusted automatically by the learning algorithm. Image and caption from Bishop (2006).

was the all-or-nothing¹ $\sigma(z) = \text{sign}(z)$ function, but was much later replaced by smoother almost-all-or-nothing functions such as the sigmoid $\sigma(z) = 1/(1 + e^{-z})$ where the derivative exist everywhere.

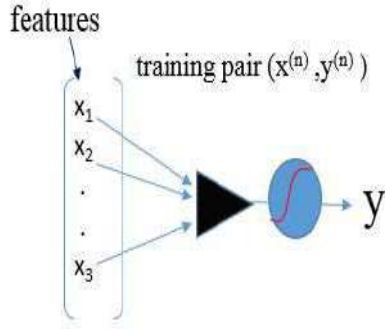
According to Wikipedia: "The perceptron was intended to be a machine, rather than a program, and while its first implementation was in software for the IBM 704, it was subsequently implemented in custom-built hardware as the "Mark 1 perceptron" shown in Figure 1.3. This machine was designed for image recognition: it had an array of 400 photocells, randomly connected to the "neurons". Weights were encoded in potentiometers, and weight updates during learning were performed by electric motors. In a 1958 press conference organized by the US Navy, Rosenblatt made statements about the perceptron that caused a heated controversy among the fledgling AI community. The New York Times reported the perceptron to be *the embryo of an electronic computer that [the Navy] expects will be able to walk, talk, see, write, reproduce itself and be conscious of its existence.*"

From a simple biological point of view the perceptron model suggests that an input electrical signal x will be transmitted by the neuron through the connecting synapse to the neighboring neuron if the input voltage exceeds a threshold value. The input values x_i are similar to the electrical impulses that travel through the many synapses that feed into the neuron.

A system of many perceptrons came to be known as a neural network in the 1980s (see

¹The *sign* function is also known as the Heavyside function.

Single Preceptron



Two-layer Neural Network

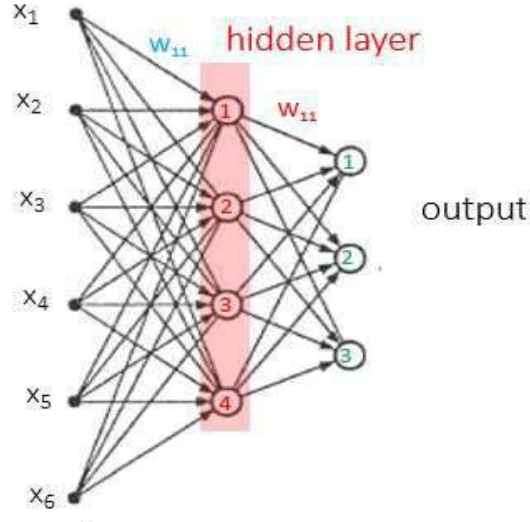


Figure 1.4: (Left) Single-layer perceptron and (right) two-layer neural network.

green-dashed curve Figure 1.1), which could be used to perform practical functions such as classification of images. Instead of one perceptron, the $N \times 1$ input signal \mathbf{x} feeds into M neurons so that equation 1.1 becomes

$$y_j = \sigma\left(\sum_{i=1}^N w_{ij}x_j + b_i\right), \quad (1.2)$$

where the $M \times 1$ output vector is \mathbf{y} , the weights $w_i \rightarrow w_{ij}$ become those associated with the $M \times N$ weight matrix \mathbf{W} . The activation function σ acts on each element of the matrix-vector product $z_i = \sum_{j=1}^N w_{ij}x_j + b_i$ to return the $M \times 1$ output vector \mathbf{y} , which is also known as the activation vector \mathbf{a} if it is a *hidden* layer and not the last column of nodes. A single perceptron with multiple inputs is shown on the left side of Figure 1.4. According to Goodfellow et al. (2016), connectionism is another name similar to that of artificial neural networks (ANN) used for ML in the 1980s and 1960s. The word connectionist refers to the speculation in the 1950's that "...the images of stimuli may never really be recorded at all, and that the central nervous system simply acts as an intricate switching network, where retention takes the form of new *connections*, or pathways, between centers of activity." (Rosenblatt, 1958).

Weighting the input values and summing them together to give the input to the non-linear activation function σ defines the two basic building blocks of a neural network. The concatenation of each weighted sum followed by the application of the activation function forms one layer, and a sequence of such layers forms a multilayer neural network. An example is shown on the right side of Figure 1.4.

Interest in neural networks grew rapidly from the 1980s and peaked around the mid 1990s but started to fall off, partly because its limitations were revealed as being computa-

tionally too expensive to fulfill all of its early promises. It also suffered from the inability to theoretically predict its ability to perform well, including IBM's Deep Blue's success in beating a Chess grandmaster² in 1997. Around the same time attention was being refocused to mathematically tractable methods such as Support Vector Machines (Bishop, 2006).

This decline in interest suddenly changed in 1998 with the development of the convolutional neural networks (CNNs) by LeCun et al. (1998). Instead of requiring massive memory and computations to perform neural network computations, CNN replaced fully connected layers and large weight matrices with relatively small convolutional matrices. For equation 1.2 this means that the matrix-vector multiplication is replaced by a correlation of the input vector with a much smaller number of weights. For $M = N$, the memory and computational requirements are $O(N^2 n_f)$ for CNN compared to $O(N^4)$ for classical neural networks. Here, the input image for a grayscale picture is an $N \times N$ grid of intensity values and the number of convolutional filter coefficients is $n_f \ll N$. The CNN algorithm allowed for the development of large neural networks with many deep layers, and gave rise to re-branding of *neural network research* as *deep learning research* (see red-dashed curve Figure 1.1).

Deep learning has exploded in the level of interest in a wide variety of fields, and has become publicly prominent with its success in popular media companies such as Facebook and Google and its use with self-driving cars. A force multiplier is the development of fast cheap GPUs that can expedite the convolutional operations. CNN and its application to geoscience problems is the main focus of these lecture notes.

Coincidentally, the rise and fall and the rebirth of full waveform inversion (FWI) is schematically traced as the black curve in Figure 1.1. Part of the reason for its rebirth are two developments: 1) multiscale techniques that tend to avoid getting stuck in local minima and 2) the exponential increase in computing power.

1.2 Three Classes of Machine Learning

Machine learning methods can be classified into the three classes shown in Figure 1.5: supervised learning, unsupervised learning, and reinforcement learning. Researchers are currently exploring their potential applications in three categories of seismic exploration: reservoir analysis, seismic data processing and seismic interpretation. This book uses many seismic examples from the first two categories to highlight the different applications of supervised and supervised learning. The supervised ML method most used today in geosciences as well as in image recognition is that of convolutional neural networks, which is introduced in Chapter ??.

1.2.1 Supervised Learning

Supervised learning is a procedure for finding a model, for example finding the coefficients of \mathbf{W} , that predicts the output \mathbf{y} from the input data \mathbf{x} . The procedure is denoted as supervised learning because \mathbf{W} is found by using a large training set that consists of many examples $(\mathbf{x}^{(n)}, \mathbf{y}^{(n)})$ for $n \in [1, 2 \dots N]$.

²https://en.wikipedia.org/wiki/Deep_Blue_versus_Garry_Kasparov

Three Major Types of Machine Learning

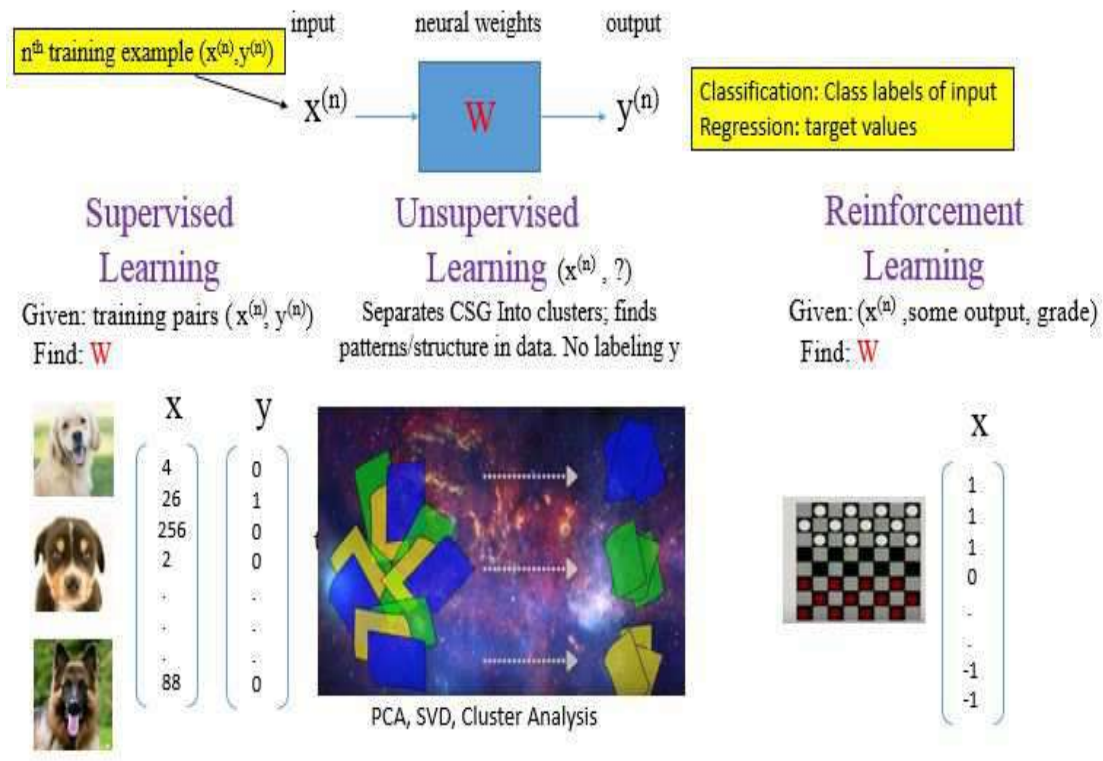


Figure 1.5: Three classes of machine learning.

One use for supervised learning is for classifying input data into different categories. For example, the goal in Figure 1.5a is to create a neural network that can distinguish pictures of dogs from other types of animals. Here, the *training pairs* consist of dog images and the label $y = 1$ for a dog and the label $y = 0$ for not a dog. The $N \times N$ dog image is *flattened* into an $N^2 \times 1$ vector $\mathbf{x}^{(n)}$, and the training pair $(\mathbf{x}^{(n)}, \mathbf{y}^{(n)})$ consist of both the input $\mathbf{x}^{(n)}$ and target output $\mathbf{y}^{(n)}$ pairs. There are N training pairs. The label vector \mathbf{y} in this case is a scalar where $y = 1$ for a dog and $y = 0$ for not a dog.

Many pairs of training data are used to *train* the neural network so that an over-determined system of equations is formed. The coefficients in \mathbf{W} are found by an iterative optimization method (see Chapter 5). An accurate estimate of \mathbf{W} will allow pictures of dogs that are outside the training set to be identified by the neural network.

Another example of supervised learning is shown in Figure 1.6 where thin sections of rocks are the input images (Patel and Chatterjee, 2016). The goal is to classify them according to the type of limestone. Instead of inputting the entire image of a thin section, they are skeletonized into smaller features, which is shown as a two part operation. Each colorized thin-section image is reduced to the histogram values of RGB colors. Then the second-order, third-order and fourth-order statistics of each of the three histograms are computed by calculating their variance, skewness, and kurtosis values. These are the values input into the neural network, and there are seven output classes. These classes correspond to the dominant type of geology in the image as determined by a geologist. A number of classified thin sections with class labels are used for training. The training estimates the optimal values of the coefficients in \mathbf{W} . A new set of thin sections are then used as input into the neural network, which then classifies these out-of-the-training set data. The results are shown in the lower right side of Figure 1.6. Comparison of the predicted classes and the actual classes show more than a 90% accuracy in labeling the data.

Weakly Supervised and Semi-supervised learning.

A subset of supervised learning is semi-supervised learning where there are only a few labeled data but there are lots of unlabeled data (Patel et al., 2016). In this case it is too expensive to label more than a few examples of data.

There is also weakly-supervised learning where each image is given a label but the goal is to find labels at the pixel level. Each image can contain features from each class, but it is given a label that denotes the dominant feature. For example, small localized images of seismic sections might be labeled as predominantly salt dome or a turbidite sequence, but they also contain other geological structures. Labeling each localized image as just one class is quickly done by an interpreter, but it ignores the detailed geology. Using a collection of these labeled images, a dictionary can be built up and be used to train a weakly supervised neural network to label each image pixel as the type of geology belonging to one of the classes. Thus, detailed geology at the pixel level can be provided by a machine-learning algorithm. A key goal of representation learning is to disentangle the factors of variation that contribute to the appearance of an image (Patel et al., 2016).

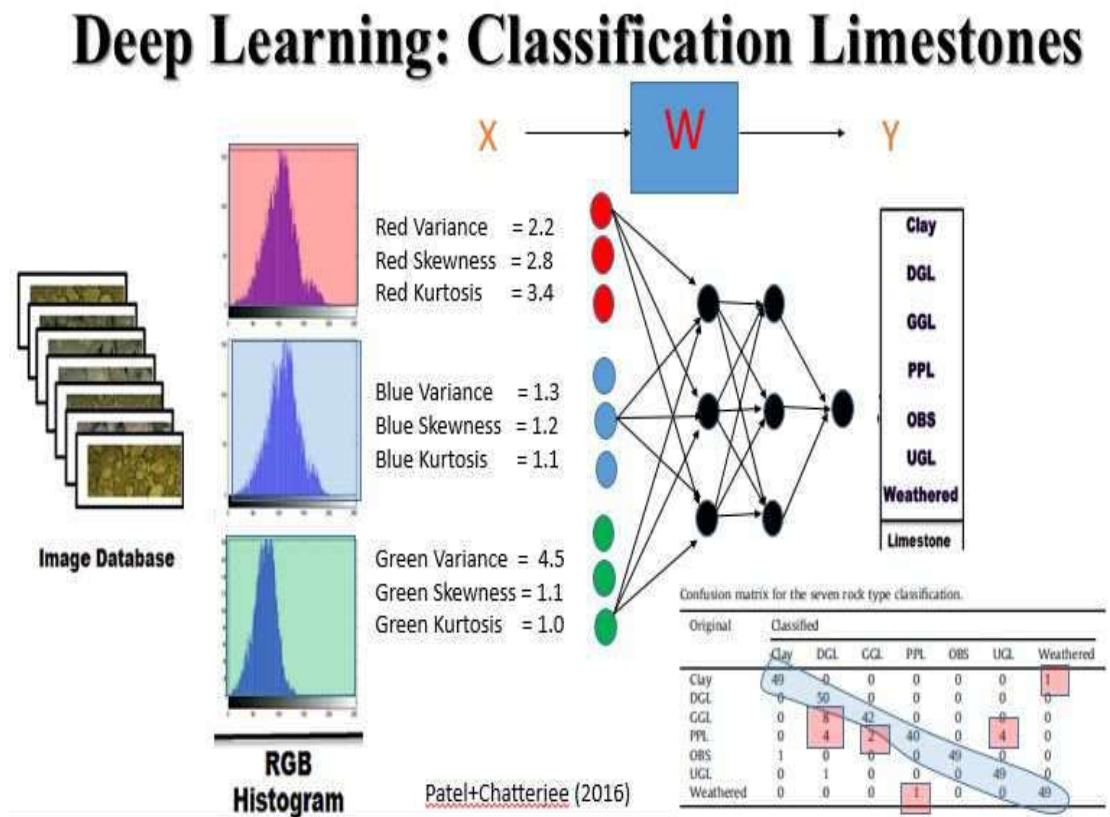


Figure 1.6: Neural layer network for classifying thin sections.

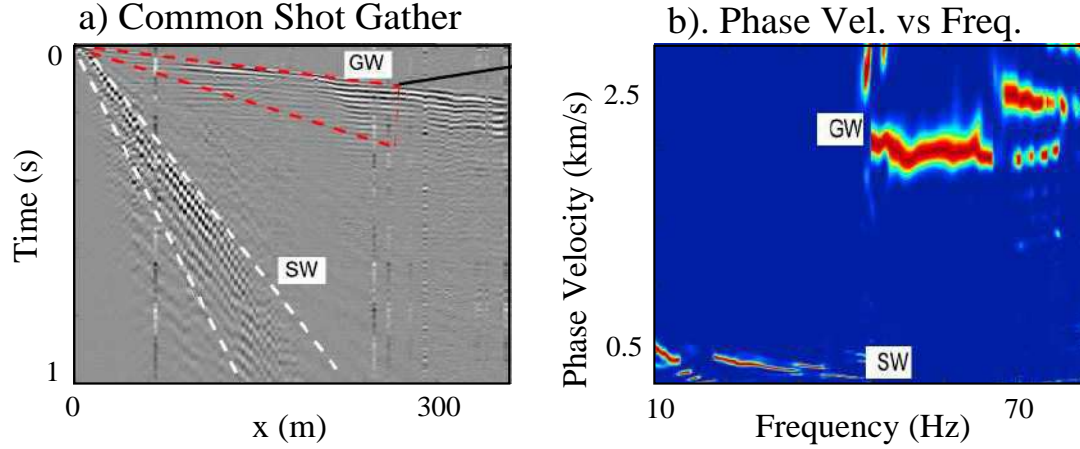


Figure 1.7: a). Common shot gather (CSG) of seismic data and b) phase velocity (ω/k) versus frequency ($f = \omega/2\pi$) plot of the CSG. Here, the Rayleigh surface waves (SW) and P-wave guided waves (GW) are now well separated after a temporal Fourier transform and a Radon transform (Li et al., 2018).

1.2.2 Unsupervised Learning

Unsupervised learning is when the training data do not specify the target vector \mathbf{y} but recognizes that there are distinct patterns in the input data \mathbf{x} . The goal is to separate distinct patterns from one another. As an example, Figure 1.7a depicts a common shot gather of seismic data and its b) transform to phase-velocity and frequency space. The Rayleigh surface waves and P-wave guided waves (GW) are tangled together in the original data but are well separated in the $C - f$ domain because they each propagate with very different propagation velocities; here, C is the phase velocity and f denotes frequency. Other examples include the separation of signal from noise by principle component analysis (PCA) in Chapter ?? or by bandpass filtering.

1.2.3 Reinforcement Learning

Reinforcement learning is used to train a system to play a game. In this case, the output is not a labeled class but it is a reward for performing the desired behavior, such as winning a checkers or chess game. Training is performed by learning from chess games played by experts, and at some point the computer can play against itself to refine the strategies.

It is tempting to think of reinforcement learning as a special case of unsupervised learning that finds hidden structures in data. Instead reinforcement learning learns the best behavior that maximizes a reward by learning the best moves previous to the current state. It then progressively explores new actions that might maximize the reward in an uncertain environment. Several examples by Sutton and Barto (2018) illustrate these ideas.

- Playing chess. The novice chess player learns from his past mistakes that led to being checkmated, e.g., he/she does not sacrifice a knight for a pawn. The player also predicts a sequence of moves that might maximize the reward of winning the game,

but also anticipates counter-moves by the opponent. In this way the environment of the chessboard is "sensed" at any one move, and different paths to winning are determined by both experience, intuition and logic.

- Birth of a gazelle. A baby gazelle stands up on wobbly legs after being born, learns by trial and error to best balance itself and move forward, and a half hour later is running at 20 miles/hour despite its uncertainty in the surrounding environment. The reward is to outrun potential predators and keep up with the mother gazelle.
- Phil prepares his breakfast. Closely examined, even this apparently mundane activity reveals a complex web of conditional behavior and interlocking goal-subgoal relationships: walking to the cupboard, opening it, selecting a cereal box, then reaching for, grasping, and retrieving the box. Other complex, tuned, interactive sequences of behavior are required to obtain a bowl, spoon, and milk carton. Each step involves a series of eye movements to obtain information and to guide reaching and locomotion. Rapid judgments are continually made about how to carry the objects or whether it is better to ferry some of them to the dining table before obtaining others. Each step is guided by goals, such as grasping a spoon or getting to the refrigerator, and is in service of other goals, such as having the spoon to eat with once the cereal is prepared and ultimately obtaining nourishment. Whether he is aware of it or not, Phil is accessing information about the state of his body that determines his nutritional needs, level of hunger, and food preferences.

1.3 Summary

Machine learning and especially deep learning seem magical, but also frustrating because they sometimes appear to be theoretically impenetrable! The trend is to reduce the size of feature map with depth but increase the number of filters. Networks jump from convolutional to fully connected layers. What justifies these operations? Unfortunately, deep learning does not have a deep theoretical basis to help us understand its performance. It is a collection of algorithmic tricks that seem to usually work and are economically driven by its success with self-driving cars, Google, IBM, etc. But this seems to be a natural evolution of early scientific discoveries, make things intuitively work by trial and error, and then make efforts to understand its theoretical basis. This is no different than the technological developments of farming, mining, and other practical tools, including full waveform inversion. Eventually a deeper understanding of the theoretical basis of deep learning will propel it forward to going beyond beyond brute-force interpolation.

Chapter 2

Data Prediction by Least Squares Inversion

The goal of inversion is to find the *model* \mathbf{w} that *best predicts* the target data \mathbf{t} from input data \mathbf{X} . Here, the governing system of equations is represented by a system of equations $\mathbf{X}\mathbf{w} = \mathbf{t}$ that are, typically, overdetermined, inconsistent and ill-conditioned. No exact solution exists so we seek the *optimal* model \mathbf{w}^* that gives the minimum prediction error $\epsilon = \frac{1}{2} \|\mathbf{X}\mathbf{w} - \mathbf{t}\|^2$ under the L_2 norm. We show how regularization and preconditioners can be used to alleviate problems with ill-conditioning, inconsistency and non-linearity. The inordinate expense of using a direct method for solving a large system of equations forces us to adopt the iterative solution method known as gradient optimization.

For general geophysical inversion, the elements of the target-data vector \mathbf{t} can take on any real-valued measurements, such as gravity readings, and the non-linear operator \mathbf{X} is characterized by the Newtonian physics of, e.g., a partial differential equation. In contrast, classification by a neural network restricts the element values of \mathbf{t} to be a restricted range of numbers that indicate the class of the input data. For example, the input data might be photographs of dogs and cats, and the classification problem is to classify the input as either a cat where $t_1 = 1$ and $t_2 = 0$ or a dog where $t_1 = 0$ and $t_2 = 1$. In this case the target vector is the 2×1 vector $\mathbf{t} = (t_1, t_2)^T$. There is typically no governing equation based on physics, instead the model \mathbf{w} is extracted from patterns detected in a large amount of input samples (\mathbf{X}, \mathbf{t}) .

2.1 Least Squares Inversion

The key ideas underlying least squares inversion will be explained by the simple example of determining the velocity of a motorcycle (see Figure 2.1a) as it travels down a gravel road of length 5 km. The procedure is to estimate the slowness $w = t/x$, i.e. the inverse speed, of the motorcycle by recording travel time t as a function of travel distance x . The timing measurements (in units of seconds) are recorded every 1 km on a gravel road next to the Bonneville Salt Flats ("https://en.wikipedia.org/wiki/Bonneville_Salt_Flats") in Utah (see Figure 2.1a). Five travel times and distances are recorded and stored in the 5×1 vectors \mathbf{t} and \mathbf{x} , respectively. The combined data set (\mathbf{x}, \mathbf{t}) is known as a *sample* and

contains errors in the traveltimes. We might also repeat the experiment at different sites (for example, see Figure 2.1c) to give us a new sample $(\mathbf{x}', \mathbf{t}')$; the total ensemble of samples is known as the *training data*.

2.1.1 Overdetermined, Inconsistent, and Ill-conditioned Equations

The relationship that links \mathbf{x} with \mathbf{t} will be hypothesized, for now, to be a linear model where

$$xw = t \rightarrow \begin{matrix} \mathbf{X} \\ \left[\begin{array}{c} x_{11} \\ x_{21} \\ x_{31} \\ x_{41} \\ x_{51} \end{array} \right] \end{matrix} \begin{matrix} \mathbf{w} \\ \left(w_1 \right) \end{matrix} = \begin{matrix} \mathbf{t}=\text{observed times} \\ \left[\begin{array}{c} t_1 \\ t_2 \\ t_3 \\ t_4 \\ t_5 \end{array} \right] \end{matrix} \rightarrow \begin{bmatrix} 0 \\ 1 \\ 2 \\ 3 \\ 4 \end{bmatrix} \left(w \right) = \begin{pmatrix} 0 \\ 0.102 \\ 0.33 \\ 0.50 \\ 0.80 \end{pmatrix}, \quad (2.1)$$

where \mathbf{X} is the 5×1 input matrix of travel distances, \mathbf{w} is the 1×1 slowness vector, and \mathbf{t} is the 5×1 vector of recorded traveltimes. The element value x_{ij} is equal to the distance traveled to the i^{th} recording station with the motorcycle traveling at the j^{th} slowness value. The distances (units of km) and times (units of hours) associated with the above equation are plotted in Figure 2.2a where \mathbf{t} is assumed to be polluted with measurements errors, denoted as noise. The goal is to find the *best* estimate of the slowness w .

Equation 2.1 is an $M \times N$ system of equations where $M = 5$ is the number of equations and $N = 1$ is the number of unknown slowness values. This is an *overdetermined* system of equations because $M > N$. It is also an *inconsistent* set of equations because there is no common solution. For example, the solution $w = .102 \text{ hr/km}$ to the 2nd-row equation contradicts the solution to the 3rd-row solution $w = .33/2 = .165 \text{ hr/km}$.

If there are many solutions that can nearly satisfy the same equations then this is known as an *ill-conditioned system* of equations. For example, if the modeling equation is $w_1 + 10^{-3}w_2 = t$, then $\delta t / \delta w_2 = 10^{-3} \rightarrow \delta w_2 = 10^3 \delta t$, which says that a small change in the traveltime δt will lead to a large change in the model w_2 . As an example, small traveltime errors in the data will lead to unrealistically large changes in the model. The term $\delta t / \delta w_i$ is denoted as a *Fréchet derivative* that characterizes the sensitivity of the data t to changes in the i^{th} model parameter.

2.1.2 Least Squares Solution

There is no exact solution to equation 2.1 so we need to define a criterion for *best solution*. The one we will discuss for now is the least squares solution¹ that minimizes the *objective*

¹The least squares solution is sometimes known as regression because it the least squares solution is the one that *regresses* to the average.

a) Road next to Bonneville Salt Flats



b) Suggestion



c) Great Gravel Road to Great Salt Lake



Figure 2.1: Pictures taken on author's motorcycle trip in Utah's West Desert with views of a) Bonneville Salt Flat region, b) wildlife sign, and c) the Great Salt Lake.

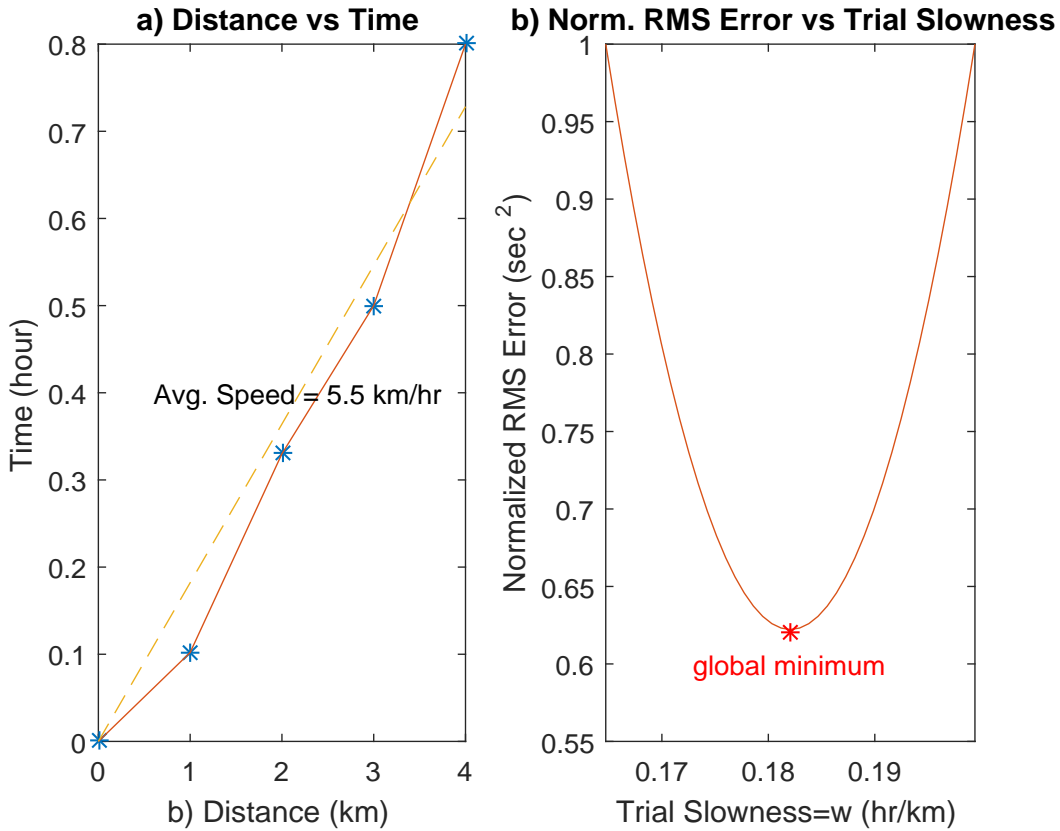


Figure 2.2: Plots for a) the observed $t(x)$ (blue stars) and b) misfit function ϵ for trial values of the slowness w . The dashed yellow line in a) represents the predicted times using the least squares estimate of the velocity and the red star in b) indicates the global minimum $\epsilon(\mathbf{w}^*)$ where $w^* = 1/5.5 = 0.182$ is the stationary point.

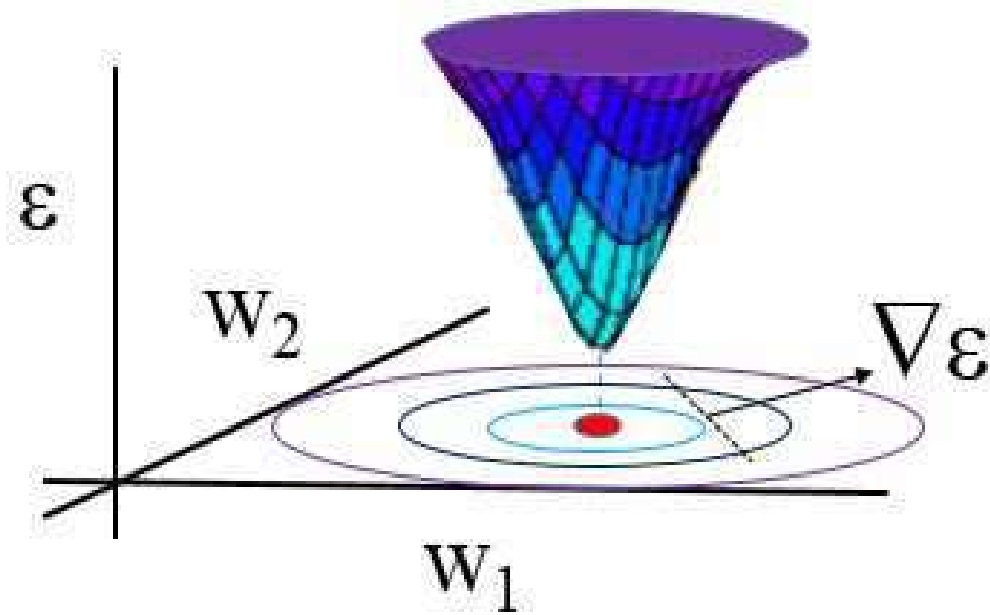


Figure 2.3: Misfit function and contours for $N = 2$, where the vertex defines the global minimum $\mathbf{w}^* = (w_1^*, w_2^*)$ at the red dot. The gradient $\nabla\epsilon = (\frac{\partial\epsilon}{\partial w_1}, \frac{\partial\epsilon}{\partial w_2})$ points along the steepest uphill direction and is perpendicular to the contour tangent (dashed line). See exercises 3-6.

function² ϵ , the sum of the squared residuals:

$$\begin{aligned}
 \epsilon &= \frac{1}{2} \overbrace{(\mathbf{X}\mathbf{w} - \mathbf{t})^T}^{\mathbf{r}^T} \overbrace{(\mathbf{X}\mathbf{w} - \mathbf{t})}^{\mathbf{r}}, \\
 &= \frac{1}{2} \mathbf{w}^T \mathbf{X}^T \mathbf{X} \mathbf{w} - \mathbf{t}^T \mathbf{X} \mathbf{w} + \frac{1}{2} \mathbf{t}^T \mathbf{t} \\
 &= \frac{1}{2} \sum_{i=1}^M \overbrace{((\mathbf{X}\mathbf{w})_i - t_i)^2}^{r_i^2},
 \end{aligned} \tag{2.2}$$

where ϵ is also denoted as a data misfit function. Here, \mathbf{r} is the $M \times 1$ residual vector which is the difference between the predicted times $\mathbf{X}\mathbf{w}$ and measured times \mathbf{t} . For $N = 1$, ϵ plots out as the parabola in Figure 2.2b for the motorcycle data, for $N = 2$ it describes the error bowl in Figure 2.3, and for $N > 2$ it describes an $N - 1$ -dimensional quadric surface.

The vertices of the parabola in Figure 2.2b and the error bowl in Figure 2.3 define the

²The machine learning community often denotes ϵ as the *loss function*, which can take many forms; ϵ is also known as a data misfit function if there is no regularization.

global minimum w^* where the gradient $\nabla\epsilon =$ is zero. This zero-slope condition³ is written as

$$\left. \frac{\partial\epsilon}{\partial w_k} \right|_{\mathbf{w}=\mathbf{w}^*} = 0, \quad \forall k, \quad (2.3)$$

where the k^{th} component of the $N \times 1$ *misfit gradient* vector is explicitly written as

$$\begin{aligned} \nabla\epsilon_k = \frac{\partial\epsilon}{\partial w_k} &= \sum_{i=1}^{M=5} r_i \frac{\partial r_i}{\partial w_k}, \\ &= \sum_{i=1}^5 r_i = \sum_{i=1}^5 \underbrace{\sum_{n=1}^N x_{in} w_n - t_i}_{r_i} \underbrace{\frac{\partial(\sum_{n=1}^N x_{in} w_n - t_i)}{\partial w_k}}_{\frac{\partial r_i}{\partial w_k} = \sum_{n=1}^N x_{in} \frac{\partial w_n}{\partial w_k} = \sum_{n=1}^N x_{in} \delta_{nk} = x_{ik}}, \\ &= \sum_{i=1}^5 x_{ik} \left(\sum_{n=1}^N x_{in} w_n - t_i \right), \end{aligned} \quad (2.4)$$

and the *Kronecker delta function* is defined to be $\delta_{ik} = 1$ if $i = k$, otherwise $\delta_{ik} = 0$. Notice that the outermost summation $\sum_{i=1}^5 x_{ik} r_i$ in the last line is over the row index i of the element x_{ik} , so in matrix-vector notation this is equivalent to multiplying the transpose matrix \mathbf{X}^T by the residual vector \mathbf{r} .

Setting the derivative in equation 2.4 to be zero $\forall k$ and rearranging gives the *normal equations*⁴

$$[\mathbf{X}^T \mathbf{X}] \mathbf{w} = \mathbf{X}^T \mathbf{t}. \quad (2.5)$$

The least squares solution to the normal equations is

$$\mathbf{w} = [\mathbf{X}^T \mathbf{X}]^{-1} \mathbf{X}^T \mathbf{t}, \quad (2.6)$$

which minimizes the sum of the squared residuals. See Box 2.1.1 for the least squares solution to equation 2.1.

³Equation 2.3 is considered to be a stationary condition because ϵ does not change much over a small range of w at the bottom of the, for example, green curve in Figure 2.2.

⁴These are called normal equations because they can be multiplied by \mathbf{w}^T and rearranged into the form $\mathbf{w}^T \mathbf{X}^T (\mathbf{X} \mathbf{w} - \mathbf{t}) = (\mathbf{X} \mathbf{w}, \mathbf{X} \mathbf{w} - \mathbf{t}) = 0$. This says that \mathbf{w}^* gives the predicted traveltime vector $\mathbf{X} \mathbf{w}^*$ that is perpendicular to the residual vector $\mathbf{X} \mathbf{w}^* - \mathbf{t}$. Here, the parentheses indicate the inner product between two vectors.

Box 2.1.1. Least Squares Solution to Equation 2.1

For equation 2.1, there is only one unknown in $\mathbf{w} = (w)$ so that the stationary condition for equation 2.2 is

$$\frac{\partial \epsilon}{\partial w} = \sum_{i=1}^5 x_{i1}(x_{i1}w - t_i) = 0. \quad (2.7)$$

Rearranging and solving for w gives

$$w = \frac{\overbrace{[\mathbf{X}^T \mathbf{X}]^{-1}}^1 \overbrace{\mathbf{X}^T \mathbf{t}}^5}{\sum_{i=1}^5 x_{i1}^2} = 0.182. \quad (2.8)$$

The stationary value $w^* = 0.182 \text{ hr/km}$ is at the global minimum indicated by the red star in Figure 2.2b.

2.1.3 Regularized Least Squares Solution

If there is a timing error δt_i at each of the i^{th} recording stations so that $t_i \rightarrow t_i^0 + \delta t_i$, then equation 2.8 becomes

$$w = \frac{\overbrace{\sum_{i=1}^5 x_{i1} t_i^0}^{w_o}}{\sum_{i=1}^5 x_{i1}^2} + \frac{\overbrace{\sum_{i=1}^5 x_{i1} \delta t_i}^{\delta w}}{\sum_{i=1}^5 x_{i1}^2}, \quad (2.9)$$

where w_o is the true slowness and δw is the slowness error caused by timing errors. If the distances x_{i1} are very small⁵ then the denominator in $\frac{1}{\sum x_{i1}^2}$ can be close to zero and so amplify timing errors $\delta t_i > x_{i1}$ into a large slowness error $|\delta w| = \left| \frac{\sum_{i=1}^5 x_{i1} \delta t_i}{\sum_{i=1}^5 x_{i1}^2} \right| \gg 0$. To avoid this *near-zero-divide* instability we add a positive *regularization* term $\eta > 0$ to the denominator so that equation 2.8 becomes the regularized solution:

$$w = \frac{\sum_{i=1}^5 x_{i1} t_i}{\sum_{i=1}^5 x_{i1}^2 + \eta}, \quad (2.10)$$

where η is typically set to be between 1% and 5% of the largest diagonal value of the matrix $\mathbf{X}^T \mathbf{X}$. This *regularization parameter* $\eta > 0$, also known as the *damping term*, increases the value of the denominator and thereby prevents an unstable near-zero divide and the strong amplification of data errors (Menke, 1984). The cost, however, is a loss of accuracy in the final solution. As discussed in Box 2.1.2, an unstable system of equations can be characterized by several properties: gentle slopes in the objective function $\frac{\partial \epsilon}{\partial w} \approx 0$ and large condition numbers associated with $\mathbf{X}^T \mathbf{X}$. See exercises 1-2.

⁵For example, assume that the five timing stations are spaced at 0.001 km intervals. In this case the timing errors can be very large compared to x_{i1} and so generate enormous slowness errors.

Box 2.1.2. Small Curvatures and Large Condition Numbers of $\mathbf{X}^T \mathbf{X} \rightarrow$ Unstable Solutions

The green curves in Figure 2.4 depict a) stable and b) less-stable misfit functions based on the magnitude of x_{i1} in \mathbf{X} . The larger value of $x_{i1} = 0.001$ in Figure 2.4a leads to the parabola with steeper sides (green line) compared to the gently dipping one in Figure 2.4b where $x_{i1} = 0.00011$. The flatter green parabola in b) means that there is a wider range of w values, i.e. a more unstable solution, that can give almost the same misfit error as that at the global minimum (green star). Equivalently, this means that a small amount of data noise can lead to a large change in the model. This is an example of an ill-conditioned system of equations that forms the objective function.

If the curvature $\frac{\partial^2 \epsilon}{\partial w^2}$ is close to zero at \mathbf{w}^* :

$$\frac{\partial^2 \epsilon}{\partial w^2} = \lim_{\delta w \rightarrow 0} \left[\frac{\epsilon}{\partial w} \Big|_{w=w^*+\delta w} - \frac{\epsilon}{\partial w} \Big|_{w=w^*} \right] \approx 0, \quad (2.11)$$

then the slope $\frac{\partial \epsilon}{\partial w}$ hardly changes around the zero-slope point w^* . This means that there are many solutions that almost minimize the sum of squared residuals. For equation 2.7 the curvature is

$$\frac{\partial^2 \epsilon}{\partial w^2} = \sum_{M=1}^5 x_{i1}^2, \quad (2.12)$$

which confirms that $\frac{\partial^2 \epsilon}{\partial w^2} \approx 0$ when $|x_{i1}| \approx 0 \forall i$.

A general indicator of an unstable system of equations is that the condition number $|\lambda_{max}/\lambda_{min}|$ of the matrix $\mathbf{X}^T \mathbf{X}$ is large, where λ_{max} (λ_{min}) is the maximum (minimum) eigenvalue of the matrix. Recall that the i^{th} orthogonal eigenvector \mathbf{x}_i of the symmetric positive definite matrix⁶ $\mathbf{X}^T \mathbf{X}$ is defined as

$$\mathbf{X}^T \mathbf{X} \mathbf{x}_i = \lambda_i \mathbf{x}_i, \quad (2.13)$$

where λ_i is the eigenvalue for the eigenvector \mathbf{x}_i . This means that the solution to the $N \times N$ normal equations 2.5 can be expanded into a sum of N weighted eigenvectors

$$\mathbf{w} = \sum_{i=1}^N \beta_i \mathbf{x}_i. \quad (2.14)$$

The unknown coefficients β_i can be found by inserting equation 2.14 into the normal equations $\mathbf{X}^T \mathbf{X} \mathbf{w} = \mathbf{X}^T \mathbf{t}$, taking its dot product with the i^{th} eigenvector \mathbf{x}_i , and solving for β_i to get

$$\beta_i = \frac{(\mathbf{x}_i, \mathbf{X}^T \mathbf{t})}{\lambda_i}. \quad (2.15)$$

This says that if there are small timing errors $\delta \mathbf{t}$ in $(\mathbf{x}_i, \mathbf{X}^T (\mathbf{t} + \delta \mathbf{t}))$ then they will strongly amplified if the i^{th} eigenvalue λ_i is small compared to errors associated with much larger eigenvalues. Thus, normal equations with condition numbers $|\lambda_{max}|/|\lambda_{min}|$ larger than about 10^4 should be regularized.

The damping term η in equation 2.10 was introduced in an ad hoc fashion to mitigate large errors in w due to an unstable system of equations. A more rigorous derivation is obtained by defining the objective function to be the weighted sum of data misfit $\mathbf{r}^T \mathbf{r} = (\mathbf{X}\mathbf{w} - \mathbf{t})^T (\mathbf{X}\mathbf{w} - \mathbf{t})$ (green curves in Figure 2.4) and model penalty $\mathbf{w}^T \mathbf{w}$ (red curves in Figure 2.4) functions:

$$\begin{aligned} \epsilon &= \overbrace{\frac{1}{2}(\mathbf{X}\mathbf{w} - \mathbf{t})^T (\mathbf{X}\mathbf{w} - \mathbf{t})}^{\text{data misfit}=\frac{1}{2}\sum_i r_i^2} + \overbrace{\frac{1}{2}\eta\mathbf{w}^T \mathbf{w}}^{\text{model penalty}=\frac{1}{2}\eta\sum_i w_i^2}, \\ &= \frac{1}{2}\mathbf{w}^T [\mathbf{X}^T \mathbf{X} + \eta \mathbf{I}] \mathbf{w} - \mathbf{t}^T \mathbf{X} \mathbf{w} + \frac{1}{2} \mathbf{t}^T \mathbf{t}, \end{aligned} \quad (2.16)$$

which plots out as the blue curves in Figure 2.4. The derivative of equation 2.16 with respect to w_k yields the k^{th} component of the *misfit gradient*:

$$\begin{aligned} \frac{\partial \epsilon}{\partial w_k} &= \frac{1}{2} \frac{\partial \sum_i r_i^2}{\partial w_k} + \frac{\eta}{2} \sum_i \frac{\partial w_i^2}{\partial w_k}, \\ &= \underbrace{\sum_i x_{ik} r_i}_{(\mathbf{X}^T (\mathbf{X}\mathbf{w} - \mathbf{t}))_k} + \underbrace{\eta w_k}_{(\eta \mathbf{I} \mathbf{w})_k}, \end{aligned} \quad (2.17)$$

where \mathbf{I} is the $N \times N$ identity matrix. Setting this gradient component to zero $\forall k \in [1, 2 \dots N]$ and rearranging yields the *regularized normal equations*

$$[\mathbf{X}^T \mathbf{X} + \eta \mathbf{I}] \mathbf{w} = \mathbf{X}^T \mathbf{t}, \quad (2.18)$$

which is solved by the regularized least squares solution:

$$\mathbf{w} = [\mathbf{X}^T \mathbf{X} + \eta \mathbf{I}]^{-1} \mathbf{X}^T \mathbf{t}. \quad (2.19)$$

As a special case, setting the derivative in equation 2.17 to zero, renaming $w_k \rightarrow w$ and solving for w gives equation 2.10.

The interpretation of equation 2.16 is that large values of η will favor solutions \mathbf{w} that are near the origin, but at the expense of a larger data misfit function $\|\mathbf{r}\|^2$. As an example, the global minimum w^* (blue star) for the blue curve in Figure 2.4b is closer to the origin than that in Figure 2.4a because η is 20% for b) and only 10% for a). However, if η is not too large then the damped solution (blue star) is close enough to the undamped solution (green star) with an acceptable loss of precision.

2.1.4 Gradient of ϵ

The gradient vector $\nabla \epsilon$ in Figure 2.3 points uphill along the steepest ascent direction. To prove this, define the vector

$$\mathbf{w} = \mathbf{w}_o + \Delta \mathbf{w}, \quad (2.20)$$

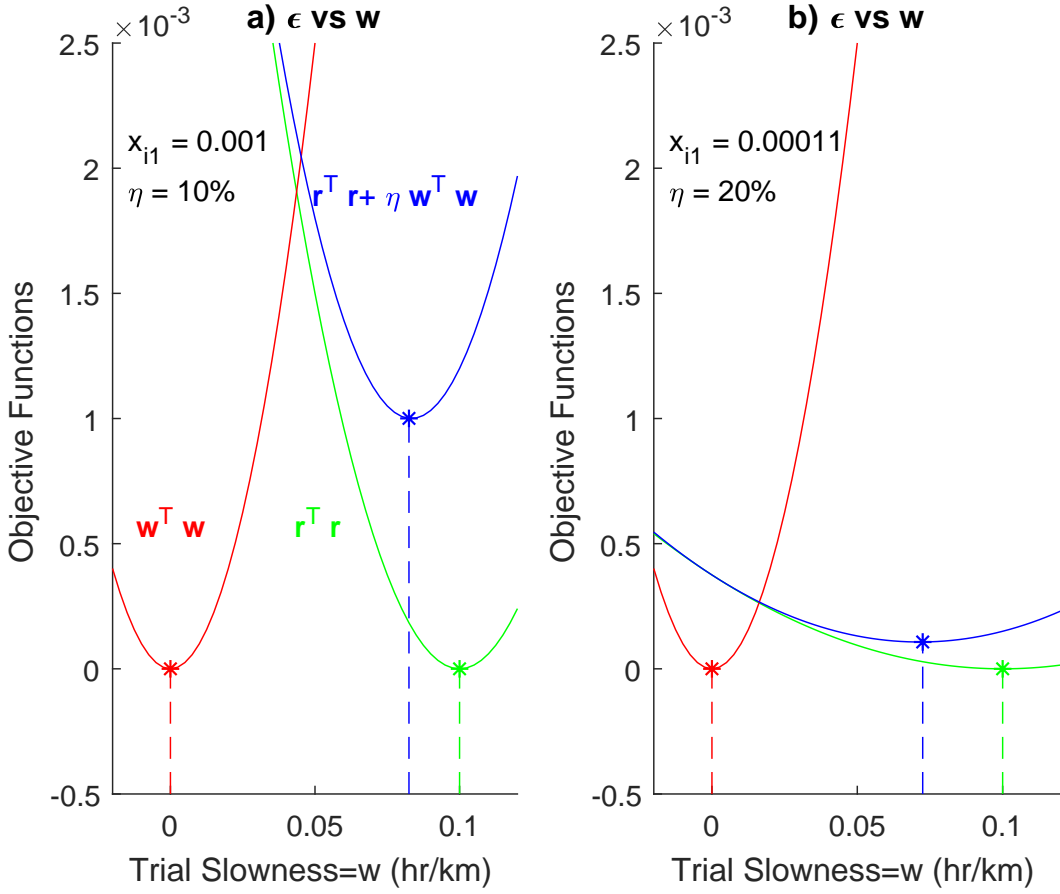


Figure 2.4: Values of the objective functions $\mathbf{r}^T \mathbf{r}$ (green curves), $\mathbf{w}^T \mathbf{w}$ (red curves) and $\mathbf{r}^T \mathbf{r} + \eta \mathbf{w}^T \mathbf{w}$ (blue curves) plotted against trial values of w for the motorcycle equations 2.1. Here, there is no noise in the data so that $(\mathbf{X}^T \mathbf{w} - \mathbf{t})^T (\mathbf{X}^T \mathbf{w} - \mathbf{t}) = 0$ at the global minimum denoted by the green stars. In contrast, the minimizer w^* for $(\mathbf{X} \mathbf{w} - \mathbf{t})^T (\mathbf{X} \mathbf{w} - \mathbf{t}) + \eta \mathbf{w}^T \mathbf{w}$ is non-zero and is closer to $w = 0$ for b) $\eta = 20\%$ compared to a) $\eta = 10\%$. Larger values of η reward solutions with smaller length $\mathbf{w}^T \mathbf{w} \approx 0$. In addition, the slope of the green parabola is gentler for b) smaller values of $x_{i1} = .00011$ compared to larger values in a) $x_{i1} = .001$ in a).

where $\Delta \mathbf{w}$ is a specified vector with very small magnitude. Expanding $\epsilon(\mathbf{w})$ in a Taylor series about \mathbf{w}_o , truncating after the first-order term in $\Delta \mathbf{w}$ and rearranging gives:

$$\epsilon(\mathbf{w}) - \epsilon(\mathbf{w}_o) = \left. \nabla \epsilon(\mathbf{w})^T \right|_{\mathbf{w}=\mathbf{w}_o} \Delta \mathbf{w}, \quad (2.21)$$

where $\nabla \epsilon = (\frac{\partial \epsilon}{\partial w_1}, \frac{\partial \epsilon}{\partial w_2} \dots \frac{\partial \epsilon}{\partial w_N})^T$ and $\Delta \mathbf{w} = (w_1, w_2 \dots w_N)^T$. If $\Delta \mathbf{w}$ is pointing to a close neighboring point on the same contour that passes through \mathbf{w}_o then $\epsilon(\mathbf{w}_o + \Delta \mathbf{w}) = \epsilon(\mathbf{w}_o)$, which implies $(\nabla \epsilon(\mathbf{w}_o + \Delta \mathbf{w}), \Delta \mathbf{w}) = 0$. This means that $\nabla \mathbf{w}$ is perpendicular to the contour's tangent vector at \mathbf{w}_o . Furthermore, if we redefine $\Delta \mathbf{w}$ to be a unit vector now pointing uphill and perpendicular to the contour at \mathbf{w}_o then $\epsilon(\mathbf{w}) - \epsilon(\mathbf{w}_o) = \nabla \epsilon^T \Delta \mathbf{w} = |\nabla \epsilon| > 0$.

As illustrated in Figure 2.3, the gradient vector points uphill along the steepest ascent direction. Therefore, $-\nabla \epsilon$ points downhill along the steepest descent direction as shown in Figure 2.5. This compares to the regularized gradient in equation 2.17 which points more towards the origin in Figure 2.5 because it is a weighted sum of the misfit gradient and the penalty function $\mathbf{w}^T \mathbf{w}$, which points toward the origin. In fact, if $\eta \gg 0$ then the penalty term dominates and $\nabla \epsilon$ points at the origin.

The Gauss-Newton arrow $\Delta \mathbf{w}$ in Figure 2.5 points toward the global minimum at \mathbf{w}^* with

$$\Delta \mathbf{w} = [\mathbf{X}^T \mathbf{X}]^{-1} \mathbf{X}^T \Delta \mathbf{t}, \quad (2.22)$$

where $\Delta \mathbf{t} = \mathbf{t} - \mathbf{t}'$, $\Delta \mathbf{w} = \mathbf{w}^* - \mathbf{w}'$ and

$$\mathbf{X} \mathbf{w}' = \mathbf{t}'. \quad (2.23)$$

Equation 2.22 can be proven by recalling that the optimal \mathbf{w}^* for the given traveltimes \mathbf{t} satisfies $\mathbf{w}^* = [\mathbf{X}^T \mathbf{X}]^{-1} \mathbf{X}^T \mathbf{t}$. The sub-optimal model \mathbf{w}' predicts the traveltimes \mathbf{t}' that exactly satisfy equation 2.23 but these traveltimes are not the same as the recorded ones \mathbf{t} . Multiplying equation 2.23 by \mathbf{X}^T and inverting gives

$$\mathbf{w}' = [\mathbf{X}^T \mathbf{X}]^{-1} \mathbf{X}^T \mathbf{t}'. \quad (2.24)$$

Subtracting \mathbf{w}' from $\mathbf{w}^* = [\mathbf{X}^T \mathbf{X}]^{-1} \mathbf{X}^T \mathbf{t}$ gives the Gauss-Newton direction $\Delta \mathbf{w} = \mathbf{w}^* - \mathbf{w}'$ where

$$\begin{aligned} \Delta \mathbf{w} &= [\mathbf{X}^T \mathbf{X}]^{-1} \mathbf{X}^T \mathbf{t} - [\mathbf{X}^T \mathbf{X}]^{-1} \mathbf{X}^T \mathbf{t}', \\ &= [\mathbf{X}^T \mathbf{X}]^{-1} \mathbf{X}^T \overbrace{(\mathbf{t} - \mathbf{t}')}^{\Delta \mathbf{t}}. \end{aligned} \quad (2.25)$$

Substituting $\Delta \mathbf{w} = \mathbf{w}^* - \mathbf{w}'$ into the above equation and rearranging gives the Gauss-Newton update formula for non-linear inversion:

$$\mathbf{w}^* = \mathbf{w}' + [\mathbf{X}^T \mathbf{X}]^{-1} \mathbf{X}^T \Delta \mathbf{t}. \quad (2.26)$$

This formula is the starting point for many gradient descent methods that iteratively search in downhill directions for the global minimum. See section 2.2.

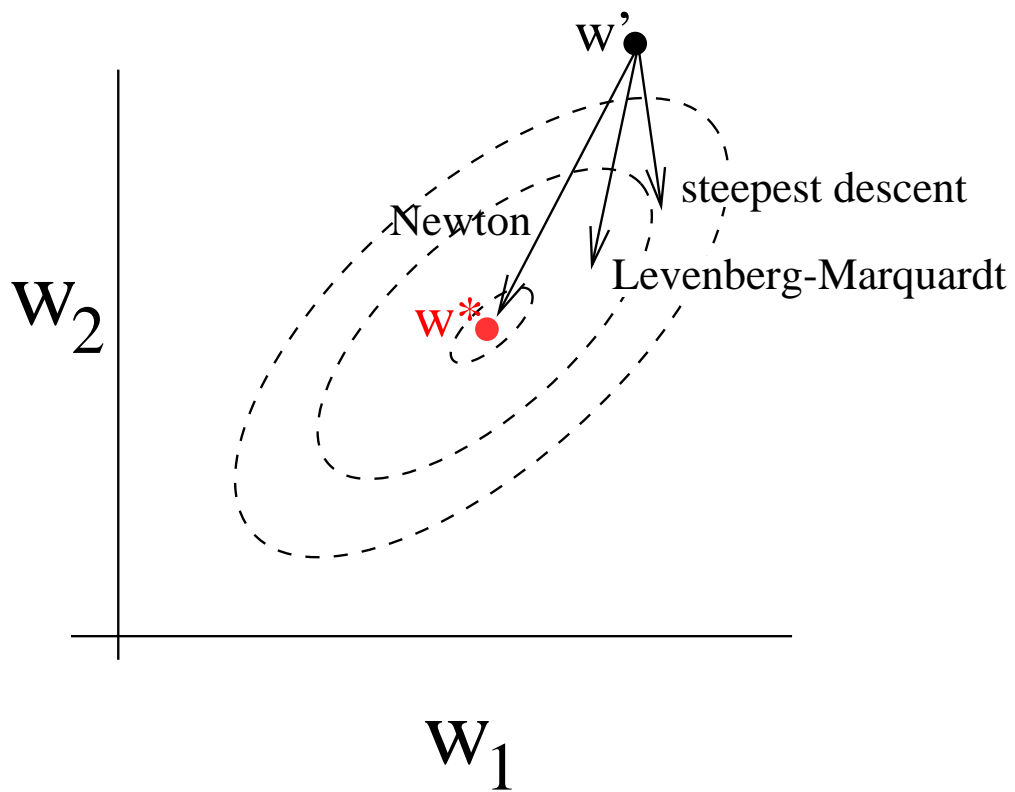


Figure 2.5: Elliptical contours associated with $\epsilon(\mathbf{w})$ and the gradient vectors associated with the Gauss-Newton, Levenberg-Marquardt, and steepest descent directions. Here, the Levenberg-Marquardt gradient is also known as the regularized gradient.

2.1.5 Preconditioning

If the number of unknowns $N = 2$ so that $\mathbf{w} = (w_1, w_2)$, then the objective function $\epsilon = 1/2 \|\mathbf{X}\mathbf{w} - \mathbf{t}\|^2$ can be described by the second-order polynomial

$$\epsilon = aw_1^2 + bw_2^2 + cw_1w_2 + dw_1 + ew_2 + f, \quad (2.27)$$

where (a, b, c, d, e, f) are functions of the input data. As a simple example, set $c = d = e = f = 0$ so equation 2.27 can be rewritten as

$$\epsilon = \begin{pmatrix} w_1 & w_2 \end{pmatrix} \begin{bmatrix} a & 0 \\ 0 & b \end{bmatrix} \begin{pmatrix} w_1 \\ w_2 \end{pmatrix}, \quad (2.28)$$

so that ϵ plots out as the concentric circles in Figure 2.6a for $a = b$, or as the ellipses in Figure 2.6b for $(a, b) = (1, .01)$. If $a \gg b$ then the ellipse become much taller than it is wide and leads to unstable solutions as discussed in Box 2.1.2. For example, a small value of b says that $|\frac{\partial \epsilon}{\partial w_2}|, |\frac{\partial^2 \epsilon}{\partial w_2^2}| \approx 0$ so that large changes in w_2 lead to small changes in ϵ . Another way of saying this is that small changes in δt and, consequently, ϵ can lead to large changes in w_2 . In contrast, the steep dip of the ellipse along the w_1 axis says that $|\partial \epsilon / \partial w_1| \gg 0$ so that w_1 is not affected too much by small timing errors.

The 2×2 matrix \mathbf{X} associated with equation 2.28 is given by

$$\mathbf{X} = \begin{bmatrix} a^{1/2} & 0 \\ 0 & b^{1/2} \end{bmatrix}. \quad (2.29)$$

Here, \mathbf{X} is severely ill-conditioned if $|a^{1/2}| \gg \gg |b^{1/2}|$ so that the associated ellipses of ϵ appear as long-narrow valleys. To transform these narrow valleys into rounder contours a diagonal *preconditioner matrix* \mathbf{C}

$$\mathbf{C} = \begin{bmatrix} a^{-1/2} & 0 \\ 0 & b^{-1/2} \end{bmatrix}. \quad (2.30)$$

can be multiplied by the original equations to give

$$\mathbf{C}\mathbf{X}\mathbf{w} = \mathbf{C}\mathbf{t}, \quad (2.31)$$

where $[\mathbf{C}]_{ij} = \frac{1}{[\mathbf{X}]_{ii}} \delta_{ij}$. In this case, $\mathbf{C}\mathbf{X} = \mathbf{I}$ and has unit-valued eigenvalues $\lambda_1 = \lambda_2 = 1$ where the condition number $|\lambda_2|/|\lambda_1| = 1$. Thus, the associated objective function of $\frac{1}{2} \|\mathbf{C}(\mathbf{X}\mathbf{w} - \mathbf{t})\|^2$ plots out as round circles.

Normalizing each row of \mathbf{X} by $\mathbf{C}\mathbf{X}$ so it has about the same strength as the other ones is one type of preconditioning method⁷ for accelerating convergence of iterative gradient methods. Preconditioning the data is also used in neural networks (see Chapter 6) where it is recommended that there should be the same number of data examples for any one type. A similar preconditioning is used for illumination compensation of seismic data (Rickett, 2003) where the weak strength of deep reflections is compensated to balance out the amplitudes of much stronger early arrivals recorded near the source.

⁷Using a diagonal preconditioner is sometimes known as scaling (Nocedal and Wright, 1999)

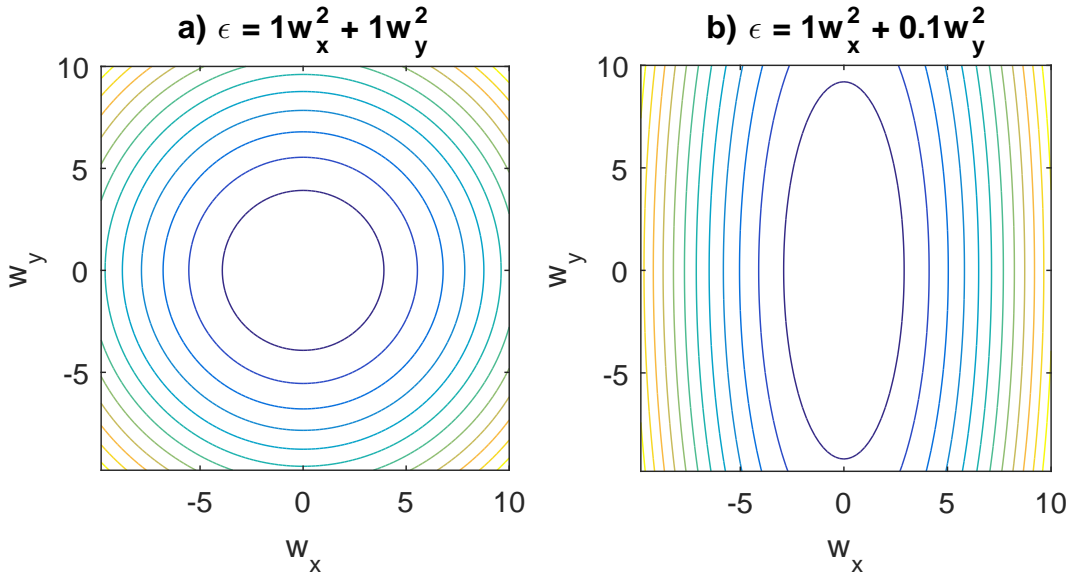


Figure 2.6: Contours of objective function $aw_1^2 + bw_2^2$ for a) $(a,b) = (1,1)$ and b) $(a,b) = (1,0.1)$.

If the system of equations is that for the normal equations then, in general, \mathbf{C} is selected so that

$$\mathbf{C}[\mathbf{X}^T\mathbf{X}]\mathbf{C}^{-1}\mathbf{C}\mathbf{w} = \mathbf{C}\mathbf{X}^T\mathbf{t}, \quad (2.32)$$

where the eigenvalues of $\mathbf{C}[\mathbf{X}^T\mathbf{X}]\mathbf{C}^{-1}$ are more favorable for convergence. For example, construct \mathbf{C} so that the condition number of $\mathbf{C}[\mathbf{X}^T\mathbf{X}]\mathbf{C}^{-1}$ is much smaller than that for $[\mathbf{X}^T\mathbf{X}]$. The condition number can also be lowered by clustering the eigenvalues of $\mathbf{C}[\mathbf{X}^T\mathbf{X}]\mathbf{C}^{-1}$ (Nocedal and Wright, 1999).

2.1.6 Overfitting Data

Equation 2.1 assumes that the simple one-dimensional model $\mathbf{w} = (w)$ can explain the data. The result is a system of equations that is inconsistent because of, presumably, timing errors. However, the timing expert might disagree and say the data errors are too small to account for deviations from the dashed line in Figure 2.2a: we must have used the wrong physics to explain the data! Instead of the linear model $t = x/v$, a quadratic model with polynomial order $P = 2$ in x might be a better fit where

$$t = w_1x + w_2x^2. \quad (2.33)$$

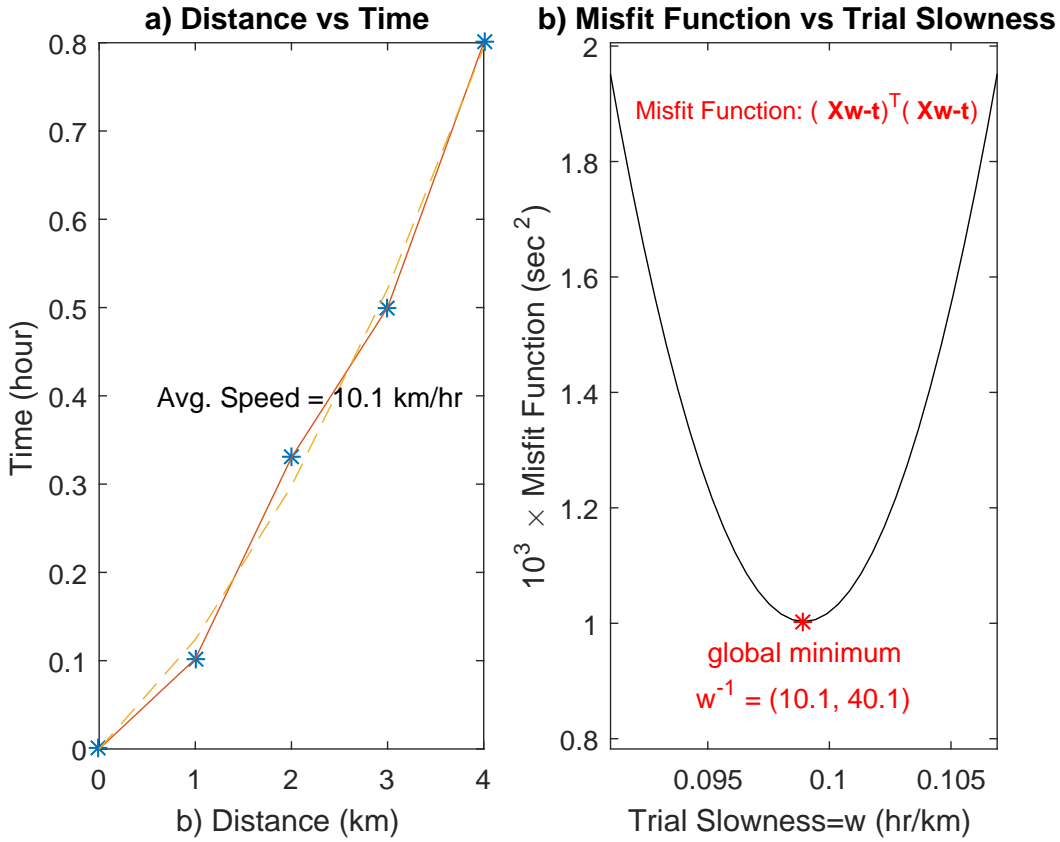


Figure 2.7: Same as Figure 2.2 except the quadratic equation $t = w_1x + w_2x^2$ is used to fit the motorcycle data. In this case, $\mathbf{w}^* = (0.099, 0.025) = (1/10.1, 1/40.1)$ and ϵ is only plotted along the slowness component w_1 , with $w_2 = 0.025$.

In this case, the corresponding system of equations for the motorcycle data becomes

$$\underbrace{\begin{bmatrix} x_{11} & x_{11}^2 \\ x_{21} & x_{21}^2 \\ x_{31} & x_{31}^2 \\ x_{41} & x_{41}^2 \\ x_{51} & x_{51}^2 \end{bmatrix}}_{\mathbf{X}} \underbrace{\begin{pmatrix} w_1 \\ w_2 \end{pmatrix}}_{\mathbf{w}} = \underbrace{\begin{pmatrix} t_1 \\ t_2 \\ t_3 \\ t_4 \\ t_5 \end{pmatrix}}_{\mathbf{t}=\text{observed times}} \rightarrow \begin{bmatrix} 0 & 0 \\ 1 & 1^2 \\ 2 & 2^2 \\ 3 & 3^2 \\ 4 & 4^2 \end{bmatrix} \begin{pmatrix} w_1 \\ w_2 \end{pmatrix} = \begin{pmatrix} 0 \\ 0.102 \\ 0.33 \\ 0.50 \\ 0.80 \end{pmatrix}. \quad (2.34)$$

The intuitive motivation for this quadratic model is that the motorcycle speed increases towards the end of the road as it becomes more paved. Thus, the quadratic term w_2x^2 dominates when x is large near the end of the road.

As an example, Figure 2.7 depicts the results from fitting the quadratic equation 2.33 to the motorcycle data. Comparing Figures 2.2 and 2.7, the quadratic model gives the closest fit to the data in a) and has about 1/7 the misfit error of the linear model. This result suggests that the misfit error can be further decreased by increasing the order P of the polynomial model. Unfortunately, increasing $P > M$ will yield an *underdetermined*

system of equations where there are more unknowns P than the number M of equations⁸. The least squares solution will then give a misfit error of zero, but at the cost of *overfitting* the data where the complexity of the model exceeds that of the noise-free data. In this case the higher-order polynomials are being fitted to the rapidly varying noise in the data.

Instead of a polynomial, one might suggest a high N -dimensional linear model:

$$t_i = \sum_{j=1}^N x_{ij} w_j, \quad (2.35)$$

where \mathbf{w} is the $N \times 1$ model vector and x_{ij} are unphysical weights specified by the mechanic. If these weights are specified to give rise to an $\mathbf{X}^T \mathbf{X}$ matrix that is invertible then this model will also overfit the data. For example, the two equations $w_1 = 1$ and $w_1 = 2$ are inconsistent and generate non-intersecting lines in the coordinate-space (w_1, w_2) . Increasing the number of unknowns to include w_2 so that the model equations are $w_1 = 1$ and $w_1 + .4w_2 = 2$ gives a consistent set of equations where the associated lines have a common intersection in (w_1, w_2) .

Sanity Test for Overfitting

How can we determine if the complexity parameter P of the proposed model is higher than that in the noiseless data? The machine learning community tries to answer this question by randomly dividing the entire training data set into several parts: *training data*, *test data* and *validation data*. One possibility is to use 90% of the original data for validation and determine the best model \mathbf{w} and regularization parameters. The remaining 10% is used for testing. For the motorcycle example this would mean repeating the time trials many times to get a large set of training data.

Wikipedia makes the following claims (https://en.wikipedia.org/wiki/Training_test_and_validation_sets): *Validation datasets can be used for regularization by early stopping: stop training when the error on the validation dataset increases, as this is a sign of overfitting to the training dataset. This simple procedure is complicated in practice by the fact that the validation dataset's error may fluctuate during training, producing multiple local minima. This complication has led to the creation of many ad-hoc rules for deciding when overfitting has truly begun. Finally, the test dataset is a dataset used to provide an unbiased evaluation of a final model fit on the training dataset.*

Confusingly the terms test dataset and validation dataset are sometimes used with swapped meaning. As a result it has become commonplace to refer to the set used in iterative training as the test/validation set and the set that is used for hyperparameter tuning as the holdout set.

As an example of tuning the architecture of the model, consider a model \mathbf{w} with complexity P that is first fitted to the validation data, and then it is tested against the holdout data. The misfit error for the holdout data is denoted as $\epsilon(P)$. This procedure is repeated except a model with different complexity value P' is computed from the training data, and

⁸In fact, if $P = N - 1$ and a column of 1's, also known as the bias vector, is appended to the matrix then its transpose is a Vandermonde matrix (Golub and van Loan, 1996), which is notoriously unstable for large values of P .



Figure 2.8: Ideal misfit error ϵ plotted against the order P of the polynomial. The misfit values ϵ are for the holdout data using the parameters obtained from the distinct training dataset.

then tested against the holdout data to give $\epsilon(P')$. The misfit errors $\epsilon(P)$ are plotted as a function of the complexity parameter P , which is shown in Figure 2.8 as an idealized plot.

If the model complexity is less than that of the noiseless data then the misfit error should decrease as P increases as long as the validation data is of the same type as the test data. A counterexample is if the training data were drawn from time trials of road motorcycles while those from the holdout data were drawn from time trials of all-terrain vehicles with four-wheel drive.

If the model complexity P becomes greater than that of the noiseless data, then the optimal model w^* obtained from the training data has largely been fitted to the noise in that data. This is realized on the rightside of the inflection in Figure 2.8 as the misfit error from the holdout data increases. A strategy for dividing up the data into different sets is also used for cross-validation studies (Golub and von Matt, 1997). See https://en.wikipedia.org/wiki/Training_test_and_validation_sets for further details.

2.1.7 Inclusion of Bias Factor

Assume that the timing clock was not properly calibrated before the motorcycle trial so that the registered starting time consisted of an error of $\Delta\tau = 0.1$ hour for the $x = 0$ position. This time-shift error will be inherited by the times recorded at the other 4 stations. Unless this bias is corrected, the estimated velocity errors will be large.

To account for this timing *bias* the linear model in equation 2.1 should be changed to

$$t = w_0 + w_1x, \quad (2.36)$$

where w_0 is the bias term. In this case the system of equations in equation 2.1 becomes

$$\overbrace{\begin{bmatrix} 1 & x_{11} \\ 1 & x_{21} \\ 1 & x_{31} \\ 1 & x_{41} \\ 1 & x_{51} \end{bmatrix}}^{\mathbf{X}} \overbrace{\begin{pmatrix} w_0 \\ w_1 \end{pmatrix}}^{\mathbf{w}} = \begin{pmatrix} t_1 \\ t_2 \\ t_3 \\ t_4 \\ t_5 \end{pmatrix}, \quad (2.37)$$

where the least squares solution (w_0^*, w_1^*) can now be computed to accurately predict the data.

The importance of accurately estimating the bias term w_0 is similar to estimating an accurate starting model for seismic inversion. That is, cycle-skipping problems can be mitigated if an accurate low-wavenumber model is used to account for the bulk of an event's traveltime (Schuster, 2017). As we will discover in later chapters, almost all neural network models include a bias term in their mathematical formulations (Bishop, 2007).

2.2 Steepest Descent Optimization

Defining $\mathbf{w}^* \rightarrow \mathbf{w}^{(k+1)}$, $\mathbf{w}' \rightarrow \mathbf{w}^{(k)}$, $\mathbf{t}' = \mathbf{t}^{(k)}$, and $\Delta\boldsymbol{\tau}^{(k)} = \mathbf{t}^{(k)} - \mathbf{t}$ in equation 2.26 gives the Gauss-Newton iteration formula (Nocedal and Wright, 1999)

$$\mathbf{w}^{(k+1)} = \mathbf{w}^{(k)} - [\mathbf{X}^T \mathbf{X}]^{-1} \mathbf{X}^T \Delta\boldsymbol{\tau}^{(k)}, \quad (2.38)$$

where $\Delta\boldsymbol{\tau}^{(k)} = \mathbf{t}^{(k)} - \mathbf{t}$ is the data-residual vector at the k^{th} iteration. For a linear system of equations with a well-conditioned $[\mathbf{X}^T \mathbf{X}]$, the global minimum should be reached in one iteration. However, the inverse to $[\mathbf{X}^T \mathbf{X}]$ is too expensive to compute for large data sets so its inverse is approximated by the diagonal matrix $[\mathbf{X}^T \mathbf{X}]_{ij}^{-1} \approx \frac{1}{[\mathbf{X}^T \mathbf{X}]_{ii}^2} \delta_{ij}$ to give the preconditioned steepest descent formula:

$$w_i^{(k+1)} = w_i^{(k)} - \alpha \frac{1}{[\mathbf{X}^T \mathbf{X}]_{ii}^2} (\mathbf{X}^T \Delta\boldsymbol{\tau}^{(k)})_i, \quad (2.39)$$

where α is a step length that can be numerically determined by a numerical line search (Gill, 1981) that $\mathbf{w}^{(k+1)}$ reduces the misfit error as much as possible⁹. Unlike the Gauss-Newton formula for linear systems, equation 2.39 does not typically give the right answer

⁹For a linear system of equations, there is an analytic formula for the step length, but it is typically not used for the non-linear problems addressed by the neural network method.

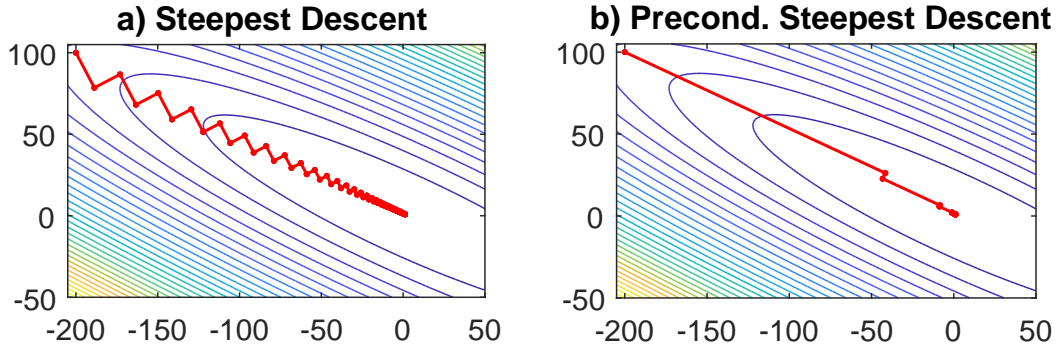


Figure 2.9: Iterative solutions to equation 2.41 by the a) steepest descent and b) preconditioned steepest descent methods.

for one *iteration*. Therefore this formula is used repeatedly to give updated solutions until convergence. The sequence of steps is as follows.

1. Specify $k = 0$ and a starting *guessed* solution $\mathbf{w}^{(0)}$. The starting solution is used to give the predicted traveltimes $\mathbf{w}^{(0)} = \mathbf{t}^{(0)}$ and the residual $\Delta\boldsymbol{\tau}^{(0)} = \mathbf{t}^{(0)} - \mathbf{t}$.
2. Equation 2.39 is used to estimate $\mathbf{w}^{(k+1)}$ after a suitable step length is computed. We will discuss step lengths in the next chapter, but for now conveniently set $\alpha = .01$
3. Compute the new predicted traveltime vector $\mathbf{w}^{(k+1)} = \mathbf{t}^{(k+1)}$ and the residual $\Delta\boldsymbol{\tau}^{(k+1)} = \mathbf{t}^{(k+1)} - \mathbf{t}$. If the length $\|\mathbf{r}^{(k+1)}\|$ of the residual vector falls below some specified limit, stop. Otherwise redefine $k := k + 1$ and repeat steps 2-3 until convergence.

If regularization and preconditioning are used then the preconditioned-regularized steepest descent formula is (see exercise 11):

$$w_i^{(k+1)} = w_i^{(k)} - \alpha \frac{1}{[\mathbf{X}^T \mathbf{X}]_{ii}^2} (\mathbf{X}^T \Delta\boldsymbol{\tau}^{(k)} + \eta \mathbf{w}^{(k)})_i, \quad (2.40)$$

where η is the regularization parameter. The next chapter will examine the properties of the steepest descent method applied to a non-linear system of equations, which is the optimization technique for the neural network method.

Figure 2.9 presents the results of using both the steepest descent and preconditioned steepest descent methods in solving an overdetermined system of equations. In this case the system of equations is given by

$$\begin{bmatrix} 4 & 6 \\ 2 & 5 \\ 0 & 3 \\ 1 & 4 \end{bmatrix} \begin{pmatrix} w_1 \\ w_2 \end{pmatrix} = \begin{pmatrix} 10 \\ 7 \\ 3 \\ 5 \end{pmatrix}, \quad (2.41)$$

and it is obvious that the preconditioned steepest descent is more than 5 times faster than the steepest descent method. A fragment of a MATLAB steepest descent code is below.


```

H=X'*X;
for i=1:100
    g=X'*(X*w-t);          % gradient
    alpha=g'*g/(g'*H*g); % step length
    w=w-alpha*g;           % model update
    r=X*w-t;               % residual
    If r*r <=.0001;i=100;end
end

```

where $\mathbf{H} = \mathbf{X}^T \mathbf{X}$ is the Hessian matrix and $\alpha = \mathbf{g}^T \mathbf{g} / (\mathbf{g}^T \mathbf{H} \mathbf{g})$ is the exact step length for an objective function that is exactly quadratic in the model parameters. This step-length formula is derived in Appendix 2.5 but is typically not used if the modeling parameters are not linearly related to the data, which is almost always the case for neural networks or seismic inversion.

2.3 Summary

Systems of equations $\mathbf{X}\mathbf{w} = \mathbf{t}$ can be ill-conditioned, inconsistent, and overdetermined. In these cases the regularized least squares solution \mathbf{w}^* minimizes a weighted combination of data misfit $\|\mathbf{X}\mathbf{w} - \mathbf{t}\|^2$ and penalty $\eta \|\mathbf{w}\|^2$, where η is the regularization parameter. A *bias column vector* is often appended to \mathbf{X} to account for bulk shifts in the input data \mathbf{t} . The \mathbf{w}^* solves the regularized normal system of equations in equation 2.16, which is now an $N \times N$ *consistent set of equations*. The solution avoids unstable models far from the origin, but at the loss of some precision for noiseless data. Another way to reduce the condition number is by applying the precondition matrix \mathbf{C} to $\mathbf{X}^T \mathbf{X}$ such that $\mathbf{C}[\mathbf{X}^T \mathbf{X}] \mathbf{C}^T$ is more well conditioned. For practical reasons, the scaling preconditioner matrix is used which is a diagonal matrix with the i^{th} diagonal element equal to the reciprocal of $[\mathbf{X}^T \mathbf{X}]_{ii}$.

Overfitting can be an issue when the complexity of the hypothetical model becomes greater than that of the theoretical model. This can lead to the problem of the theoretical model explaining both the signal and the noise. One ad hoc remedy is to divide the training data into several data sets, and once the optimal parameters of the model are found on validation/testing data, determine their effectiveness of the holdout data.

The penalty function can be the misfit between an a priori model \mathbf{w}_0 and the estimated one, in which case it takes the form $\|\mathbf{w} - \mathbf{w}_0\|^2$. This is known as a model misfit function. The tradeoff between honoring the data misfit and penalty functions is determined by the value of the regularization parameter η . The penalty function can be defined to enforce certain characteristics of the model, such as the final model should smoothly vary in the spatial coordinates. In this case the penalty function can be, e.g., $\sum_i (\frac{\partial^n \mathbf{w}}{\partial x_i^n})^2$, where n is the specified order of the spatial derivative.

We learned the meaning of the following terms used in the machine learning (ML) community.

- Ill-conditioned, inconsistent, and overdetermined system of equations.

- Objective function, misfit function, and penalty function. The objective function is often denoted as the *loss* function in the ML community.
- Training data, validation data, and testing data. The training data are divided into several data sets and used to decide which is the best model and regularization parameters should be used without overfitting the data. Details for implementing this anti-overfitting strategy will be given in the chapter in neural networks.
- Normal equations, least squares solution, preconditioning and regularized least squares solutions. Regularized least squares is sometimes denoted as damped least squares.
- The bias term is used to account for bulk shifts in the data and is almost always used for neural network methods.
- Iterative optimization methods, Gauss-Newton method for a linear system of equations, the steepest descent method, and the regularized and preconditioned steepest descent method.

For most geoscience problems, the number of unknowns is too large for a direct inverse to $[\mathbf{X}^T \mathbf{X} + \eta \mathbf{I}]$, which will cost $O(N^3)$ algebraic operations. The alternative is an iterative solution method that costs $O(KN^2)$, where the number of iterations is $K \ll N$, we hope! Regularized and preconditioned gradient optimization, which will be discussed in the next chapter, is the solution method used for neural networks.

2.4 Exercises

1. Why don't we allow the regularization parameter η in equations 2.9 or 2.10 to be less than zero?
2. For noiseless data where $\delta t_i = 0$, derive the formula for the error δw introduced by the damping parameter $\eta = .01x_{i1}$ in equation 2.10. Hint: Recall the approximation $\frac{1}{x^2 + \eta} \approx \frac{1}{x^2} (1 - \frac{\eta}{x^2})$ for $\eta \ll x^2$.
3. Define $\mathbf{w} = \mathbf{w}_o + \alpha \hat{\mathbf{s}}$ where α is a scalar and $\hat{\mathbf{s}}$ is a specified unit vector. Show that $\frac{\partial f(\mathbf{w})}{\partial \alpha} = \hat{\mathbf{s}}^T \nabla f(\mathbf{w})$, which is known as a directional derivative. Explain why $\frac{\partial f(\mathbf{w})}{\partial \alpha}$ gives the slope of $f(\mathbf{w})$ in the direction $\hat{\mathbf{s}}$.
4. Assume a function $f(\mathbf{w})$ that can be approximated by a first-order Taylor series expanded about the point \mathbf{w}_o :

$$\begin{aligned} f(\mathbf{w}) - f(\mathbf{w}_o) &= \frac{\partial f(\mathbf{w}_o)}{\partial w_1} \delta w_1 + \frac{\partial f(\mathbf{w}_o)}{\partial w_2} \delta w_2, \\ &= \delta \mathbf{w}^T \nabla f(\mathbf{w}_o), \end{aligned} \quad (2.42)$$

where $\mathbf{w} = (w_1, w_2)^T$, $\delta \mathbf{w}^T = (\delta w_1, \delta w_2)$ and the magnitude $|\delta \mathbf{w}|$ is very small. If \mathbf{w}_o is on the contour where $f(\mathbf{w}_o) = \text{const}$ and $\mathbf{w} = \mathbf{w}_o + \delta \mathbf{w}$ is on the same contour then $f(\mathbf{w}) = f(\mathbf{w}_o)$ and $\delta \mathbf{w}$ is parallel to the tangent of the contour at \mathbf{w}_o . Therefore, the leftside of the above equation is zero if \mathbf{w} and \mathbf{w}_o are on the same contour. Explain

why this also says that the gradient $\nabla \mathbf{w} = (\frac{\partial f(\mathbf{w})}{\partial w_1}, \frac{\partial f(\mathbf{w})}{\partial w_2})^T$ is perpendicular to the tangent of this contour.

5. Prove that $\nabla f(\mathbf{w}_o)$ points toward increasing values of $f(\mathbf{w})$ by defining $\delta \mathbf{w}$ in equation 2.42 to be pointing uphill where $f(\mathbf{w} = \mathbf{w}_o + \delta \mathbf{w}) > f(\mathbf{w}_o)$. Hint: recall that two vectors point in similar directions if $(\mathbf{x}, \mathbf{y}) = |\mathbf{x}||\mathbf{y}| \cos \theta > 0$.
6. Prove that $\nabla f(\mathbf{w})$ is parallel to the direction of maximum increase in $f(\mathbf{w})$ at \mathbf{w} .
7. Define the second-order Taylor expansion of $f(x)$ about \mathbf{w}_o as

$$f(\mathbf{w}) = f(\mathbf{w}_o) + \sum_{i=1}^2 \frac{\partial f(\mathbf{w}_o)}{\partial w_i} \delta w_i + \frac{1}{2} \sum_{j=1}^2 \sum_{i=1}^2 \frac{\partial^2 f(\mathbf{w}_o)}{\partial w_i \partial w_j} \delta w_i \delta w_j, \quad (2.43)$$

and define $\nabla f(\mathbf{w}_o) = (\frac{\partial f(\mathbf{w}_o)}{\partial w_1}, \frac{\partial f(\mathbf{w}_o)}{\partial w_2})^T$. Show that equation 2.43 can be written as

$$f(\mathbf{w}) = f(\mathbf{w}_o) + \delta \mathbf{w}^T \nabla f(\mathbf{w}_o) + \frac{1}{2} \delta \mathbf{w}^T \mathbf{H} \delta \mathbf{w}, \quad (2.44)$$

where

$$\mathbf{H} = [\nabla \nabla^T] f(\mathbf{w}_o) = \begin{bmatrix} \frac{\partial^2 f}{\partial w_1^2} & \frac{\partial^2 f}{\partial w_1 \partial w_2} \\ \frac{\partial^2 f}{\partial w_1 \partial w_2} & \frac{\partial^2 f}{\partial w_2^2} \end{bmatrix}. \quad (2.45)$$

Show that $\hat{\mathbf{s}}^T \mathbf{H} \hat{\mathbf{s}}$ gives the curvature of $f(\mathbf{w})$ along the direction specified by $\hat{\mathbf{s}}$. Hint: Define $\mathbf{w} = \mathbf{w}_o + \alpha \hat{\mathbf{s}}$ so that

$$\frac{d^2 f}{d\alpha^2} = \frac{d}{d\alpha} \frac{df}{d\alpha} = \frac{d}{d\alpha} [(\nabla f)^T \hat{\mathbf{s}}] = \hat{\mathbf{s}}^T [\nabla (\nabla f)^T] \hat{\mathbf{s}} = \hat{\mathbf{s}}^T \overbrace{[\nabla \nabla^T f(\mathbf{w})]}^{\text{Hessian}} \hat{\mathbf{s}}. \quad (2.46)$$

8. Can there ever be more than one isolated minimum for a quadratic function? Prove your answer. Can there ever be more than one isolated minimum for a non-quadratic function?
9. Same question as the previous one except find the maximum and minimum curvatures of the Rosenbrock function instead of the slope. What is the curvature along the slope direction?
10. Prove that the gradient vector of $f(\mathbf{x})$ is perpendicular to the contour line tangent at \mathbf{x} and points uphill. Hint: $f(\mathbf{x})$ does not change along a contour, so the directional derivative along the tangent $df(\mathbf{x})/dt \rightarrow 0$. This says that $df(\mathbf{x})/dt = d\mathbf{x}^T/dt \nabla f(\mathbf{x}) = 0$.
11. Starting from the regularized objective function, derive equation 2.40.

2.5 Appendix: Exact Step Length

The derivation of the step length for the exact line search is now given. The 1D line search problem is defined as finding the optimal value of the scalar α that minimizes $\epsilon(\mathbf{w} + \alpha\Delta\mathbf{w})$ for a fixed \mathbf{w} and $\Delta\mathbf{w}$. Without loss of generality, we can set $\mathbf{w} = 0 + \alpha\Delta\mathbf{w}$ and $\eta = 0$ in equation 2.16 to get

$$\begin{aligned}\epsilon(\mathbf{w} + \alpha\Delta\mathbf{w}) &= \frac{1}{2}\alpha^2(\mathbf{w} + \Delta\mathbf{w})^T[\mathbf{X}^T\mathbf{X}](\mathbf{w} + \Delta\mathbf{w}) - \alpha\mathbf{t}^T\mathbf{X}(\mathbf{w} + \Delta\mathbf{w}) + \frac{1}{2}\mathbf{t}^T\mathbf{t}, \\ &= \frac{1}{2}\alpha^2\Delta\mathbf{w}^T[\mathbf{X}^T\mathbf{X}]\Delta\mathbf{w} + \frac{1}{2}\alpha^2\mathbf{w}^T[\mathbf{X}^T\mathbf{X}]\mathbf{w} + \alpha^2\Delta\mathbf{w}^T[\mathbf{X}^T\mathbf{X}]\mathbf{w} \\ &\quad - \mathbf{t}^T\mathbf{X}(\mathbf{w} + \Delta\mathbf{w}) + \frac{1}{2}\mathbf{t}^T\mathbf{t}.\end{aligned}\tag{2.47}$$

Setting $\eta = 0$ in equation 2.16 and subtracting it from equation 2.47 gives

$$\epsilon(\mathbf{w} + \alpha\Delta\mathbf{w}) - \epsilon(\mathbf{w}) = \frac{1}{2}\alpha^2\Delta\mathbf{w}^T[\mathbf{X}^T\mathbf{X}]\Delta\mathbf{w} + \alpha\Delta\mathbf{w}^T\mathbf{X}^T(\mathbf{X}\mathbf{w} - \mathbf{t}).\tag{2.48}$$

Differentiating the above equation with respect to α and setting the result equal to zero yields the stationary condition where $\epsilon(\mathbf{w} + \alpha\Delta\mathbf{w})$ achieves a minimum along the steepest descent direction $\Delta\mathbf{w}$:

$$\begin{aligned}\frac{\partial\epsilon(\mathbf{w} + \alpha\Delta\mathbf{w})}{\partial\alpha} &= \alpha\Delta\mathbf{w}^T\mathbf{H}\Delta\mathbf{w} + \Delta\mathbf{w}^T\mathbf{g}, \\ &= 0,\end{aligned}\tag{2.49}$$

where the $N \times N$ Hessian matrix is defined as $\mathbf{H} = \mathbf{X}^T\mathbf{X}$ and the gradient is $\mathbf{g} = \mathbf{X}^T(\mathbf{X}\mathbf{w} - \mathbf{t})$. Solving for α gives the exact step length:

$$\alpha = \frac{-\mathbf{g}^T\Delta\mathbf{w}}{\Delta\mathbf{w}^T\mathbf{H}\Delta\mathbf{w}}.\tag{2.50}$$

This step-length calculation is exact if $\epsilon(\mathbf{w})$ is a quadratic functional. For the steepest descent method $\Delta\mathbf{w} = -\mathbf{g}$ so that

$$\alpha = \frac{\mathbf{g}^T\mathbf{g}}{\mathbf{g}^T\mathbf{H}\mathbf{g}}.\tag{2.51}$$

For non-linear problems, such as neural networks or full waveform inversion, this exact line search formula does not work well because it is suited only for linear problems where the data and model are linearly related. For non-linear problems a numerical line search method is used to find α .

Chapter 3

Non-Linear Gradient Optimization

Many geophysical problems have a non-linear relationship between the data \mathbf{t} and the actual earth model \mathbf{w} . This means that the misfit function is more wiggly than a quadratic function, leading to a misfit function with many local minima. Such holes can easily trap an iterative gradient method into a solution far from the global minimum. In this case non-linear gradient and multiscale optimization methods can be used to sometimes steer clear of such traps and converge to near the global minimum. This chapter now presents an overview of such methods applied to simple problems. Lessons learned can be used to help understand problems with the neural network method. Non-linear optimization is also the starting point for deriving the neural network method, as will be shown in the next Chapter.

3.1 Non-linear Gradient Optimization

The previous chapter mainly addressed the linear problem where the data \mathbf{t} were linearly related to the model \mathbf{w} by the modeling equation $\mathbf{X}\mathbf{w} = \mathbf{t}$, where the elements in \mathbf{X} were independent of the model. However, many geophysical problems are non-linear where the \mathbf{X} is a function of the model parameters. For the motorcycle time trials, the modeling equation 2.1 might be non-linear such that

$$xw^3 = t, \quad (3.1)$$

and the goal is to find the optimal value of w that explains the inconsistent timing data. In this case equation 2.1 becomes

$$xw^3 = t \rightarrow \underbrace{\begin{bmatrix} w_1^2 x_{11} \\ w_1^2 x_{21} \\ w_1^2 x_{31} \\ w_1^2 x_{41} \\ w_1^2 x_{51} \end{bmatrix}}_{\mathbf{X}(\mathbf{w})} \underbrace{\begin{pmatrix} w_1 \end{pmatrix}}_{\mathbf{w}} = \underbrace{\begin{pmatrix} t_1 \\ t_2 \\ t_3 \\ t_4 \\ t_5 \end{pmatrix}}_{\mathbf{t}=\text{observed times}}, \quad (3.2)$$

where $\mathbf{X}(\mathbf{w})$ now depends quadratically on the model \mathbf{w} we are inverting for.

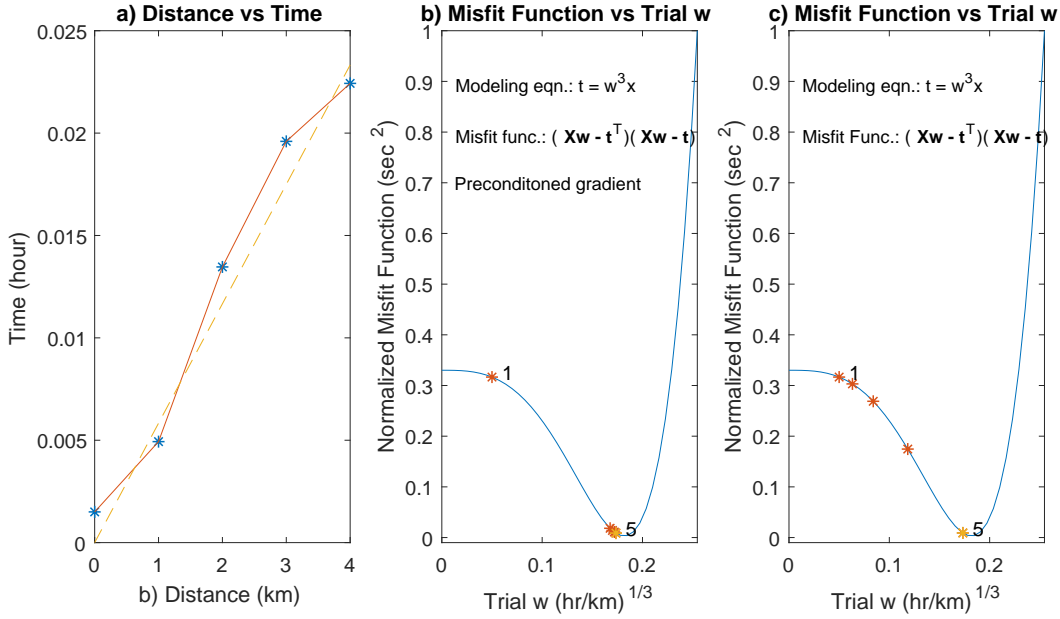


Figure 3.1: Same as Figure 2.2 except the modeling equation is $t = xw^3$ so that the objective function has more than one stationary point. The numbers and stars in b) and c) indicate the iteration numbers and associated misfit errors for solutions determined by the b) non-linear Newton and c) steepest descent methods.

For the motorcycle data, Figure 3.1a plots the recorded noisy times (blue stars) against x for $w = 0.18$, and the dashed line is the predicted data computed with equation 3.1. The value $w = 0.18$ minimizes the misfit function¹ at the vertex of Figure 3.1b. Compared to the single minimum in Figure 2.1, the non-linear misfit function in Figure 3.1b has several minima, the one at $w = 0.018$ and the one at the flat portion of the curve near $w \approx 0$. We say that the one near the origin is a *local minimum* while the one at $\mathbf{w} = 0.18$ is the *global minimum*.

The global minimum in Figure 3.1b can be found by inspection, but how can we find it by the least squares solution $[\mathbf{X}^T \mathbf{X}]^{-1} \mathbf{X}^T \mathbf{t}$ when we need to know \mathbf{w} in order to compute $\mathbf{X}(\mathbf{w})$ and $[\mathbf{X}^T \mathbf{X}]^{-1}$? This is like a short-tailed cat chasing its tail, eternally chasing but not catching.

Luckily, optimization can usually solve this *tail-catching* problem by sequentially computing a series of trial solutions $\mathbf{w}^{(k)}$ $k \in [1, 2, \dots]$ where a new search direction $\Delta \mathbf{w}^{(k)} = \mathbf{w}^{(k+1)} - \mathbf{w}^{(k)}$ is defined at each point. This is known as a non-linear gradient optimization method where the search directions use the slope (and sometimes curvature) information of the misfit function at each point.

For example, the iterative non-linear Newton formula with regularization is obtained by attaching the iteration index (k) to \mathbf{X} in equation 2.40 to give:

$$\mathbf{w}_i^{(k+1)} = \mathbf{w}_i^{(k)} - \alpha [\mathbf{X}^{(k)T} \mathbf{X}^{(k)}]^{-1} (\mathbf{X}^{(k)T} \Delta \boldsymbol{\tau}^{(k)} + \eta \mathbf{w}^{(k)})_i. \quad (3.3)$$

¹There is a non-zero error at the vertex but it is too small to visible.

In this case the search direction $\Delta \mathbf{w}^{(k)} = \mathbf{w}^{(k+1)} - \mathbf{w}^{(k)}$ is parallel to $-[\mathbf{X}^{(k)T} \mathbf{X}^{(k)}]^{-1}(\mathbf{X}^{(k)T} \Delta \boldsymbol{\tau}^{(k)} + \eta \mathbf{w}^{(k)})$ at the k^{th} point $\mathbf{w}^{(k)}$. The next solution is found by searching along $\Delta \mathbf{w}^{(k)}$ until the misfit function no longer decreases. When this happens at $\mathbf{w}^{(k+1)}$ the new value $\mathbf{x}^{(k+1)}$ is inserted into $\mathbf{X}(\mathbf{w}) \rightarrow \mathbf{X}^{(k+1)}$ and $\Delta \boldsymbol{\tau}^{(k+1)} = \mathbf{X} \boldsymbol{\tau}^{(k+1)}$ is computed to give the updated search direction $-[\mathbf{X}^{(k+1)T} \mathbf{X}^{(k+1)}]^{-1}(\mathbf{X}^{(k+1)T} \Delta \boldsymbol{\tau}^{(k+1)} + \eta \mathbf{w}^{(k)})$. If $[\mathbf{X}^T \mathbf{X}]^{-1}$ is too expensive to compute then we have the preconditioned and regularized steepest descent formula:

$$\mathbf{w}_i^{(k+1)} = \mathbf{w}_i^{(k)} - \alpha \frac{1}{[\mathbf{X}^{(k)T} \mathbf{X}^{(k)}]_{ii}^2} (\mathbf{X}^{(k)T} \Delta \boldsymbol{\tau}^{(k)} + \eta \mathbf{w}^{(k)})_i, \quad (3.4)$$

which avoids calculating the inverse of $[\mathbf{X}^T \mathbf{X}]$.

In summary, the non-linear Newton gradient method is given in 4 steps.

1. Define a starting guess model $\mathbf{w}^{(0)}$ so that $\mathbf{X}^{(0)}$ and $\Delta \boldsymbol{\tau}^{(0)}$ can be computed. Set $k = 0$.
2. Use a numerical line search to find $\mathbf{w}^{(k+1)}$ in equation 3.3.
3. Use $\mathbf{w}^{(k+1)}$ to compute $\mathbf{X}^{(k+1)}$ and $\Delta \boldsymbol{\tau}^{(k+1)}$.
4. Set $k := k + 1$ and repeat steps 2-4 until $\|\Delta \boldsymbol{\tau}^{(k)}\|$ falls below some user specified threshold. A fragment of the MATLAB code for applying the Newton method to the motorcycle data is shown below.

```
w0=0.18 % Actual model
x=[0 1 2 3 4]';
t=[0 .102 .33 .5 .8]'; % Observed noiseless data
e=.3*[-.005 -.003 .006 .007 -.003]'; % Data errors
n=3;t=x*w0^n+e; % noisy input data
w11(1)=.05; % Starting solution
res = (x*w11(1).^n-t); % Starting residual
for i=2:nit
    X = x*w11(i-1).^(n-1); % Matrix X=x*w^(n-1)
    adjoint = X'*res; % Compute adjoint X'(Xw-t)
    w11(i) = w11(i-1)-.05*inv(X'*X)*adjoint; % Newton update
    res = (x*w11(i).^n-t); %data residual
end
```

The above Newton algorithm is used to explain the motorcycle timing data plotted in Figure 3.1a. In this case we assume the cubic modeling equation in equation 3.2 and iteratively solve for $\mathbf{w}^{(k)}$ from the starting model $\mathbf{w}^{(1)} = 0.05$. Preconditioning in the form of $[\mathbf{X}^T \mathbf{X}]^{-1}$ is used and the step length is set to be 0.01 for the results in Figure 3.1b, and no preconditioning is used for the results in Figure 3.1c. The stars denote the misfit values for the iteration number denoted by the numbers next to each star.

$$\mathbf{w}_i^{(k+1)} = \mathbf{w}_i^{(k)} - \alpha \frac{1}{[\mathbf{X}^{(k)T} \mathbf{X}^{(k)}]_{ii}^2} (\mathbf{X}^{(k)T} \Delta \boldsymbol{\tau}^{(k)} + \eta \mathbf{w}^{(k)})_i. \quad (3.5)$$

3.2 Rigorous Derivation of the Newton Formula

The non-linear Newton formula was derived in a hand-waving manner from the linear Newton method for an overdetermined system of linear equations. We will now derive it from a more general point of view by assuming a smooth objective function $\epsilon(\mathbf{w})$ and expanding it in a Taylor's series about the starting point \mathbf{w}_o . This approach is much more general and less cumbersome than the approach in Chapter 2 that started from an $M \times N$ system of equations for a finite set of data.

Assume $\epsilon(\mathbf{w})$ is a smooth real function which can be accurately expanded about the starting point \mathbf{w}_o with only three terms in the Taylor series:

$$\begin{aligned}\epsilon(\mathbf{w}_o + \Delta\mathbf{w}) &\approx \epsilon(\mathbf{w}_o) + \sum_{i=1}^N \frac{\partial\epsilon(\mathbf{w}_o)}{\partial w_i} \Delta w_i + \frac{1}{2} \sum_{i=1}^N \sum_{j=1}^N \frac{\partial^2\epsilon(\mathbf{w}_o)}{\partial w_i \partial w_j} \Delta w_i \Delta w_j, \\ &= \epsilon(\mathbf{w}_o) + \mathbf{g}^T \Delta\mathbf{w} + \frac{1}{2} \Delta\mathbf{w}^T \nabla \nabla^T \epsilon(\mathbf{w}_o) \Delta\mathbf{w} + o(\|\Delta\mathbf{w}\|^3),\end{aligned}\quad (3.6)$$

where the $N \times 1$ gradient vector is explicitly written as

$$\nabla\epsilon(\mathbf{w}) := \begin{bmatrix} \frac{\partial\epsilon}{\partial w_1} \\ \vdots \\ \frac{\partial\epsilon}{\partial w_N} \end{bmatrix}, \quad (3.7)$$

and the $N \times N$ Hessian matrix \mathbf{H} is defined as $\nabla \nabla^T \epsilon(\mathbf{w})$ with components

$$H_{ij} := [\nabla \nabla^T \epsilon(\mathbf{w})]_{ij} = \frac{\partial^2 \epsilon(\mathbf{w})}{\partial w_i \partial w_j}. \quad (3.8)$$

The matrix \mathbf{H} is symmetric because $\frac{\partial^2 \epsilon(\mathbf{w})}{\partial w_i \partial w_j} = \frac{\partial^2 \epsilon(\mathbf{w})}{\partial w_j \partial w_i}$. It will be shown in the next section that the Hessian matrix contains information about the curvature or type of bumps associated with $f(\mathbf{x})$, while the negative gradient $-\nabla\epsilon(\mathbf{w})$ points in the steepest downhill direction at \mathbf{w} .

Rosenbrock Function. A geometrical interpretation of the gradient and the Hessian can be illustrated with the Rosenbrock function

$$f(\mathbf{x}) = 100(x_2 - x_1^2)^2 + (1 - x_1)^2, \quad (3.9)$$

a smooth but highly non-linear function plotted in Figure 3.2. In this case the gradient vector becomes

$$\nabla f(\mathbf{x}) = \mathbf{g} = \begin{bmatrix} \frac{\partial f}{\partial x_1} \\ \frac{\partial f}{\partial x_2} \end{bmatrix} = \begin{bmatrix} -400x_1(x_2 - x_1^2) - 2(1 - x_1) \\ 200(x_2 - x_1^2) \end{bmatrix}. \quad (3.10)$$

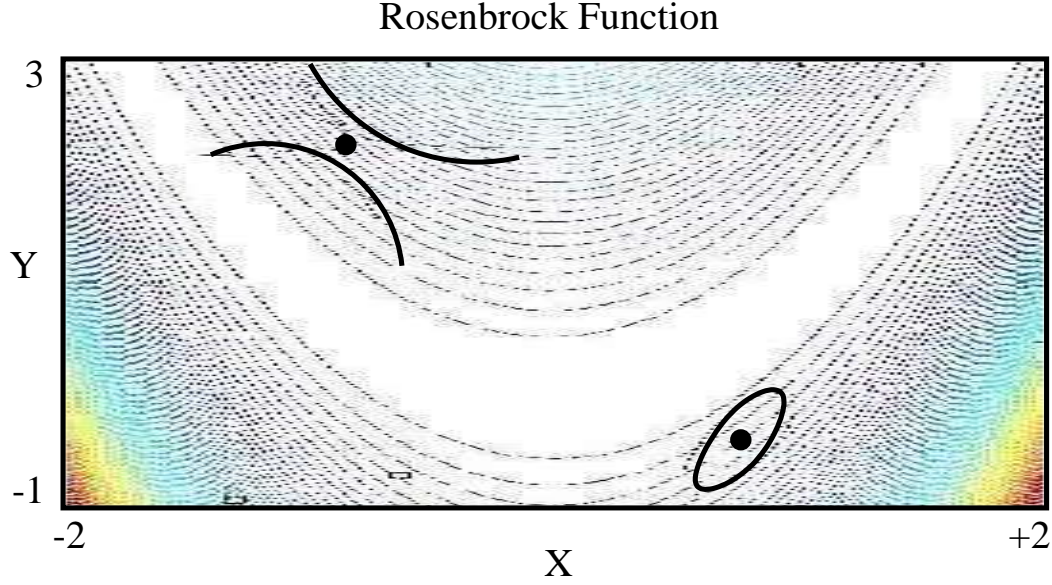


Figure 3.2: Contours of the Rosenbrock function along with icons (thick contours) indicating either a saddle-like or elongated ellipse geometry of $\mathbf{x}^T \mathbf{H} \mathbf{x}$ at the points indicated by solid circles (courtesy of Yunsong Huang). See exercise 1.

To assess the physical meaning of the gradient, we define the points on a line in multidimensional space by

$$\mathbf{x}(\alpha) = \mathbf{x}_o + \alpha \hat{\mathbf{s}}, \quad (3.11)$$

where $\hat{\mathbf{s}}$ is the unit vector parallel to the line and α is the scalar parameter that controls how far \mathbf{x} is from the specified starting point $\mathbf{x}(\alpha = 0) = \mathbf{x}_o$. A directional derivative along the line direction $\hat{\mathbf{s}}$ in equation 3.11 is defined as $df/d\alpha$:

$$\frac{df(\mathbf{x})}{d\alpha} = \sum_i \overbrace{\frac{df(\mathbf{x})}{dx_i}}^{\nabla f(\mathbf{x})} \overbrace{\frac{dx_i}{d\alpha}}^{\hat{s}} = \hat{\mathbf{s}}^T \nabla f(\mathbf{x}), \quad (3.12)$$

where $\hat{\mathbf{s}}^T \nabla f(\mathbf{x})$ is the projection of the gradient along the direction parallel to $\hat{\mathbf{s}}$. If $\hat{\mathbf{s}}$ is parallel to the contour tangent, then $f(\mathbf{x})$ does not change in this direction so $\hat{\mathbf{s}}^T \nabla f(\mathbf{x}) = 0$. This means that the gradient $\mathbf{g} = \nabla f(\mathbf{x})$ is perpendicular to the contour tangent, or parallel to the direction of steepest descent. For a 1D function, this gradient is also known as the slope: if it is positive then the uphill direction is to the right of the origin, otherwise it is to the left.

The second derivatives of $f(\mathbf{x})$ for the Rosenbrock function form the 2×2 Hessian

matrix:

$$\mathbf{H} = [\nabla \nabla^T] f(\mathbf{x}) = \begin{bmatrix} \frac{\partial^2 f}{\partial x_1^2} & \frac{\partial^2 f}{\partial x_1 \partial x_2} \\ \frac{\partial^2 f}{\partial x_1 \partial x_2} & \frac{\partial^2 f}{\partial x_2^2} \end{bmatrix} = \begin{bmatrix} 1200x_1^2 - 400x_2 + 2 & -400x_1 \\ -400x_1 & 200 \end{bmatrix}. \quad (3.13)$$

Unlike a quadratic function with elliptical contours and a constant Hessian matrix, equation 3.13 says that the curvature values in the Hessian matrix depend on \mathbf{x} for $f(\mathbf{x})$ with polynomial order > 2 .

Similar to defining $\hat{\mathbf{s}}^T \nabla f$ to be the slope of $f(\mathbf{x})$ along the line direction $\hat{\mathbf{s}}$, the second derivative or curvature of $f(\mathbf{x})$ along the same line is given by

$$\frac{d^2 f}{d\alpha^2} = \frac{d}{d\alpha} \frac{df}{d\alpha} = \frac{d}{d\alpha} [(\nabla f)^T \hat{\mathbf{s}}] = \hat{\mathbf{s}}^T [\nabla (\nabla f)^T] \hat{\mathbf{s}} = \hat{\mathbf{s}}^T \overbrace{[\nabla \nabla^T f(\mathbf{x})]}^{\text{Hessian}} \hat{\mathbf{s}}. \quad (3.14)$$

Therefore, $\hat{\mathbf{s}}^T \mathbf{H} \hat{\mathbf{s}}$ gives the curvature of $f(\mathbf{x})$ along the direction specified by $\hat{\mathbf{s}}$: that is, it can be used to find how quickly and where the slope is changing most rapidly.

3.3 MATLAB Examples of Newton's Method

Newton's methods are now used to solve some specific 1D and 2D non-linear functions. MATLAB codes are provided so the reader can explore finding optimal points for different non-linear functions.

Example 3.3.1. 1D function

For a 1D equation ?? becomes

$$\frac{\partial f(x_o)}{\partial x} = -\frac{\partial^2 f(x_o)}{\partial x^2} \Delta x, \quad (3.15)$$

which can be solved for Δx to give

$$\Delta x = -\frac{\partial f(x_o)}{\partial x} / \frac{\partial^2 f(x_o)}{\partial x^2}. \quad (3.16)$$

The Newton iteration formula ?? for a 1D non-linear function reduces to

$$x^{(k+1)} = x^{(k)} - \alpha \frac{\partial f(x^{(k)})}{\partial x} / \frac{\partial^2 f(x^{(k)})}{\partial x^2}. \quad (3.17)$$

In general, the convergence rate of Newton's method depends on the topography, determined by the curvature and slope terms, of the function and how far the starting point is from the global minimum.

The MATLAB script which implements Newton's method for the 1D non-quadratic function $f(x) = ax^4 + x^2 - 2x$ is given below,

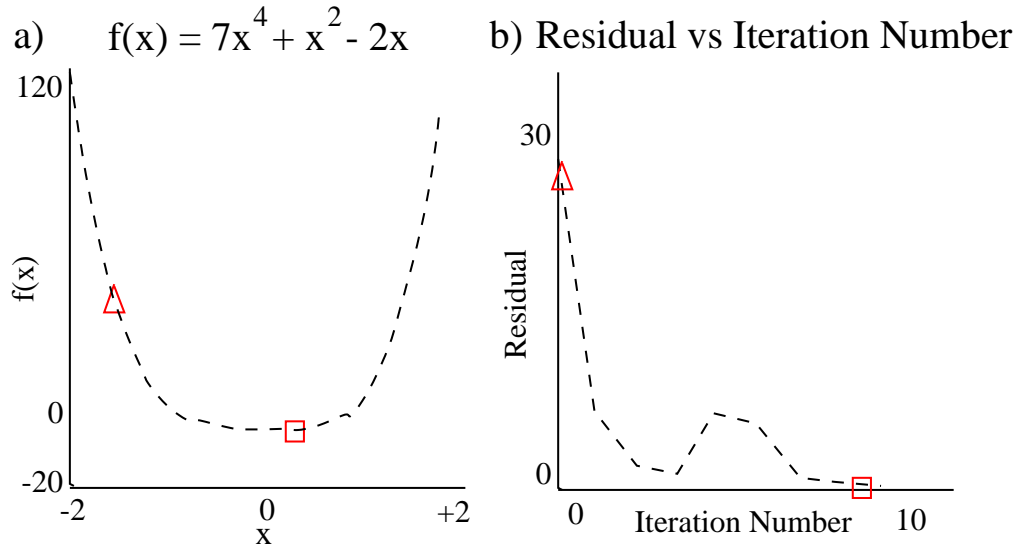


Figure 3.3: Plot of a) quartic function and b) residual vs iteration curve. The diamond (square) represents the starting (ending) model.

```

%%%%%%%%%%%%%%%%%%%%%%%%%%%%%%%%%%%%%%%%%%%%%%%%%%%%%%%%%%%%%%%%%%%%%%%%%%%%%%
% 1D Newton method to find zeros of a quartic function
%
%%%%%%%%%%%%%%%%%%%%%%%%%%%%%%%%%%%%%%%%%%%%%%%%%%%%%%%%%%%%%%%%%%%%%%%%%%%%%%
clear all;
a = 7;
subplot(121); x = [-2:.1:2];
plot(x, a*x.^4 + x.^2 - 2*x);
%
x = -1.5; % starting point
f(1) = (a*x.^4 + x.^2 - 2*x); % Quartic Function
xx(1) = x;
for it = 2:10 % Start iterations
    f1prime = a*4*x.^3 + 2*x - 2;
    f2prime = a*12*x.^2 + 2;
    x = x - f1prime/f2prime; % Newton formula
    xx(it) = x;
    f(it) = (a*x.^4 + x.^2 - 2*x);
    residual(it-1) = abs(f(it) - f(it-1));
end

```

The values of $f(x^{(k)})$ are plotted against $x^{(k)}$ in Figure 3.3.

Example 3.3.2. 2D Function

The Rosenbrock function is plotted in Figure 3.2 and a MATLAB code for finding its minimum by Newton's method is below. Unlike a quadratic objective function, the curvature value depends on the location of (x_1, x_2) .

```

%%%%%%%%%%%%%%%%%%%%%%%%%%%%%%%%%%%%%%%%%%%%%%%%%%%%%%%%%%%%%%%%%%%%%%%%%%%%%%
% Iterative Newton method for finding minimizer
% of Rosenbrock function
% f=100.*(x2-x1.^2).^2+(1-x1).^2
% Minimizer point=(1,1)

```

```

%%%%%%%%%%%%%%%%%%%%%%%%%%%%%%%%%%%%%%%%%%%%%%%%%%%%%%%%%%%%%%%%%%%%%%%%
iter = 10;
x1=-.9;x2=1*x1;
xx = zeros(2,iter);
xx(1,1) = x1;
xx(2,1) = x2;
x=[x1;x2];
%
for it = 2:iter % Begin non-linear iterations
g=[-400*x1*(x2-x1^2)-2*(1-x1); 200*(x2-x1^2)]; % 2x1 gradient vector
H=[1200*x1^2-400*x2+2 -400*x1; -400*x1 200]; % 2x2 Hessian matrix
x = x-inv(H)*g; % Non-linear Newton formula
xx(1,it) = x(1); % Update iterative solution
xx(2,it) = x(2);
x1 = x(1);
x2 = x(2);
end
xmx = max(xx(1,:)).+2; % Define plotting parameters
xmin = min(xx(1,:)).-2;
ymin0 = min(xx(2,:)).-2;
ymx = max(xx(2,:)).+2;
x = [xmin:.01:xmx];
y = [ymin0:.01:ymx];
[X,Y] = meshgrid(xmin:.01:xmx,ymin0:.01:ymx );
f = 100.*(Y-X.^2).^2+(1-X).^2; % Rosenbrock Function
imagesc(x,y,f);
hold on;
contour(X,Y,f,80,'w'); % Plot Rosenbrock function ith contours
hold off
hold on;

plot(x1,x2,'r');
plot(xx(1,:),xx(2,:),'*-y');
plot(xx(1,iter),xx(2,iter),'r*');
hold off;
xlabel('X');
ylabel('Y');
title('f(X,Y)=100*(Y-X^2)^2+(1-X)^2 and Newton Iterates (Red * = Final)')

```

3.3.1 Inexact Newton Method

A variation of the non-linear steepest descent method is to use about five iterations of linear steepest descent where \mathbf{X} is not updated, and then update \mathbf{X} with the most recent estimate of \mathbf{w} . This pairing of 5 linear iterations and 1 non-linear iteration is repeated until convergence. Nocedal and Wright (1999) define this procedure as an inexact Newton method because it is similar to using a rough approximation to the inverse Hessian after 5 iterations of linear steepest descent. A similar strategy is used in full waveform inversion for exploration seismology except a linear conjugate gradient method is used (Schuster, 2017).

3.4 Multiscale Optimization

An iterative multiscale inversion strategy (Bunks et al., 1995) is often used in seismic inversion to mitigate the problem of getting stuck in a local minimum. The key idea is to start out the iterations with a coarse model and low-pass filtered data. This leads to a simpler objective function with fewer local minima. Iterate for 5 or so iterations until the

residual reduction has stalled. We are now, presumably, closer to the global minimum and the path to it is less cluttered with local minima. Later iterations refine the grid size of the model and incorporate higher frequencies into the data.

As examples, Figures 3.4a-3.4b depict a shot gather and its associated misfit function, respectively. The data were generated for a two-layer model and most of the events seen in the traces are reflection multiples within the top layer. Each trace $d(t)_i$ is quite complicated so that small changes in the upper-layer velocity will lead to significant time shifts in the data. Plotting the misfit function $\epsilon = 1/2 \sum_i \sum_t (d(t)_i - d(t)_i^{pred})^2$ against trial values of the upper-layer velocity V yields the bumpy misfit plot in Figure 3.4b. Any shift in the velocity that leads to a cycle shift such that the predicted and observed events are roughly in phase will lead to a smaller ϵ compared to when the predicted traces are mostly out of phase. Thus, the objective function is characterized by many local minima denoted by the red circles in Figure 3.4b.

To reduce the number of local minima the data or model should be simplified. One way to do this is to skeletonize both the data and model. In our case, we replace the waveform data with its traveltimes picks in Figure 3.4c. These simple traveltimes are for the primary reflections and lead to the relatively simple misfit function seen in Figure 3.4d. In this case, an iterative gradient method will rapidly converge to a velocity model that is close to the true model. Another example for simplifying the data is to apply a low-pass filter to the data as shown in Figure 3.4e. The associated misfit function in Figure 3.4f is much simpler than the waveform misfit function in Figure 3.4b and so will have less tendency to getting stuck in a local minimum. Another example is in Figure 3.5 where the velocity model is refined every few iterations, and at every model refinement higher frequencies are added to the low-pass filtered data. In this case full waveform inversion is used to invert the seismic traces.

Reducing the complexity of the model and data to enhance convergence is also employed in the neural network community. Here they use the technique of max pooling (see Figure 3.6) where the number of model parameters is halved at one of the stages in the neural network. As will be shown in a numerical example in Chapter 5, this complexity reduction results in better convergence for the example presented.

3.5 Diagram for Matrix-Vector Multiplication

In practice, each iteration in gradient optimization typically requires multiplications of matrices and vectors. These are the same operations used for a neural network as illustrated in Figure 3.7. Here, two sets of model parameters are assumed: w_{1i} for the red motorcycle at the top left and w_{2i} for the gray motorcycle at the bottom left. Now there are a total of six unknowns compared to one unknown associated with the one-motorcycle equation ???. These extra unknowns are introduced to account for more complexity in the model and data. These extra unknowns will demand many more equations of constraint with more time trials over different roads.

The diagrams for representing matrix-vector multiplication in Figure 3.7 is the same that is used in the neural network community. The first column of circles represent the input nodes for the data, the second column denotes the nodes for the neural network for the output elements of the matrix-vector multiplication. However, these output elements

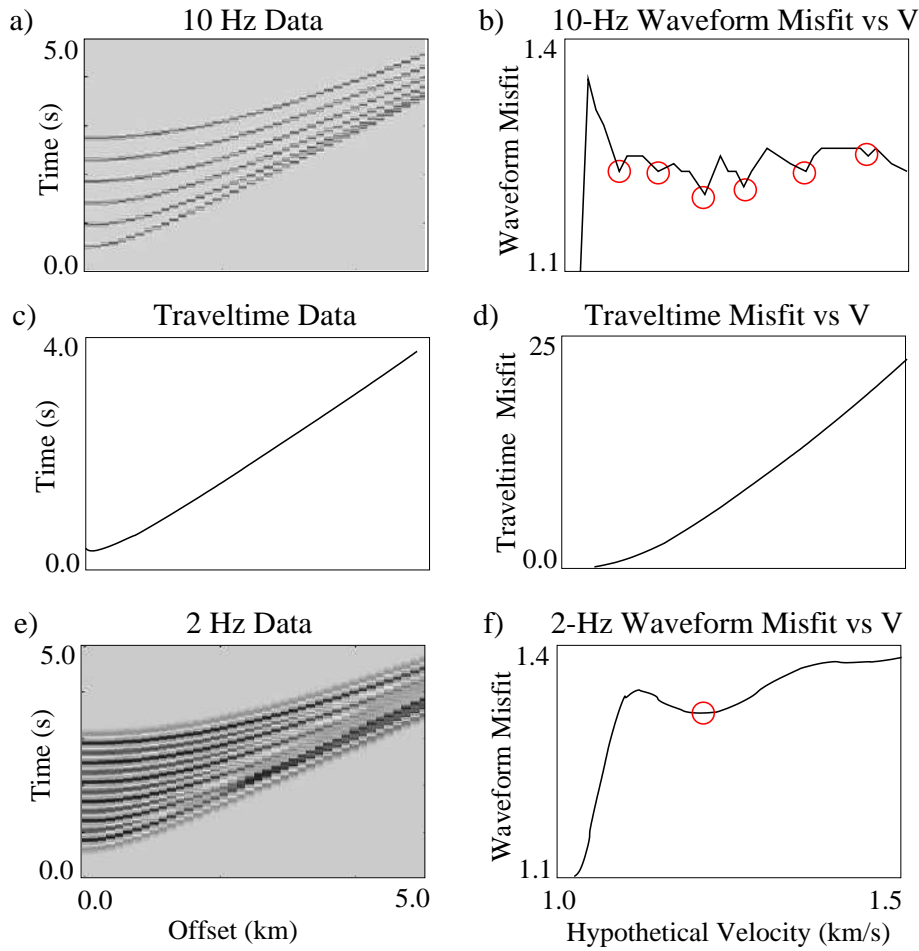


Figure 3.4: Synthetic reflection data in left column, and right column depicts associated plots of misfit functions vs trial velocity values of the first layer in the two-layer model. The correct value of V is 1.0 km/s , where the misfit functions tend to zero. Notice the fewer local minima (red circles) for the 2-Hz data than the 10-Hz data.

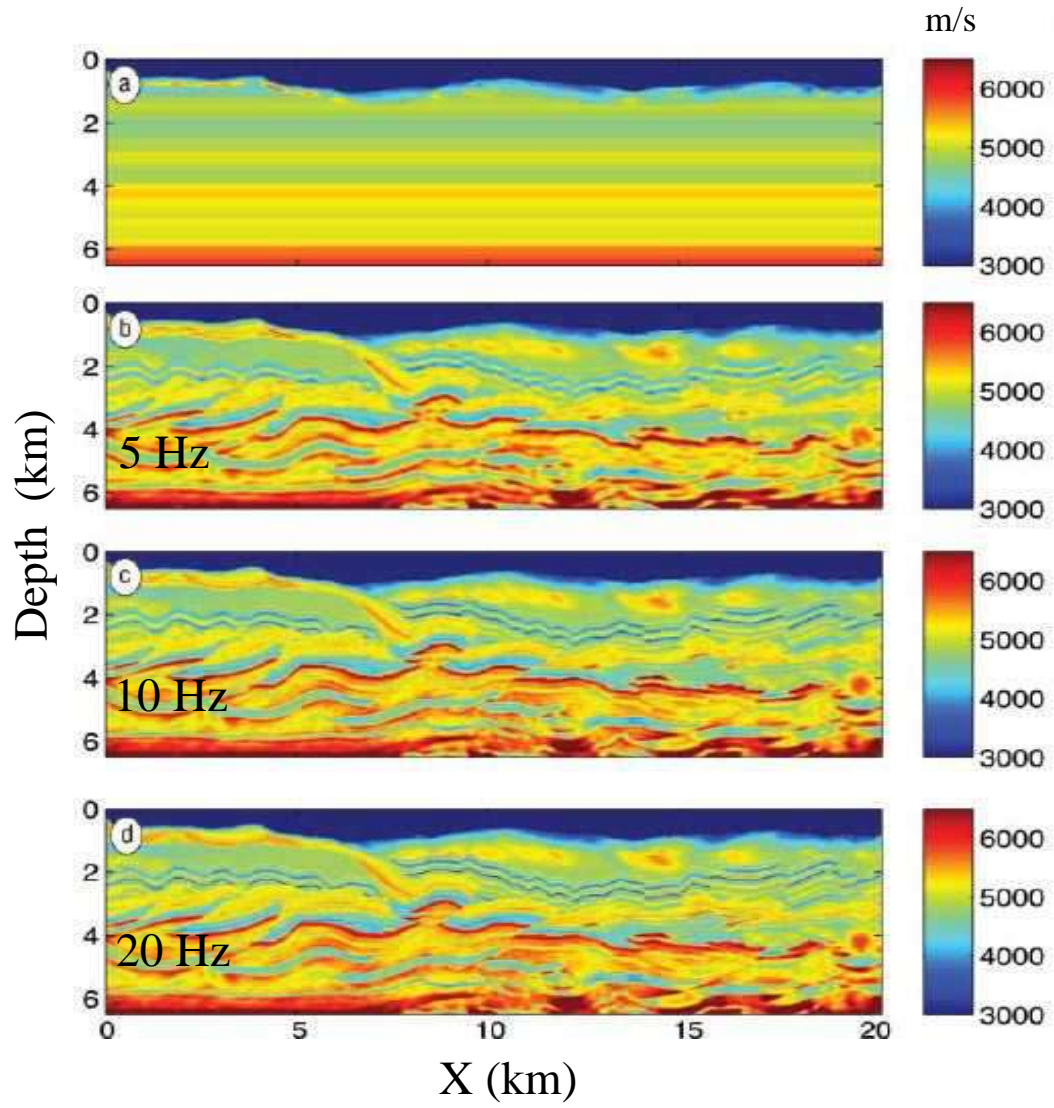


Figure 3.5: a) Initial velocity model. Waveform tomograms inverted from seismic data (204 shots with 1601 receivers per shot) with a peak frequency of b) 5 Hz, c) 10 Hz, and d) 20 Hz. Figure courtesy of Boonyasiriwat et al. (2009).

Max Pooling = Multiscaling?

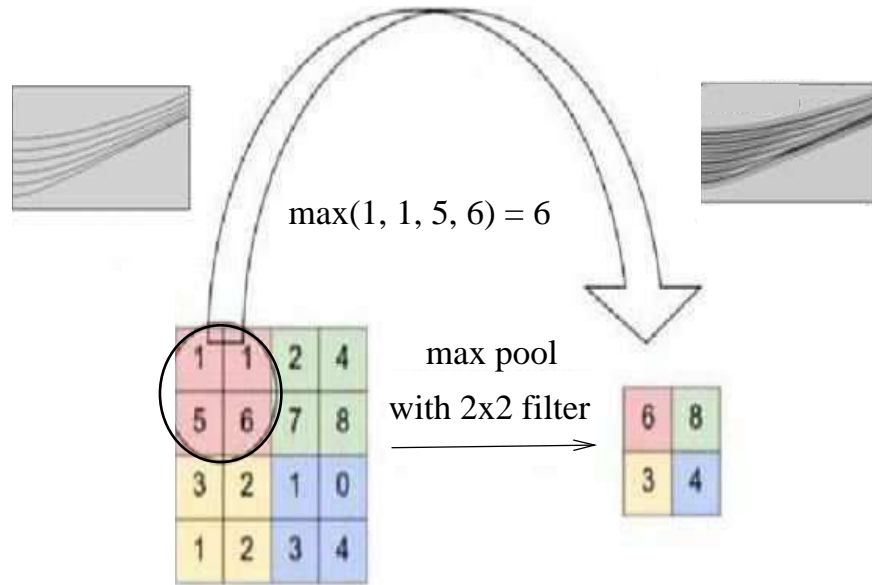


Figure 3.6: Detailed seismic data in the upper left are simplified by low-pass filtering to give the low-pass filtered shot gather in the upper right. The model is also simplified by reducing the number of pixels, which can lead to a simpler objective function and faster convergence. A similar procedure is used for reducing the number of model parameters in a neural network and is denoted as max pooling (see Chapters 5 and 6).

Neural Network Schematic Diagram

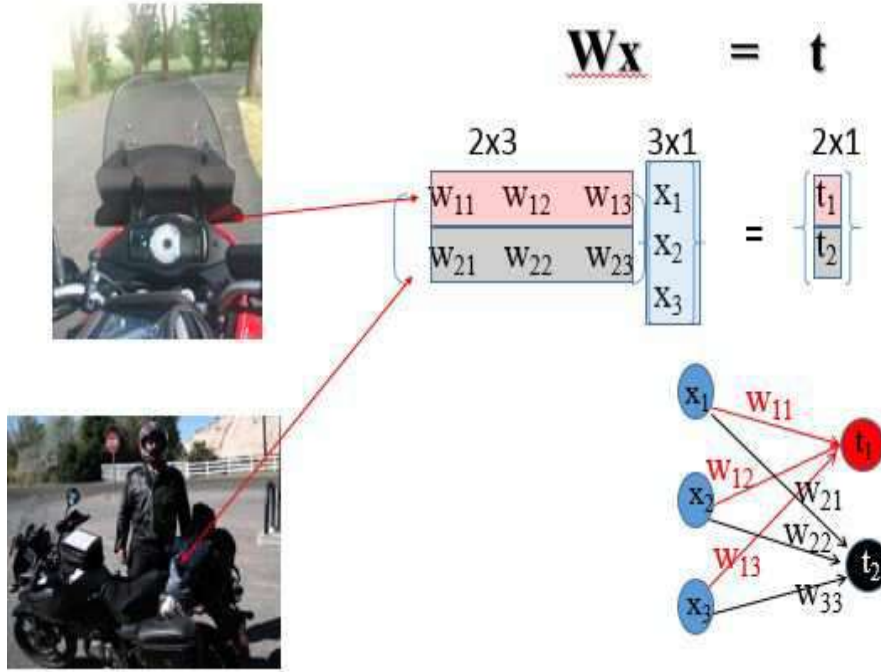


Figure 3.7: Two different types of unknown model parameters are now introduced: w_{i1} $i \in [1, 2, 3]$ for the red motorcycle and $w_{i2} \in [1, 2, 3]$ for the gray motorcycle. Instead of the 1×1 vector \mathbf{w} of model parameters in equation 2.1, the model parameters are assembled into the 2×3 matrix where some new parameters have been added to spice up the story.

also undergo an all-or-almost-nothing activation operation briefly described in Chapter 1, with a more detailed explanation in Chapters 5 and 6.

3.6 Summary

When the data are non-linearly related to the model then non-linear optimization methods are used. Unlike the linear model $\mathbf{X}\mathbf{w} = \mathbf{t}$, the matrix $\mathbf{X}(\mathbf{w})$ for the non-linear problem is a function of the model parameters \mathbf{w} so it must be updated after each iteration, i.e. $\mathbf{X} \rightarrow \mathbf{X}^{(k)}$. This introduces a new problem: convergence to a local minimum because the actual objective function is higher order than a quadratic polynomial in w_i $i \in [1, 2 \dots N]$. The partial cure is multiscale optimization.

The starting point for non-linear gradient methods is to approximate the objective function as a Taylor series truncated after the second-order terms. This truncated series is a sum of 1) an inner product between the $N \times 1$ gradient vector and the search direction $\Delta\mathbf{w}$ and 2) the curvature term represented by a Hessian and its projection along the search direction vector. The solution that minimizes this sum leads to the iterative Newton formula for non-linear optimization.

3.7 Exercises

1. The sign and magnitude of the eigenvalue λ_i of \mathbf{H} determine the shape of $f(\mathbf{w})$ along the i^{th} coordinate direction. For a 2D geometry this can be shown by setting $\mathbf{w} = \mathbf{w}^* + \alpha \mathbf{e}_1 + \beta \mathbf{e}_2$, where \mathbf{e}_i is the i^{th} orthonormal eigenvector of the symmetric matrix \mathbf{H} , \mathbf{w}^* is the point where $f(\mathbf{w})$ is a minimum (i.e., $\mathbf{g}(\mathbf{w}^*) = 0$), and α and β are scalars. Expanding $f(\mathbf{w})$ about the minimum point \mathbf{w}^* so that equation 2.44 becomes

$$\begin{aligned} f(\mathbf{w}^* + \alpha \mathbf{e}_1 + \beta \mathbf{e}_2) &= f(\mathbf{w}^*) + [\alpha^2 \mathbf{e}_1^T \mathbf{H} \mathbf{e}_1 + \beta^2 \mathbf{e}_2^T \mathbf{H} \mathbf{e}_2]/2, \\ &= f(\mathbf{w}^*) + [\lambda_1 \alpha^2 \mathbf{e}_1^T \mathbf{e}_1 + \lambda_2 \beta^2 \mathbf{e}_2^T \mathbf{e}_2]/2, \\ &= f(\mathbf{x}^*) + [\lambda_1 \alpha^2 + \lambda_2 \beta^2]/2, \end{aligned} \quad (3.18)$$

where the gradient term $\mathbf{g}^T \Delta \mathbf{w}$ is zero at the minimum point \mathbf{w}^* . The eigenvalues are positive if \mathbf{H} is a SPD matrix, so any move along an eigenvector direction from \mathbf{w}^* will increase the value of the function. Hence, $f(\mathbf{w})$ describes a bowl-like surface around the minimum point \mathbf{w}^* (see left column of plots in Figure 3.8). Large positive eigenvalues suggest that small changes in position lead to large changes in $f(\mathbf{w})$ so that the bowl has steeply curving sides; conversely, small positive eigenvalues suggest a bowl with gently curving sides.

If the Hessian is negative definite (i.e., \mathbf{H} has only negative eigenvalues) then equation 3.18 says that any move from \mathbf{w}^* along an eigenvector direction will decrease the function, i.e., $f(\mathbf{w})$ describes an inverted bowl about the *maximal* point \mathbf{w}^* . Show that an indefinite Hessian (both positive and negative eigenvalues) has the property that a move along one eigenvector direction will decrease the function value while a move along the other eigenvector direction will increase the function value. This latter surface describes the saddle depicted in 3.8f.

2. Plot the Rosenbrock function with the MATLAB commands:

```
x1=-1.25;xr=1.05;dx=.05; y1=-.3;yr=1.2;dy=.05; facx=1;facy=1;
[xx,yy]=meshgrid([x1:dx:xr]*facx,[y1:dy:yr]*facy);
%[xx,yy]=meshgrid([-0.05:0.005:0.45],[-0.06:0.005:0.12]);
mis=100*(yy - xx.^2).^2 + (1-xx).^2; contour(xx,yy,mis,252)
```

Now plot the contours for $\partial f / \partial x_1$ and $\partial f / \partial x_2$. Is $f(\mathbf{x})$ a quadratic or non-quadratic function? Are the elements of the Hessian matrix, the components of the gradient, or the curvature along the x_1 direction functions of (x_1, x_2) ? For an objective function that is strictly quadratic, are the elements of the Hessian and gradient a function of spatial position? Same question, except the objective function is a cubic polynomial.

3. Assume $f(\mathbf{x}) = x_1^2 + x_2^2 - 2x_1x_2$. Plot the contours of $f(\mathbf{x})$. Is $f(\mathbf{x})$ a quadratic or non-quadratic function? Are the elements of the Hessian matrix, the components of the gradient, or the curvature along the x_1 direction functions of (x_1, x_2) ? For the above quadratic function, how many minima are there in the objective function? Identify the local and global minimum points for $f(\mathbf{x})$.

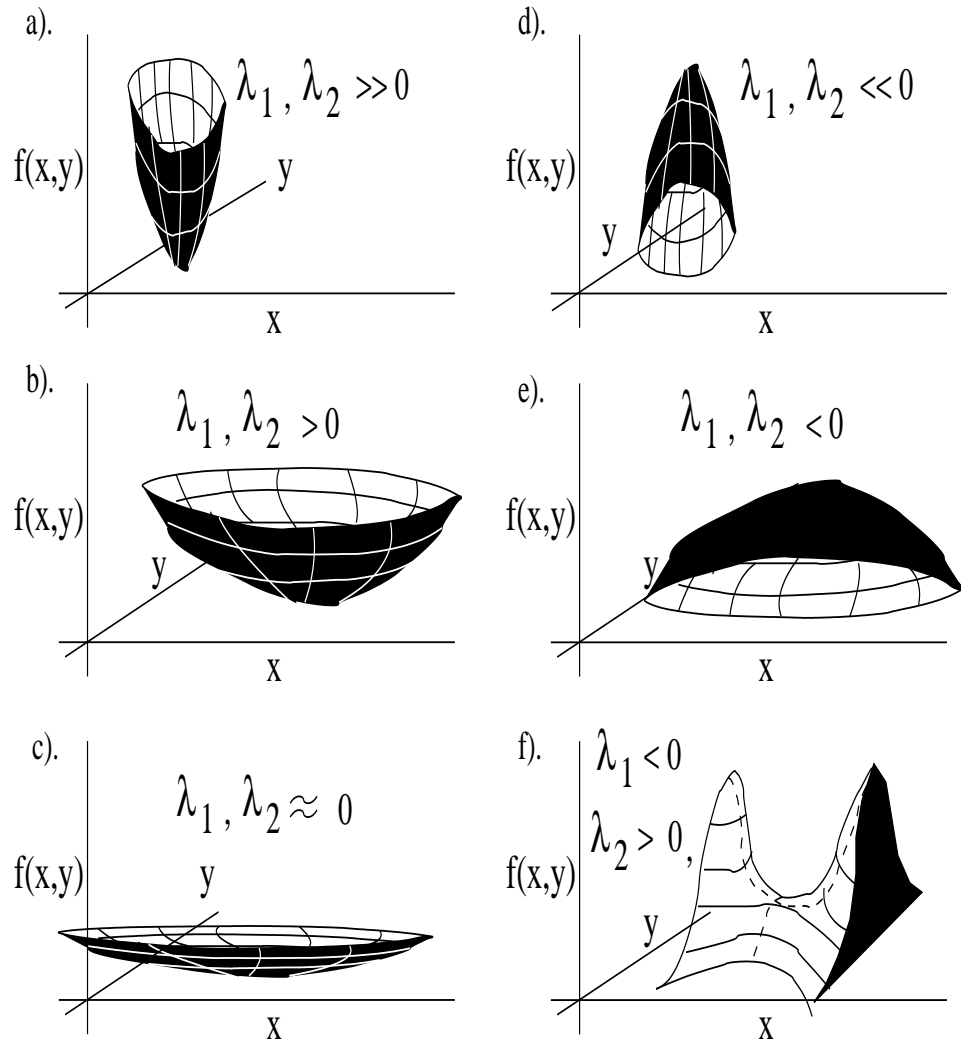


Figure 3.8: Plots of functions with different eigenvalues λ_1 and λ_2 for the 2×2 Hessian matrix. Left column of figures are associated $\lambda_1, \lambda_2 > 0$ while the right column corresponds to examples where at least one of the eigenvalues is negative.

4. Can there ever be more than one isolated minimum for a quadratic function? Prove your answer. Can there ever be more than one isolated minimum for a non-quadratic function?
5. Find the slope of the Rosenbrock function $f(\mathbf{x})$ at $\mathbf{x} = (2, 3)$ along the line direction parallel to the vector $(1, 1)$. Find the slope of $f(\mathbf{x})$ at $(2, 3)$ that is parallel to the vector orthogonal to the vector $(1, 1)$. Show work using the 2×1 gradient vector.
6. Same question as the previous one except find the maximum and minimum curvatures of the Rosenbrock function instead of the slope. What is the curvature along the slope direction? Is the greatest curvature always along the gradient direction?
7. Show that a general quadratic function $f(\mathbf{x}) = (1/2)\mathbf{x}^T \mathbf{H} \mathbf{x} + \mathbf{g}^T \mathbf{x} + c$ where \mathbf{H} is symmetric, can also be described as $f(\mathbf{x}) = (1/2)(\mathbf{x} - \mathbf{x}')^T \mathbf{H}(\mathbf{x} - \mathbf{x}') + c'$ where $\mathbf{H}\mathbf{x}' = -\mathbf{g}$ and $c' = c - (1/2)\mathbf{x}'^T \mathbf{H}\mathbf{x}'$. What is the geometrical meaning of this transformation?
8. Design the elements of a 2×2 Hessian matrix so all of the shapes shown in Figure 3.8 are obtained. Use a MATLAB plotting code similar to

```
[X,Y,Z] = peaks(30);
figure
surfc(X,Y,Z)
```

9. Starting from an objective function with multiple minima, devise a gradient descent method and multiscale strategy to mitigate getting stuck in a local minima. An example of an objective function with local minima is shown below.

```
[X Y Z]=peaks(100);
s=sqrt(X.^2+Y.^2);
surfc(cos(2*pi*s*2)+s);
```

One-dimensional and 2D examples are shown in Figure 3.9 along with the MATLAB script. To compute the element values of the gradient and Hessian you will have to use finite-difference approximations.

```
clear all
x = -1:.05:2;
y = -humps(x);n=length(y);
subplot(121)
plot(x,y)
xlabel('x')
ylabel('humps(x)')
grid on;subplot(122)
[X Y Z]=peaks(n);
yy=y'*y+10;
```

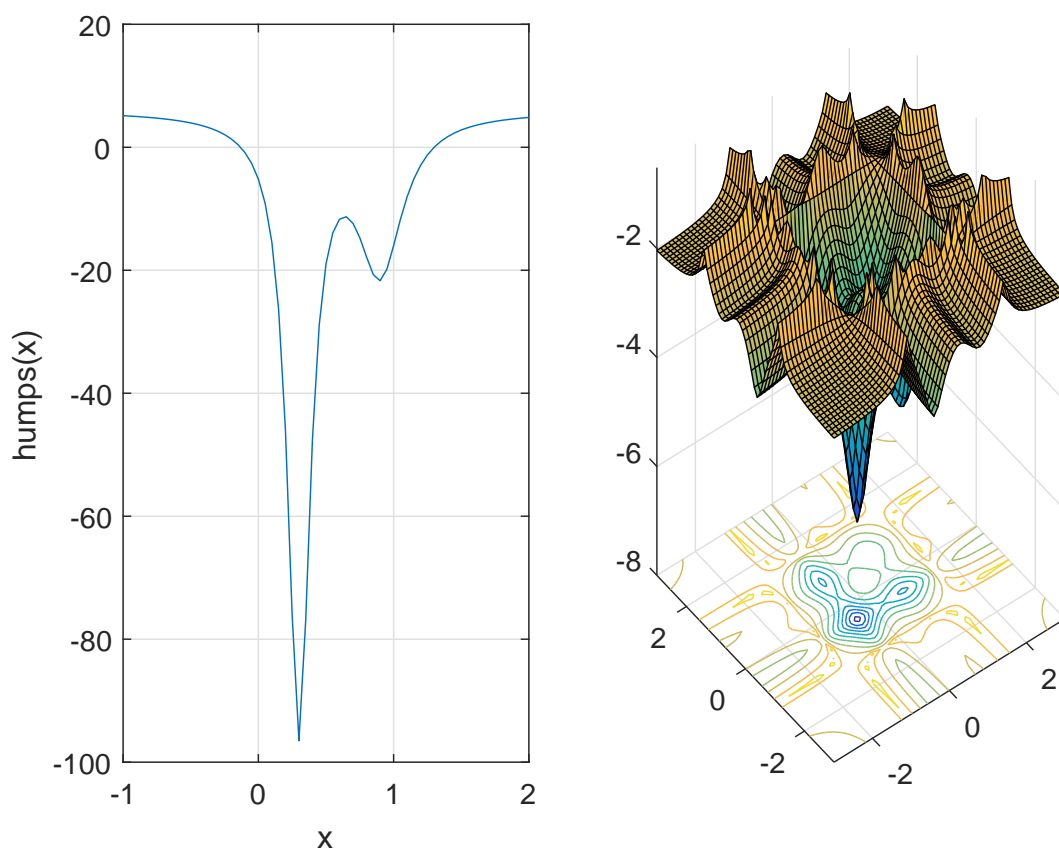


Figure 3.9: Objective functions with local minima.

```
yy=real((yy).^(.2));  
surf(X , Y, -yy)
```

Chapter 4

Introduction to Neural Networks

The previous two chapters sought to find the best model parameters in the matrix \mathbf{W} that explains the data vector \mathbf{t} , where the elements of \mathbf{t} can take on the value of any real number. The classification problem is similar, except the element values of the predicted vector \mathbf{t} denote the *class* of the input \mathbf{x} , where the element values of a 1×1 vector $\mathbf{t} = t$ might be restricted to be either 1 or 0. For example, $t = 1$ indicates the class of red motorcycles and $t = 0$ indicates the class on non-red motorcycles.

We now introduce the method of neural networks, which is often used as a supervised machine learning method for classifying input images. Unlike the unsupervised methods of cluster analysis, the neural network method finds the optimal \mathbf{W} from a large *training* set of classified data $[(\mathbf{x}^{(1)}, \mathbf{t}^{(1)}), (\mathbf{x}^{(2)}, \mathbf{t}^{(2)}), \dots]$ such that, for example, $\sum_i \|\mathbf{W}\mathbf{x}^{(i)} - \mathbf{t}^{(i)}\|_2$ is minimized. Here, $(\mathbf{x}^{(i)}, \mathbf{t}^{(i)})$ is the i^{th} training *example* and it is denoted as a *supervised training pair* because the input vector $\mathbf{x}^{(i)}$ has been classified and its classification is coded into the sparse target vector $\mathbf{t}^{(i)}$. There are a large number of training examples so that the neural network can estimate the optimal \mathbf{W} that can capture the hidden patterns in these training examples. Once \mathbf{W} is *learned* it can be applied to a new set of data, sometimes denoted as the *holdout data*, which needs to be classified.

4.1 Neural Networks

The goal of neural networks is to estimate model parameters \mathbf{W} that non-linearly explain the given training pair of vectors (\mathbf{x}, \mathbf{t}) . The fundamental modeling equation of neural networks is defined as

$$a_i = g(z_i) = \sum_{j=1}^J w_{ij}x_j. \quad (4.1)$$

where a_i is the i^{th} element of the $I \times 1$ predicted data vector \mathbf{a} . Here, $g(z_i)$ is known as the i^{th} activation function that forms the $I \times 1$ activation vector \mathbf{a} from the $\mathbf{J} \times 1$ input vector \mathbf{z} . Its role in the context of classification is to *squash* a wide range of input values z_i into a tiny range of output values, e.g. $-1 \leq a_i \leq 1$. A series of these two elementary operations, matrix-vector multiplication followed by the squashing function, makes up the architecture of the neural network.

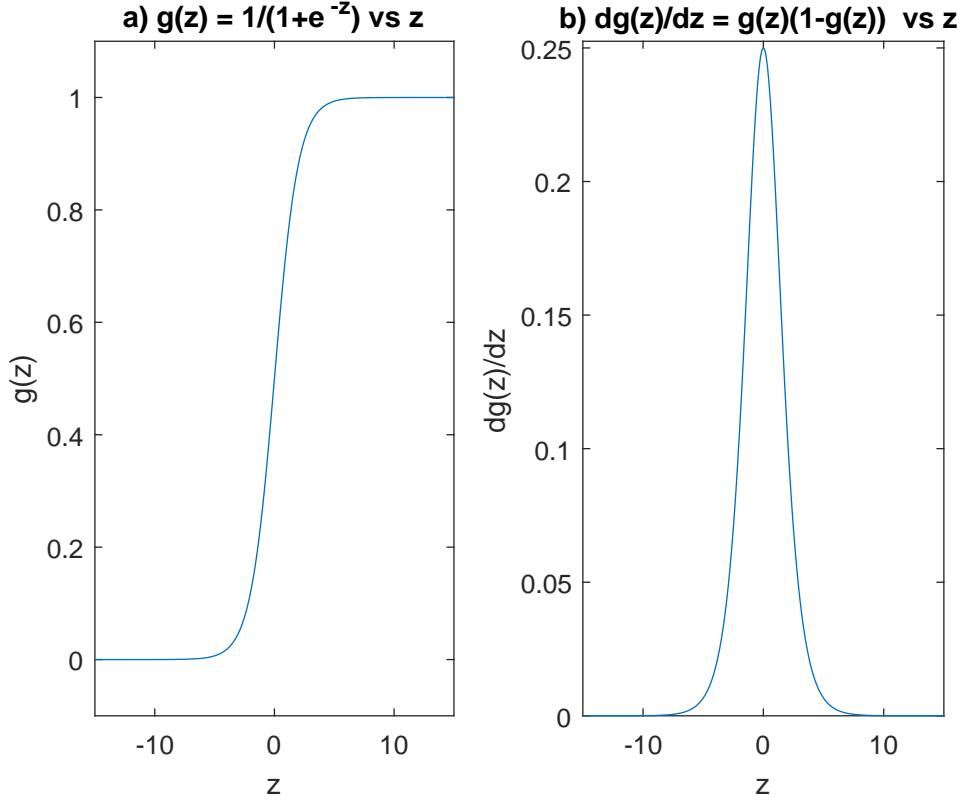


Figure 4.1: a) Sigmoid function and b) its derivative.

A typical shrinking function is the non-linear *sigmoid* threshold function¹ shown in Figure 4.2a and its derivative in Figure 4.2b:

$$g(z) = \frac{1}{1 + e^{-z}} \quad \text{and} \quad \frac{\partial g(z)}{\partial z} = \frac{e^{-z}}{(1 + e^{-z})^2} = g(z)[1 - g(z)]. \quad (4.2)$$

This non-linear function is suited for binary classification problems because its *sparsified* output approximates an all-or-nothing function by returning the values 1 and 0 for, respectively, z somewhat larger and somewhat smaller than 0. The output of the squashing function $g(z)$ resembles the activation of a brain's neuron: if the strength of an electrochemical impulse into a neuron is above a certain threshold, the neuron will transmit this information to a neighboring neuron.

The word *network* in *neural networks* indicates that there is a series, i.e. network, of threshold-matrix-vector operations that are applied to \mathbf{x} , as depicted in the Figure 4.2 diagram. Each column of round nodes represents a *layer* and the number in the i^{th} node of the n^{th} layer is denoted as the activation element $a_i^{[n]}$ in equation ???. The weights next to

¹The sigmoid function is also known as the logistic function (Bishop, 2006) and is used as a probability density function for binary regression analysis. For example, the probability $P(h)$ for passing an exam increases with the number of hours h studied. Thus, the chance for success is $P(h) = 1/(1 + e^{-h})$ and that for failure is $1 - P(h)$.

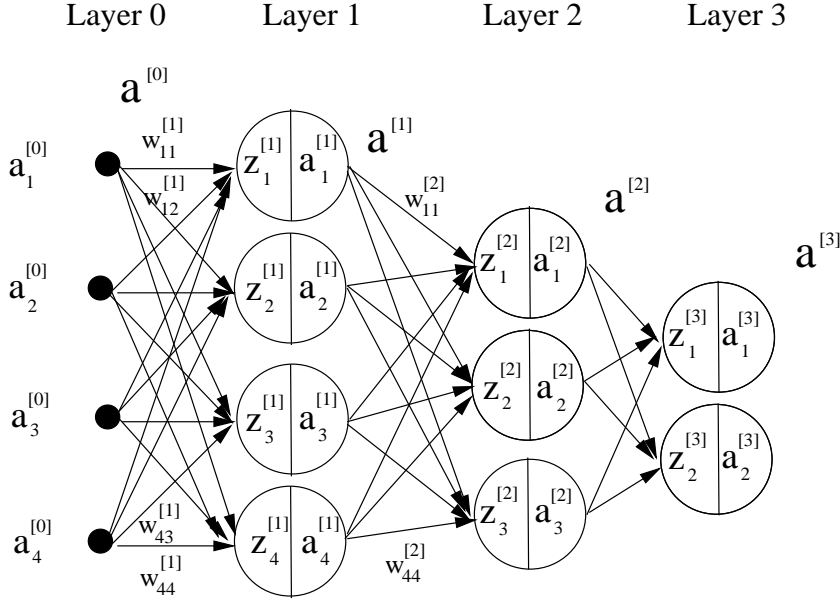


Figure 4.2: Notation for a three-layer, i.e. $N = 3$, neural network with four input nodes at the first layer. The activation output from the i^{th} node in the n^{th} layer is denoted as $a_i^{[n]} = g(z_i^{[n]})$, where $z_i^{[n]} = \sum_j w_{ij}^{[n]} a_j^{[n-1]}$. The input data \mathbf{x} is the activation vector $\mathbf{a}^{[n]}$ for the 0^{th} layer and the predicted data are the activation vector $\mathbf{a}^{[3]}$ at the last layer. The layers between the first and last are denoted as hidden layers.

each arrow are the weights of the matrix elements w_{ij} , except we append the superscript $[n]$ to indicate the layer number so that equation 4.1 becomes

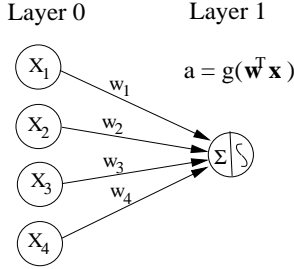
$$\begin{aligned}
 z_i^{[n]} &= \sum_{j=1}^J w_{ij}^{[n]} x_j^{[n]}, \quad i \in [1, 2 \dots I], \\
 a_i &= g\left(\sum_{j=1}^J w_{ij} x_j\right).
 \end{aligned} \tag{4.3}$$

Here, the layer number n is denoted as the superscript $[n]$ for both the input $z_i^{[n]}$ and its squashed output $a_i^{[n]} = g(z_i^{[n]})$.

The threshold function is non-linear with respect to the components of \mathbf{w} , so the neural network problem to-be-defined below is a non-linear problem². Consequently, the iterative solution can get stuck in a local minimum and requires regularization and multiscale preconditioning such as *max pooling* discussed in the previous chapter.

²The operation $\mathbf{w}^T \mathbf{x}$ is a linear operation. However, $g(\mathbf{w}^T \mathbf{x})$ gives an output that is non-linearly related to the parameters \mathbf{w} because it does not pass one of the simple linearity tests $g(\alpha z) = \alpha g(z)$, where α is a scalar.

a) Single-node neural network



b) Two-node neural network

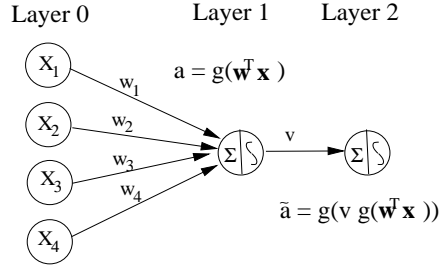


Figure 4.3: Diagrams of a) single-node and b) two-node neural networks.

4.1.1 Single-node Neural Network

Assume we are given M training pairs $(\mathbf{x}^{(k)}, t^{(k)})$ of data, where $\mathbf{x}^{(k)}$ is a $N \times 1$ vector and $\mathbf{t}^{(i)} = t^{(k)}$ is the 1×1 vector with the element value that is either 1 or 0. We define the 1-node classification problem as the following.

$$\textbf{Given: } (\mathbf{x}^{(k)}, t^{(k)}) \text{ and the model } \overbrace{g\left(\sum_{j=1}^J w_j x_j^{(k)}\right)}^{\text{predicted class}} = \overbrace{t^{(k)}}^{\text{obs. class}},$$

$$\textbf{Find: } \mathbf{w} := \arg \min_{\mathbf{w}} \frac{1}{2} \sum_{k=1}^K \underbrace{\left[g\left(\sum_{j=1}^J w_j x_j^{(k)}\right) - t^{(k)} \right]^2}_{g(\mathbf{w}^T \mathbf{x}^{(k)}) - t^{(k)} = r^{(k)}},$$

$$\textbf{Solution: } w_i := w_i - \alpha \frac{\partial \epsilon}{\partial w_i}, \quad (4.4)$$

where $r^{(k)}$ is a scalar rather than a vector for the k^{th} example because the target vector $\mathbf{t} = t$ for this one-node classification problem is a scalar. A diagram of the forward modeling operation is illustrated in Figure 4.3a, where the round node in the middle is divided into two parts: the left half indicates the inner product $\mathbf{z} = \mathbf{w}^T \mathbf{x}$ between \mathbf{w} and the input vector \mathbf{x} , and the right indicates the operation of the squashing function on this. This is considered to be a one-layer single node neural network.

The optimal solution to equation 4.4 in the least-squares sense is found by defining the objective function as

$$\epsilon = \frac{1}{2} \sum_{k=1}^K (r^{(k)})^2 = \frac{1}{2} \sum_{k=1}^K \left[g\left(\overbrace{\mathbf{w}^T \mathbf{x}^{(k)}}^{z^{(k)}}\right) - t^{(k)} \right]^2, \quad (4.5)$$

where the gradient is given by

$$\begin{aligned}\frac{\partial \epsilon}{\partial w_i} &= \sum_{k=1}^K r^{(k)} \frac{\partial r^{(k)}}{\partial w_i} \\ &= \sum_{k=1}^K (g(\mathbf{w}^T \mathbf{x}^{(k)}) - t^{(k)}) \frac{\partial g(z^{(k)})}{\partial z^{(k)}} \frac{\partial z^{(k)}}{\partial w_i}.\end{aligned}\quad (4.6)$$

Recognizing that $\frac{\partial z^{(k)}}{\partial w_i} = \frac{\partial \mathbf{w}^T \mathbf{x}^{(k)}}{\partial w_i} = x_i^{(k)}$ and substituting equation 4.2 into equation 4.6 gives the gradient for the non-linear steepest descent formula :

$$\mathbf{w}_i := \mathbf{w}_i - \alpha \sum_{k=1}^K \overbrace{g(z^{(k)}) (1 - g(z^{(k)})) x_i^{(k)}}^{\frac{\partial r^{(k)}}{\partial w_i}} \overbrace{(g(\mathbf{w}^T \mathbf{x}^{(k)}) - t^{(k)})}^{r^{(k)} = k^{th} \text{ residual}}, \quad (4.7)$$

where α is the step length and the computer science notation $:=$ redefines w_i on the left side as the update to itself on the right-hand side of the equation. This avoids the introduction of an iteration index, and the fewer the better.

Equation 4.7 is similar to equation 2.4 in that the i^{th} component of the gradient is a dot product between the residual vector and the derivative of the residual with respect to the i^{th} model parameter. For the linearized motorcycle problem the derivative of the residual with respect to the i^{th} model parameter is the i^{th} row vector of the matrix \mathbf{X}^T . In contrast, $\partial r_i / \partial w_i$ for the non-linear neural network weights the components of \mathbf{X} by $g(\mathbf{w}^T \mathbf{x})(1 - g(\mathbf{w}^T \mathbf{x}))$ because the modeling equation is non-linear. Thus, $g(\mathbf{w}^T \mathbf{x})(1 - g(\mathbf{w}^T \mathbf{x}))$ must be updated with the new estimate of \mathbf{w} after each iteration in the non-linear steepest descent equation 3.5.

Equation 4.4 only contains one activation function that is applied to each input vector $\mathbf{x}^{(k)}$, so it is denoted as a single-node neural network. This model was initially developed in the context mathematically describing the function of neurons in animals (Rosenblatt, 1958; Hubel and Wiesel, 1962), and later developed into multi-nodal models. The single neuron equation for a single input vector is diagramed in Figure 4.3a, where the circular input nodes are connected to the activation node by solid lines. The weights on each solid line make up the elements of the weight vector \mathbf{w} . The two operations of the matrix-vector multiplication and thresholding are denoted by the symbols in the activation node. The two-node neural network is shown in Figure 4.3b, where the layer number is denoted by the superscript in square brackets.

The following MATLAB pseudo-code implements equation 4.7 as the solution to the 1-node neural network problem.

```
% x(N,M) - input- M input feature vectors with size Nx1
% t(1,M) - input- M input target vectors with size 1x1
%          t= 1 or 0
% alpha   - input- step size
%
clear all
```

```

M=100; % # of equations constraint
N=5;   % # of unknowns (w0, w1, wN)
x=zeros(N,M);t=zeros(M,1);tp=t;
[x,t,alpha,lim,beta,io]=Datain(M,N,x,t); % Create training data
nit=10000;res=zeros(nit,1);
x=[ones(1,M);x]; N=N+1;w=rand(N,1);% start model, Bias Inclusion:
                                     % Append 1st row of x with 1's
%% -----
for k=2:nit % Looping over gradient iterations
    [grad,res]=gradient(M,N,x,t,w,beta,res,k,io);
    alpha=.01*sqrt(grad'*grad);
    w=w-alpha*grad; % Gradient descent update
    if res(k)<=lim;k=nit;end
end
Display(M,res,nit,w,x,t,beta,io)

```

and the MATLAB code for the gradient is below.

```

function [grad,res]=gradient(M,N,x,t,w,beta,res,k,io);
% M - input- # data examples
% N - input- # unknowns in layer
% t - input- # observed data
%io=0- input- cross-entropy gradient
grad=zeros(N,1);grade=grad;
residual=zeros(M,1);
for m=1:M % Loop over M data examples in training set
    z=w'*x(:,m);
    g=1/(1+exp(-z*beta));
    dg=beta*g*(1-g);
    residual(m)=g-t(m); % residual by Zongcai
    grad0 = dg*x(:,m)*residual(m); % Stochastic gradient
    grad1 = x(:,m)*residual(m); % Stochastic cross-entropy gradient
    grad = grad+grad0; % Batch gradient
    grade = grade+grad1; % Batch gradient
end
res(k)=sqrt(residual'*residual)/M;

```

In this code the input training pairs consisted of (\mathbf{x}, t) where \mathbf{x} is a 5×1 vector with elements restricted to be either 1 or 0. The output is the binary classification of $t = 1$ if \mathbf{x} contains just a single 1, otherwise $t = 0$. One hundred training examples are used to train the network to give the results shown in Figure 4.4. Here, the predicted values of $t^{pred.} = g(\mathbf{w}^T \mathbf{x})$ never get to be equal to 1 as plotted in Figure 4.4b. Thus one might consider this a failure. However, the correct classifications can be determined by noticing that any predicted classification above the threshold value of 0.4 could be considered as the class denoted as $t = 1$. With this threshold constraint there is almost 100% accuracy in the predicted class shown in Figure 4.4c. Here, the actual class is a red star and the

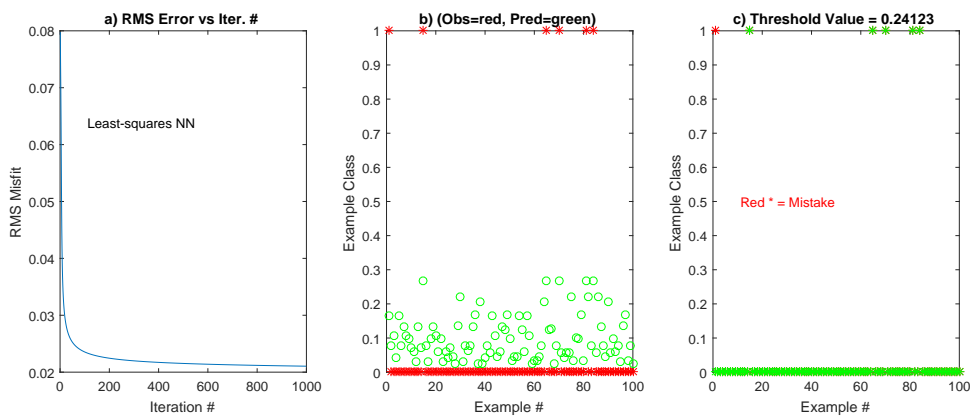


Figure 4.4: a) RMS vs iteration number, b) predicted (green) versus actual (red) classes after 10000 iterations, and c) classes predicted after assigning $t = 1$ to green stars above the threshold of 0.24 in b).

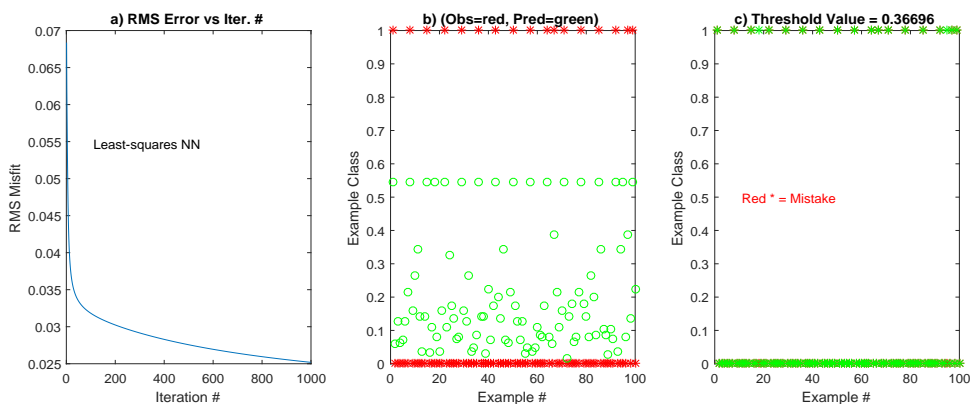


Figure 4.5: Same as Figure 4.4 except the input examples are almost evenly balanced between those with $t = 0$ and $t = 1$. Here the threshold value is 0.36 to get c).

predicted class (after the threshold constraint) is a green star printed over the red stars. If the predictions are correct then the red stars should be completely hidden by green stars, which is largely the case.

To expedite convergence, we must balance out the number of $t = 1$ samples with the number of $t = 0$ examples, otherwise the system of equations can become ill-conditioned as was pointed out in earlier chapters. An unbalanced training set was used for the Figure 4.4 tests and so resulted in a weak separation between the $t = 0$ and $t = 1$ classes in Figure 4.4b. To remedy this problem another test was conducted except the number of $t = 1$ examples were about the same number as the $t = 0$ samples. The results are shown in Figure 4.5. and show a much better separation between the $t = 1$ and $t = 0$ examples.

4.1.2 One-node Neural Network with Cross-Entropy Objective Function

Instead of the least squares objective function, the neural network community often uses the cross-entropy objective function for solving the binary classification problem. Empirical evidence suggests it has better convergence properties compared to the least squares approach.

The starting point for the cross-entropy method (<https://rdipietro.github.io/friendly-intro-to-cross-entropy-loss/>) is to assume that the sigmoid function $0 \leq g(z) \leq 1$ can be used as the likelihood function for the binary random variable t :

$$P(t|\mathbf{w}, \mathbf{x}) = g(\mathbf{w}^T \mathbf{x})^t (1 - g(\mathbf{w}^T \mathbf{x}))^{1-t}, \quad (4.8)$$

which says that, given \mathbf{w} and \mathbf{x} , the probability for $t = 1$ is $g(\mathbf{w}^T \mathbf{x})$, and for $t = 0$ it is $1 - g(\mathbf{w}^T \mathbf{x})$. Finding the optimal \mathbf{w} that maximizes $P(t|\mathbf{w}, \mathbf{x})$ is known as the maximum likelihood solution. Equation 4.8 is in too clumsy of a form so we take the natural logarithm of its negative to get the cross-entropy error function (Bishop, 2006):

$$\epsilon = -t \ln g(\mathbf{w}^T \mathbf{x}) - (1 - t) \ln(1 - g(\mathbf{w}^T \mathbf{x})). \quad (4.9)$$

Since the logarithm is a monotonic function then the optimal \mathbf{w} that maximizes the likelihood function in equation 4.8 also minimizes ϵ in equation 4.9.

If we have K training pairs $(\mathbf{x}^{(k)}, t^{(k)})$ then the likelihood of K training pairs having the specific outcome of $(t^{(1)}, t^{(2)} \dots t^{(K)})$ is the product the individual likelihood functions. Taking the negative logarithm of this product of likelihood functions gives a summation of cross-entropy error functions:

$$\epsilon = -\frac{1}{K} \left[\sum_{k=1}^K t^{(k)} \ln g(\mathbf{w}^T \mathbf{x}^{(k)}) + (1 - t^{(k)}) \ln(1 - g(\mathbf{w}^T \mathbf{x}^{(k)})) \right]. \quad (4.10)$$

Two properties of this error function are suggestive that it is a useful cost function.

1. The arguments of the logarithms are between 0 and 1, so the logarithmic terms are always negative. This flips the sign in front of the summation to be positive.
2. If the predicted output $g(\mathbf{w}^T \mathbf{x}^{(k)}) \rightarrow 1$ correctly predicts the actual class $t = 1$, then $\epsilon \rightarrow 0$. Similarly, if the predicted output $g(\mathbf{w}^T \mathbf{x}^{(k)}) \rightarrow 0$ predicts the actual output $t = 0$ then $\epsilon = 0$ as well. Thus, correct predictions provide a zero-valued misfit function while incorrect ones force $\epsilon > 0$. The worse the prediction the larger the misfit function. the observed

As an example, the the cross-entropy error function for $K = 1$ is plotted in Figure 4.6b for $t^{(1)} = 1$ and $t^{(1)} = 0$. Here, the objective function rises much more steeply than the squared error misfit function in Figure 4.6a for wrong estimates of the solution. This means that the cross entropy misfit function penalizes wrong solutions much more than the squared error one does so that iterative solutions might converge more quickly with the cross-entropy objective function. For the same value of the step length, we move downhill much more rapidly when the gradient is steeper.

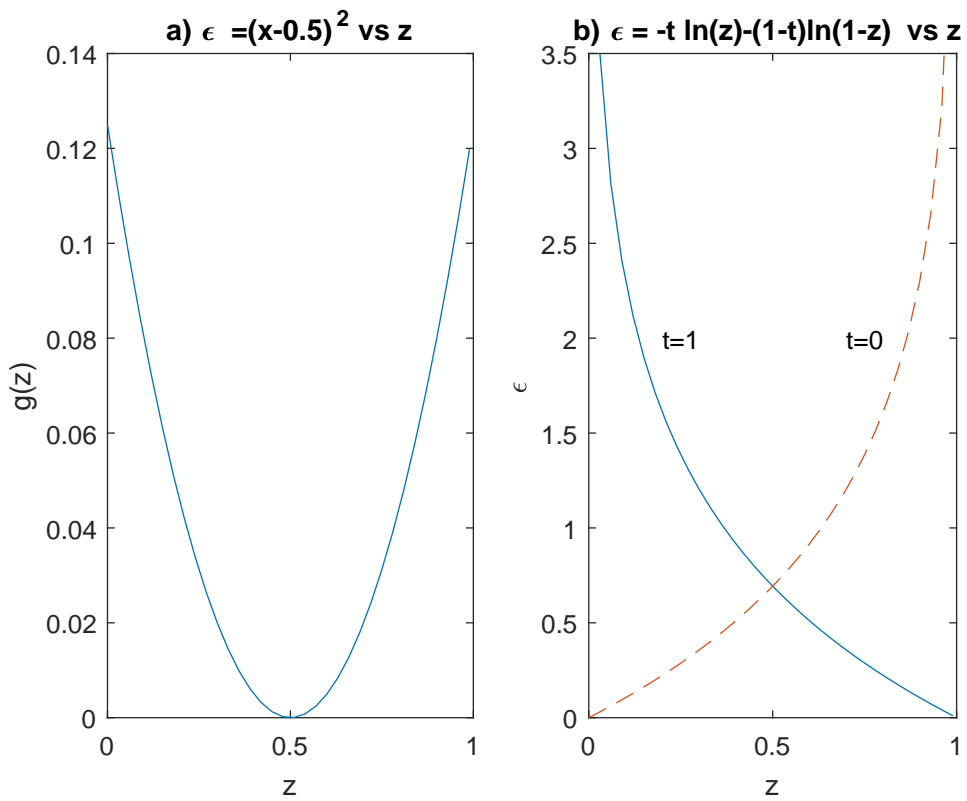


Figure 4.6: Objective functions plotted for a) L_2 misfit function $\frac{1}{2}(0.5 - z)^2$ and b) cross-entropy function $\ln t g(z) + (1 - t) \ln[1 - g(z)]$.

The gradient for the cross entropy function is similar to that in equations 4.7 for the least squares objective function, except

$$\begin{aligned}
 \frac{\partial \epsilon}{\partial w_i} &= -\frac{1}{K} \sum_{k=1}^K \left(\frac{t^{(k)}}{g(\mathbf{w}^T \mathbf{x}^{(k)})} - \frac{1-t^{(k)}}{1-g(\mathbf{w}^T \mathbf{x}^{(k)})} \right) \overbrace{g(\mathbf{w}^T \mathbf{x}^{(k)})(1-g(\mathbf{w}^T \mathbf{x}^{(k)}))}^{\text{eqn. 4.2: } \frac{\partial g}{\partial w_i}} x_i^{(k)}, \\
 &= \frac{1}{K} \sum_{k=1}^K \left(\overbrace{g(\mathbf{w}^T \mathbf{x}^{(k)})}^{\text{pred.}} - \overbrace{t^{(k)}}^{\text{obs.}} \right) x_i^{(k)}.
 \end{aligned} \tag{4.11}$$

In this case the predicted data ($g(\mathbf{w}^T \mathbf{x}^{(k)})$) is a squashed version of the original prediction $\mathbf{w}^T \mathbf{x}^{(k)}$. The cross-entropy gradient promotes a much faster learning rate than that for the squared error loss function. Large residual values in equation 4.11 lead to large gradients, and hence a fast learning rate. In comparison, a large residual in equation 4.7 for $t^{(k)} = 0$ means that $g(z^{(k)})$ is nearly one so $1 - g(z^{(k)})$ is nearly zero. Hence, the gradient is nearly zero as well and leads to a slow learning rate.

4.1.3 Two-node Neural Network

The two-node neural network in Figure 4.3b feeds the weighted output θ

$$\theta = g(\mathbf{w}^T \mathbf{x})v, \tag{4.12}$$

of the single-node neural network in Figure 4.3a into another squashing function to get the class prediction and its derivative:

$$g(\theta) = 1/(1 + e^{-\theta}); \quad \frac{\partial g(\theta)}{\partial \theta} = g(\theta)(1 - g(\theta)), \tag{4.13}$$

where the superscript k will be mercifully silent for both $\theta = g(\mathbf{w}^T \mathbf{x}^{(k)})v$ and $z = \mathbf{w}^T \mathbf{x}^{(k)}$. Here, we assume that $g(\theta)$ is a sigmoid function and v is the scalar weight associated with layer two. The least squares misfit function is given by

$$\begin{aligned}
 \epsilon &= \frac{1}{2} \sum_{k=1}^K \overbrace{[g(\theta) - t^{(k)}]^2}^{r^{(k)}}, \\
 &= \frac{1}{2} \sum_{k=1}^K \overbrace{[1/(1 + e^{-g(\mathbf{w}^T \mathbf{x}^{(k)})v}) - t^{(k)}]^2}^{\theta}.
 \end{aligned} \tag{4.14}$$

where there are two sets of unknowns, the weights w_i in the first layer and v for the second layer. Two gradients now need to be computed, a gradient for the components w_i and one for v .

Plugging $\frac{\partial r^{(k)}}{\partial v} = g(\theta)(1 - g(\theta))g(z)$ from equation 4.19 into equation 4.18 gives

$$\frac{\partial \epsilon}{\partial w_i} = \sum_{k=1}^K r^{(k)} \frac{\partial r^{(k)}}{\partial v} (1 - g(z)) v x_i^{(k)}, \quad (4.20)$$

which says that the gradient $\partial r^{(k)} / \partial v$ of the residual computed at a higher-order layer can be reused for the gradient calculation at the next lower-order layer. This is called backward recursion because we are reusing the calculation of the higher-order gradient for the gradient computation at the next lower-order layer. Chapter 5 derives the recursive back-propagation formula for a general neural network, which results in a significant savings in computational costs.

4.1.4 Multiple-node and Multiple-layer Neural Network

In general, the one-node neural network cannot emulate complex relationships between the input feature vectors and the target vectors (Bishop, 2006). However, multi-node and multi-layer neural networks have been found to be universal approximators (Hornik et al., 1989; Hornik, 1991; Ripley, 1996).

Therefore we need to increase the complexity of the neural network by incorporating more nodes and layers into the network (see Figure 4.2). This means that we will have to use a more general notation that includes identification of layer numbers and node numbers. As a simple example, Figure 4.2 depicts a neural network with three layers, an input layer and several nodes per layer. In the previous chapters we denoted the input or as the $N \times 1$ feature vector \mathbf{x} and the last output as the vector \mathbf{t} ; each element of \mathbf{x} occupied a different input node in this vertical layer of N nodes. We now denote this starting vertical layer of nodes as the 0^{th} layer, $\mathbf{x} \rightarrow \mathbf{a}^{[0]}$ and the last N^{th} column of output nodes as $\mathbf{t} \rightarrow \mathbf{a}^{[N]}$.

To summarize, the output activation function from the i^{th} node at the n^{th} layer is denoted by

$$a_i^{[n]} = g(z_i^{[n]}) \rightarrow \text{activation function output at } i^{th} \text{ node in layer } n \quad (4.21)$$

where

$$z_i^{[n]} = \sum_j w_{ij}^{[n]} a_j^{[n-1]} \rightarrow \text{weighted sum inputs at } i^{th} \text{ node in layer } n. \quad (4.22)$$

For convenience the bias term is absorbed into the weights so that the input feature vector is $\mathbf{a}^{[0]} = [1, x_1, x_2, \dots, x_M]$; a bias term is included for most of the layers. The activation function is denoted as $g(z_i^{[n]})$ for the input scalar $z_i^{[n]}$ at the i^{th} node. Here, $\mathbf{W}^{[n]}$ denotes the matrix that contains the filter weights associated with the n^{th} layer. The last layer in the neural network is denoted as the N^{th} layer.

The neural network problem can now be succinctly defined as finding the weights $w_{ij}^{[n]}$ that minimize the objective function:

$$\epsilon = 1/2 \sum_i (\overbrace{a_i^{[N]}}^{\text{predicted}} - \overbrace{y_i}^{\text{observed}})^2 + \text{regularization term}, \quad (4.23)$$

where y_i is the observed output at the i^{th} node and $a_i^{[N]}$ is the predicted output at the i^{th} node of the N^{th} layer. Previously we denoted the target vector as \mathbf{t} but we now denote it as $\mathbf{a}^{[N]}$.

The simplified³ update formula for iterative steepest descent without regularization is given by

$$\begin{aligned}
 & \text{for } j = 1 : niter \\
 & \quad \text{for } n = 1 : N \\
 & \quad \quad w_{ij}^{[n]} := w_{ij}^{[n]} - \alpha \frac{\partial \epsilon}{\partial w_{ij}^{[n]}}, \\
 & \quad \text{end} \\
 & \text{end}
 \end{aligned} \tag{4.24}$$

where $:=$ indicates that the variable $w_{ij}^{[n]}$ is reset to the value given on the righthand side and α is the step length. The above iterative formula appears simple, but the next chapter will derive the gradient terms for a multi-node multi-layer neural network.

4.2 Multinomial Classifiers

The logistic function $g(z) = 1/(1 + e^{-z})$ was used to squash down a wide range of numbers $-\infty < z < \infty$ into a small range of numbers between 0 and 1. This function was also used to define the likelihood function for a binary classifier, which is the starting point for the cross-entropy error function as the objective function.

If there are $C > 2$ independent classes of input objects, then we can use a network with C output nodes, each of which has a sigmoid activation function. Each output node has a separate binary class label $t_c \in 0, 1$, where $c = 1, 2, \dots, C$. In this case the input image can have a classification that is labeled with the value 1 for more than one output node. For example, consider the first output node which is defined for the class of input images which have eyes and the second output node indicates whether they have a tongue. Therefore, the input image of a human will be classified as 1 for both the first and second output nodes. In this case the cross-entropy error function for a single output node is generalized to that of C output nodes:

$$\epsilon = -\frac{1}{K} \sum_{c=1}^C \sum_{k=1}^K [t_c^{(k)} \ln g_c(\mathbf{w}^T \mathbf{x}^{(k)}) + (1 - t_c^{(k)}) \ln(1 - g_c(\mathbf{w}^T \mathbf{x}^{(k)}))], \tag{4.25}$$

where the extra summation is over the C output nodes and the c subscript indicates the index for the c^{th} output node.

The standard multiclass classification is when the input image is exclusively labeled as 1 for just one of the output nodes; all the rest of the output nodes are labeled as 0. This is known as a 1-of- C coding scheme (Bishop, 2006). For example, the output class for

³To reduce notational tyranny, we exclude notation for different training examples and assume just one example. The input layer in Figure 4.2 where the features are inserted is not enumerated as a layer because it is devoid of weights.

node 1 is for the input image being a cat, node 2 is for dogs, and node 3 is for an animal being neither a dog or cat. Clearly any input image of a single animal can only be labeled as 1 for just one of the output nodes. In this case the network outputs are interpreted as the probability of the output being labeled as 1, that is $p(t_c = 1|\mathbf{x}) = g_c(\mathbf{x}\mathbf{w})$ so that the loss function is

$$\epsilon = -\left[\sum_{c=1}^C \sum_{k=1}^K t_c^{(k)} \ln g_c(\mathbf{w}^T \mathbf{x}^{(k)})\right], \quad (4.26)$$

where we have dropped the $1/K$ factor because it does not influence the location of the minimum. Here, the $g_c(\mathbf{w}^T \mathbf{x}^{(k)})$ is defined as the soft-max function

$$g_c(\mathbf{w}^T \mathbf{x}^{(k)}) = \frac{\exp(a_c^{(k)})}{\sum_{c'=1}^C \exp(a_{c'}^{(k)})}, \quad (4.27)$$

which satisfies the characteristics of a probability function where $0 \leq g_c(\mathbf{w}^T \mathbf{x}^{(k)}) \leq 1$ and $\sum_{c=1}^C g_c(\mathbf{w}^T \mathbf{x}^{(k)}) = 1$.

In summary, we have different loss functions for different types of outputs.

1. For regression problems where the output nodes can take on any value, the activation functions at the last layer are linear weights at each of the C nodes. In this case we use the sum of the squared errors as the loss function.
2. If the output is labeled as just one of two classes, then there is only a single output node. The binary cross entropy loss function in equation 4.25 is used with $C = 1$.
3. If the class labels are independent of one another, then equation 4.25 is used for the loss function.
4. If the labeling is 1 - of - C coding then equation 4.26 is used for the loss function.
5. An alternative for a binary classification scheme with just one output node is to use two output nodes and use the softmax output activation function at each node.

4.3 ReLu Activation Function

The sigmoid function was often used as the activation function for neural networks in the 1990s. Empirical experience now shows a preference for other activation functions, especially the *rectified linear unit* $ReLu(z)$ function:

$$ReLu(z) = \begin{cases} 0 & \text{if } z < 0 \\ z & \text{if } z \geq 0 \end{cases} \quad (4.28)$$

The derivative $\frac{\partial ReLu(z)}{\partial z} = 0$ for $z < 0$ and $\frac{\partial ReLu(z)}{\partial z} = 1$ if $z > 0$ and so the gradient does not tend to zero so readily as that of the sigmoid function. The benefit of using $ReLu(z)$ as an activation function is often a significantly faster convergence rate.

4.4 Summary

The equations for solving a neural network are presented, and details for implementing it with a one-layer network are presented. MATLAB codes are provided and should be used to get a feel for how different parameters such as damping, iteration number, step length, and input data affect the final result. The much more complex equations for finding the gradient of a general neural network are presented in the next chapter.

4.5 Exercises

1. A linear operator $A(z)$ has the property that $A(\alpha z) = \alpha A(z)$. Show that $g(\alpha z) = \alpha g(z)$ is not true for $g(z)$ being the sigmoid function.
2. The `Datain.m` and `Dipslay.m` codes are given below. Use these codes in conjunction with the one presented in the text to test the performance of a single neural network code that classifies 5×1 vectors \mathbf{x} whose element values are either 1 or 0. The goal is to train a neural network that can recognize an input vector \mathbf{x} where there is only a single 1 in one of its elements.
 - Compare the performance of the least squares algorithm against that of the cross-entropy algorithm. Which has a faster convergence rate.
 - The number of data examples that are classified as 1 should be about the same as the ones that are classified as 0, otherwise the system of equations will be ill-conditioned and convergence will slow down. Numerically demonstrate this fact.

```
function [x,t,alpha,lim,beta,io]=Datain(M,N,x,t)
for i=1:M
    x(:,i)=round(rand(N,1));
end
for i=1:M
    if sum(x(:,i))==0;t(i)=1;end
end

% Now we are biasing the data set to be about 1/2
% of x(:, :) to only have a single 1 in the 4x1 vector
% so about 1/2 data are classed at t=1
for i=1:100:M
    x(:,i)=0;
    x(1,i)=1; t(i)=1;
    % x(3,i+49)=1; t(i+49)=1;
end

alpha=.001;          % step size
lim=.00001;          % stopping criterion
```

```
beta=1;io=1; % io=0 cross-entropy
```

and the Display.m code is below.

```
function Display(M,res,nit,w,x,t,beta,io)
tp=t*0;tpp=tp;
thresh=.34;
for m=1:M
    tp(m)=w'*x(:,m);
    tp(m)=1./(1+exp(-tp(m)*beta)); %corrected by Zongcai
    if tp(m)>=thresh;tpp(m)=1;end
    if tp(m)<thresh;tpp(m)=0;end
end
subplot(131);plot(res(2:nit));
title('a) RMS Error vs Iter. #')
if io==0;text(nit/9,max(res)*.8,'Cross-entropy NN');end
if io==1;text(nit/9,max(res)*.8,'Least-squares NN');end
ylabel('RMS Misfit');xlabel('Iteration #')
subplot(132);plot([1:M],t,'r',[1:M],tp,'go')
ylabel('Example Class');xlabel('Example #')
title('b) (Obs=red, Pred=green)')
[xx,thresh]=ginput(1)
for m=1:M
    tp(m)=w'*x(:,m);
    tp(m)=1./(1+exp(-tp(m)*beta)); %corrected by Zongcai
    if tp(m)>=thresh;tpp(m)=1;end
    if tp(m)<thresh;tpp(m)=0;end
end
subplot(133);plot([1:M],t,'r',[1:M],tpp,'g')
ylabel('Example Class');xlabel('Example #')
title(['c) Threshold Value = ',num2str(thresh)])
text(M/9,.5,'Red * = Mistake','color','red')
```

3. Create a large training set and tune the parameters (such as step length, starting model etc) to give reasonably good convergence and a small error rate. Now take a holdout data set that was not used for training and use the trained coefficients \mathbf{w} to classify each example in the holdout data set. Is the error rate similar to that of the training data? Did you overfit the data? Was your training set sufficiently diverse to account for the characteristics of the holdout data? if you overfitted, what are the remedies.
4. Sprinkle noise into your training data (i.e., deliberately misclassify some of the training data). Repeat the previous exercise.
5. Compare the two-node MATLAB algorithm with the single-node algorithm. Which one is more tolerant to complexity and noise in the training examples.

6. What is the result if the starting model is $\mathbf{w}^{(0)} = 0$? What is the result if the starting model is $\mathbf{w}^{(0)} = (1111)^T$? Show results.
7. In exercise 2, how do you determine if you are stuck in a local minima? Hint: try different starting models. Show results.

Chapter 5

Multilayer Neural Networks

The recursive equations for both the feed-forward and backward-propagation operations are derived for a multi-layered neural network. For each iteration, the feed-forward and gradient computations cost about $O(N^2M)$ algebraic operations for N layers, each one associated with an $M \times M$ weight matrix. The workflow and pseudo-MATLAB codes are presented for implementing the multi-layer neural network algorithm.

5.1 Introduction

A neural network consists of a sequence of computational nodes arranged in distinct layers (see Figure 4.2). Each layer is a vertical sequence of computational nodes, where we assume N layers in the neural network and each layer can have a different number of nodes. The input nodes are not counted as a network layer because there is no computational processing at these nodes.

There are two operations required for computing the gradient in equation 4.24: feed-forward and back-propagation. The next two sections derive the formulas for these two operations so they can be computed in an efficient recursive fashion.

5.2 Feed-forward Operation

The feed-forward operation of the neural network inputs the features $a_i^{[0]}$ from the starting 0^{th} layer and produces the predicted target value $a_i^{[N]}$ at the last N^{th} layer:

$$a_i^{[N]} = g\left(\overbrace{\sum_{j=1}^{\mu_N} w_{ij}^{[N]} a_j^{[N-1]}}^{z_i^{[N]}} \left(\overbrace{\sum_{k=1}^{\mu_{N-1}} w_{jk}^{[N-1]} a_k^{[N-2]}}^{z_j^{[N-1]}} \left(\dots \overbrace{a_m^{[1]} \left(\sum_{n=1}^{\mu_1} w_{mn}^{[1]} a_n^{[0]} \right)}^{z_m^{[1]}} \right) \right) \right), \quad (5.1)$$

where μ_i is the number of nodes in the i^{th} layer. Here, the variable $z_i^{[k]}$ and output parameters $a_i^{[k]} = g(z_i^{[k]})$ of the k^{th} layer can be assembled into the $\mu_k \times 1$ vectors $\mathbf{z}^{[k]}$ and $\mathbf{a}^{[k]} = g(\mathbf{z}^{[k]})$, respectively. The activation function $g(\cdot)$ is applied to each element of $\mathbf{a}^{[k]}$ so that $g(\mathbf{z}^{[n]})$ is a vector of the same dimension as $\mathbf{z}^{[n]}$.

The computation of the components of the $\mu_n \times 1$ vector $\mathbf{a}^{[n]}$ can be recursively computed from the components of $\mathbf{a}^{[n-1]}$ in the lower-order $(n-1)^{th}$ layer. This recursion can lead to a significant gain in efficient computations as seen in the pseudo-MATLAB code below.

```

load  $\mathbf{a}^{[0]}$ ;
for  $n = 1 : N$ 
    load  $\mathbf{W}^{[n]}$ 
     $\mathbf{z}^{[n]} = \mathbf{W}^{[n]} \mathbf{a}^{[n-1]}$ 
     $\mathbf{a}^{[n]} = g(\mathbf{z}^{[n]})$ 
end

```

where the matrix coefficients $w_{kl}^{[n]}$ for the n^{th} layer are the elements of the $\mu_n \times \mu_{n-1}$ matrix $\mathbf{W}^{[n]}$ and the $\mu_n \times 1$ vector $\mathbf{z}^{[n]}$ contains the components $z_i^{[n]}$ in equation 4.22. For convenience the bias terms $b_i^{[n]}$ for the n^{th} layer are implicitly represented in the first column of the matrix $\mathbf{W}^{[n]}$. Assuming that all of the layers have the same number M of nodes, then each matrix-vector product/layer costs $O(M^2)$ operations. Thus, the computational count for computing the predicted target vector $\mathbf{a}^{[n]}$ is $O(M^2N)$. Without using this recursive procedure, the computational count is $O(M^2N^2)$ to compute the activation vector $\mathbf{a}^{[n]}$ at each layer.

5.3 Back-propagation Operation

The gradient term in equation 4.24 can be recursively computed *backward* by updating $w_{ij}^{[N-1]}$ from the higher-order terms in the N^{th} layer. Unlike forward propagation where recursion computes the higher-order activation term from the previous-order one, back-propagation recursively computes lower-order terms from the higher-order ones. Similar to forward propagation, the computational count for recursively computing gradients at all of the layers is $O(M^2N)$.

5.3.1 Formula for $\partial\epsilon/\partial w_{ij}^{[N]}$

The gradient of the misfit function in equation 4.24 for the weights in the N^{th} layer is

$$\frac{\partial\epsilon}{\partial w_{jk}^{[N]}} = \sum_{i=1}^{\mu_N} \overbrace{(a_i^{[N]} - y_i)}^{residual} \frac{\partial a_i^{[N]}}{\partial w_{jk}^{[N]}}, \quad (5.2)$$

where we set $\lambda = 0$ for pedagogical simplicity. From the chain rule and equations 4.21-4.22 we have

$$\frac{\partial a_i^{[N]}}{\partial w_{jk}^{[N]}} = \frac{\partial a_i^{[N]}}{\partial z_i^{[N]}} \frac{\overbrace{\partial \sum_p w_{ip}^{[N]} a_p^{[N-1]}}^{\partial z_i^{[N]}}}{\partial w_{jk}^{[N]}} = g(z_j^{[N]})' a_k^{[N-1]} \delta_{ij}, \quad (5.3)$$

and

$$\frac{\partial a_m^{[N]}}{\partial a_i^{[N-1]}} = \frac{\partial g(z_m^{[N]})}{\partial z_m^{[N]}} \frac{\partial z_m^{[N]}}{\partial a_i^{[N-1]}} = g(z_m^{[N]})' w_{mi}^{[N]}, \quad (5.4)$$

where $g(z_j^{[N]})' = \frac{\partial g(z_j^{[N]})}{\partial z_j^{[N]}}$ and δ_{ij} represents the Kronecker delta function. Plugging equation 5.3 into equation 5.2 gives the gradient wrt $w_{jk}^{[N]}$ in the N^{th} layer:

$$\frac{\partial \epsilon}{\partial w_{jk}^{[N]}} = \overbrace{(a_j^{[N]} - y_j) g(z_j^{[N]})'}^{\delta_j^{[N]}} a_k^{[N-1]}, \quad (5.5)$$

where $\delta_j^{[N]}$ is the j^{th} component of the weighted residual that vector multiplies the "forward" field value $a_k^{[N-1]}$ at the k^{th} node in the $(N-1)^{th}$ layer. If $g(z)$ is a sigmoid function then $g(z)' = g(z)(1 - g(z))$. Other types of activation functions will provide different formulas for the derivative.

Can we recursively use the term $\delta_j^{[N]}$ in the formula for the calculation of the next lower-order gradient? The answer is yes as the next section demonstrates.

5.3.2 Formula for $\partial \epsilon / \partial w_{ij}^{[N-1]}$

To derive the expression for $\partial \epsilon / \partial w_{ij}^{[N-1]}$, recall the multidimensional chain rule where $f(a_1(t), a_2(t), a_3(t), \dots, a_M(t))$ is a regular function of M smooth functions $a_i(t)$. In this case the derivative $\partial f(t) / \partial t$ can be expressed as

$$\frac{\partial f(a_1^{[N]}, a_2^{[N]}, \dots, a_M^{[N]})}{\partial t} = \sum_{m=1}^M \frac{\partial f(a_1^{[N]}, a_2^{[N]}, \dots, a_M^{[N]})}{\partial a_m^{[N]}} \frac{\partial a_m^{[N]}}{\partial t}, \quad (5.6)$$

where we append the superscript $[N]$ to the a_i variables. Setting $t \rightarrow a_i^{[N-1]}$, this equation says that, for forward propagation of the feature values, a perturbation in $a_i^{[N-1]}$ will affect the values of the outputs $a_i^{[N]}$ in the next highest-order layer. Since this perturbation t will also affect the misfit function $\epsilon(a_1^{[N]}, a_2^{[N]}, \dots, a_{\mu_n}^{[N]})$, then according to the chain rule in equation 5.6 the gradient w/r to the weights in the $N-1$ layer becomes

$$\begin{aligned} \frac{\partial \epsilon}{\partial w_{jk}^{[N-1]}} &= \sum_{m=1}^{\mu_N} \overbrace{\frac{\partial \epsilon}{\partial a_m^{[N]}}}^{(a_m^{[N]} - y_m)} \sum_{i=1}^{\mu_{N-1}} \overbrace{\frac{\partial a_m^{[N]}}{\partial a_i^{[N-1]}}}^{eq. 5.4: g(z_m^{[N]})' w_{mi}^{[N]}} \overbrace{\frac{\partial a_i^{[N-1]}}{\partial w_{jk}^{[N-1]}}}^{eq. 5.3: g(z_j^{[N-1]})' a_k^{[N-2]} \delta_{ij}}, \\ &= \sum_{m=1}^{\mu_N} \overbrace{(a_m^{[N]} - y_m)}^{\mathbf{r}^{[N]}} g(z_m^{[N]})' g(z_j^{[N-1]})' a_k^{[N-2]} \sum_{i=1}^{\mu_{N-1}} w_{mi}^{[N]} \delta_{ij}, \\ &= \overbrace{g(z_j^{[N-1]})'}^{\mathbf{dg}^{[N-1]}} \overbrace{a_k^{[N-2]}}^{\mathbf{a}^{[N-2]}} \left(\sum_{m=1}^{\mu_N} \overbrace{w_{mj}^{[N]}}^{\mathbf{W}^{[N]T}} \overbrace{g(z_m^{[N]})'}^{\mathbf{dg}^{[N]}} \overbrace{(a_m^{[N]} - y_m)}^{\mathbf{r}^{[N]}} \right). \end{aligned} \quad (5.7)$$

Here, the role of the $\{\mathbf{W}^{[N]T} \mathbf{d}\mathbf{g}^{[N]} \cdot \mathbf{r}^{[N]}\}_j$ term is to back-propagate the weighted residual vector from the N^{th} layer to the j^{th} node in the $(N-1)^{th}$ layer. Note that $\mathbf{d}\mathbf{g} \cdot \mathbf{a}$ indicates an element-by-element MATLAB multiplication of the two vectors and the summation associated with the matrix-vector multiplication is over the first subscript m of $w_{mj}^{[N]}$. Thus, we use the transpose symbol T in the superscript of $\mathbf{W}^{[N]}$.

5.3.3 Formula for $\partial\epsilon/\partial w_{ij}^{[N-2]}$

The previous section derived the gradient formula for the $N-1$ hidden layer next to the output layer N . We now derive the gradient $\partial\epsilon/\partial w_{ij}^{[N-2]}$ for the hidden layer surrounded only by hidden layers. In this case the objective function will be a function of the activation parameters in two neighboring links of the chain of layers. This means we need a two-link chain rule for $f = f(g(h(t)))$, where $f(g)$ is a function of g and $g(h)$ is a function of $h(t)$. Therefore, the single-link chain rule in equation 5.6 can be extended to the two-link chain rule where $a_i(t) \rightarrow a_i(b_1(t), b_2(t) \dots b_M(t))$:

$$\frac{\partial f(a_1, a_2, \dots a_M)}{\partial t} = \sum_{m=1}^M \sum_{n=1}^M \frac{\partial f(a_1, a_2, \dots a_M)}{\partial a_m} \frac{\partial a_m}{\partial b_n} \frac{\partial b_n}{\partial t}. \quad (5.8)$$

Setting $a_i \rightarrow a_i^{[N]}$, $b_i \rightarrow a_i^{[N-1]}$, $f \rightarrow \epsilon$ and $t \rightarrow a_i^{[N-2]}$ gives the formula for $\frac{\partial\epsilon}{\partial w_{jk}^{[N-2]}}$:

$$\begin{aligned} \frac{\partial\epsilon}{\partial w_{jk}^{[N-2]}} &= \sum_{i=1}^{\mu_{N-2}} \frac{\partial\epsilon}{\partial a_i^{[N-2]}} \frac{\partial a_i^{[N-2]}}{\partial w_{jk}^{[N-2]}}, \\ &= \sum_{m=1}^{\mu_N} \underbrace{\frac{\partial\epsilon}{\partial a_m^{[N]}}}_{\mathbf{d}\mathbf{g}^{[N-2]}} \sum_{n=1}^{\mu_{N-1}} \underbrace{\frac{\partial a_m^{[N]}}{\partial a_n^{[N-1]}}}_{\mathbf{a}^{[N-3]}} \sum_{i=1}^{\mu_{N-2}} \underbrace{\frac{\partial a_n^{[N-1]}}{\partial a_i^{[N-2]}}}_{\mathbf{W}^{[N-1]T}} \underbrace{\frac{\partial a_i^{[N-2]}}{\partial w_{jk}^{[N-2]}}}_{\mathbf{d}\mathbf{g}^{[N-1]}}, \\ &= \underbrace{g(z_j^{[N-2]})' a_k^{[N-3]}}_{\mathbf{d}\mathbf{g}^{[N-2]} \cdot \mathbf{a}^{[N-3]}} \left(\underbrace{\sum_{n=1}^{\mu_{N-1}} w_{nj}^{[N-1]} g(z_n^{[N-1]})'}_{\mathbf{W}^{[N-1]T}} \right) \left(\underbrace{\sum_{m=1}^{\mu_N} w_{mn}^{[N]} g(z_m^{[N]})'}_{\mathbf{d}\mathbf{g}^{[N]}} \underbrace{(a_m^{[N]} - y_m)}_{\mathbf{r}^{[N]}} \right), \end{aligned} \quad (5.9)$$

where the boldface variables are also seen in equation 5.7 and $g(z_m^{[N]})'(a_m^{[N]} - y_m)$ is the residual component in equation 5.5.

Each layer of the neural network has the same type of structure, so the formula for the gradient in the P^{th} layer, where $1 < P < N-2$, is given by

$$\frac{\partial\epsilon}{\partial w_{jk}^{[P]}} = g(z_j^{[P]})' a_k^{[P-1]} \left(\mathbf{V}^{[P+1]} \mathbf{V}^{[P+2]} \dots \mathbf{V}^{[N-1]} \mathbf{V}^{[N]} \mathbf{r}^{[N]} \right)_j, \quad (5.10)$$

where

$$(\mathbf{V}^{[P]})_{ij} = w_{ij}^{[P]} g(z_i^{[P]})', \quad i \in [1, 2 \dots \mu_P], \quad j \in [1, 2 \dots \mu_{P-1}], \quad (5.11)$$

The numerical implementation of equation 5.10 is ripe for recursion. Unlike the recursive algorithm of forward propagation that starts at layer 1, backward recursion starts from the N^{th} layer to get $\mathbf{V}^{[N]}\mathbf{r}^{[N]}$, and then recursively computes the next lower-order terms until reaching the layer of interest. This is known as backward propagation of the residual.

The pseudo-code for recursively computing the $M \times M$ gradient matrix $d\epsilon$ at the $(J-1)^{th}$ layer is given below. Here we assume the bias values are absorbed into the matrix $\mathbf{W}^{[N]}$ and $N > J > 1$, where J is a positive integer. Assume $\mathbf{W}^{[i]}$, $\mathbf{a}^{[i]}$, $\mathbf{dg}^{[i]}$ are the $M \times M$ weight, $M \times 1$ activation and $M \times 1$ gradient $\frac{\partial g}{\partial z}$ matrices, respectively, that have been pre-computed for all N layers. For notational simplicity we assume that the number of nodes in each layer is M .

```

Load ( $\mathbf{a}^{[0]}$ ,  $\mathbf{a}^{[1]} \dots \mathbf{a}^{[N]}$ ),  $\mathbf{y}$ , ( $\mathbf{dg}^{[0]}$ ,  $\mathbf{dg}^{[1]} \dots \mathbf{g}^{[N]}$ ), ( $\mathbf{W}^{[0]}$ ,  $\mathbf{W}^{[1]} \dots \mathbf{W}^{[N]}$ )
     $\mathbf{in} = \mathbf{a}^{[N]} - \mathbf{y}$ 
for    $i = N : -1 : J$ 
     $\mathbf{in} = \mathbf{dg}^{[i]} * \mathbf{in}$ 
     $\mathbf{in} = \mathbf{W}^{[i]} * \mathbf{in}$ 
end
     $\mathbf{in} = \mathbf{in} * \mathbf{dg}^{[i-1]}$ 
     $d\epsilon(j, k) = in(j) * a(k)^{[i-2]}$ 

```

Each gradient calculation for a layer's weights will cost about $O(M^2)$ algebraic operations per iteration because of the matrix-vector product. If the number of layers is N then the total cost will be about $O(M^2N)$ algebraic operations for computing the weight gradients for all the layers.

5.4 MATLAB Code

The MATLAB code for the fully-connected neural network can be derived from the above pseudo-code. There are two principal portions of the code, forward and backward propagation in *gradientnn.m* and the main code *NNode.m*. Below is the major fragment from *NNode.m*:

```

% To train your neural network, we will now use steepest decent and line search

fprintf('\nTraining Neural Network... \n')

for k=2:nit      % Looping over iterations
    alpha=1;
    %gradientnn ouput: grad =gradient and res(k) = objective function value
    [grad,res(k)]=gradientnn(M,x,t',ww,layer_size,obj_option,act_option,lambda);

    for ilayer=1:layer_num-1
        ww{ilayer}=ww{ilayer}-alpha*grad{ilayer};    %update the weights
    end
end

```

```

end
% Start line search
[~,res1]=gradientnn(M,x,t',ww,layer_size,obj_option,act_option,lambda);
while (res1>res(k)) && (alpha>0.00001)
    alpha=alpha*0.5;
    for ilayer=1:layer_num-1
        ww{ilayer}=ww{ilayer}-alpha*grad{ilayer};
    end
    [~,res1]=gradientnn(M,x,t',ww,layer_size,obj_option,act_option,lambda);
end
%-----
%kk=kk+1
end

```

A fragment of the pseudo-code for forward propagation modeling in *gradientmm.m* is shown below

```

% Do forward propagation
for iter =1:layer_num-1
    % N = # of layers

    aa{iter} = [ones(1, M); aa{iter}]; % ones(1, m) is for bias
    zz{iter}=ww{iter}*aa{iter}; % z[n]=W[n]a[n-1]
    %%----- a[n]=g(z[n])-----%%
    if iter ==layer_num-1 % output layer sigmoid
        [aa{iter+1},~] = activation(zz{iter},1);
    else
        [aa{iter+1},~] = activation(zz{iter},act_option);
    end
end

penalize =penalize+ sum(sum(ww{iter}.^ 2)); % Bias regularization
end
% final output for forward propagation predicted target
t_pred = aa{layer_num};

% calculate the objective function and the derivative of objective
% function with respect to t_pred using likelihood or L2 type
% obj_option=1 for L2, 2 for likelihood

[res,in]= misfit( t_pred,t,1/M,obj_option);

res = res + (lambda/(2*M)) * penalize; % add regularization
and the back-propagation MATLAB code is below

% Implement back-propagation algorithm to compute the gradients
% written according to Back-propagation Operation

```

```

% Implement back-propagation

for iter=layer_num-1:-1:1
    %'sigmoidgrad' means compute the gradient of the sigmoid function
    if iter ==layer_num-1 %output layer = sigmoid
        [~,dg]=activation(zz{iter},1);
    else
        [~,dg]=activation(zz{iter},act_option); % in=dg[i].*in
    end

    in=dg.*in; % in=backward field, A=forward field

    grad{iter}=in*aa{iter}'+(lambda/M)*ww{iter};% de(j,k)=in*(a[i-2])^T
    % update gradient with respect to next weights
    in=ww{iter}'*in; % in=W'[i]*in
    in = in(2:end, :);
end

end

```

The activation function *activation.m* is given by

```

function [ g,dg ] = activation( z,type )
%z - input- for activation function
%type: objective function type: 1 for sigmoid, 2 for ReLU
% g - output- value of the activation function
% dg- output- gradient of g with respective to z

if type==1 % for sigmoid
    g = 1.0 ./ (1.0 + exp(-z));
    dg = g .* (1 - g); %Compute the gradient of the sigmoid function
elseif type==2 % for ReLU
    g=z*0.0; dg=z*0.0;
    g(z>0)=z(z>0);
    g(z<=0)=z(z<=0)*0.0;
    dg(z>0)=1.0;
    dg(z<=0)=0.0;
else
    display('You entered the wrong type for the activation function');
    stop
end
end

```

A vectorized version of the back-propagation and forward propagations algorithms are in Appendix 5.9.

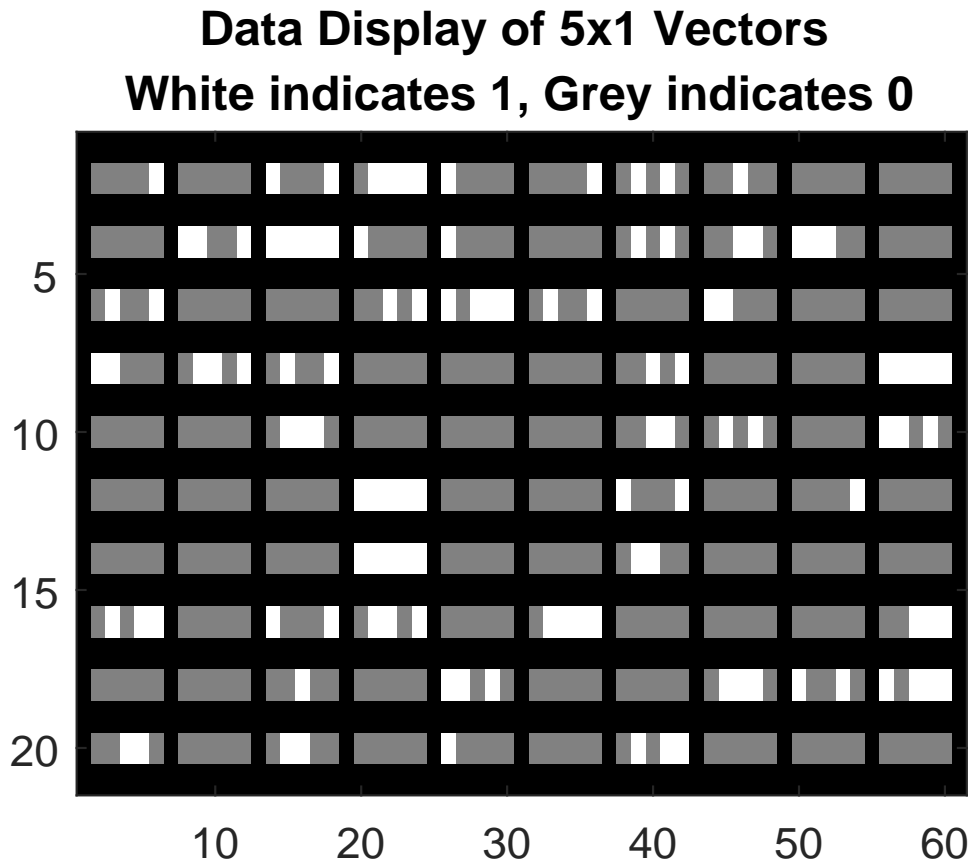


Figure 5.1: Examples of 5×1 vectors with element values equal to either 1 (gray) or 0 (white). Approximately half the vectors only contain 0 values.

5.5 Numerical Examples

As a test example, the input data were 5×1 vectors where the vector-element values were either 1s or 0s. Figure 5.1 graphically depicts a large number of vector examples, where gray (white) means an element value of 1 (0). The goal is to train a network so that it can classify any vector which only has 0 values as class 1, otherwise it is class 0. Using one-hundred training examples and a 4-layer neural network (we don't count the input layer) gives the results shown in Figure ???. The top row of figures shows the results for a neural network with an L2 loss function and a sigmoid activation function, while the bottom row is for a ReLu activation function and a cross-entropy loss function. It is obvious that the ReLU and cross-entropy network provides the fastest convergence and most accurate results.

Figure 5.3 is similar to Figure ??? except for different combinations of loss and activation functions. It appears that the ReLu and the cross-entropy loss function in Figure ??c- ??d gives the best results in terms of accuracy and fast convergence rate.

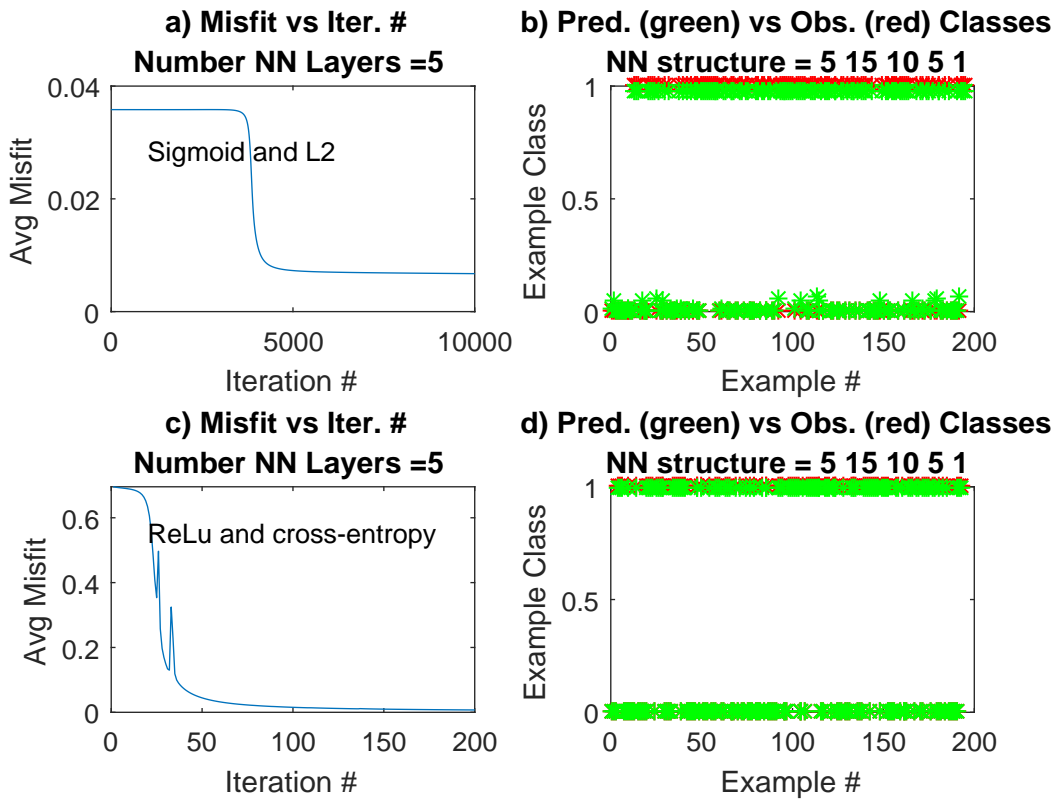


Figure 5.2: Convergence plots and comparison of predicted (green) and observed (red) classes of 5×1 input vectors for a 5-layer neural network. The 5 layers have 5, 15, 10, 5 and 1 nodes, starting from the input layer with 5 nodes. The top row is for the network with a sigmoid activation function and L2 loss function, while the bottom row is for a ReLu activation function and cross-entropy loss function. If only red stars appeared in the right column of figures then no classification errors were encountered.

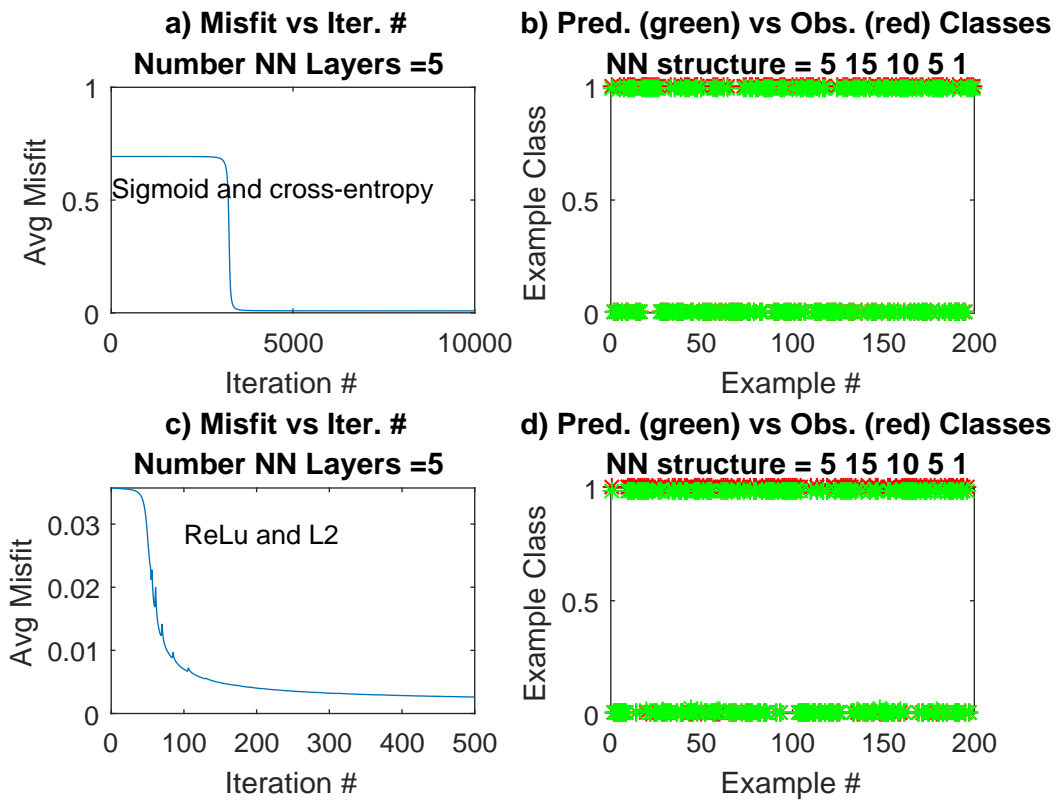


Figure 5.3: Same as previous figure except different combinations of activation and loss functions.

5.6 Summary

The recursive equations are derived for the forward propagation and back-propagation operations of a neural network. These operations can be used to find the weights $w_{ij}^{[n]}$ in each layer that minimize the objective function. The recursive nature of these equations provide for an efficient steepest descent procedure that requires $O(M^2N)$ computation per iteration, where M is the number of nodes per layer and N is the number of layers. Here, we assume that the number of nodes M is the same for each layer. Numerical examples are provided that empirically demonstrate the superior performance of the ReLu+cross-entropy network over the other types of networks.

5.7 Exercises

1. Derive the formula for the three-link chain rule.
2. Derive the formula for the weight gradient at the $N = 12$ layer.
3. Show that equation 5.7 reduces to equation 4.16 for the two-layer neural network.
4. Write the pseudo-MATLAB code where the bias vector and its gradient are explicitly computed.
5. Derive the steepest descent formula for the cross-entropy objective function.
6. Write the pseudo-MATLAB code where regularization is used.
7. Write the pseudo-MATLAB code where the input is a batch matrix that represents the training set.
8. Write the pseudo-MATLAB code where the number of nodes per layer is different from one another.

5.8 Computational Labs

1. Go to Fully Connected Neural Network lab in *LAB1/Chapter.Book.FCN/Chapter.GenNN/lab.html* and run the MATLAB code. It uses a fully connected neural network to classify input vectors that have 1's and 0's for its elements.

5.9 Appendix: Vectorized Steepest Descent Formula for Neural Networks

Assume a network architecture where there are M nodes per layer. The vectorized stochastic steepest descent formula for computing $w_{ij}^{[n]}$ for each layer is given by the following MATLAB

pseudo-code.

```

Load  $\mathbf{a}^{[0]}$ ,  $\mathbf{y}$ ; Initialize  $\alpha$ , matrices  $\mathbf{W}^{[i]}$  for  $i = [1, 2, \dots N]$ 
  for  $m = 1 : N$ 
     $\mathbf{a}^{[m]} = \text{forw}(\mathbf{a}^{[0]}, \mathbf{W}^{[1]} \dots \mathbf{W}^{[N]})$  Compute predicted data  $\mathbf{a}^{[N]}$ 
     $\mathbf{dg}^{[m]} = \text{deriv}(\mathbf{a}^{[m]})$  Compute predicted derivative  $\mathbf{dg}^{[m]}$ 
  end
  for  $n = 1 : \text{niter}$  Iterate steepest descent
     $\mathbf{in} = \mathbf{a}^{[N]} - \mathbf{y}$  Residual
    for  $i = N : -1 : 1$  Compute  $\mathbf{W}^{[i]}$  at each layer
       $\mathbf{in} = \mathbf{dg}^{[i]} \cdot \mathbf{in}$ 
       $\mathbf{d\epsilon} = (\mathbf{in} \cdot \mathbf{dg}^{[i-1]}) \cdot \mathbf{a}^{[i-1]T}$ 
       $\mathbf{in} = \mathbf{W}'^{[i]} \cdot \mathbf{in}$ 
       $\mathbf{W}^{[i]} := \mathbf{W}^{[i]} - \alpha \mathbf{d\epsilon}$ 
    end
    for  $m = 1 : N$  Compute new prediction  $\mathbf{a}^{[N]}$ 
       $\mathbf{a}^{[m]} = \text{forw}(\mathbf{a}^{[0]}, \mathbf{W}^{[1]}, \dots \mathbf{W}^{[N]})$ 
       $\mathbf{dg}^{[m]} = \text{deriv}(\mathbf{a}^{[m]})$ 
    end
  end
end

```

The above code is vectorized because we have almost entirely eliminated the explicit use of *for loops*, which can speed up computations by more than order-of-magnitude. If the input data are a batch of data then this can be accommodated by an outer loop over the different training examples. However, this is inefficient so a vectorized version can be obtained by replacing the input $M \times 1$ data vector $\mathbf{a}^{[0]} \rightarrow \mathbf{A}^{[0]}$, where the $M \times P$ batch-data matrix has P columns, each one a different training example of input values. Similarly, the $M \times 1$ target vector \mathbf{y} can be transformed into a $M \times P$ target matrix. This assumes that there are M nodes per layer.

Chapter 6

Convolutional Neural Networks

The theory and practice of convolutional neural networks (CNNs) is introduced where the fully-connected layers are replaced by convolutional layers. In a convolutional neural network the summation in $a_i = g(\sum_{j=1}^M w_{ij}a_j)$, is replaced by the weighted sum $a_i = g(\sum_{j=1}^{M'} \hat{w}_{i-j}a_j)$ over a limited number $M' \ll M$ of nodes in the layer, where $\hat{w}_{i-j} = w_{ij}$. Thus the weights \hat{w}_i are spatially invariant and reused at every input node. Therefore, the weight w_{ij} in the $O(M \times M)$ $\mathbf{W}^{[n]}$ matrix is replaced by the convolutional weight $w_{ij} \rightarrow w_{i-j}$ with a memory requirement of $O(M)$. This leads to a significant reduction in storage and computational requirements. Moreover, the local nature of the "convolution" operation appears to be consistent with the local identification of objects by the brain's neurons in the visual cortex.

6.1 Introduction

The problem with the classical neural network is that it leads to enormous computational and memory demands for input data of reasonable size. For example, if images of cats are to be distinguished from those of other animals, then the training set might consist of 1024×1024 photos of cats with $O(10^6)$ pixels/photo. For a fully-connected layer, this means that there are 10^6 nodes in the first layer, which will lead to a $10^6 \times 10^6$ $\mathbf{W}^{[1]}$ weight matrix. Thus, the storage and computational demands for large sized input vectors can be prohibitive and discourage the use of neural networks in all but the largest computers.

Another problem with feeding in an entire image into a fully-connected layer (FCL) is overfitting. In the previous example, all of the intensity values of a 1024×1024 image are weighted and summed as an input value into any one node. Thus a FCL will lead to more than a million unknowns with just one layer. This suggests that the conventional neural network might lead to an undetermined set of equations that can almost exactly explain the training data, but do very poorly on data outside the training set. This type of neural network overfits the data.

To mitigate overfitting and reduce the storage and computational demands, convolutional neural networks are now in widespread use today. Instead of feeding forward all of the input data into each node, only a small localized portion is fed into each node. This localized portion of data is weighted by the same weights for any node. This type of neural

network is known as a convolutional neural network (CNN) and is the most popular form of supervised learning since the early 2000's.

CNN can trace its roots back to the biology experiments in the 1950-1960s where it was discovered that a cat's visual cortex greatly responded to certain orientations of an object. Figure 6.1 shows how a cat's visual neurons are most responsive to horizontal or oblique orientations of a bar that it views. Thus, a cluster of neurons in the cat's brain was suited to significantly responding to the view of a small orientation range of a long skinny object. This is similar to the actions of a *localized* dip filter that only lights up for certain dips of an object.

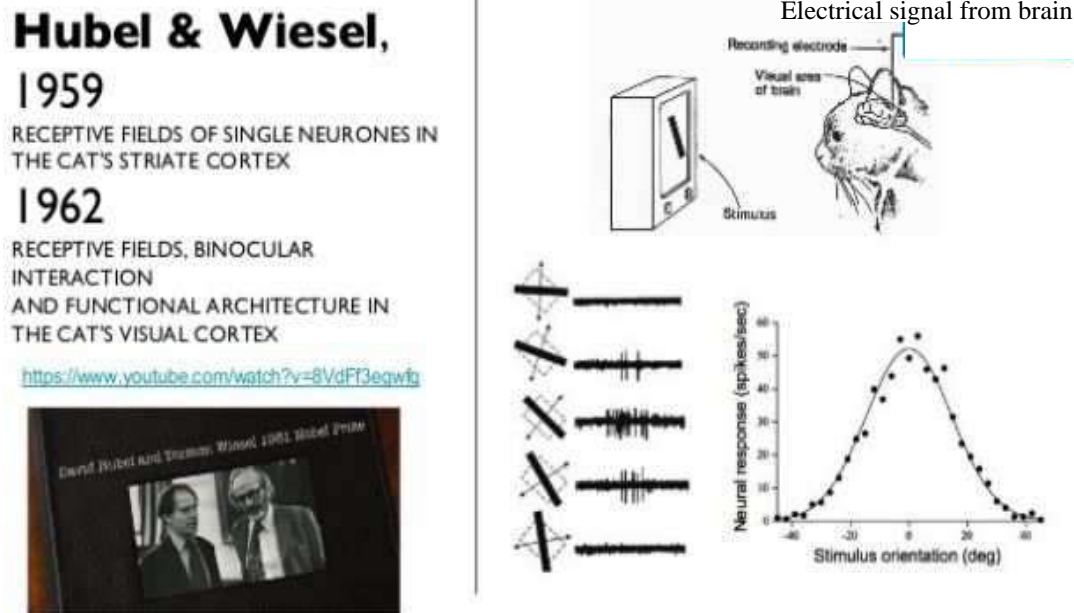


Figure 6.1: Cat and graph of its neural visual response for different orientations of the black bar. Figure extracted from Youtube video of Deep Learning for Computer Vision (Andrej Karpathy, OpenAI).

In the 1980s a spatially invariant neural-network architecture was inspired by the feline visual processing system. Fukushima (1980) proposed a spatially invariant operation, the summation of a localized set of input values with neural weights, as a working hypothesis for some neural mechanisms of a cat's visual pattern recognition. This is a classical neural network model except the number of convolutional weights is much less than the number of input nodes and the weights are spatial invariant. That is, $\hat{w}_{i-j} = w_{ij}$. Thus, the input z_i to i^{th} node can be mathematically computed as a correlation of a small patch of input image values with a small set of spatially invariant weights. Instead of feeding forward all of the input data into each node, only a small localized portion, with the same weights, is fed into each node.

More precisely, the fully-connected neural network input value at the i^{th} node is given

by

$$z_i^{[n]} = \sum_{j=1}^M w_{ij}^{[n]} a_j^{[n-1]}, \quad (6.1)$$

while $z_i^{[n]}$ for the convolutional network illustrated in Figure 6.2 is

$$z_i^{[n]} = \sum_{j \in B} \hat{w}_{i+j}^{[n]} a_j^{[n-1]}. \quad (6.2)$$

Here, w_j for $j \in [1, 2, 3 \dots M']$, $M' \ll M$, and B is a small set of integers that describe the available weights \hat{w}_j . Thus, CNN has a computational and storage requirement of $O(M)$ compared to $O(M^2)$ for a fully-connected neural network. Moreover, the local nature of the "convolution" operation appears to be consistent with the local identification of objects by the brain's neurons in the visual cortex.

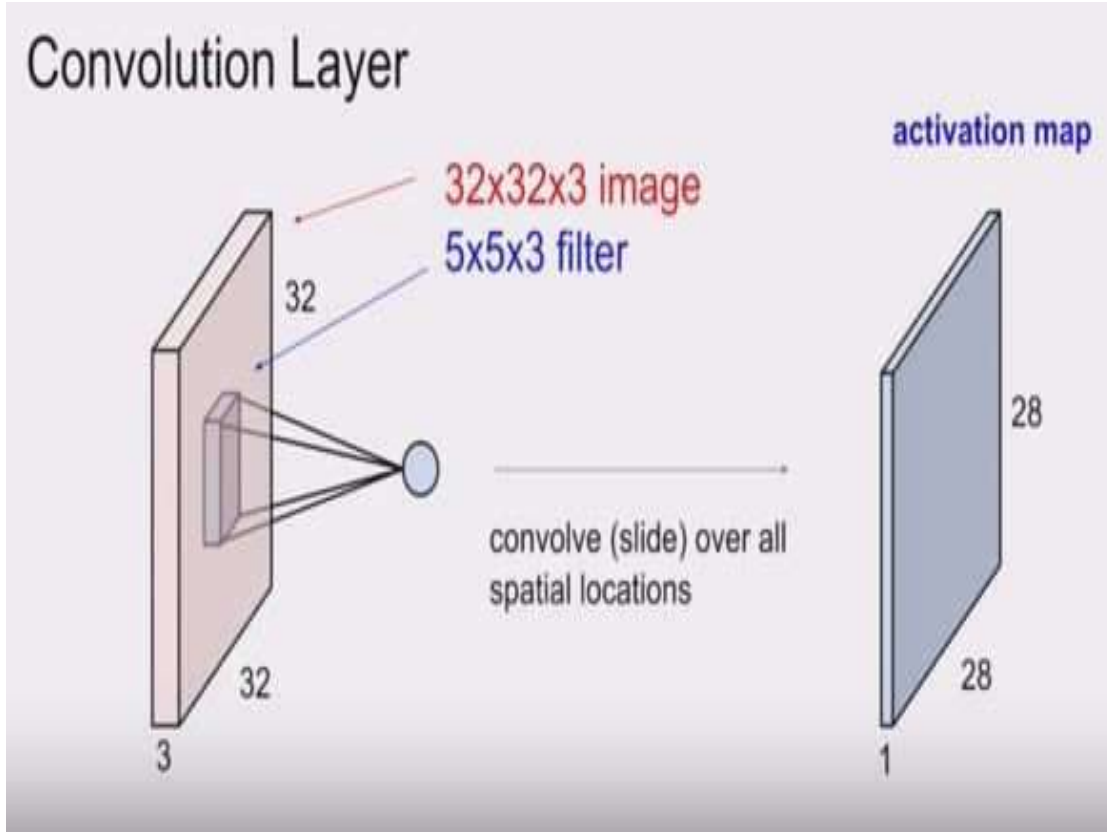


Figure 6.2: Convolution where the input is the $32 \times 32 \times 3$ image and the convolutional filter has dimension $5 \times 5 \times 3$. The output z_i at the i^{th} node is computed by taking the dot product of the weights and the activation values $z_i = \sum_{j \in B} \hat{w}_{i-j} a_j$, where B is the set of indices associated with the small gray window on the left. Figure extracted from Youtube video of Deep Learning for Computer Vision (Andrej Karpathy, OpenAI).

The earliest gradient-based learning of a convolutional network was presented by LeCun et al. (1998). Its architecture is illustrated in Figure 6.3 and depicts the image of the letter *A* as the input data. The intensities of the pixel values a_i over a small patch of *A* centered at the i^{th} pixel are multiplied by the convolutional weights and summed to give the input $z_i = \sum_j \hat{w}_{i-j} a_i$ to the i^{th} node of the next layer. This gray patch is shifted over by one pixel and the dot product operation is repeated with the same neural weights. There are three images depicted in the C1 layer, which means that there are 6 different types of filters. In this case, the index for the k^{th} filter might be designated as $\hat{w}_i^{[n](k)}$ for $k \in [1, 2 \dots 6]$. The reduction in storage and computational requirements is significantly less than that for

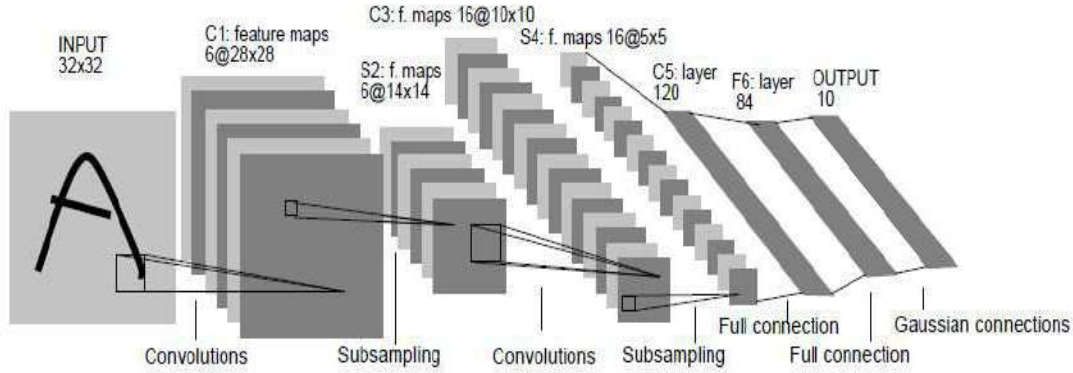


Figure 6.3: LeNet5 CNN architecture (LeCun et al. 1998). Each plane is a feature map.

fully-connected network, which is sometimes designated the classical neural network.

This chapter describes the technical characteristics of the CNN used in the past and some of the ones now being used in 2018. The basis for using different architectures does not currently have a theoretical justification, but it seems to evolve over time to latest CNN architectures that have significantly reduced testing errors and sped up convergence. As an example, Figure 6.4 depicts the speedups over the last decade for different CNN architectures. The trend is deeper CNN networks with larger numbers of layers and more accurate networks.

6.2 Building Blocks of CNN

There are five building blocks that comprise a typical CNN architecture are shown in Figure 6.5: convolution layer, filter, pooling layer, FCC, and Soft-Max Layer.

6.2.1 Convolution Layer

Assume the input image of the gray-scale robot is represented by a 32×32 matrix of intensity values. The filter size for the first convolution layer in Figure 6.5 is a $5 \times 5 \times 1$ filter for the values of $w_i^{[n]}$ in equation 6.2. In this case there is only one channel for the input image. Taking the dot product of this $5 \times 5 \times 1$ filter with different $5 \times 5 \times 1$ patches of the input *A* image gives rise to one of the four $5 \times 5 \times 1$ feature maps. Each FM one has size 28×28

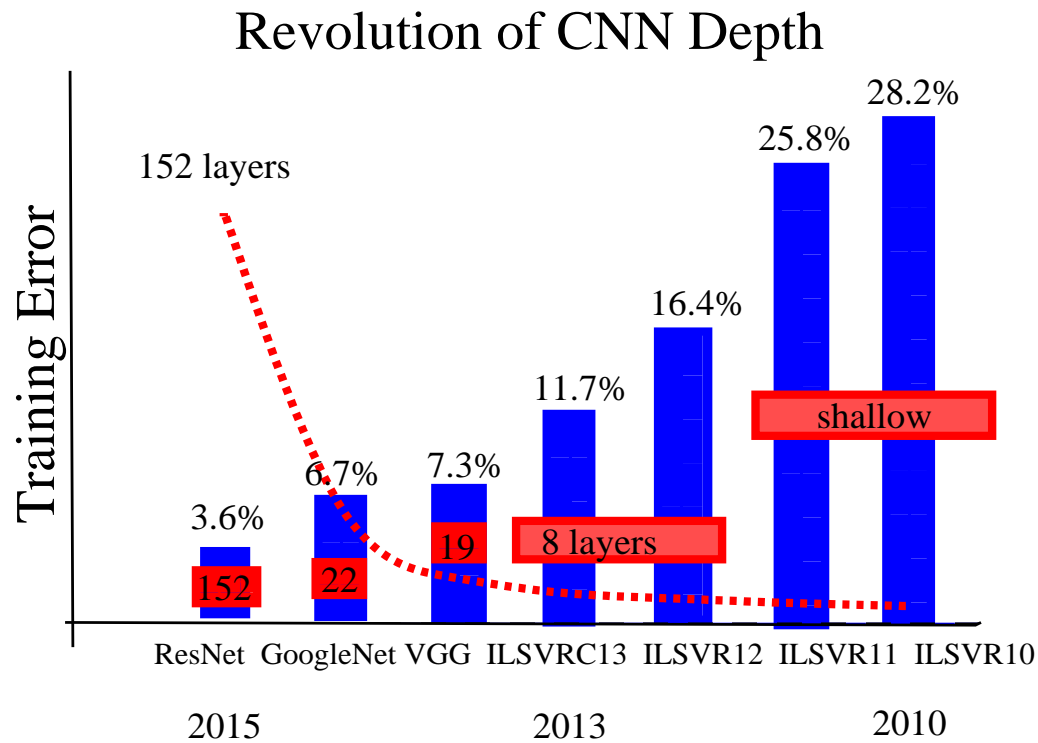


Figure 6.4: Training error vs calendar years for different CNN architectures developed over the last decade. Figure adapted from Youtube video of Deep Learning for Computer Vision (Andrej Karpathy, OpenAI).

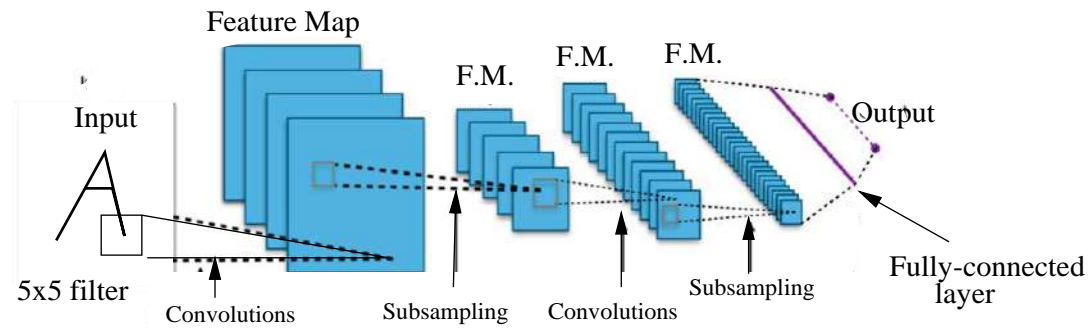


Figure 6.5: Schematic of building blocks in a CNN where the input is a 32×32 image of the letter A. Figure from en.wikipedia.org/wiki/Convolutional_neural_network.

and was created with a different $5 \times 5 \times 1$ filter. In this case we say that the output of layer 1 has four channels, each with a 28×28 image. The reduced size of each FM results from the fact that the filter is 5 pixels wide and tall, so that the filter can only be slid 28 pixels

across or down the image before part of it falls outside the input image.

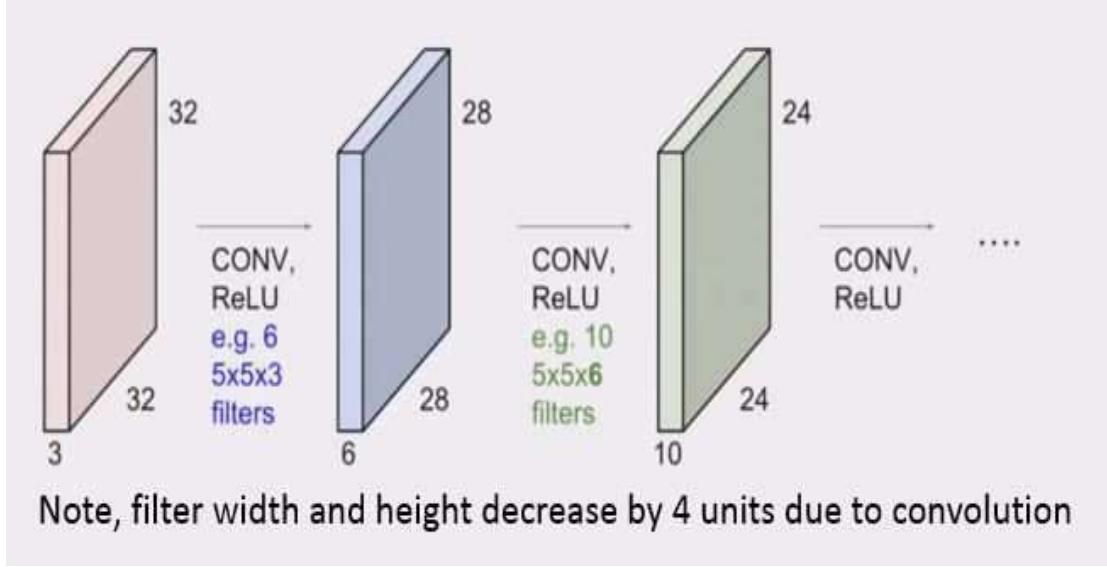


Figure 6.6: Example of reduction in size of FMs by sequential convolutions with 5×5 filters with stride $n_s = 1$. In this example the first layer has three FMs, the second one has 6 because 2 unique filters are used for each FM. The evolution of CNN architectures shows that the number of FMs per layer typically increase the deeper into the CNN. Figure adapted from Youtube video of Deep Learning for Computer Vision (Andrej Karpathy, OpenAI).

For the second layer associated with convolution, the filter will have a third dimension equal to the number of channels in the previous layer. For example, the tan layer in Figure 6.6 consists of three channels so the convolution filter will be of dimension $32 \times 32 \times 3$. In this example there are 6 different $5 \times 5 \times 3$ filters to give the blue stack of six images, each with dimension 28×28 . To get the green images ten $5 \times 5 \times 6$ filters are convolved with the blue images.

In general, if the input image has size $n \times n \times n_{ch}$ then the filter size is $n_f \times n_f \times n_{ch}$ and the output feature map dimension is $n_c \times n_c$. Here,

$$n_c = \frac{n - n_f + 1}{n_s} + n_p, \quad (6.3)$$

and n_p is the width and height of the zero-padding added to the feature map. Here, n_{ch} is the number of channels, $n \times n$ is the dimension of the input image, and n_s is the stride of the filter which is equal to the number of pixels the filter is shifted between each dot product of the dot-product operation. In the Figure 6.5 example $n_s = 1$, $n = 32$, $n_p = 1$ and $n_f = 32$ to give $n_c = 28$.

6.2.2 Activation Functions

Most activation functions use the rectified linear unit (ReLU) defined as

$$g(z_i) = \max(0, z_i), \quad (6.4)$$

which eliminates negative values of the input z and gives has the same value of $dg(z_i)/dz$ for any $z_i > 0$. The steepest descent backpropagation formula contains the factor $dg(z_i)/dz_i$ so its value will determine the type of residuals that will be used to updates the weights. Thus the $dg(z)/dz$ term for the ReLU function weights the residuals with equal magnitude to find the correct adjustment of the weights w_i that minimize the objective function.

In comparison, the sigmoid activation function has the derivative $dg(z)/dz = g(z)(1 - g(z)) \approx 0$ unless $z_i \approx 0$. Since the backprojected residual is multiplied by $dg(z_i)/dz_i$ at the i^{th} node, then updating occurs only when the input z_i is nearly equal to zero. This means that z_i terms much larger than zero are ignored. Thus convergence can slow down if the gradient is mostly zero as evidenced by the observation that deep-layer CNNs with sigmoid or tanh activation functions stall after a certain number of iterations, even though the residual is far from zero. To include all non-zero residuals in the update of weights the ReLU function is now preferred over most activation functions.

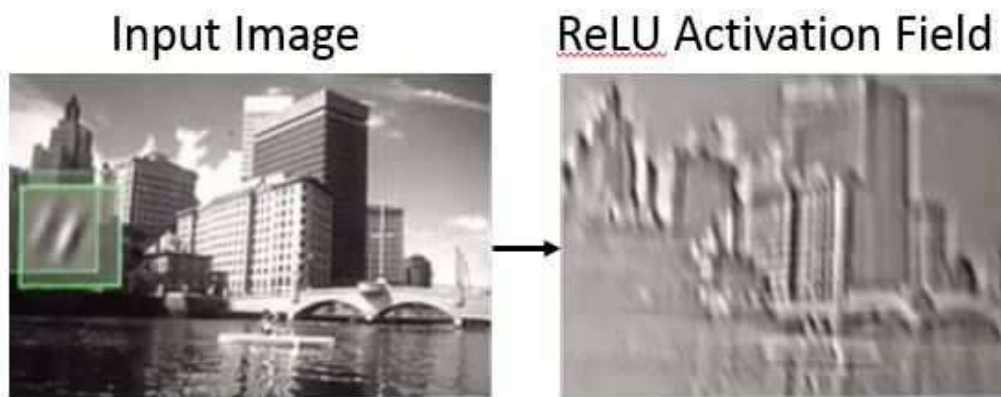


Figure 6.7: (Left) Input image and (right) activation image after convolution of the small filter (see green patch on left) with the input image and application of the ReLU activation function to the output. In this example, a "same" convolution was used to output the same sized-sized image after convolution. Notice that all the values in the activation image are positive. Figure adapted from Youtube video of Deep Learning for Computer Vision (Andrej Karpathy, OpenAI).

Figure 6.8 compares ReLU vs a sigmoid activation function for learning in a CNN with 9 layers. Obviously the ReLU learns the fastest for this test

A variation ReLU is Leaky ReLU as shown in Figure 6.9. Here α is a small number and Leaky ReLU reduces to standard ReLU if $\alpha = 0$. Leaky ReLU accelerates convergence in some cases.

ReLU vs Sigmoid

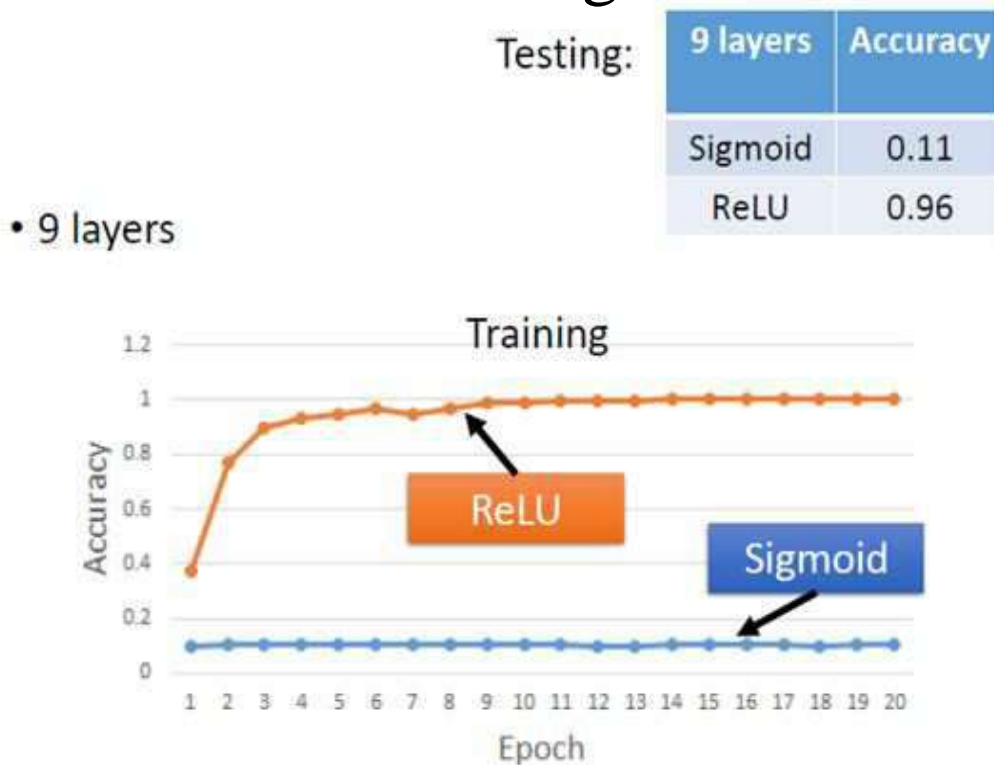


Figure 6.8: Comparison of accuracy of CCN learning using ReLu compared against sigmoid activation functions. Figure adapted from Hung-yi Lee PPT.

6.2.3 Feature Maps

There are four feature maps (FMs) just after the leftmost convolution in Figure 6.5 that result from applying four different 5×5 filters $\mathbf{w}^{(i)}$ (for $i \in [1, 2, 3, 4]$) to the input image. The role of each filter is to, hopefully, decompose the original image into four different images, each one associated with one of the four local features associated with the filters. For example, if $\mathbf{w}^{(1)}$ and $\mathbf{w}^{(2)}$ are the matrices

$$\mathbf{w}^{(1)} = \begin{bmatrix} 0 & 0 & 1 & 0 & 0 \\ 0 & 0 & 1 & 0 & 0 \\ 0 & 0 & 1 & 0 & 0 \\ 0 & 0 & 1 & 0 & 0 \\ 0 & 0 & 1 & 0 & 0 \end{bmatrix}; \quad \mathbf{w}^{(2)} = \begin{bmatrix} 0 & 0 & 0 & 0 & 0 \\ 0 & 0 & 0 & 0 & 0 \\ 1 & 1 & 1 & 1 & 1 \\ 0 & 0 & 0 & 0 & 0 \\ 0 & 0 & 0 & 0 & 0 \end{bmatrix}, \quad (6.5)$$

then the FM for $\mathbf{w}^{(1)}$ would be largely composed of the vertical parts of the letter *A* while the FM for $\mathbf{w}^{(2)}$ would consist of the horizontal parts. These filters act as *matching* filters and extract parts of the image that are similar to the pattern in the filter.

Leaky ReLU

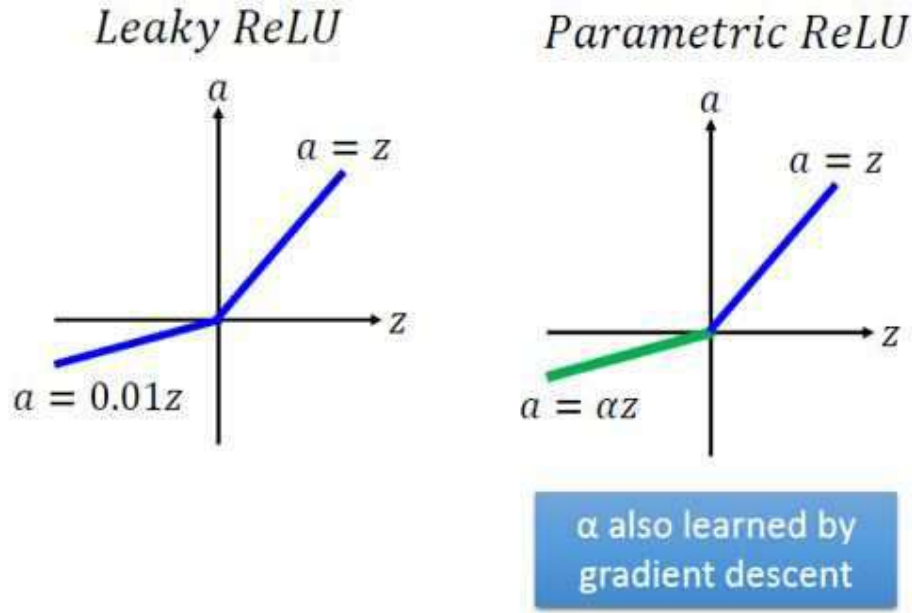


Figure 6.9: Leaky ReLU on left and the parameter value α can be determined by gradient descent on the right. Figure adapted from Hung-yi Lee PPT.

The one puzzle is that the backpropagation algorithm determines the patterns in these filters $\mathbf{w}^{(i)}$ so it is a mystery as to which patterns will emerge in the FM. What is not mysterious is that these patterns are for small features in the original image because the filters are usually very small and localized. They are equivalent to high-wavenumber pass filters.

6.2.4 Pooling Layer

The pooling layer is created by a subsampling operation that reduces the size of the input map by an integer multiple. For example, the leftmost pooling or subsampling operation in Figure 6.5 reduces the $28 \times 28 \times 4$ FMs to $14 \times 14 \times 4$ FMs. After pooling, the activation function is applied to each sample in the pixel to give four 14×14 activation images $\mathbf{a}^{[1](i)}$, where i denotes the i^{th} activation image in layer 1. Note, the layer number is in square brackets and the channel number is in the rounded superscript¹.

There are several pooling strategies such as replacing the intensity value at a pixel by

¹We often eliminate an abundance of superscript or subscripts when trying to quickly get across a key idea. For example, no channel superscripts are in equations 6.1 or 6.2.

the average value of its neighbors. The most widely used one is the maximum as illustrated in Figure 6.10. Here, the maximum value of four neighbors replaces the intensity value of the central point. The 2×2 patch is slid over by two pixels, i.e. a stride of 2, and the max-pool process is repeated. In this example, the 4×4 patch of pixels is reduced to a 2×2 patch. Typically, a pooling filter no larger than 2×2 is used, otherwise high-wavenumber

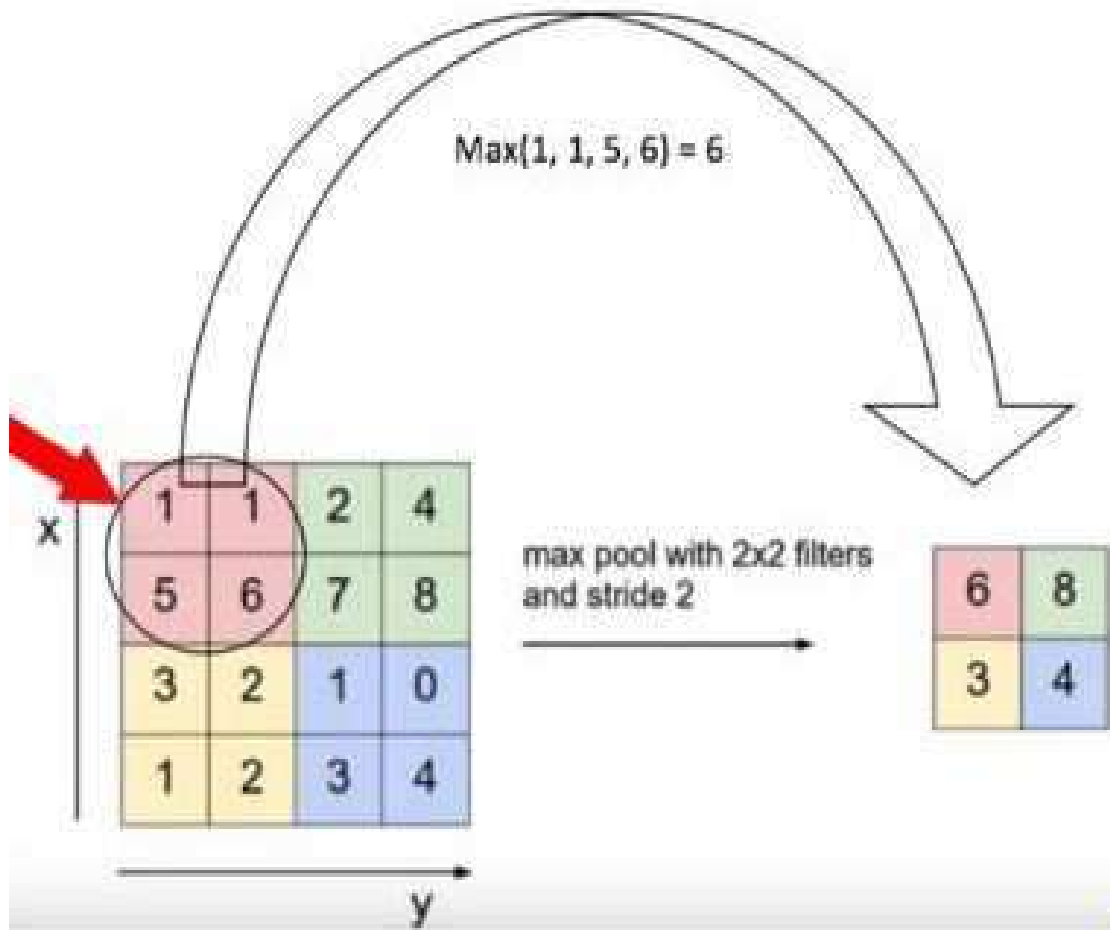


Figure 6.10: Example of max-pooling applied to a 4×4 image to reduce it to a 2×2 image. This size reduction leads to greater computational efficiency. According to Karpathy and others, CNN architectures should move away from subsampling. Figure adapted from Youtube video of Deep Learning for Computer Vision (Andrej Karpathy, OpenAI).

information gets lost.

The combination of the operations *convolution* – *activation* and *pooling* is considered one layer. This sequence of layers is repeated with different hyperparameters for each layer until we get to the last few layers. The hyperparameters are the design parameters, such as number of filters, filter size, number of layers, that don't get updated in the iterative backprojection operations. In contrast, the weights $w_{i-j}^{[n]}$ get updated every iteration and are denoted as parameters.

6.2.5 Fully-Connected Layer

The last few layers combine all the local FMs into a *fully – connected* image by concatenating all of the vectors associated with each FM into one tall vector. For example, if there are two 3×3 FMs then each one can be transformed into a 9×1 vector, and these two vectors are concatenated to form the *tall* 18×1 vector. This tall vector is then used as input into a fully-connected layer. A fully-connected layer combines all other parts of the input image into every node of the next layer. It can bring together many local features to form a much larger image.

6.2.6 Soft-Max Layer

In image classification there might be dozens of classes, not just two as in binary classification. In this case a soft-max activation function $g(\mathbf{z})$ can be used in the output layer such that

$$g(\mathbf{z}_i) = \frac{e^{z_i}}{\sum_{i=1}^M e^{z_i}}, \quad (6.6)$$

where the summation is over all the M nodes in the last output layer. The typical output vector will typically consist of positive numbers between 0 and 1 and can be interpreted as the probability of the input image being in one of the M classes. Each of the M output nodes is associated with a unique class. The one with the highest probability is selected as the class of the input image.

6.2.7 Loss Function

Which loss function should be used? For binary classification the cross-entropy loss function

$$\epsilon = \sum_{i=1}^M y_i \ln y_i, \quad (6.7)$$

over the mean square error (MSE) loss function

$$\epsilon = 1/2 \sum_{i=1}^M (i_i - y_i^{obs})^2. \quad (6.8)$$

is preferred (see Figure 6.11). Cross entropy has the fastest convergence rate as depicted in the example shown in Figure 6.12.

6.2.8 Dropout Regularization

Too many fully-connected layers can lead to overfitting. Thus, a regularization method such as damping is needed to stabilize the solution. However, overfitting does always occur because with some deep networks the data cannot be fitted well even with many layers (see Figure 6.13). There are many regularization methods, some of them are listed below.

1. More training sets? longer computation

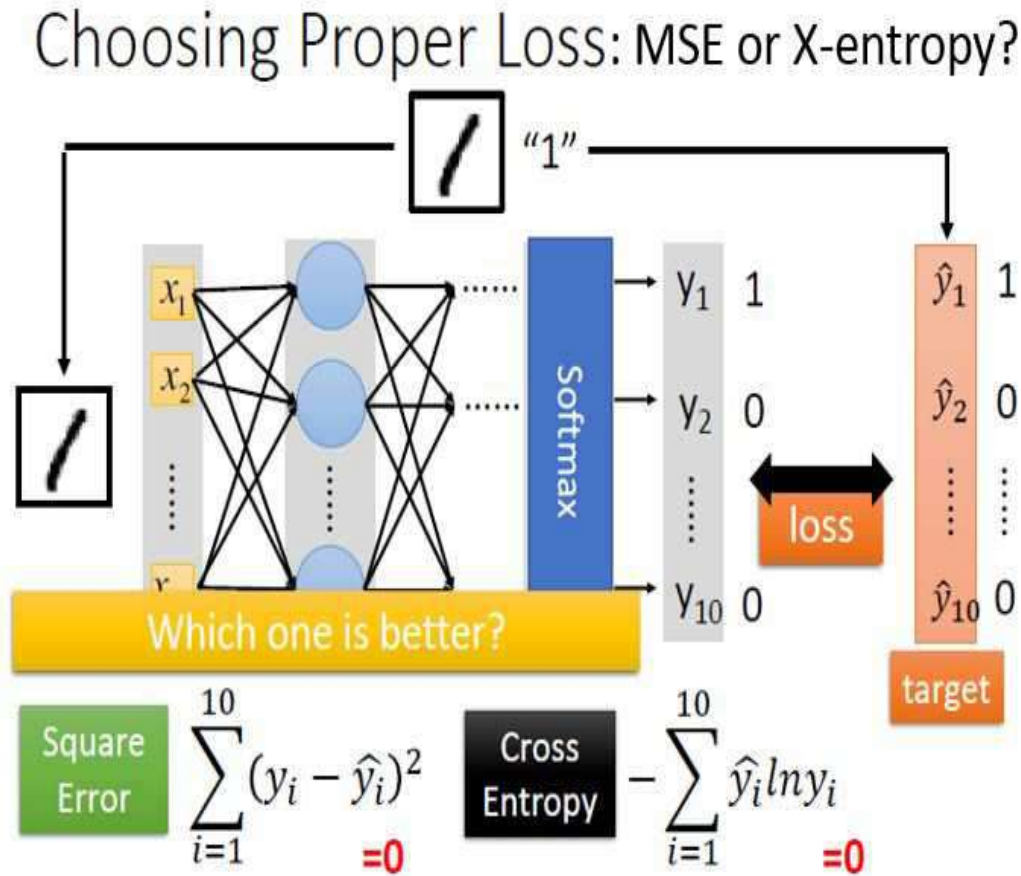


Figure 6.11: Which loss function is preferred? Figure adapted from Hung-yi Lee PPT.

2. Early stopping
3. Marquardt damping: large weights are penalized or constrained
4. Bootstrap: classify different subsets of the training data, and fit a model which is based on these subsets.
5. Limiting the number of hidden layers and units
6. Dropout: A successful way to prevent overfitting is to perform a dropout. Here units are randomly removed from the neural network, which can also be seen as a form of adding noise to the network. $p=0.5$ and removing units in the input layer with $p=0.2$

A popular regularization method is dropout regularization (Nitish et al., 2014). As indicated in the wikipedia page *At each training stage, individual nodes are either "dropped out" of the net with probability $1 - p$ or kept with probability p , so that a reduced network is left; incoming and outgoing edges to a dropped-out node are also removed. Only the reduced network is trained on the data in that stage. The removed nodes are then reinserted into the network with their original weights.*

MSE vs Cross-Entropy

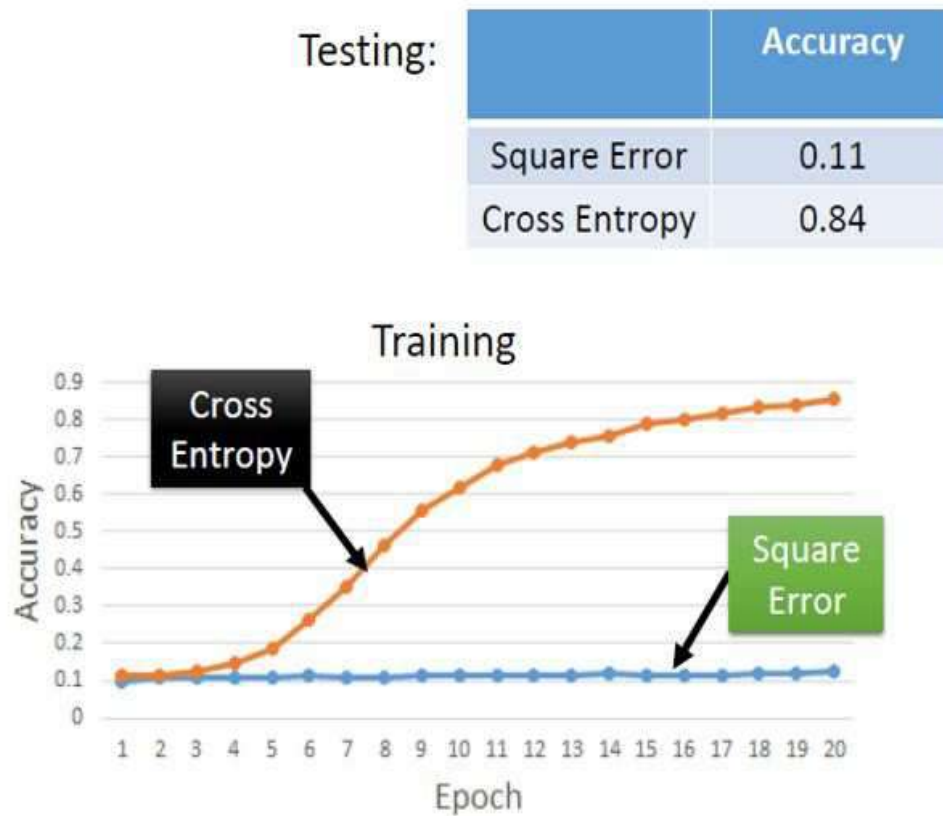


Figure 6.12: Accuracy vs iteration number for MSE and cross-entropy loss functions. Figure adapted from Hung-yi Lee PPT.

In the training stages, the probability that a hidden node will be dropped is usually 0.5; for input nodes, this should be much lower, intuitively because information is directly lost when input nodes are ignored.

At testing time after training has finished, we would ideally like to find a sample average of all possible 2^n dropped-out networks; unfortunately this is unfeasible for large values of n . However, we can find an approximation by using the full network with each node's output weighted by a factor of p , so the expected value of the output of any node is the same as in the training stages. This is the biggest contribution of the dropout method: although it effectively generates 2^n neural nets, and as such allows for model combination, at test time only a single network needs to be tested.

By avoiding training all nodes on all training data, dropout decreases overfitting. The method also significantly improves training speed. This makes model combination practical, even for deep neural nets. The technique seems to reduce node interactions, leading them to learn more robust features that better generalize to new data.

Do not always blame Overfitting

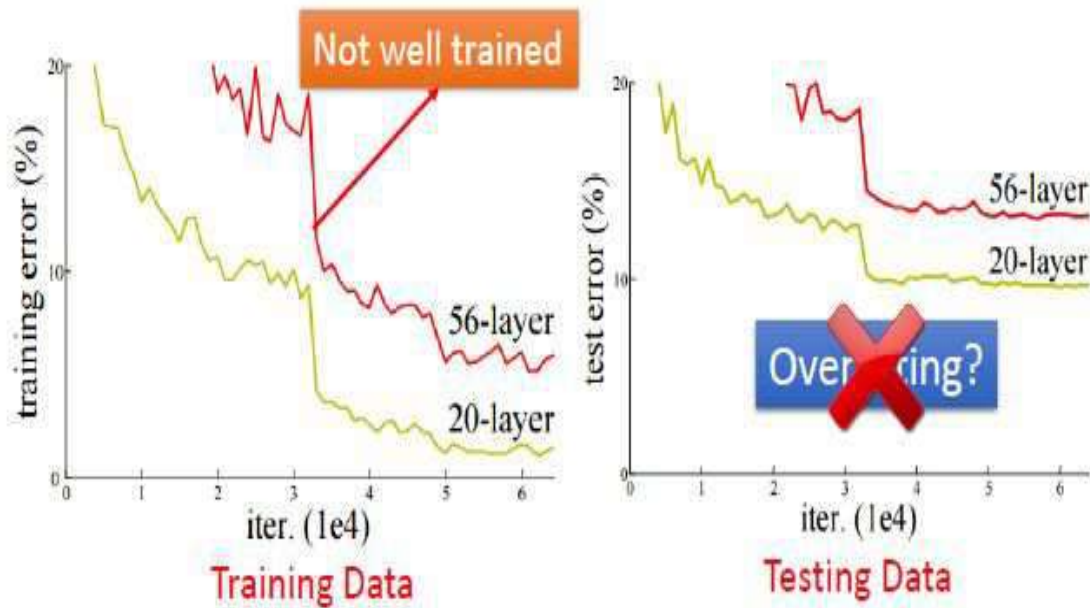


Figure 6.13: Even with deep networks with many unknowns overfitting does not always occur. The deeper the network for standard architectures, the more likely the gradient tends to vanish so the convergence stalls. ResNet tends to fix this problem. Figure adapted from Hung-yi Lee PPT.

6.2.9 DropConnect Regularization

Again, wikipedia says the following about DropConnect regularization: DropConnect (Perez, 2013) is the generalization of dropout in which each connection, rather than each output unit, can be dropped with probability $1 - p$. Each unit thus receives input from a random subset of units in the previous layer.

DropConnect is similar to dropout as it introduces dynamic sparsity within the model, but differs in that the sparsity is on the weights, rather than the output vectors of a layer. In other words, the fully connected layer with DropConnect becomes a sparsely connected layer in which the connections are chosen at random during the training stage.

6.2.10 Local Response Normalization(LRN) Regularization

Local Response Normalization(LRN) type of layer turns out to be useful when using neurons with unbounded activations (e.g. rectified linear neurons), because it permits the detection

of high-frequency features with a big neuron response, while damping responses that are uniformly large in a local neighborhood. See <https://stats.stackexchange.com/questions/145768/importance-of-local-response-normalization-in-cnn>.

To excite all the neurons equally in a layer LRN is used. There are some reports that claim it is not used very much anymore. However its definition is below.

Original Formula: For every particular position (x, y) and kernel i that corresponds to a single 'pixel' output we apply a 'filter', that incorporates information about outputs of other n kernels applied to the same position. This regularization is applied before activation function.

$$b_{xy}^i = \frac{a_{xy}^i}{(k + \alpha \sum_{\min(N-1, i+n/2)}^{\max(0, i-n/2)} (a_{xy}^i)^2)^\beta} \quad (6.9)$$

where b_{xy}^i is the regularized output for kernel i at position (x, y) , where a_{xy}^i is the source output for kernel i applied at position (x, y) , N is the total number of kernels, n is the size of the normalization neighborhood, and α , β , k and n are hyperparameters.

In practice two approaches can be used:

1. Within Channel. Normalize over local neighborhood of a single channel (corresponding to a single convolutional filter). In other words, divide response of a single channel of a single pixel according to output values of the same neuron for pixels nearby.
2. Across Channels. For a single pixel normalize values of every channel according to values of all channels for the same pixel.

LRN was used more often during the days of early convolution nets like LeNet-5. Current implementation of GoogLeNet (Inception) in Caffe often uses LRN in connection with pooling techniques, but it seems to be done for the sake of just having it. Neither original Inception/GoogLeNet (here) nor any of the following versions mention LRN in any way. Also, TensorFlow implementation of Inception (provided and updated by the team of original authors) networks does not use LRN despite it being available.

Many types of normalization layers have been proposed for use in ConvNet architectures, sometimes with the intentions of implementing inhibition schemes observed in the biological brain. However, these layers have recently fallen out of favor because in practice their contribution has been shown to be minimal, if any.

6.2.11 Mini-Batch

The preferred approach to finding the weights is to divide up the training set into mini-batches of training examples. The starting weights are randomized, and the updated weights are found by one iteration for one mini-batch of input data (see Figure 6.14). That is, the gradient is formed from

$$\nabla \epsilon = \nabla (l^1 + l^{31} \dots) \quad (6.10)$$

where l^i represents the loss function in Figure 6.14. These updated weights are used as the starting weights for the next mini-batch and this process is repeated until all the mini-batches have been used. This is known as one epoch. In the next epoch the data are

resorted into non-overlapping mini-batches and the weights are updated for the next epoch.

Mini-Batch

We do not really minimize total loss!

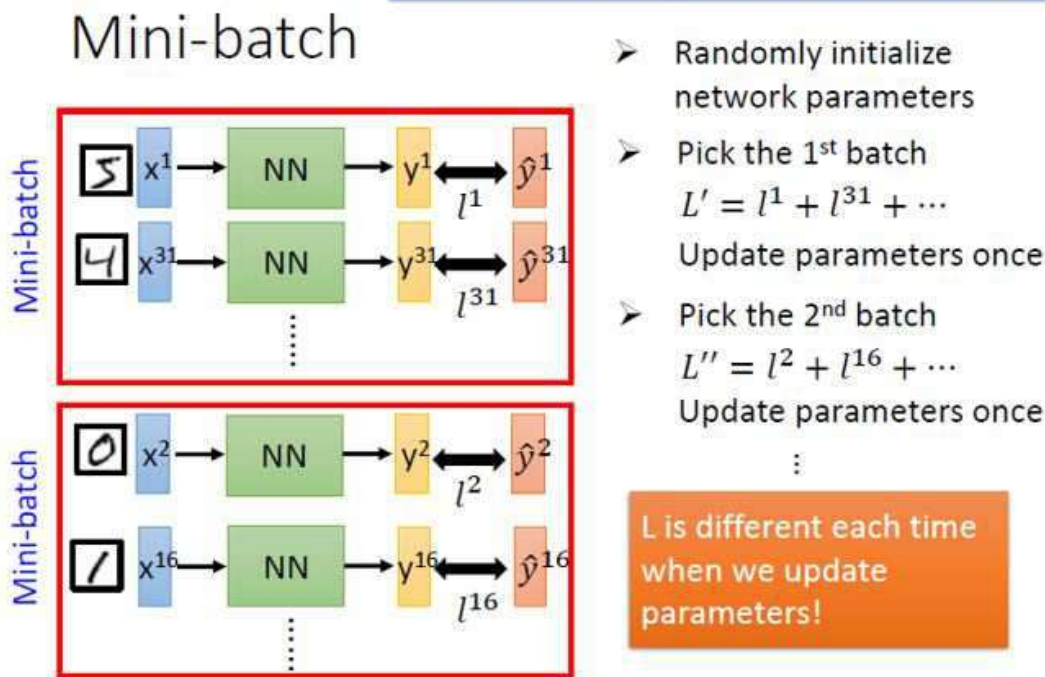


Figure 6.14: Weights are updated by one pass through each mini-batch of data in the training set. It is recommended that the training examples are reshuffled after each epoch. Figure adapted from Hung-yi Lee PPT.

6.2.12 Step Length

The step length α in the steepest descent formula is also known as the learning rate. Typically the learning rate is large for the early iterations (e.g., $\alpha = .0.5$) and then decrease α after several epochs. One formula suggested by Hung-yi Lee is

$$\alpha^k = \frac{\alpha}{\sqrt{k+1}}, \quad (6.11)$$

where k is the iteration index for different epochs.

Another strategy is to replace $\sqrt{k+1}$ by $\sum_{i=1}^k g_i^2$ where g_i is the gradient for the i^{th} iteration. According to Hung-yi Lee this is known as John Duchi's Adagrad. In this case smaller gradients get greater learning rates in order to increase their importance. Of course we should also use momentum as discussed in an earlier chapter.

In summary the training strategy is summarized in Figure 6.15. We first train in the training set and then test the validity of the weights on a non-overlapping validation set. The validation sets should have the same character as the original training set and usually it is about 20% in size.

CNN Workflow

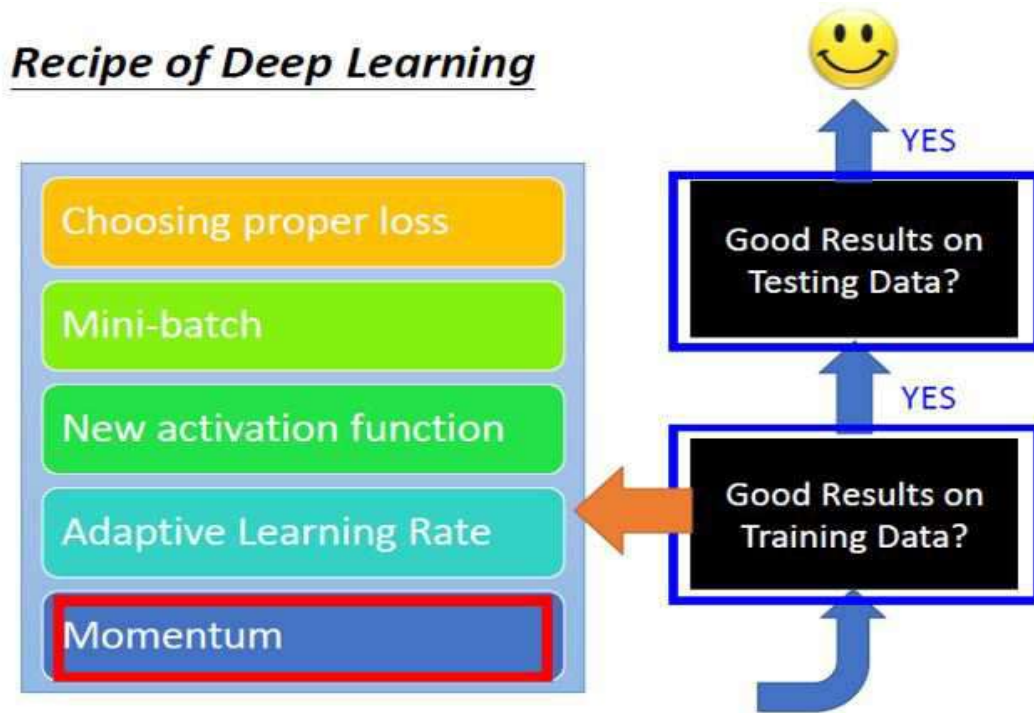


Figure 6.15: Weights are updated by one pass through each mini-batch of data in the training set. It is recommended that the training examples are reshuffled after each epoch. Figure adapted from Hung-yi Lee PPT.

6.3 Architectures of CNN

There are several CNN architectures that are most popular today and their performances are graphed in Figure 6.4. The VGG net is quite appealing from a programming point of view because it uses the same number of nodes in each layer. These different architectures appear to have evolved by trial and error, where some intuition is used to help improve the design. No mathematical basis appears to justify their usage.

6.3.1 AlexNet

The AlexNet architecture is shown in Figure 6.16. Alexnet is one of the pioneer Deep Neural Networks which aim to classify images. It was developed by Alex Krizhevsky, Ilya Sutskever, and Geoffrey Hinton and won an Image classification Challenge (ILSVRC) in 2012 by a large margin. At that time the other competing algorithms were not based on Deep Learning. Now, and since then, they almost all are. This net had a huge impact on the domain and most of following nets were more or less based on its architecture. Alexnet (Figure 6.16) is composed of 5 convolutional layers (C1 to C5 on schema) followed by two fully connected (FC6 and FC7), and a final softmax output layer (FC8). It was initially trained to recognize 1000 different objects.

The intuition behind this net is that each convolutional layer learns a more detailed representation of the images (feature map) than the previous one. For example the first layer is able to recognize very simple forms or colors, and the last one more complex forms such as full faces for instance

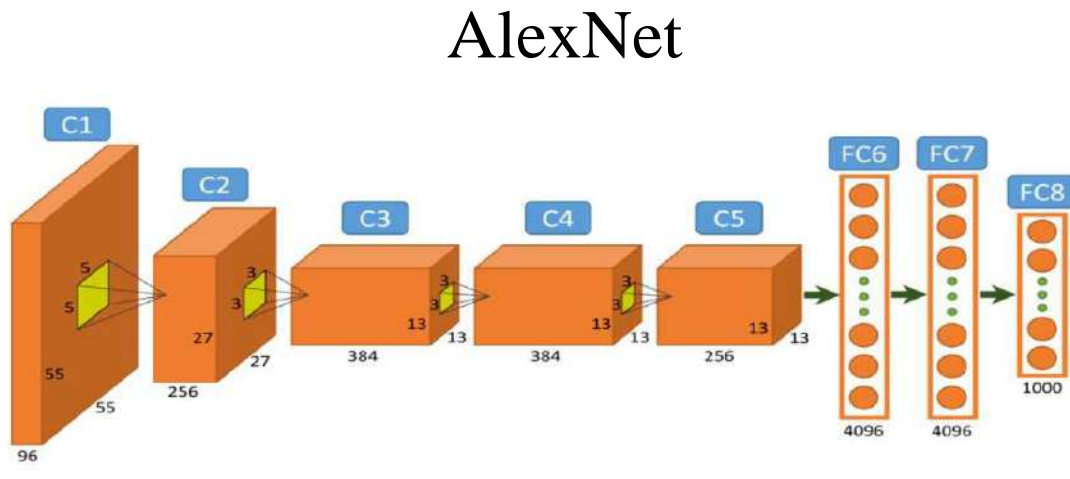


Figure 6.16: AlexNet architecture. Figure and text from <https://www.saagie.com/blog/object-detection-part1>.

6.3.2 ZFNet

The ZFNet architecture is shown in Figure 6.17. ZFNet has the same global architecture as Alexnet, that is to say 5 convolutional layers, two fully connected layers and an output softmax one. The differences are, for example, better sized convolutional kernels.

6.3.3 VGGNet

The pleasing feature of VGGNet in Figure 6.18 is that the filter size ($3 \times 3 \times n_c$ and down-sampling fraction stays the same for every layer. Figure 6.4 shows that it also outperforms earlier architectures such as the LeCUN one shown in Figure 6.3.

ZFNet

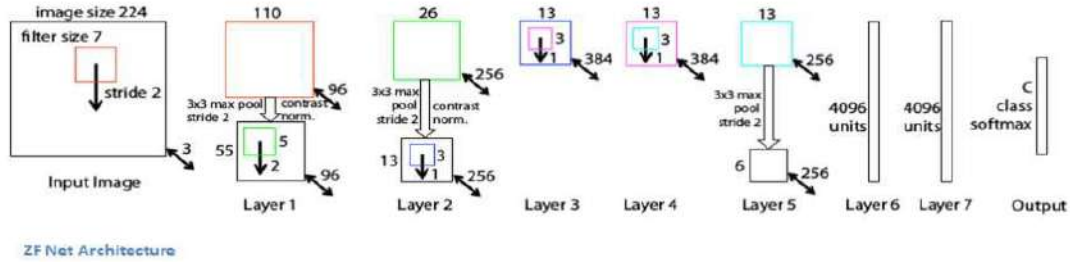


Figure 6.17: ZFNet architecture. Figure and text from <https://www.saagie.com/blog/object-detection-part1>.

VGGNet

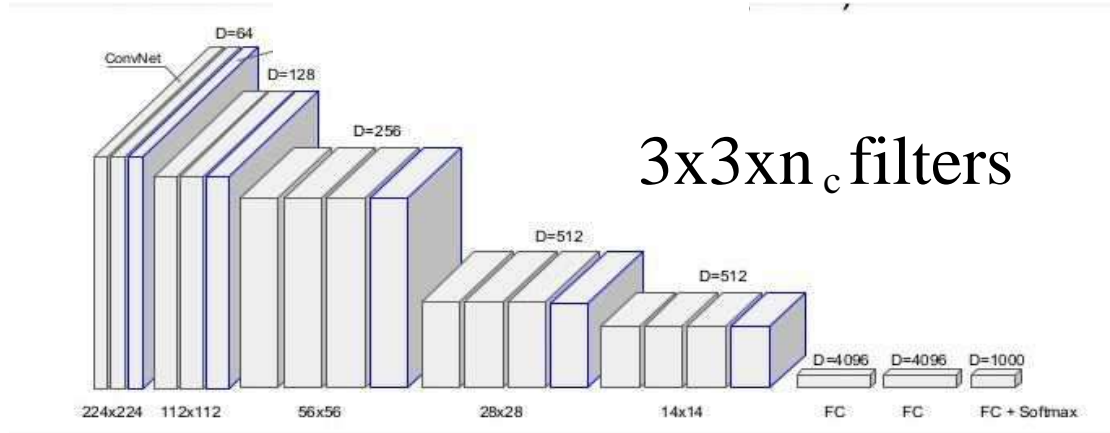


Figure 6.18: Architecture of VGGnet where D is the number of channels and the $x - z$ size of each feature map decreases the deeper into the CNN.

A schedule for a VGG CNN is depicted in Figure 6.19 where the filter $x - z$ size stays the same for every layer. However, the number of channels or filter dimension in the channel dimension doubles after every pooling. The input image has a dimension of $224 \times 224 \times 3 = O(150K)$. There are 64 filters in the first layer so there are 64 feature maps in the first layer, each of them with a dimension of 224×224 . The filter size is $3 \times 3 \times 3$ for each FM so that the total number of unknowns in the 1st-layer is $(3 \times 3 \times 3) \times 64 = 1,728$, not counting biases. The 64 FMs requires a total storage of $224 \times 224 \times 64 = O(3 \times 10^6)$ variables. Another convolution layer is used with the filter size of $3 \times 3 \times 64$ with $O(36K)$ unknowns. Then pooling is applied to halve the size of the FM. The number of channels doubles after every pooling.

VGG is a very deep and simple net. In the most common version, it has 16 layers (The blue pooling layers aren't counted on the schema). However the global architecture is very similar to the Alexnet one. Actually the Alexnet convolutional layers are here represented

Case Study: VGGNet

[Simonyan and Zisserman, 2014]

INPUT: [224x224x3]	memory: 224*224*3=150K	params: 0	(not counting biases)
CONV3-64: [224x224x64]	memory: 224*224*64=3.2M	params: (3*3*3)*64 = 1,728	
CONV3-64: [224x224x64]	memory: 224*224*64=3.2M	params: (3*3*64)*64 = 36,864	
POOL2: [112x112x64]	memory: 112*112*64=800K	params: 0	
CONV3-128: [112x112x128]	memory: 112*112*128=1.6M	params: (3*3*64)*128 = 73,728	
CONV3-128: [112x112x128]	memory: 112*112*128=1.6M	params: (3*3*128)*128 = 147,456	
POOL2: [56x56x128]	memory: 56*56*128=400K	params: 0	
CONV3-256: [56x56x256]	memory: 56*56*256=800K	params: (3*3*128)*256 = 294,912	
CONV3-256: [56x56x256]	memory: 56*56*256=800K	params: (3*3*256)*256 = 589,824	
CONV3-256: [56x56x256]	memory: 56*56*256=800K	params: (3*3*256)*256 = 589,824	
POOL2: [28x28x256]	memory: 28*28*256=200K	params: 0	
CONV3-512: [28x28x512]	memory: 28*28*512=400K	params: (3*3*256)*512 = 1,179,648	
CONV3-512: [28x28x512]	memory: 28*28*512=400K	params: (3*3*512)*512 = 2,359,296	
CONV3-512: [28x28x512]	memory: 28*28*512=400K	params: (3*3*512)*512 = 2,359,296	
POOL2: [14x14x512]	memory: 14*14*512=100K	params: 0	
CONV3-512: [14x14x512]	memory: 14*14*512=100K	params: (3*3*512)*512 = 2,359,296	
CONV3-512: [14x14x512]	memory: 14*14*512=100K	params: (3*3*512)*512 = 2,359,296	
CONV3-512: [14x14x512]	memory: 14*14*512=100K	params: (3*3*512)*512 = 2,359,296	
POOL2: [7x7x512]	memory: 7*7*512=25K	params: 0	
FC: [1x1x4096]	memory: 4096	params: 7*7*512*4096 = 102,760,448	
FC: [1x1x4096]	memory: 4096	params: 4096*4096 = 16,777,216	
FC: [1x1x1000]	memory: 1000	params: 4096*1000 = 4,096,000	

Figure 6.19: Hyperparameter values for a VGG CNN. The input image has a dimension of $224 \times 224 \times 3 = O(150K)$. Figure adapted from Youtube video of Deep Learning for Computer Vision (Andrej Karpathy, OpenAI).

by two or three following convolutional layers. Another difference is that each convolutional layers has a 3x3 kernel unlike the other nets that have different sized kernels for each layer.

6.3.4 GoogleNet

The Google CNN architecture is depicted in Figure 6.20 and has an inception layer with several convolutions with different filters and a pooling layer. It won the ILSVRC contest for 2014 by having the lowest percent errors for the testing set.

6.3.5 ResNet

ResNet is the 2016 ILSVRC contest winner with an error rate of less than 5%. Its architecture (He et al., 2016) is shown in Figure 6.21, where the innovation is that it adds an identity operator to the output of an activation function. Assume the i^{th} input is $z_i^{[n]}$ and the i^{th} output of a layer's standard operations is $a_i^{[n]}$. The ResNet architecture says the i^{th}

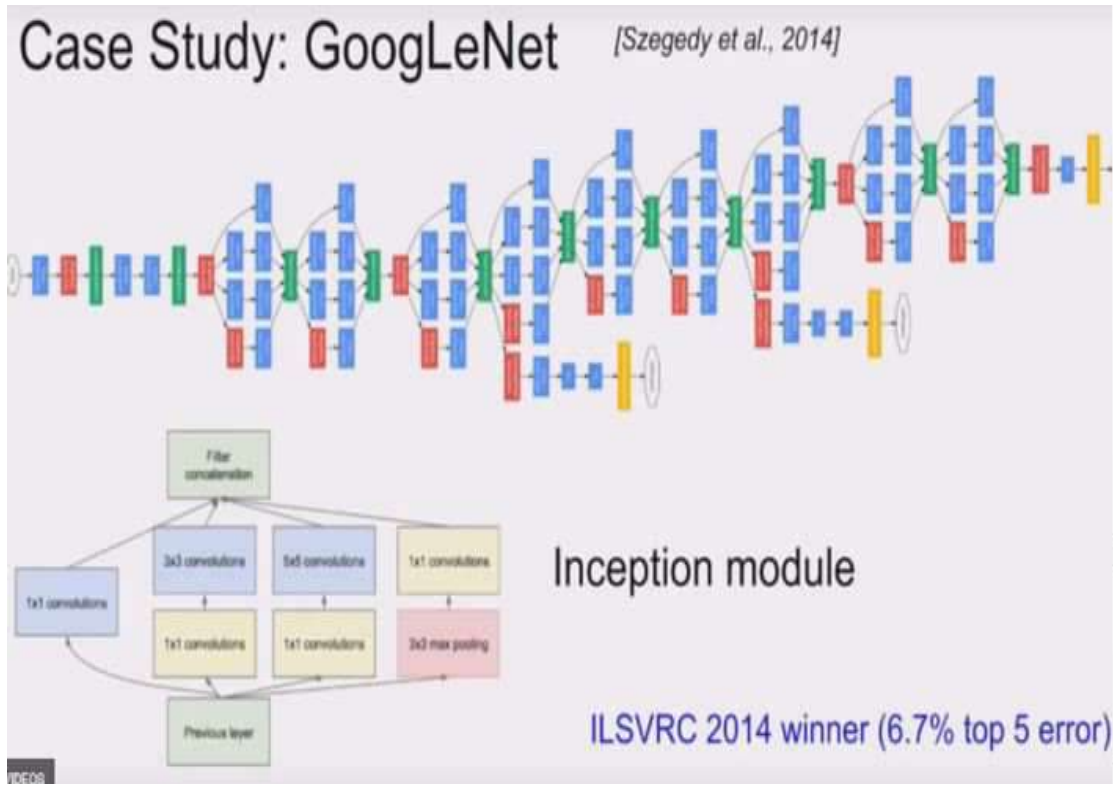


Figure 6.20: Architecture for GoogLeNet CNN. The inception module contains several convolution operations with different filters. Figure adapted from Youtube video of Deep Learning for Computer Vision (Andrej Karpathy, OpenAI).

output is $a_i^{[n]} + z_i^{[n]}$. This can be modified by saying the i^{th} output is $a_i^{[n+x]} + z_i^{[n]}$, where x is some integer larger than 1. If the dimension of the input feature map \mathbf{x} into the skip layer is the same as that of the output \mathbf{y} then the square identity matrix \mathbf{I} is used to connect the output \mathbf{y} with the input \mathbf{x} :

$$\mathbf{y} = H(\mathbf{x}, \mathbf{W}) + \mathbf{I}\mathbf{x}, \quad (6.12)$$

where $\mathbf{H}(\mathbf{x}, \mathbf{W})$ represents the convolution and activation operations associated with the skip layer, and \mathbf{W} represents the weights of the convolution and bias filters. If the dimension of \mathbf{x} is less than that of \mathbf{y} then \mathbf{I} will be rectangular and have zero-padding to account for this mismatch in dimensions. This matrix \mathbf{I} can also have weights associated with a linear mapping according to He et al. (2016). He et al. (2016) shows skip layers every two layers of a standard conv-net network.

ResNet-152 introduced the concept of residual learning in which the subtraction of features is learned from the input of that layer by using shortcut connections (directly connecting input of n^{th} layer to some $(n+x)^{th}$ layer, which is shown as curved arrow). It has proven that the residual learning can improve the performance of model training, especially when the model has deep network with more than 20 layers, and also revolve the problem of degrading accuracy in deep networks.

Do not always blame Overfitting

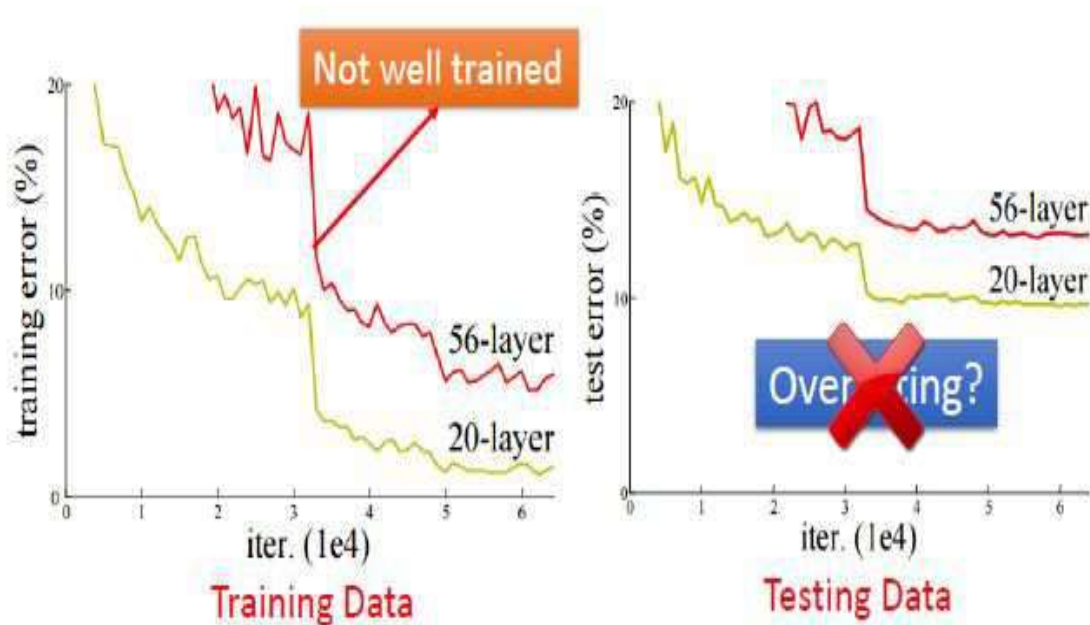


Figure 6.21: Architectures for (left) VGG and (middle) ResNet CNN.

Which CNN architecture should one use and should one try to innovate with new ones? The answer according to Hinton, Karpathy and Ng is to "not be a hero". Use one of the latest ones that work best with the ILSVRC contest, perhaps delete some parts. Karpathy says to play with the regularization strength and dropout rates.

6.4 Deep Learning Software and Youtube Classes

Karpathy points out a number of CNN software packages, and recommends Keras as the easiest to use, similar to Python. It is high level language based on the Torch/Tensorflow software which is for pros. Once you master the Torch language, you can develop your own special architectures. For some reason he doesn't list Cafe as one of his top three favorites, but he notes the nice features of 1). Run a script to convert data, 2). define CNN architecture, 3). define solver, and 4). train with pretrained weights. Now I understand, you don't train you simply feedforward! He doesn't list Theano or Lasagne as his favorites.

What about MATLAB? More details of his course are at cs231n.stanford.edu, he seems like an excellent lecturer. I also recommend Andrew Ng's Youtube videos on Deep Learning.

If you want to start your own company, the advice in 2016 is to buy NVIDIA DGX-1

(P100 GPUs) or NVIDIA DIGITS DevBox (Titan X GPUs). Karpathy claims the cloud does not offer good GPU services yet.

6.5 Seismic Fault Interpretation by CNN

Xiong et al. (2018) used a CNN system to identify faults in seismic data. Unlike previous attempts that used features extracted from seismic data as input (Zhang et al., 2014), Xiong et al. (2018) used three slices from the migration image as the input (see Figure 6.22) and used an attribute image as the output image (see Figure ??). In the attribute image they identified the faults and labeled them as such. Xiong et al.’s (2018) schematic for the CNN architecture is shown in middle of Figure 6.22. Some examples from the training set are given in Figure 6.23.

The target output values in the training set at each point O can be interpreted as faults or not by interpreters or auto-picking algorithms. In their paper, they classified eight different 3D seismic image cubes of real data using a skeletonized-seismic-coherence-based auto-picking method (Qi et al., 2017). After annotation, every point in the training cubes is labeled as fault or non-fault using a threshold strategy: the points with skeletonized coherence value larger than a predefined threshold is classified as fault, others are non-fault.

Before the input of three slices is fed into the network, it is normalized by subtracting the mean and dividing by the standard deviation. Similar to the classical CIFAR-10 classification problem (Krizhevsky and Hinton, 2009; Google, 2017), the network consists mainly of two convolutional (Conv) layers and two fully-connected (FC) layers followed by a softmax classifier, which gives the label prediction output (Bishop, 2006). The Conv layers both have 64 filters with sizes of 5×5 . There are 384 and 192 feature maps in the two FC layers, respectively. After every Conv layer and FC layer, they applied rectified linear activation (ReLU). Max-pooling with both size and stride being 22 and local response normalization (LRN) are used after both Conv layers. The final softmax classifier produces a probability indicating the likelihood of a fault being presented in the center point of the input. The prediction of the label is then generated by applying a threshold (0.5) to the output likelihood values, such that the one above the threshold would be considered to be a fault location, while those below would not.

The network is trained from scratch by initializing the weights of all the layers as in the CIFAR-10 tutorial of Tensorflow (Google, 2017; Abadi et al., 2016). A gradient descent optimizer is implemented in Tensorflow with the default parameters and the initial learning rate, i.e. step length, being 0.1. The training samples are randomly shuffled before they are fed into the network for every epoch, which is a critical step to obtain good network performance. The model is saved when the error (or loss) function

$$\epsilon = \frac{1}{n} \sum_{i=1}^n \ln p(Y = y_i | \mathbf{x}_i) \quad (6.13)$$

reaches a plateau during the optimization process, and it is then validated with the validation dataset. The saved model achieved classification accuracies of about 73% on both the training and validation datasets.

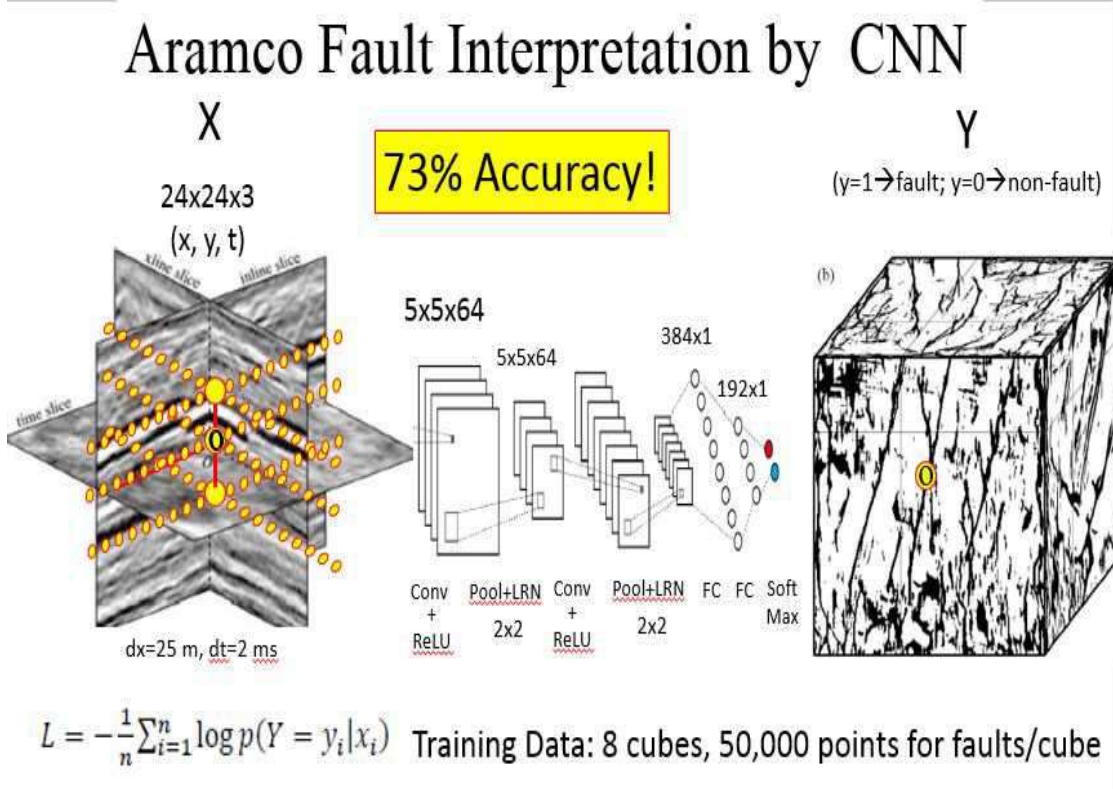


Figure 6.22: Three slices on the left are taken from a 3D migration cube and used as the input data to the CNN. The output is the point y_i at o on the right which is taken to be either a fault ($y_i = 1$) or not ($y_i = 0$). The $24 \times 24 \times 3$ filter is shifted over to a new position o' , and the dot product of the filter with the image points is computed again. Repeating this for all input points gives the first feature map. Note, the filter is not shifted up or down and only shifted along the lateral directions for this training example. A new training example will have the center point of the filter shifted up or down. Figure adapted from Xiong et al. (2018).

The weights for the trained model are applied to the testing cube comprising a 3D seismic image volume of real data. The cube size is $1000 \times 655 \times 1083$. The top, front and side panels are showing time section ($T = 312$), inline section ($Y = 423$) and cross-line section ($X = 417$), respectively. Locations of the sections are marked by the black lines in the figure. One of the eight cubes is randomly selected for validation and will not be seen by the network during the training process, while the other seven cubes are used to generate the training dataset. The training dataset is constructed by randomly selecting 50000 points from each cube labeled as faults (which is approximately 0.2% of all fault points in the cubes), and another 50000 points labeled non-fault. The number of non-fault points is much larger than fault points in the cubes. For this real data cube, the CNN obtains about 74% classification accuracy; close to that obtained for training and validation datasets.

Figure 6.23 shows some representative fault and non-fault samples randomly selected from the training dataset. While it is not easy for human eyes to distinguish every single

fault and non-fault sample, we can see a systematic difference between the two classes. Non-fault samples show more continuous seismic events. A validation dataset of the same size is constructed in the same way as the training dataset, which is used to monitor the training process and determine the termination of training.



Figure 6.23: Samples labeled as (a) fault and (b) non-fault. All samples are randomly selected from the training dataset, except the first row showing synthetic samples. Each sample is composed of front, side and top panels which are inline, cross-line and time slices, respectively. The size of each slice is 24×24 . The spatial grid size is 25 meters while the vertical time sampling interval is either 0.002 or 0.004 seconds for different cubes. Figure adapted from YXiong et al. (2018).

The trained model is applied to the testing cube comprising a 3D seismic image volume of real data as shown in Figure 6.24. The cube size is $1000 \times 655 \times 1083$. The top, front and side panels are showing time section ($T=312$), inline section ($Y=423$) and cross-line section ($X=417$), respectively. Locations of the sections are marked by the black lines in the figure. For this real data cube, the CNN obtains about 74% classification accuracy; close to that obtained for training and validation datasets.

The fault probability cube output by the CNN is shown in Figure 6.24a along with results from a seismic coherence cube (Figure 6.24b). Seismic coherence is a well-known and widely used attribute to highlight discontinuities in seismic image (Bahorich and Farmer, 1995).

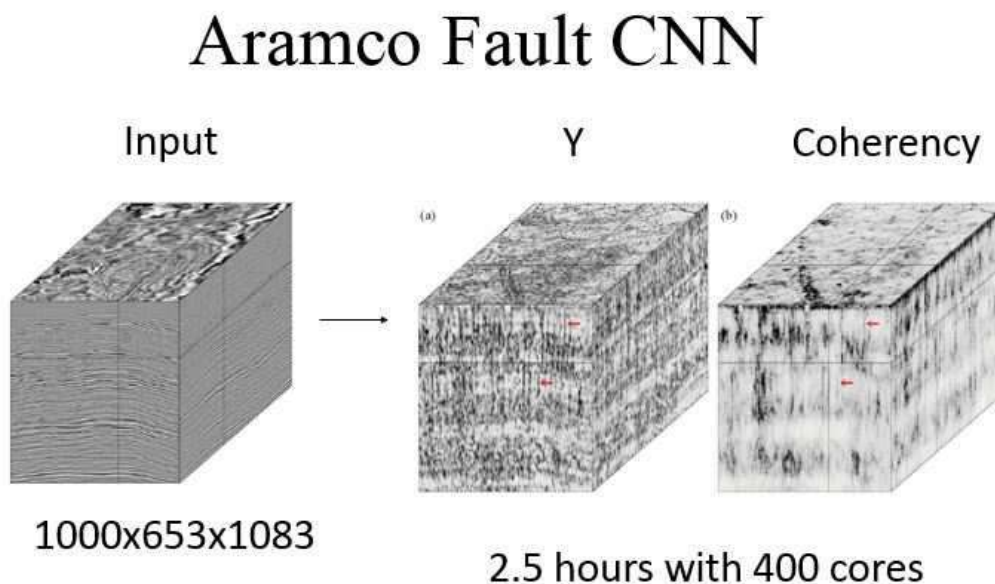


Figure 6.24: Real data example showing the fault probability cube from the CNN prediction, compared with the corresponding coherence cube. The cube size is $1000 \times 655 \times 1083$. The spatial grid size is 25 meters while the vertical time sampling interval is 0.002 seconds. Figure adapted from Xiong et al. (2018).

As we can be seen in Figures 6.24 and 6.25, the CNN results show a higher resolution compared to the coherence volume. The seismic faults as well as channels are clearer in the CNN results. Recalling that the fault probability calculation is made independently for different points, the clear continuous outlines of discontinuities in the fault probability images show that the trained network performs robustly in the presence of noise.

For the test with the 3D image cube of size $1000 \times 655 \times 1083$, it took about 2.5 hours to obtain the fault probability result using a computer cluster with 20 nodes (40 CPU cores in each node). So this method is still practical even without possible improvements by reducing duplicate calculations in adjacent locations.

6.6 Summary

The characteristics of a CNN are described. Its main advantage over classical neural networks is that its convolutional nature leads to a significant increase in computational efficiency by more than several orders of magnitude. It also more closely mimicks the actual processing of the brain's neurons in processing visual information in the brain. The CNN uses a weighted sum of local pixel values to give the input the j^{th} node of the next layer. The set of N weights w_i for $i \in [1, 2 \in N]$ are shared for computing the input into any node of the next layer.

An example is presented for using a CNN to identify faults in a migration image. The result is a more accurate identification of faults than provided by the interpretation of a

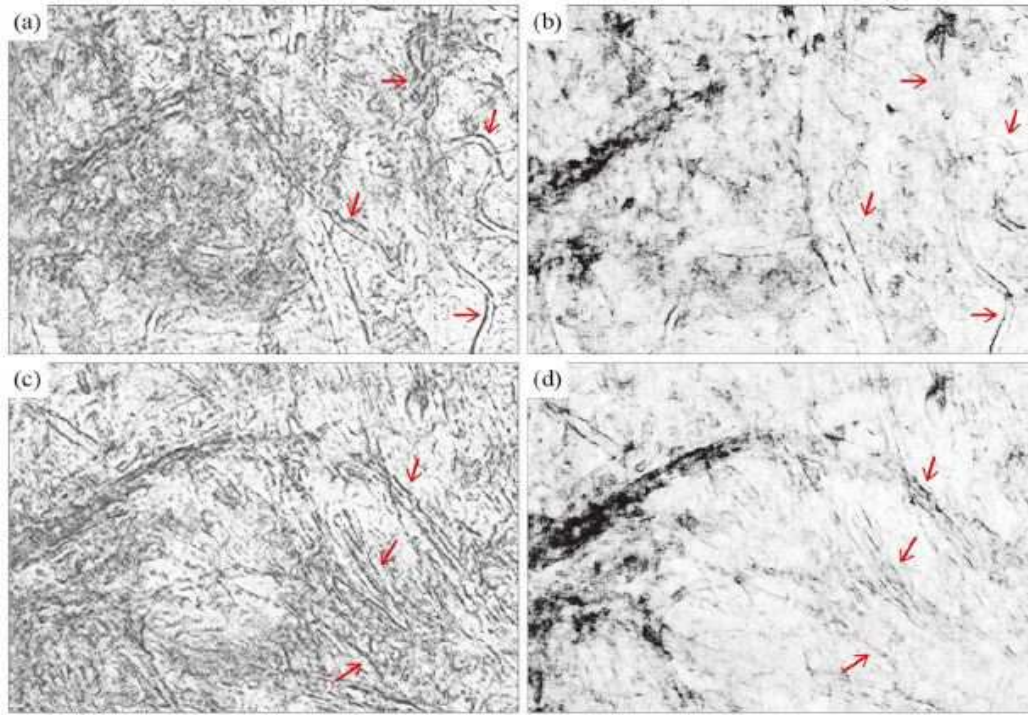


Figure 6.25: Time slices of fault probability [(a) and (c)] from CNN prediction, compared with seismic coherence [(b) and (d)], at two different time slices, $T = 312$ (top row) and $T = 387$ (bottom row), respectively. The section size is 655×1083 . The spatial grid size is 25 meters. Figure adapted from YXiong et al. (2018).

coherency cube. This is a promising result and gives optimism that CNN's will be a useful tool for many aspects of exploration geophysics.

6.7 Exercises

1. Describe how a migration deconvolution filter might be computed using CNN. Describe the effects of using convolution filters less than a wavelength or much larger than a wavelength.
2. Describe how a Hessian inverse might be obtained by computing $m = L^T d$, $Lm = \tilde{d}$, and $\tilde{m} = L^T \tilde{d}$, so that $\tilde{m} = L^T Lm$. In this show how to design a CNN so that the weights for an inverse Hessian are obtained such that $m = [L^T L]^{-1} \tilde{m}$. Is this the same inverse Hessian computed in exercise 1? Explain.
3. The first layer of a CNN supposedly decomp[oses an image into smaller components associated with edges oriented at certain angles. How can one use local damped regularization and local slant stacking to encourage the filters in the first layer to output FMs with edges oriented in different directions?

4. Too large of a filter means that the high wavenumber data have been lost. Develop a multiscale CNN that first finds weights that fit the low-wavenumber features of the input data, and then finds the weights for the high-wavenumber features. Explain why this might be important for speeding up convergence as is done in a multigrid method. Would it be useful to have a low-pass filter or high-pass filter in each FM to reduce noise?
5. Write the pseudo-MATLAB code for dropout regularization.
6. Sketch the outline for developing CNN as a perfect absorbing boundary condition near the sides of the finite-difference computational grid. Should the constraint $\|Lp = 0\|^2$ be included in the objective function, where Lp represents the acoustic wave equation. Test your CNN algorithm on analytical solutions to the acoustic wave equation in a homogeneous 2D medium.
7. How can FWI be combined with CNN to improve the performance of FWI below salt?

Chapter 7

Machine Learning Methods Applied to Geoscience Problems

This chapter presents some examples of applying Machine Learning (ML) methods to geoscience problems. The CNN examples include identification of salt dome boundaries in seismic images, rock cracks in color photos, and a basalt boundary in GPR data. A support vector machine is used to suppress migration artifacts in the extended domain of migration images. A fully convolutional neural network is used to detect salt bodies in migration images. All of these examples include code to reproduce the results.

7.1 Interpretation of Seismic Images by ML

Interpretation of seismic data is one of the most labor intensive tasks in data analysis of seismic images. Seismic data are processed into 3D migration images and the interpreter's goal is to find the likely hydrocarbon locations. This involves integrating the 3D images with existing well-log and geology information. This is similar to a medical doctor who diagnoses a patient from his/her CAT scan and biomedical data. In both cases a misdiagnosis can occur if subtle clues are not noticed or misdiagnosed. In addition, there is now a much greater volume of information to interpret, including the many different seismic attributes derived from migration images (Chen and Sidney, 1997; Chopra and Marfurt, 2006; Barala et al., 2016).

Machine Learning is now being used to assist both the interpreter (AlRegib et al., 2018), the medical doctor (Ciresan et al., 2012; Ciresan et al., 2013; Roth et al., 2016) in diagnosing their patients. It is also being used to interpret images for self-driving cars, industrial robots, and computer vision (Kivinen et al., 2014; Zhang et al., 2015; Zhang et al., 2016). The impressive performances highlight the effectiveness of deep neural networks, which are likely to replace the conventional manual interpretation of features (LeCun et al., 2015).

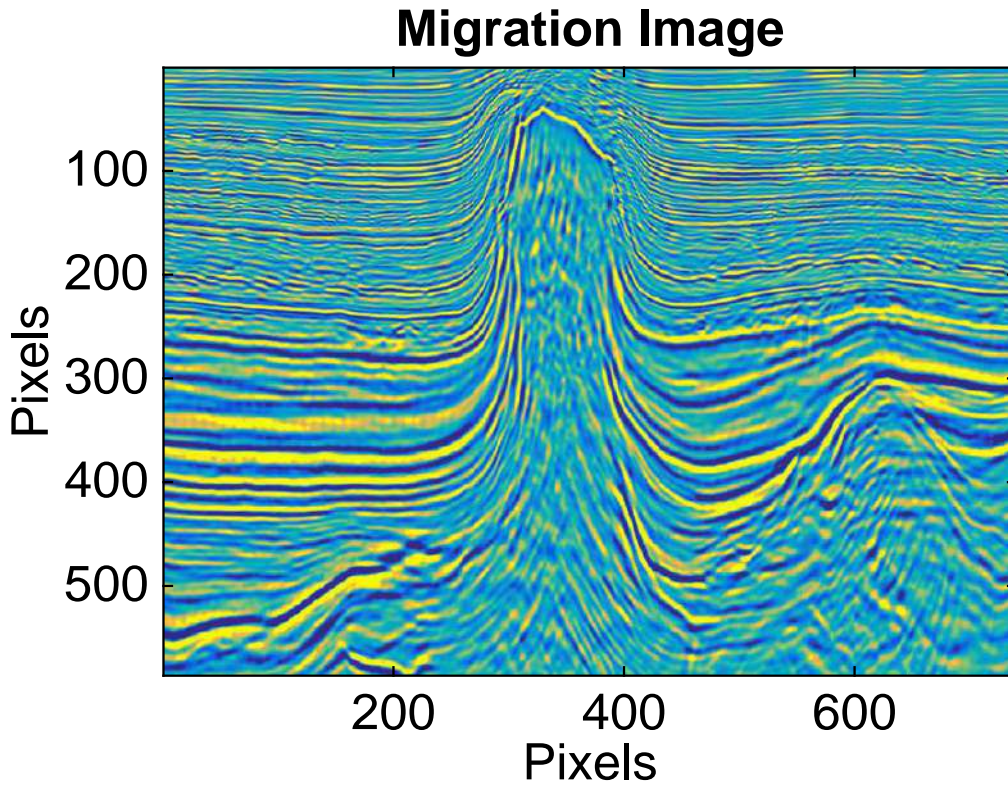


Figure 7.1: 2D seismic migration image of a salt dome.

7.2 Detection of Salt Body Boundaries by CNN

CNN is applied to a 2D seismic migration image shown in Figure 7.1. The goal is to automatically identify the boundary of the salt body without using time-intensive manual picking. Identifying and picking salt boundaries is the first step for velocity model building for subsalt imaging of hydrocarbons (Yilmaz, 2001).

Here we will use both a monoparameter CNN method and a multiparameter CNN method. The local dip angle in Figures 7.2 and the instantaneous frequency in 7.3 (Yilmaz, 2001) are selected as the multiparameters. These parameters inside the salt differs noticeably from those outside the salt. Approximately 700 positive patches (i.e. $y = 1$) and 700 negative patches (i.e. $y = 0$) are picked manually in the images. Around 80% of the patches are used as the training set and the others are used as the validation set. The CNN parameters for salt body classification are listed in Table 1.

Table 7.1: CNN parameters for Salt Body Classification

Image Size	Image Patch	Channels	Convolution path	Convolution Layers	Max Pooling	Iterations
586×740	39×39	6	2×2	3	2×2	50

The input data to the supervised CNN training consist of the migration amplitude values at different center points in the migration image. The output at the center point is a label

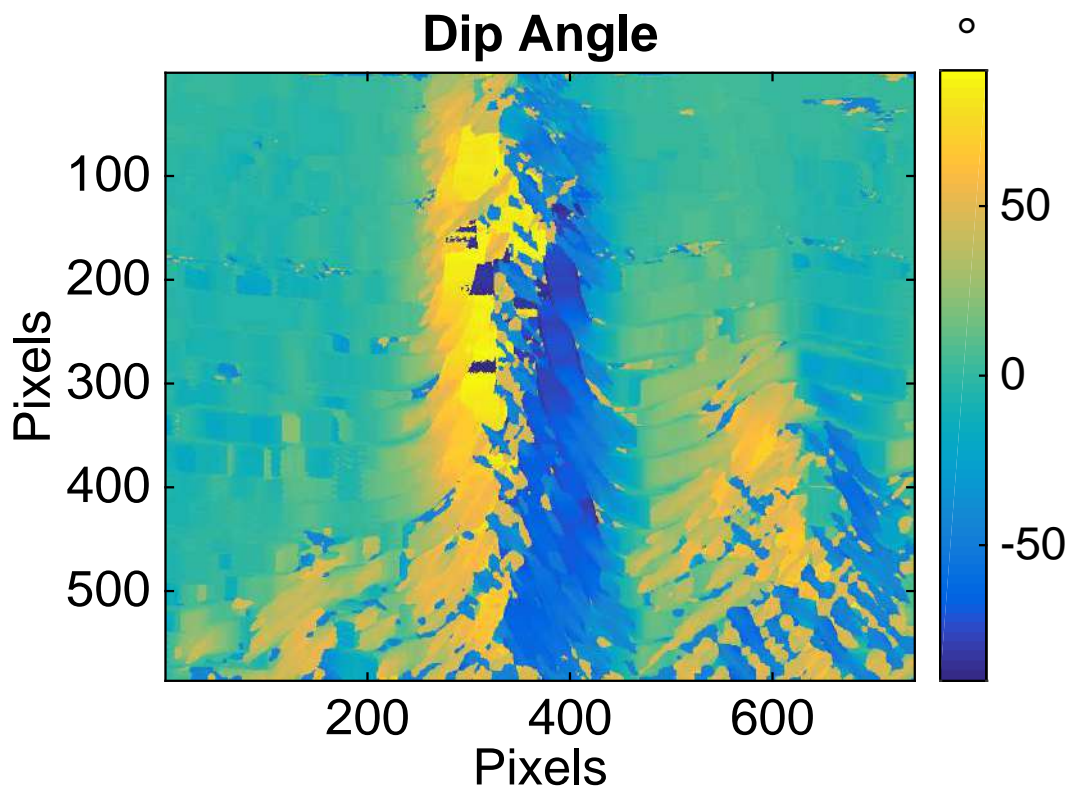


Figure 7.2: Dip angles computed from the migration image by a local slant stack operation (Yilmaz, 2001).

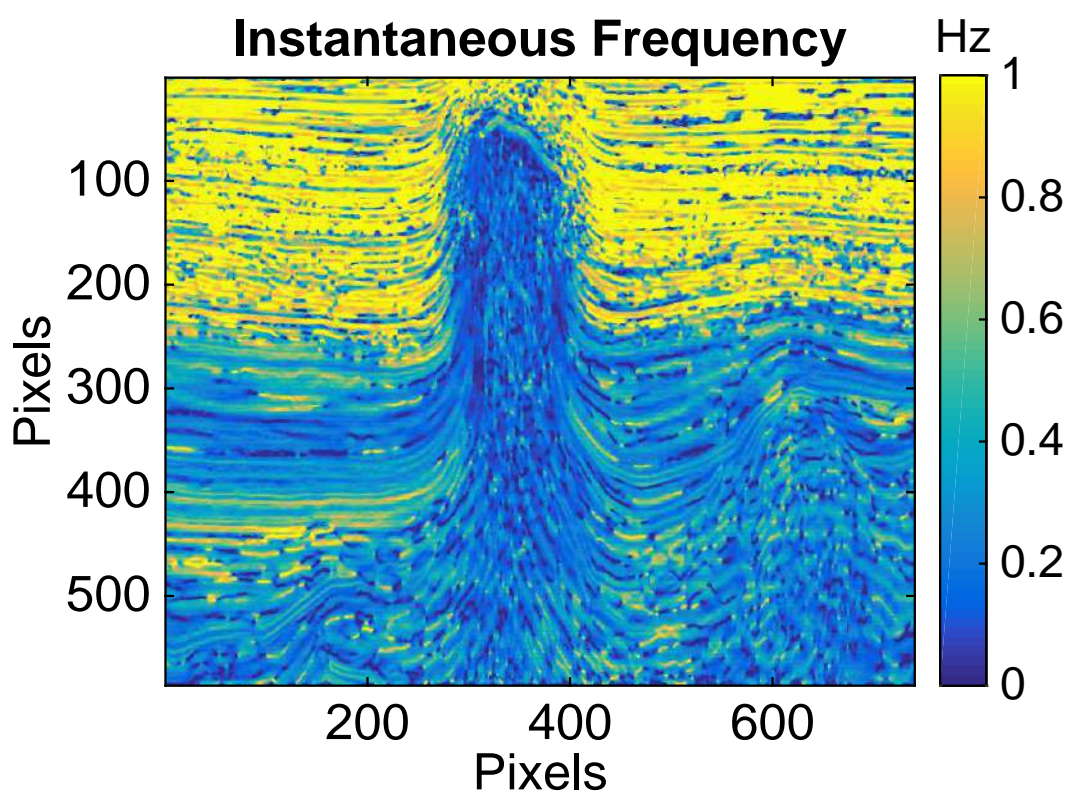


Figure 7.3: Instantaneous frequency image computed from the migration image.

$y = 1$ for a salt body and $y = 0$ for no salt.

7.2.1 CNN Architecture

An image patch whose center point is a salt body is labeled as a positive patch, otherwise it is labeled as a negative patch where no salt is extant. For a center point in the migration image, we extract a small image patch with dimension 39×39 and interpolate it into a 32×32 patch.

The network takes 32×32 patches of the migration image and attributes as input and the label of the center point is the output. The network is composed of three convolution (Conv) layers and two fully-connected (FC) layer followed by a softmax classifier. There are 6 convolution filters with size 2×2 in the first Conv layer. The number of channels is doubled in the deeper convolution layers. Rectified linear activation (ReLU) and a 2×2 max-pooling are applied after each Conv layer. There are 128 feature maps in the first fully-connected (FC) layer and we dropout 50% of them in the second FC layer. The softmax classifier gives the probability of the center point being a reflection event or not. The probability of two classifiers are compared and the one with the higher probability is selected as the prediction label. All convolutional filter kernel elements are trained from the data in a supervised fashion by learning from the labeled set of training examples. A training set $S = (x^i, y^i)$ is given which contains n image patches, where x^i is the i^{th} image patch and $y_i \in 0, 1$ is the corresponding class label. Then the corresponding cross-entropy cost function is given by

$$L = -\frac{1}{N} \sum_{i=1}^N \ln p(Y = y^i | x^i), \quad (7.1)$$

where $p(Y = y^i | x^i)$ is the probability that the label of x^i and y^i .

After training, the network is tested with a validation set to check the success of training. If the network is trained properly, it will recognize and correctly classify only those cases included in the training set. For new conditions not included in the training set, they will likely be misclassified.

7.2.2 Monoparameter CNN

The architecture of monoparameter CNN is illustrated in Figure 7.4a and only the migration image is used as the input layer. The accuracy of the training set and the validation set is 96.5% and 95.0%, respectively. The CNN labels in the migration image are shown in Figure 7.5. The points in yellow and in blue denote the salt body and the non-salt. The salt bodies in the image have been identified successfully. However, there are a lot of misclassifications around the salt bodies.

7.2.3 Multiparameter CNN

The multiparameter CNN uses dip angle, instantaneous frequency and original image as the input layers and the architecture is shown in Figure 7.4b. The accuracy of both the training set and the validation set are over 98%. Figure 7.6 shows the multiparameter CNN labels of

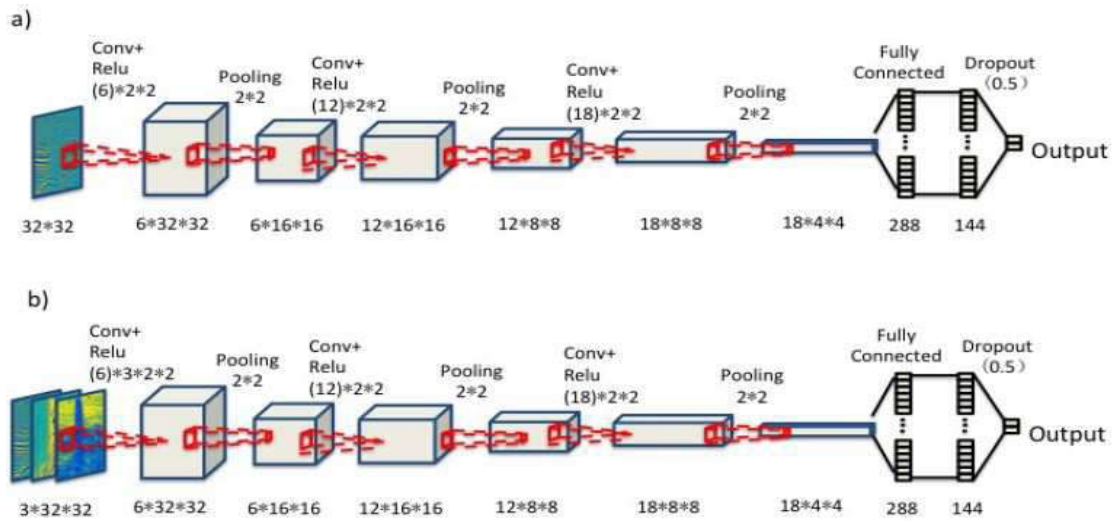


Figure 7.4: Illustration of a) the monoparameter CNN architecture and b) the multiparameter CNN architecture.

Monoparameter CNN Labels

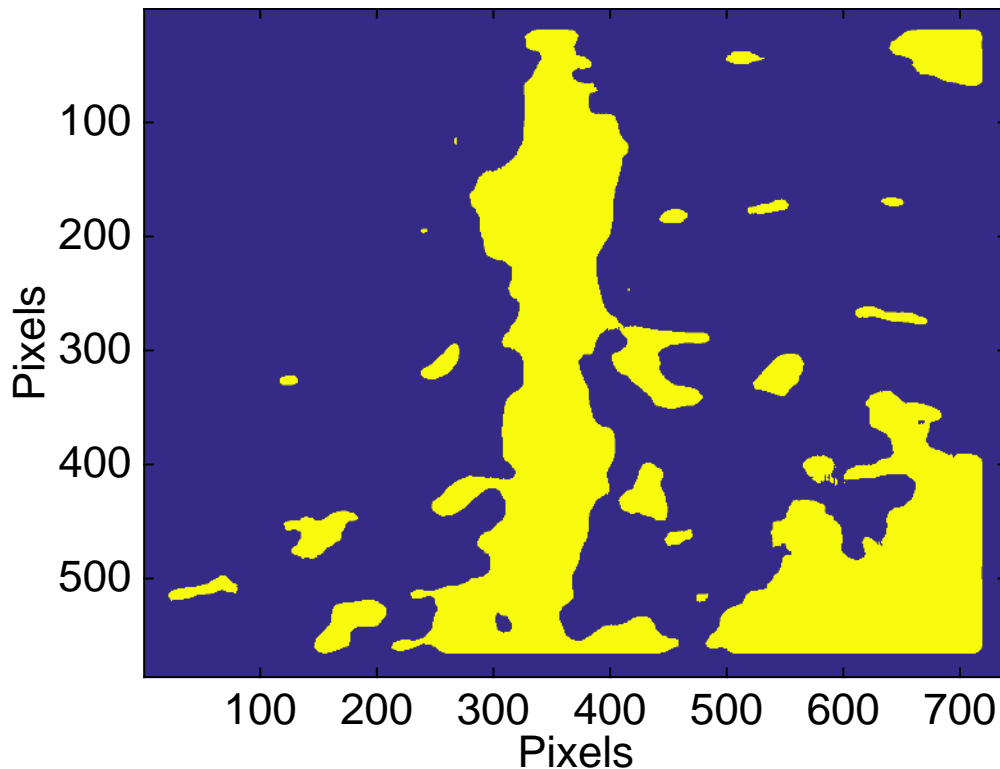


Figure 7.5: The image obtained from the monoparameter CNN.

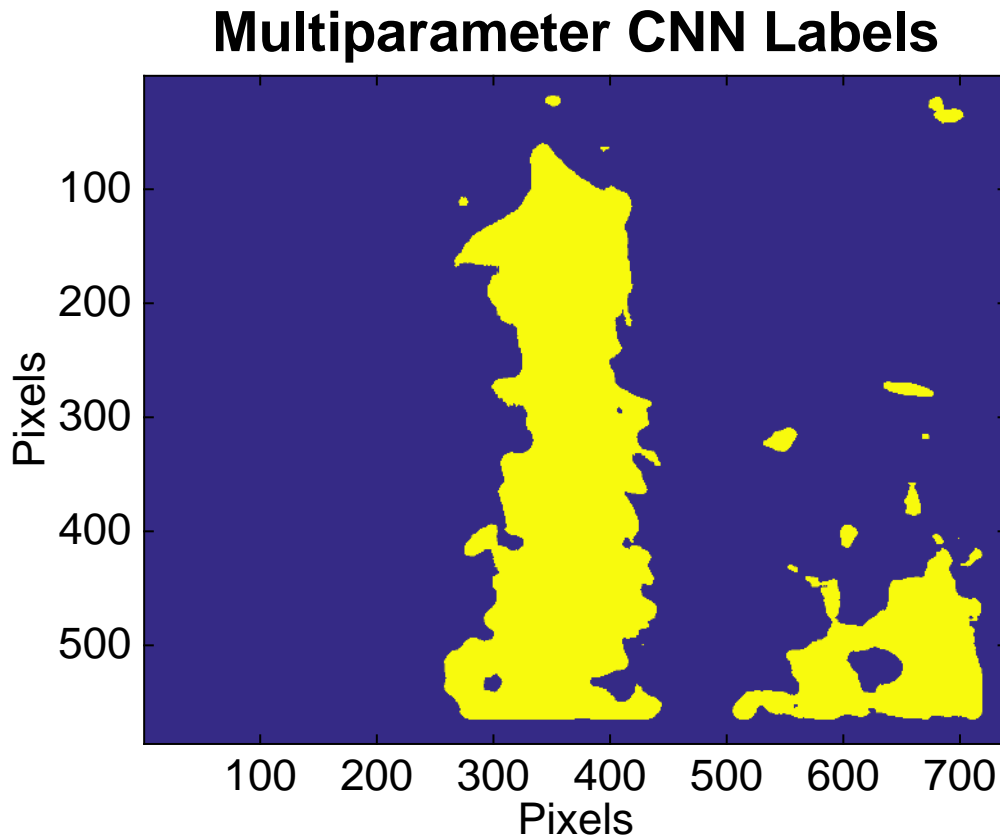


Figure 7.6: The image obtained from the multiparameter CNN.

the migration image. The misclassifications around the salt body have been greatly reduced and the salt bodies are located correctly. This suggests that adding more physical features such as dip and instantaneous frequency in the input will greatly improve the performance of CNN. However, there is still not a sharp delineation of the salt body boundary.

7.3 Detecting Rock Cracks by CNN

Detecting the density of rock cracks in boreholes is an important means for identifying breakout zones, permeable zones and lithology. For example, a borehole televiewer tool (see Figure 7.7a) can be used to produce panoramic images of the borehole wall. In this case cracks correspond to dark horizontal features seen in Figure 7.7b.

In addition, optical images from cameras can be used to assess the crack distribution in outcrops and trenches across faults. Counting and determining crack orientations can be invaluable in assessing the geology of the site, especially that in earthquake-prone regions. However, the problem with determining crack orientations and density is that it often involves labor-intensive efforts that can take days or weeks to complete. In this case it is important to automate the crack-detection process. We now show that CNN can be used to automatically detect cracks in optical photographs of rocks.

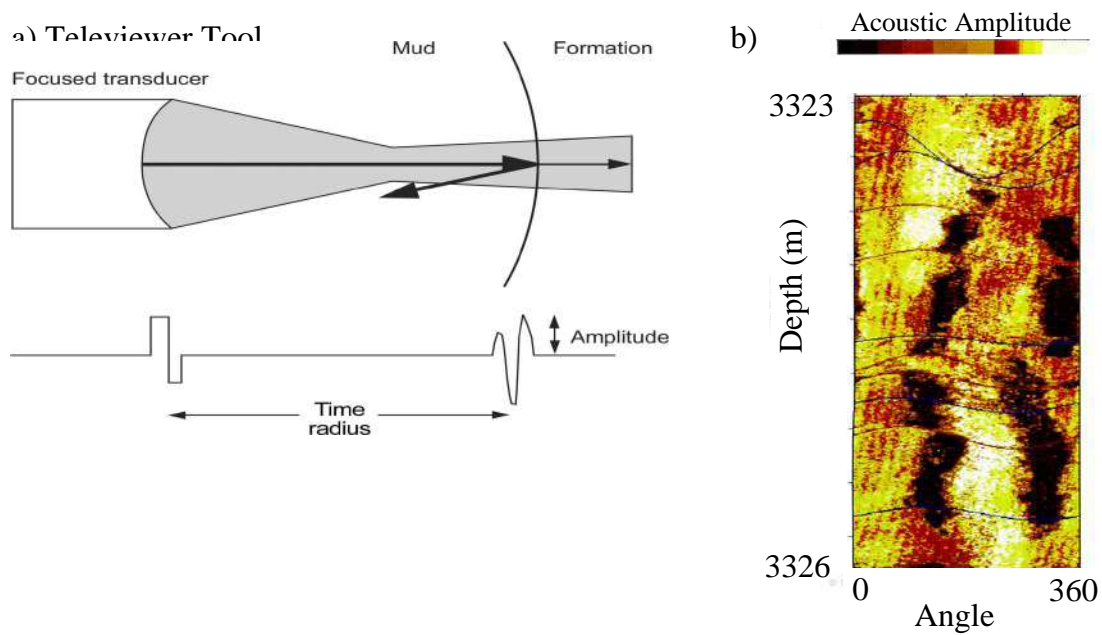


Figure 7.7: a) Ultrasonic Borehole Imager (UBI). The UBI measures reflection amplitude and radial distance using a direct measurement of mud velocity. b) Example of breakout detection using an ultrasonic borehole televviewer. Breakouts are indicated by the low acoustic amplitude of the reflected signal, shown here as darker areas. The breakouts are rotated because of a drilling-induced slippage of localized faults. Image and caption from https://petrowiki.org/Borehole_imaging and SPWLA.

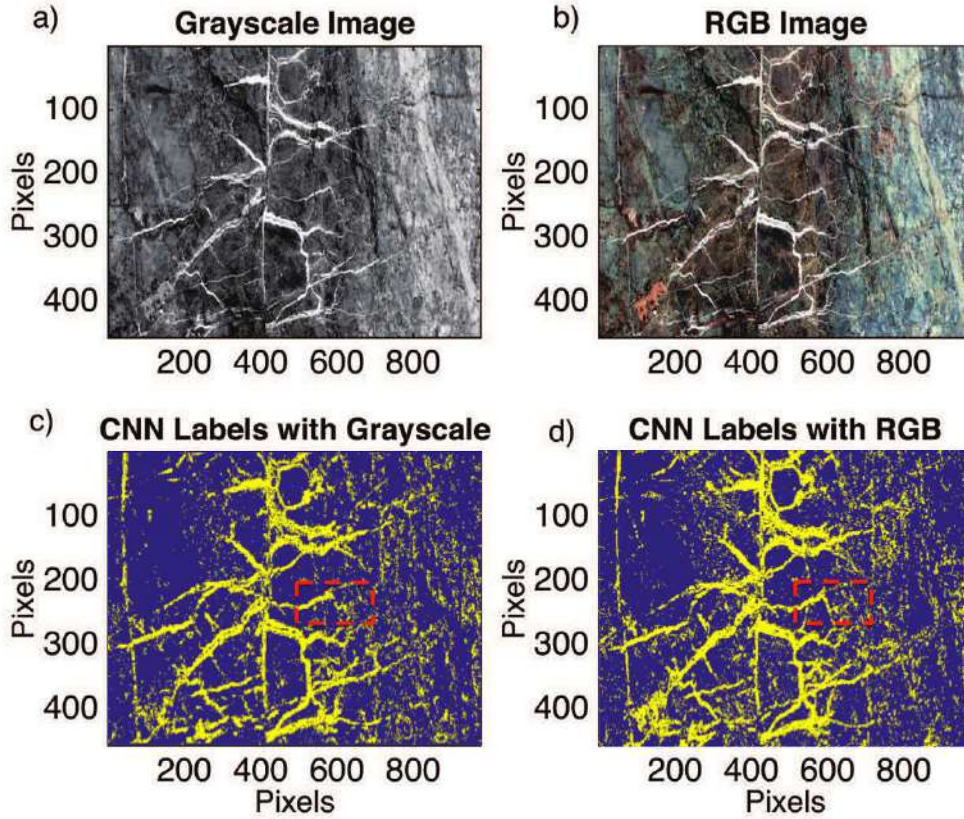


Figure 7.8: a) Grayscale and b) RGB images of the rock cracks. c) and d) are the CNN labeled images where yellow is the color of a crack.

The optical photo of a cracked rock is shown in Figure 7.8 and the inputs are the grayscale image in Figure 7.8a and the RGB image in Figure 7.8b. The input of the network for the RGB image has three RGB channels, so that the convolution filters in the last Conv layer also have three channels.

The CNN parameters for rock crack identification are listed in Table 2 and the CNN architecture is shown in Figure 7.9. For training, 100 positive patches ($y = 1$) and 100 negative patches ($y = -1$) are randomly selected from the image. More than 80% of the patches are used as the training set and the others are used as the validation set.

Table 7.2: CNN Parameters for Salt Body Classification

Image Size	Image Patch	Channels	Convolution path	Convolution Layers	Max Pooling	Iterations
457×977	17×17	8	4×4	5	2×2	250

400 positive patches and 400 negative patches are selected randomly from the image shown in Figure 7.10a. 80% of the patches are used as the training set and the others are used as the validation set.

In the first test, only the big cracks are picked in the training set. Figure 7.10b shows the

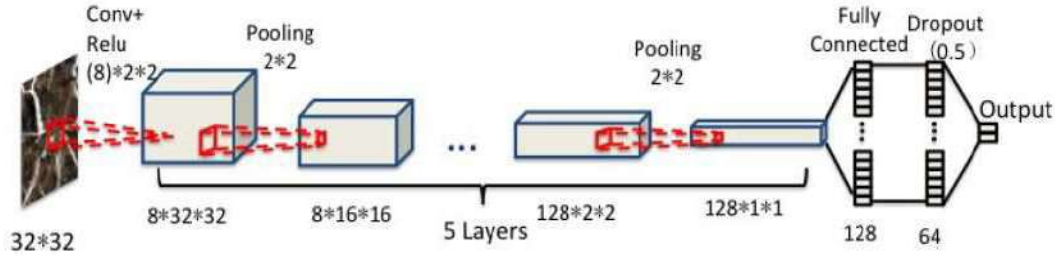


Figure 7.9: CNN architecture for detecting rock cracks.

crack detection results with big cracks only. The pixels in yellow and blue denote the cracks and the non-cracks. The big rock cracks are identified correctly from the background. The cracks in the left side of the image are not included in the training set, so they cannot be recognized in the testing set. The target of the detection can be easily changed by changing the training set. To identify all the cracks in the image, both the small and big cracks are included in the training set. Figure 7.10c shows the crack detection results with all the cracks.

To improve the classification results, the RGB image is set as the input image instead of the grayscale image. The input of the network for the RGB image has three RGB channels, then the convolution filters in the first Conv layer also have three channels.

Figures 7.11c and 7.11d compare the crack detection results for the grayscale and RGB images. Since the rock cracks in the images are mostly white, both the RGB value and the grayscale values are high for the rock cracks. The identification of the rock cracks for both case are similar and mostly correct. The RGB image contains more information than the grayscale image, so the CNN result for RGB image is slightly better than it of grayscale image, such as in the red boxes of Figures 7.11c and 7.11d. If the targets are colored, the RGB value of the target could be high but the grayscale value is an average value. In this case, the RGB image should be more easily CNN classified than the grayscale image.

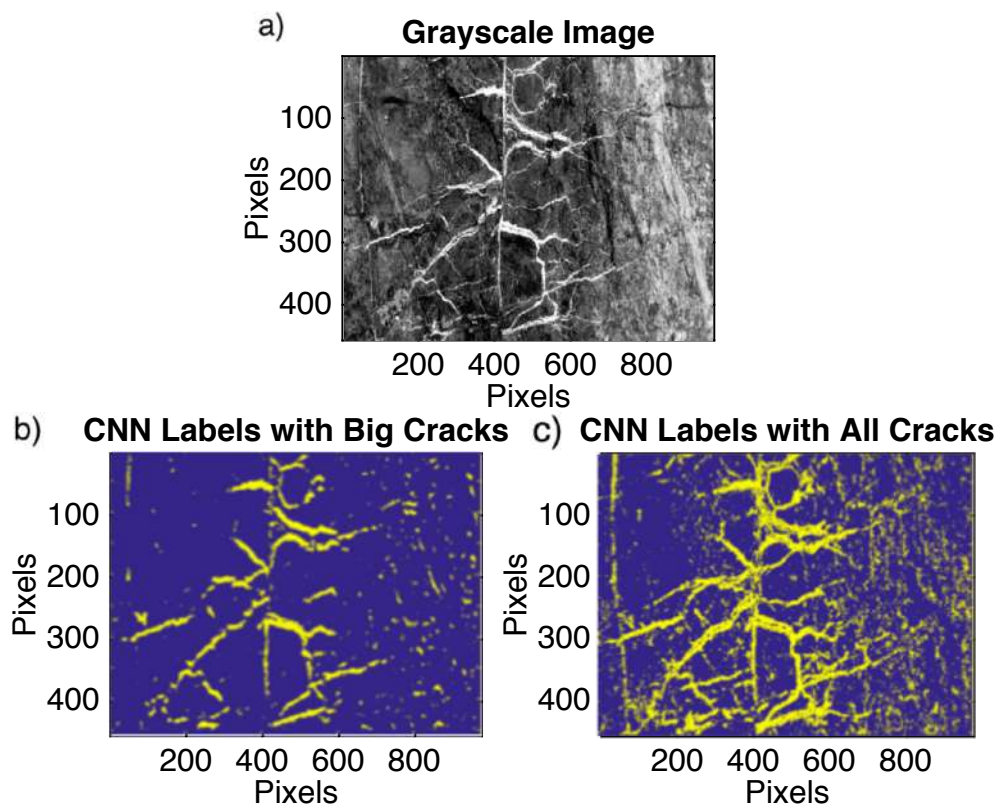


Figure 7.10: a) Grayscale of the rock cracks. The CNN labels for the c) big cracks only and d) all the cracks.

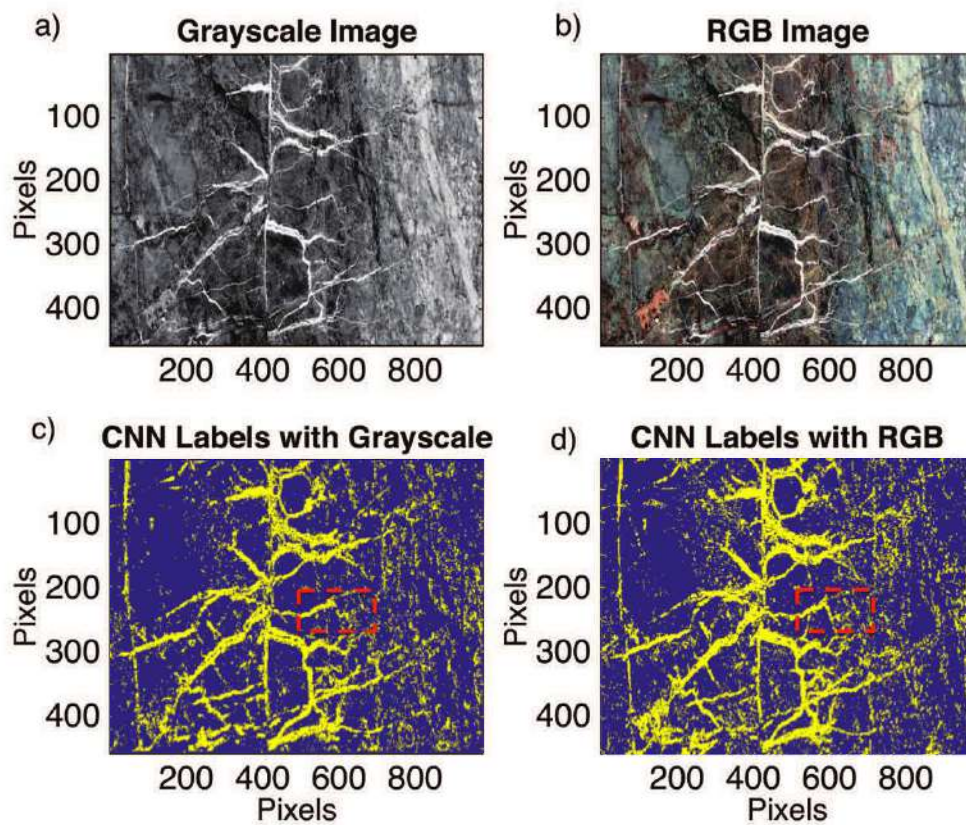


Figure 7.11: a) Grayscale and b) RGB images of the rock cracks. The CNN labels for the c) grayscale and d) RGB images.

Chapter 8

Recurrent Neural Networks

Recurrent Neural Networks (RNNs) are popular models that have shown great promise in many natural language processing (NLP) tasks. We will first explain the key ideas underlying RNN in the context of NLP. This is followed by some applications to seismic data. The high level overview is largely borrowed from Denny Brtíz's blog ([http : //www.wildml.com/2015/09/recurrent-neural-networks-tutorial-part-1-introduc](http://www.wildml.com/2015/09/recurrent-neural-networks-tutorial-part-1-introduc)) on RNN.

8.1 Theory of Recurrent Neural Networks

The idea behind RNNs is to make use of sequential information. In a traditional neural network we assume that all inputs (and outputs) are independent of each other. But for many tasks that's a very bad idea. If you want to predict the next word in a sentence you better know which words came before it. RNNs are called recurrent because they perform the same task for every element of a sequence, with the output being depended on the previous computations. Another way to think about RNNs is that they have a memory which captures information about what has been calculated so far. In theory RNNs can make use of information in arbitrarily long sequences, but in practice they are limited to looking back only a few steps (more on this later). Figure 8.1 what a typical RNN looks like, where a RNN is unrolled (or unfolded) into a full network. By unrolling we simply mean that we write out the network for the complete sequence. For example, if the sequence we care about is a sentence of 5 words, the network would be unrolled into a 5-layer neural network, one layer for each word. The formulas that govern the computation happening in a RNN are as follows:

1. \mathbf{x}_t is the input at time step t . For example, $\mathbf{x}_1 = (0, 0, 0, \dots, 1, \dots, 0)$ could be a one-hot vector corresponding to the second word of a sentence. The one-hot vector can refer to one of the words in a dictionary of frequently used words.
2. \mathbf{s}_t is the hidden state vector at time step t . It's the memory of the network. The vector \mathbf{s}_t is calculated based on the previous hidden state and the input at the current step:

$$\mathbf{s}_t = f(\mathbf{U}\mathbf{x}_t + \mathbf{W}\mathbf{s}_{t-1}). \quad (8.1)$$

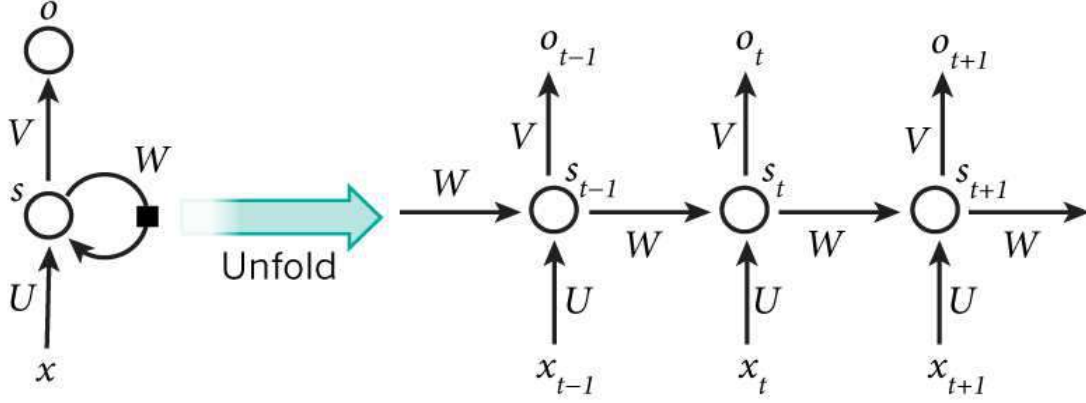


Figure 8.1: A recurrent neural network and the unfolding in time of the computation involved in its forward computation. Source Nature.

The function $f(\mathbf{x})$ usually is a nonlinearity such as tanh or ReLU. The initial hidden state vector at $t = -1$ is denoted as \mathbf{s}_{-1} , which is required to calculate the first hidden state. It is typically initialized to all zeroes.

3. ϕ_t is the output at step t . For example, if we wanted to predict the next word in a sentence it would be a vector of probabilities across our vocabulary. That is,

$$\phi_t = \text{softmax}(\mathbf{V}\mathbf{s}_t). \quad (8.2)$$

Some comments are now

8.1.1 What can RNN's Do?

RNNs have shown great success in many NLP tasks. At this point I should mention that the most commonly used type of RNNs are Long short-term memories (LSTMs), which are much better at capturing long-term dependencies than vanilla RNNs are¹. LSTMs are essentially the same thing as the RNN we will develop in this tutorial, they just have a different way of computing the hidden state. Here are some example applications of RNNs in NLP (by non means an exhaustive list).

- **Language Modeling and Generating Text.** Given a sequence of words we want to predict the probability of each word given the previous words. Language Models allow us to measure how likely a sentence is, which is an important input for Machine Translation (since high-probability sentences are typically correct). A side-effect of being able to predict the next word is that we get a generative model, which allows

¹Long short-term memory (LSTM) units are units of a recurrent neural network (RNN). An RNN composed of LSTM units is often called an LSTM network. A common LSTM unit is composed of a cell, an input gate, an output gate and a forget gate. The cell remembers values over arbitrary time intervals and the three gates regulate the flow of information into and out of the cell. See https://en.wikipedia.org/wiki/Long_short-term_memory.

us to generate new text by sampling from the output probabilities. And depending on what our training data is we can generate all kinds of stuff. In Language Modeling our input is typically a sequence of words (encoded as one-hot vectors for example), and our output is the sequence of predicted words. When training the network we set $\phi_t = \mathbf{x}_{t+1}$ since we want the output at step t to be the actual next word.

- **Machine Translation.** Machine Translation is similar to language modeling in that our input is a sequence of words in our source language (e.g. German). We want to output a sequence of words in our target language (e.g. English). A key difference is that our output only starts after we have seen the complete input, because the first word of our translated sentences may require information captured from the complete input sequence.
- **Speech Recognition.** Given an input sequence of acoustic signals from a sound wave, we can predict a sequence of phonetic segments together with their probabilities.
- **Generating Image Descriptions.** Together with convolutional Neural Networks, RNNs have been used as part of a model to generate descriptions for unlabeled images. Its quite amazing how well this seems to work. The combined model even aligns the generated words with features found in the images.

8.2 Training RNNs

Training a RNN is similar to training a traditional Neural Network. We also use the backpropagation algorithm, but with a little twist. Because the parameters are shared by all time steps in the network, the gradient at each output depends not only on the calculations of the current time step, but also the previous time steps. For example, in order to calculate the gradient at $t = 4$ we would need to backpropagate 3 steps and sum up the gradients. This is called Backpropagation Through Time (BPTT). If this doesn't make a whole lot of sense yet, don't worry, we'll have a whole post on the gory details. For now, just be aware of the fact that vanilla RNNs trained with BPTT have difficulties learning long-term dependencies (e.g. dependencies between steps that are far apart) due to what is called the vanishing/exploding gradient problem. There exists some machinery to deal with these problems, and certain types of RNNs (like LSTMs) were specifically designed to get around them.

Some extensions of RNN include bidirectional RNNs, which include information about both the past and future to process the current word. For example, to predict a missing word in a sequence you want to look at both the left and the right context as illustrated in Figure 8.2. Bidirectional RNNs are quite simple. They are just two RNNs stacked on top of each other. The output is then computed based on the hidden state of both RNNs. Deep (Bidirectional) RNNs are similar to Bidirectional RNNs, only that we now have multiple layers per time step. In practice this gives us a higher learning capacity (but we also need a lot of training data).

We now have a basic understanding of RNNs, and so now let's look at some applications in geoscience.

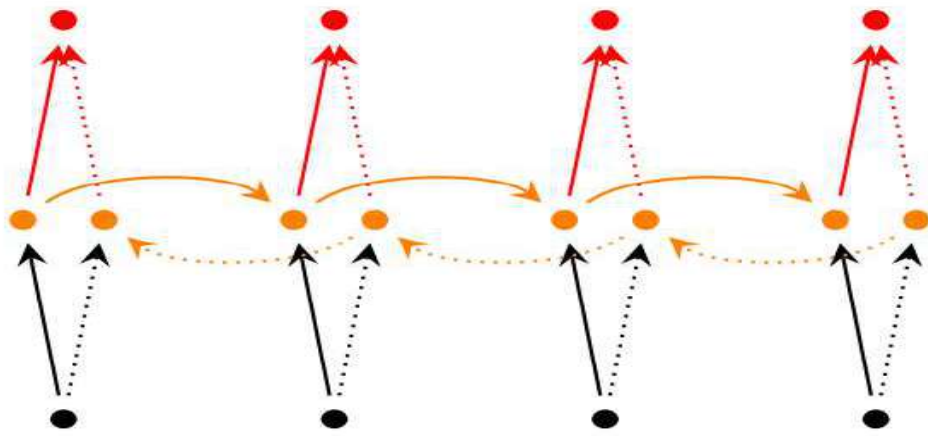


Figure 8.2: Simple bi-directional RNN.

Chapter 9

Wave Equation Inversion and Neural Networks

We compare the full waveform inversion (FWI), skeletonized wave equation inversion (SWI), and supervised Machine Learning (ML) algorithms with one another. For velocity inversion the advantage of SWI over FWI is it is more robust and has less of a tendency in getting stuck at local minima. This is because SWI only needs to explain the kinematic information in the seismograms, which is less demanding than FWI's difficult task of explaining all of the wiggles in every arrival. The disadvantage of SWI is that it provides a tomogram with theoretically less resolution than the ideal FWI tomogram. In this case, the SWI tomogram can be used as an excellent starting model for FWI. SWI is similar to supervised Machine Learning in that both use skeletonized representations of the original data. Simpler input data lead to simpler misfit functions characterized by quicker convergence to useful solutions. I show how a hybrid ML+SWI method and the implicit function theorem can be used to extract almost any skeletal feature in the data and invert it using the wave equation. This assumes that the skeletal data are sensitive to variations in the model parameter of interest.

9.1 Introduction

Full waveform inversion is very ambitious, it seeks an earth model \mathbf{m} that explains every complicated wiggle in a large set of very wiggly seismograms denoted by \mathbf{d} (Tarantola, 1987). A basic assumption is that the forward modeling operator \mathbf{L} (see Figure 9.1a) is a "good enough" representation of the actual physics of wave propagation in the Earth. Such ambitions and assumptions can sometimes lead to getting stuck in local minima, slow convergence and tomograms with unacceptable errors. To partly mitigate these problems a multiscale strategy can be employed. As an alternative, we present wave equation inversion of skeletonized data. Here, the large complicated data set is reduced to skeletonized data $\tilde{\mathbf{d}}$ which are much less complicated yet still contain essential information about the model parameters of interest. This means that the skeletonized data lead to a less complicated objective function that does not contain so many local minima associated with the one for FWI.

To invert the skeletonized data, skeletonized wave equation inversion (SWI) uses nu-

merical solutions to the wave equation to update the model by back-propagation of the weighted skeletonized data residual (Luo and Schuster, 1991; Lu et al., 2017). The result is a largely robust inversion algorithm free of layered media or high-frequency approximations. The main benefits are that the inversion algorithm is less prone to getting stuck in a local minimum, but at the cost of a reduction in model resolution. However, the inverted tomogram can be used as the starting model for FWI because it is likely to be sufficiently close to the actual earth model.

Recent examples (Lu et al., 2017) of skeletonized wave equation inversion include the following cases. 1). **Inversion of $Q(\mathbf{x})$ from diving waves and surface waves.** Here the skeletonized data $\tilde{\mathbf{d}}$ are the peak frequencies associated with the arrivals of diving waves or surface waves, and the output model is $Q(\mathbf{x})$. 2). **$V(\mathbf{x})$ inversion by migration velocity analysis.** The skeletonized data $\tilde{\mathbf{d}}$ are the depth residuals or static shifts associated with plane-wave migration images in the common image gather domain. 3). **Inversion of $V(\mathbf{x})$ from the dispersion curves of surface waves.** Here, the input skeletonized data $\tilde{\mathbf{d}}$ are the dispersion curves of surface waves in the $k - \omega$ domain and the output model is the shear velocity for Rayleigh waves, Love waves, and the P-velocity model for near-surface guided waves.

The skeletonization strategy of SWI is similar to that of neural networks, where a complex data set is often reduced to its *essential features* (Bishop, 2006). These skeletonized "features" are input into the system of neural network layers depicted in Figure 9.1c. Here, the original data can be very complex but complexity can be reduced by an unsupervised learning algorithm such as a principle component analysis, singular value decomposition (Bishop, 2006) or some statistical measure of important features (Patel and Chatterjee, 2016). In principle, these less complex features are still rich in information about the model. As an example, Figure 9.2 depicts the workflow for classifying rock types using a supervised learning method (Patel and Chatterjee, 2016). Here the original input data consist of images \mathbf{d} of thin sections and their classification \mathbf{m} , each one classified as a type of limestone by a geologist. For example, if there are three types of classified rocks then the 3×1 target model vector $\mathbf{m} = (m_1, m_2, m_3)$ might be assigned $\mathbf{m} = (1, 0, 0)$ if it is a pure limestone, $\mathbf{m} = (0, 1, 0)$ if it is a weathered rock, and $\mathbf{m} = (0, 0, 1)$ if it is a shale-limestone. In practice, the assignment is over a range of classification numbers and \mathbf{m} is a 7×1 vector according to Figure 9.2.

To simplify the input data, the thin-slice images are skeletonized into histograms of red, blue, and green colors. These histograms are further skeletonized into second-order (variance), 3rd-order (skewness), and 4th-order (kurtosis) statistical parameters for each color histogram. The examples from this skeletonized training set are denoted as $(\tilde{\mathbf{d}}, \mathbf{m})$, where for each image the input is a 9×1 vector of statistical values from the three histograms. For pedagogical simplicity we avoid the superscript notation that denotes the i^{th} example from the training set. After sufficient training with N training examples, the coefficients of the neural network are inverted for and used to classify thin sections from out of the training set. In their case history, Patel and Chatterjee achieved more than a 90% accuracy in the classification of thin sections taken from outside the training set.

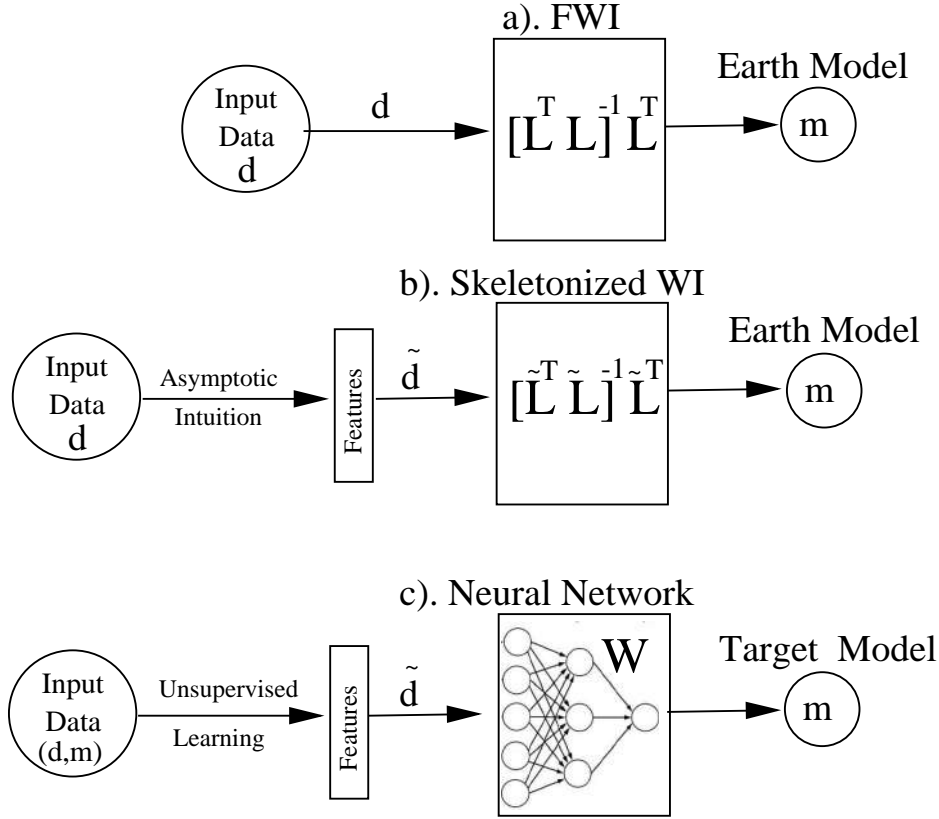


Figure 9.1: System diagrams for a) FWI, b) SWI, and c). a neural network. The neural network and SWI are similar in that the input data are skeletonized features of the raw data strongly influenced by small changes in the model. However, the neural network is first trained to get an estimate of \mathbf{W} , which is then used to estimate the target model \mathbf{m} from untrained data.

9.2 Theory for Wave Equation Inversion of Skeletonized Data

The starting point for wave equation inversion of skeletonized data is to define an objective function

$$\epsilon = \frac{1}{2} \sum_{j=1}^N (\tilde{d}_j - \tilde{d}_j^{obs})^2, \quad (9.1)$$

where d_j is the predicted data for $j \in [1, 2, \dots, N]$ and the *obs* superscript denotes the observed data. Different norms can be employed, and different objective functions can be used such as a correlation objective function. For simplicity of exposition, we do not include regularization or preconditioning terms and assume that d_j is always real.

An iterative gradient descent method can be used to find the model parameters that

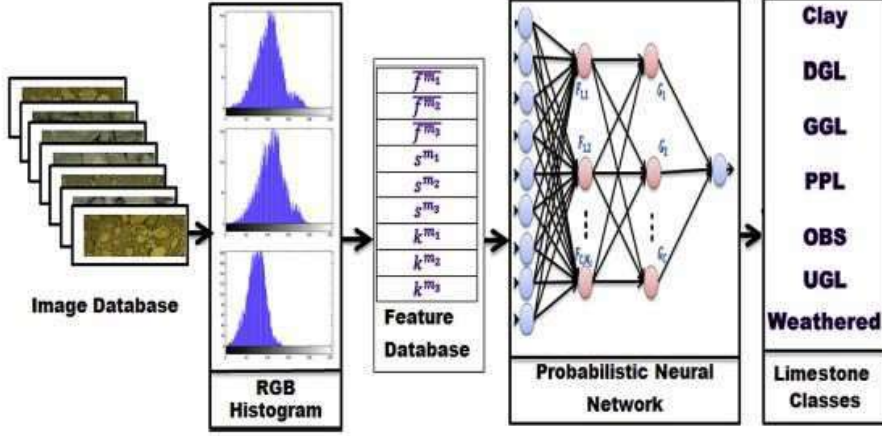


Figure 9.2: System diagram for the probabilistic neural network for classifying thin sections (from Patel and Chatterjee, 2016).

best explain the data in the least squares sense:

$$m_i^{(k+1)} = m_i^{(k)} - \alpha \sum_{j=1}^N \overbrace{(\tilde{d}_j - \tilde{d}_j^{obs})}^{r_j = \text{residual}} \overbrace{\frac{\partial \tilde{d}_j}{\partial m_k}}^{\text{Fr\'echet}}, \quad (9.2)$$

where α is the step length and $m_i^{(k)}$ is the model parameter of interest in the i^{th} cell at the k^{th} iteration. If the skeletal data value d_i is not explicitly contained in the wave equation, e.g. reflection traveltimes are not explicit variables in the wave equation, then a connective function $\Phi(d_j, m_k)$ is required to get a formula for the Fréchet derivative $\frac{\partial \tilde{d}_j}{\partial m_k}$. For example, Luo and Schuster (1991) proposed the crosscorrelation between the observed and predicted pressure traces for wave equation travelttime inversion. Lu et al. (2017) presents examples where the correlation is between the observed and predicted magnitude spectra of dispersion curves from surface waves. There are many other examples, some of which are described in Lu et al. (2017). Once the connective function is properly defined then the implicit function theorem (Luo and Schuster, 1991) can be used to define the formula for the Fréchet derivative:

$$\frac{\partial \tilde{d}_j}{\partial m_k} = A \frac{\partial P_j}{\partial m_k}, \quad (9.3)$$

where A is a scalar that acts as a normalization term and P_j is defined a fundamental field variable that explicitly appears in the wave equation. Fortunately, the formula for the Fréchet derivative $\frac{\partial P_j}{\partial m_k}$ of a fundamental field variable is straightforward to derive by the adjoint-state method. For acoustic data, the field variable is the pressure field recorded at the surface and the formula for its Fréchet derivative is well known. If more than one type of unknown is inverted for the multidimensional implicit function theorem can be used to compute the Fréchet derivatives for each type of model parameter (Lu et al., 2017). Note,

if $d_i \rightarrow P_i$ and m_i denotes the velocity value in the i^{th} cell then the update formula in equation 9.1 is that for FWI.

9.2.1 Feature Extraction

The most important step in SWI is the identification of skeletonized features that are simple and also greatly influenced by changes in the model parameter of interest. Towards this goal we look to the past where theoreticians identified skeletal data and derived asymptotic formulas that connected the skeletal data with the model parameter of interest. An obvious example is that of asymptotic ray-based tomography where, under the high-frequency approximation, traveltimes can be quickly generated by tracing rays through a sufficiently smooth model (Aki and Richards, 2002). If the physics of the problem is well understood, then the identification of the skeletonized data can be straightforward. If the physics between skeletal data and the model parameters is not well understood, then the sensitivity of the skeletal Fréchet derivative can be estimated by a combination of intuition and numerical sensitivity tests.

Can we go one step further by asking a Machine Learning algorithm to identify an important skeletal data set. Once identified, these skeletonized data can be inverted by a SWI method. For example, Figure 9.3 suggests a hybrid Machine Learning and SWI algorithm where an unsupervised machine learning method can be used to extract simplified but important features in the data set. Then the SWI method and the implicit function theorem can be used to discover the skeletal Fréchet derivative to be used in the update formula in equation 9.2. One possibility is that the skeletonized data can be obtained by principle component analysis (PCA) and the connective function is the spatial crosscorrelation between the observed and predicted PCA images. These PCA images can be localized in space. Can a general machine learning algorithm be used to identify the connection between skeletal features which are most sensitive to the model parameters of interest? This might be possible using a suitable training set obtained with numerically simulated data in realistic models.

We can go beyond skeletal data and define skeletal models as well. But this is another story.

9.3 Conclusions

We compared FWI, SWI and a supervised Machine Learning algorithm with one another. The advantage of SWI over FWI is it is more robust but provides less resolution. Thus, the SWI model can be used as the starting model for FWI. SWI is similar to supervised Machine Learning in that both use skeletonized representations of the original data. The next step is to combine the elements of SWI with Machine Learning to produce a Newtonian Machine Learning algorithm that employs Machine Learning, Newton's laws and solutions to the wave equation to invert for the model parameters from the skeletonized features of a complicated data set.

1. Derive the formula for the three-link chain rule.
2. Derive the formula for weight gradient at the $N = 12$ layer.

Machine Learning+Skeletonized WI

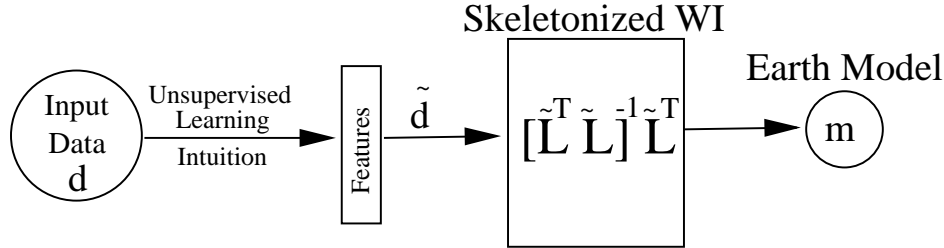


Figure 9.3: System diagram for a hybrid Machine Learning and SWI algorithm. Here, the skeletonized data \tilde{d} can be obtained by, for example, a principle component analysis (PCA), where the connective function is the crosscorrelation between the observed and predicted PCA images. Machine Learning combined with WI gives rise to a Newtonian Machine Learning algorithm, where the optimal skeletonized features are learned from the data and then inverted by numerical solutions to the wave equation.

3. Write the pseudo-MATLAB code where the bias vector and its gradient are explicitly computed.
4. Derive the steepest descent formula where the objective function is the one where the gradient is the cross-entropy term.
5. Write the pseudo-MATLAB code where regularization is used.
6. Write the pseudo-MATLAB code where the input is a batch matrix that represents the training set.
7. Write the pseudo-MATLAB code where the number of nodes per layer is different from one another.

Chapter 10

Neural Network Least Squares Migration

Sparse least squares migration (SLSM) estimates the reflectivity distribution $m(\mathbf{x})$ that honors a sparsity condition. This problem can be reformulated by finding both the sparse coefficients $\tilde{m}(\mathbf{z})$ and basis functions $\tilde{\Gamma}(\mathbf{x}|\mathbf{z})$ from the data to predict the migration image $m(\mathbf{x})^{mig} = \sum_{\mathbf{z}} \tilde{\Gamma}(\mathbf{x}|\mathbf{z})\tilde{m}(\mathbf{z})$. This is designated as neural network least squares migration (NLSM), which is a more general formulation of SLSM. This reformulation opens up new thinking for improving SLSM by adapting ideas from the machine learning community.

10.1 Sparse Least Squares Migration

The sparse least squares problem (SLSM) is defined as finding the reflectivity coefficients m_i in the $N \times 1$ vector \mathbf{m} that minimize the objective function ϵ :

$$\epsilon = \frac{1}{2} \|\mathbf{\Gamma}\mathbf{m} - \mathbf{m}^{mig}\|_2^2 + \lambda S(\mathbf{m}), \quad (10.1)$$

where $\mathbf{\Gamma} = \mathbf{L}^T \mathbf{L}$ represents the migration Green's function (Schuster and Hu, 2000), $\lambda > 0$ is a positive scalar, $\mathbf{m}^{mig} = \mathbf{L}^T \mathbf{d}$ is the migration image obtained by migrating the recorded data \mathbf{d} with the migration operator \mathbf{L}^T , and $S(\mathbf{m})$ is a sparseness function. For example, the sparseness function might be $S(\mathbf{m}) = \|\mathbf{m}\|_1$ or $S(\mathbf{m}) = \log(1 + \|\mathbf{m}\|_2^2)$.

The solution to equation 1.5 is

$$\mathbf{m}^* = \arg \min_{\mathbf{m}} \left[\frac{1}{2} \|\mathbf{\Gamma}\mathbf{m} - \mathbf{m}^{mig}\|_2^2 + \lambda S(\mathbf{m}) \right], \quad (10.2)$$

which can be approximated by an iterative gradient descent method:

$$\begin{aligned} m_i^{(k+1)} &= m_i^{(k)} - \alpha [\mathbf{\Gamma}^T \overbrace{(\mathbf{\Gamma}\mathbf{m} - \mathbf{m}^{mig})}^{\mathbf{r}=\text{residual}}]_i - \lambda S(\mathbf{m})'_i, \\ &= m_i^{(k)} - \alpha [\mathbf{\Gamma}^T \mathbf{r}]_i - \lambda S(\mathbf{m})'_i. \end{aligned} \quad (10.3)$$

Here, $S(\mathbf{m})'_i$ is the derivative of the sparseness function with respect to the model parameter m_i and the step length is α . Vectors (matrices) are denoted by boldface lowercase

(uppercase) letters and Appendix A derives the gradient of the sparseness function for the special case of $S(\mathbf{x}) = \|\mathbf{x}\|_1$

As shown in Schuster and Hu (2000), the poststack migration (Yilmaz, 2000) image $m(\mathbf{x})^{mig}$ in the frequency domain is computed by weighting each reflectivity value $m(\mathbf{z})$ by $\Gamma(\mathbf{x}|\mathbf{z})$ and integrating over the model-space coordinates \mathbf{z} :

$$\text{for } \mathbf{x} \in D_{model} : \quad m(\mathbf{x}) = \int_{D_{model}} d\mathbf{z} \overbrace{\int_{D_{data}} d\mathbf{y} \omega^4 G(\mathbf{x}|\mathbf{y})^{2*} G(\mathbf{y}|\mathbf{z})^2}^{\Gamma(\mathbf{x}|\mathbf{z})} m(\mathbf{z}), \quad (10.4)$$

where the migration Green's function $\Gamma(\mathbf{x}|\mathbf{z})$ is given by

$$\text{for } \mathbf{x}, \mathbf{z} \in D_{model} : \quad \Gamma(\mathbf{x}|\mathbf{z}) = \int_{D_{data}} d\mathbf{y} \omega^4 G(\mathbf{x}|\mathbf{y})^{2*} G(\mathbf{y}|\mathbf{z})^2. \quad (10.5)$$

Here we implicitly assume a normalized source wavelet in the frequency domain, and D_{model} and D_{data} represent the sets of coordinates in, respectively, the model and data spaces. The term $G(\mathbf{x}'|\mathbf{x}) = e^{i\omega\tau_{xx'}} / \|\mathbf{x} - \mathbf{x}'\|$ is the Green's function for a source at \mathbf{x} and a receiver at \mathbf{x}' in a smoothly varying medium¹. The traveltime $\tau_{xx'}$ is for a direct arrival to propagate from \mathbf{x} to \mathbf{x}' .

The physical interpretation of the kernel $\Gamma(\mathbf{x}'|\mathbf{x})$ is that it is the migration operator's² response at \mathbf{x}' to a point scatterer at \mathbf{x} , otherwise known as the MGF or the migration Green's function (Schuster and Hu, 2000). It is analogous to the point spread function (PSF) of an optical lens for a point light source at \mathbf{x} in front of the lens and its optical image at \mathbf{x}' behind the lens on the image plane. In discrete form, the modeling term $[\Gamma\mathbf{m}]_i$ in equation 10.4 can be expressed as

$$[\Gamma\mathbf{m}]_i = \sum_j \Gamma(\mathbf{x}_i|\mathbf{z}_j) m_j. \quad (10.6)$$

with the physical interpretation that $[\Gamma\mathbf{m}]_i$ is the migration Green's function response at \mathbf{x}_i . An alternative interpretation is that $[\Gamma\mathbf{m}]_i$ is the weighted sum of basis functions $\Gamma(\mathbf{x}_i|\mathbf{z}_j)$ where the weights are the reflection coefficients m_j and the summation is over the j index. We will now consider this last interpretation and redefine the problem as finding both the weights m_i and the basis functions $\Gamma(\mathbf{x}_i|\mathbf{z}_j)$. This will be shown to be equivalent to the problem of a fully connected (FC) neural network.

10.2 Neural Network LSM

The neural network least squares migration (NNLSM) algorithm in the image domain is defined as solving for *both* the basis functions $\tilde{\Gamma}(\mathbf{x}_i|\mathbf{z}_j)$ and \tilde{m}_j that minimize the objective function defined in equation 1.5. In contrast, SLSM only finds the least squares migration

¹If the source and receiver are coincident at \mathbf{x} then the zero-offset trace is represented by the squared Green's function $G(\mathbf{x}|\mathbf{x})^2$.

²This assumes that the zero-offset trace is generated with an impulsive point source with a smoothly varying background velocity model, and then migrated by a poststack migration operation. It is always assumed that the direct arrival is muted and there are no multiples.

image in the image domain and uses the pre-computed migration Green's functions that solve the wave equation.

The NNLSM solution is defined as

$$(\tilde{\mathbf{m}}^*, \tilde{\mathbf{\Gamma}}^*) = \arg \min_{\tilde{\mathbf{m}}, \tilde{\mathbf{\Gamma}}} \left[\frac{1}{2} \|\tilde{\mathbf{\Gamma}}\tilde{\mathbf{m}} - \mathbf{m}^{mig}\|_2^2 + \lambda S(\tilde{\mathbf{m}}) \right], \quad (10.7)$$

where now both $\tilde{\mathbf{\Gamma}}$ and $\tilde{\mathbf{m}}$ are to be found. The functions with tilde's are mathematical constructs that are not necessarily identical to those based on the physics of wave propagation in equation 1.5.

The explicit matrix-vector form of equation 1.5 is given by

$$\epsilon = \frac{1}{2} \sum_i \left[\sum_j \tilde{\Gamma}(\mathbf{x}_i | \mathbf{z}_j) \tilde{m}_j - m_i^{mig} \right]^2 + \lambda S(\tilde{\mathbf{m}}). \quad (10.8)$$

and its Fréchet derivative with respect to $\tilde{\Gamma}(\mathbf{x}_{i'} | \mathbf{z}_{j'})$ is given by

$$\frac{\partial \epsilon}{\partial \tilde{\Gamma}(\mathbf{x}_{i'} | \mathbf{z}_{j'})} = \sum_j (\tilde{\Gamma}(\mathbf{x}_{i'} | \mathbf{z}_j) \tilde{m}_j - \tilde{m}_{i'}^{mig}) \tilde{m}_{j'}. \quad (10.9)$$

The iterative solution of equation 10.7 is given in two steps (Olshausen and Field, 1996).

1. Iteratively estimate \tilde{m}_i by the gradient descent formula used with SLSM:

$$\tilde{m}_i^{(k+1)} = \tilde{m}_i^{(k)} - \alpha [\tilde{\mathbf{\Gamma}}^T (\tilde{\mathbf{\Gamma}}\tilde{\mathbf{m}} - \mathbf{m}^{mig})]_i - \lambda S(\tilde{\mathbf{m}})'_i. \quad (10.10)$$

However, one migration image \mathbf{m}^{mig} is insufficient to find so many unknowns. In this case the original migration image is broken up into many small pieces so that there are many migration images to form examples from a large training set. For prestack migration, there will be many examples of prestack migration images, one for each shot.

2. Update the basis functions $\tilde{\Gamma}(\mathbf{x}_i | \mathbf{z}_j)$ by inserting equation 10.9 into the gradient descent formula to get

$$\begin{aligned} \tilde{\Gamma}(\mathbf{x}_{i'} | \mathbf{z}_{j'})^{(k+1)} &= \tilde{\Gamma}(\mathbf{x}_{i'} | \mathbf{z}_{j'})^{(k)} - \alpha \frac{\partial \epsilon}{\partial \tilde{\Gamma}(\mathbf{x}_{i'} | \mathbf{z}_{j'})}, \\ &= \tilde{\Gamma}(\mathbf{x}_{i'} | \mathbf{z}_{j'})^{(k)} - \alpha \left(\left\{ \sum_j \tilde{\Gamma}(\mathbf{x}_{i'} | \mathbf{z}_j) \tilde{m}_j \right\} - m_{i'}^{mig} \right) \tilde{m}_{j'}. \end{aligned} \quad (10.11)$$

It is tempting to think of $\tilde{\Gamma}(\mathbf{x} | \mathbf{x}')$ as the migration Green's function and \tilde{m}_i as the component of reflectivity. However, there is yet no justification to submit to this temptation and so we must consider, unlike in the SLSM algorithm, that $\tilde{\Gamma}(\mathbf{x} | \mathbf{x}')$ is a sparse basis function and \tilde{m}_i is its coefficient. To get the true reflectivity then we should equate equation 10.6 to $\sum_j \tilde{\Gamma}(\mathbf{x}_i, \mathbf{x}_j) \tilde{m}_j$ and solve for m_j .

10.3 Numerical Results

We will test the feasibility of estimating for basis functions and coefficients for NNLSM in the image domain. No particular application is addressed, except the success of the following tests should point the way towards using unsupervised learning methods for extracting features that can be inverted by the wave equation (Schuster, 2018).

The three-layer velocity model shown in Figure 1.1a is used to test NNLSM by the unsupervised feature learning method of convolutional sparse coding (Liu and Lu, 2018). The grid size of the model is 101 by 101. The grid interval is 10 m in both the x and z directions. There are 26 shots evenly spaced at a distance of 40 m on the surface. Each shot is recorded by 101 receivers with a sampling interval of 10 m. Figure 1.1b show the reverse time migration (RTM) image.

The first test is for a 1D model where we extract the image located at $X = 0.5$ km, which is displayed as the blue curve in Figure 1.1c. The red curve in Figure 1.1c is the reflectivity model. Assume that there is only one basis function (feature) $\tilde{\Gamma}$ and it extends over the depth of 400 m (41 grid points). Equation 10.7 is solved for both $\tilde{\mathbf{m}}$ and $\tilde{\Gamma}$ by the two-step iterative procedure denoted as the alternating descent method. The computed basis function is shown in Figure 10.2a where the phase of the basis function $\tilde{\Gamma}$ is nonzero. However, the “physical” Γ is zero phase according to equation 10.5. If we use a nonzero-phase basis function $\tilde{\Gamma}$ to calculate its coefficient vector $\tilde{\mathbf{m}}$, the phases of the coefficient vector $\tilde{\mathbf{m}}$ (also known as the feature map) and the true reflectivity \mathbf{m} will be different. So, we need to modify the phase and polarity of the basis function $\tilde{\Gamma}$. The modified basis function is shown in Figure 10.2b, and its coefficients are displayed as the blue curve in Figure 10.2b. Compared with the true reflectivity \mathbf{m} (red curve in Figure 10.2), the feature map can give the correct positions but wrong values of the reflectivity distribution.

Next, we perform a 2D test where the input is the 2D migration image in Figure 1.1b. Three 35-by-35 (grid point) features are learned (see Figure 10.3a), where a feature is also denoted as a basis function. The modified features are shown in Figure 10.3b. The feature maps of these three features are displayed in Figures 10.4a, b and c. Figure 10.4d shows the sum of these three feature maps. It is evident that the stacked feature maps can estimate the correct locations of the reflectivity spikes.

10.4 Summary

Sparse least squares migration (SLSM) finds the optimal reflectivity distribution $m(\mathbf{x})$ that minimizes a sum of migration misfit and sparsity functions. This problem can be reformulated by finding both the sparse coefficients $\tilde{m}(\mathbf{z})$ and basis functions $\tilde{\Gamma}(\mathbf{x}|\mathbf{z})$ from the data to predict the migration image $m(\mathbf{x})^{mig} = \sum_{\mathbf{z}} \tilde{\Gamma}(\mathbf{x}|\mathbf{z}) \tilde{m}(\mathbf{z})$. This generalization of SLSM is designated as neural network least squares migration (NLSM). If the basis functions are required to be from the migration Green’s functions then NLSM reduces to SLSM. One possibility is to invert the feature maps using the wave equation as described in Schuster (2018). NLSM provides new ideas from the technology of machine learning for improving least squares migration.

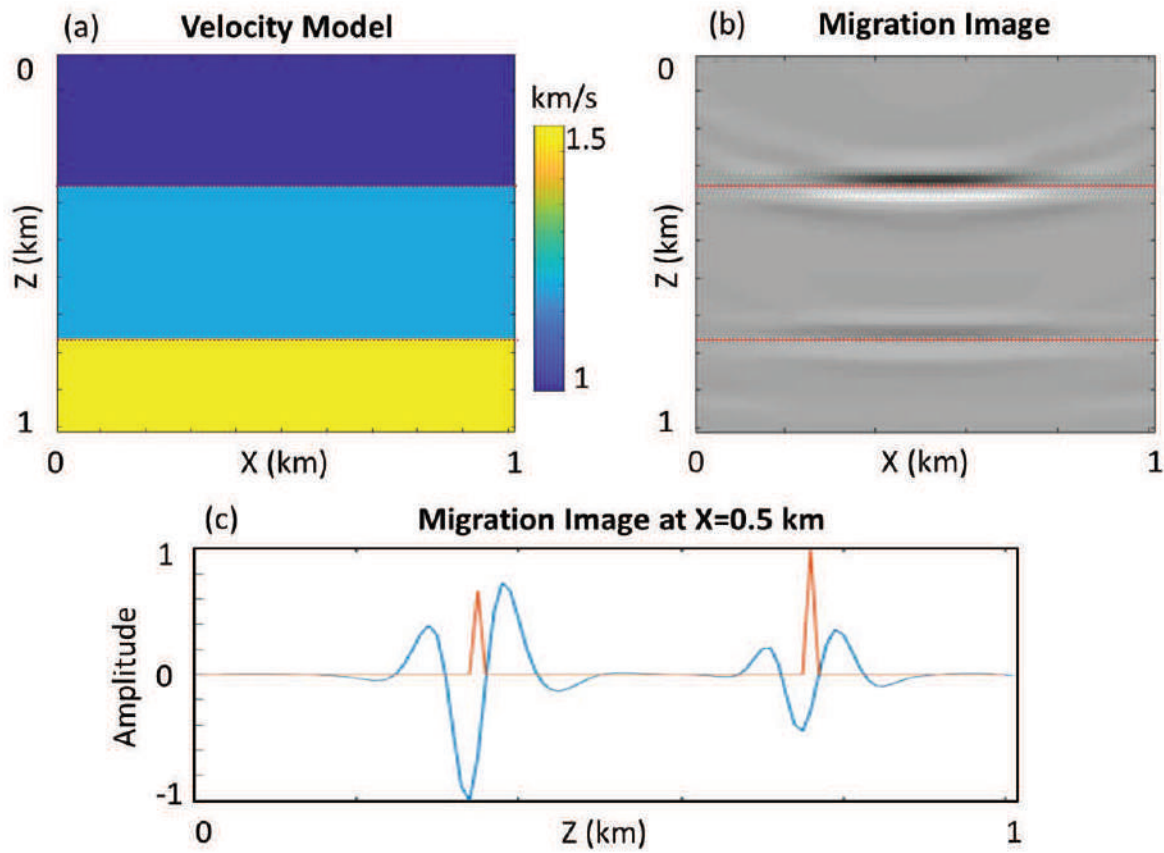


Figure 10.1: a) Three-layer velocity model, b) RTM image, and c) migration image (blue curve) at $X=0.5$ km, where the red curve is the normalized reflectivity model.

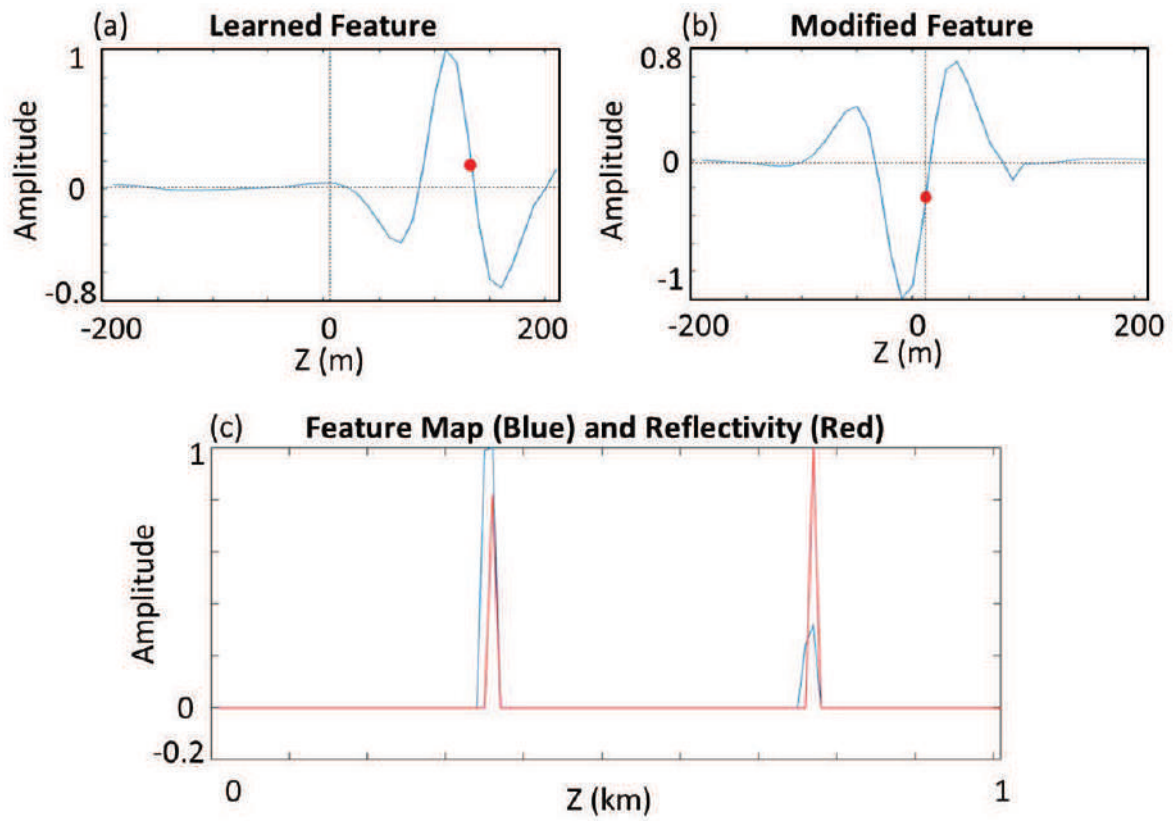


Figure 10.2: a) Basis function (also known as a feature), b) modified feature, and c) calculated coefficients (also known as a feature map) $\tilde{\mathbf{m}}$ (blue) and reflectivity model (\mathbf{m}).

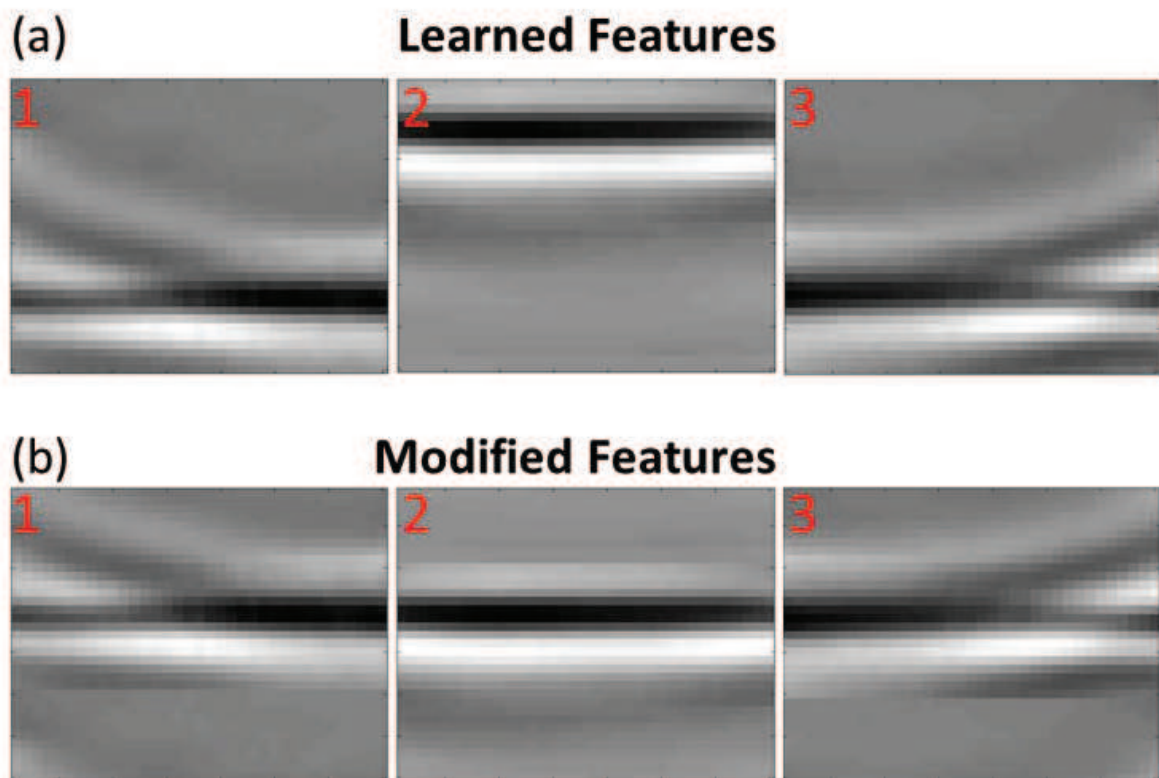


Figure 10.3: a) Learned and b) modified features.

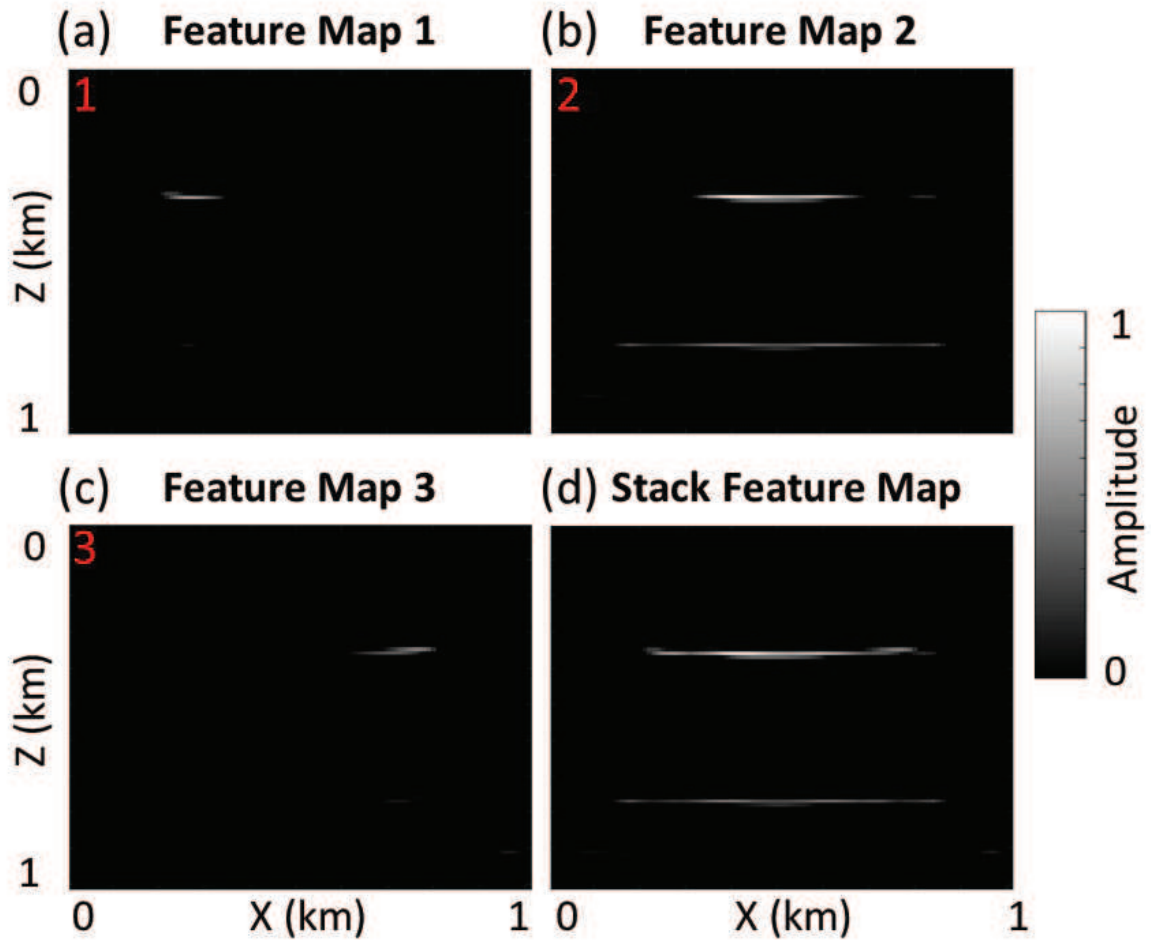


Figure 10.4: Feature maps for the features a) 1, b) 2, and c) 3 shown in Figure 10.3. The stacked feature map is shown in d).

10.5 Appendix

Define the sparse inversion problem as finding the optimal value x^* that minimizes the objective function

$$\epsilon = \frac{1}{2} \|\mathbf{z} - \mathbf{x}\|_2^2 + \lambda \|\mathbf{x}\|_1, \quad (10.12)$$

where the L_1 norm demands sparsity in the solution \mathbf{x} . An example is where \mathbf{z} is a noisy $M \times N$ image such that $\mathbf{z} = \mathbf{x} + \text{noise}$, and we seek the optimal vector \mathbf{x} that satisfies equation ???. Here, the noisy $M \times N$ image has been flattened into the tall $MN \times 1$ vector \mathbf{z} .

The stationary condition for equation ??? is

$$\begin{aligned} \frac{\partial \epsilon}{\partial x_i} &= (x_i - z_i) + \lambda \frac{\partial \|\mathbf{x}\|_1}{\partial x_i}, \\ &= 0, \end{aligned} \quad (10.13)$$

where

$$\frac{\partial \|\mathbf{x}\|_1}{\partial x_i} = 1 \text{ for } x_i \geq 0; \quad \frac{\partial \|\mathbf{x}\|_1}{\partial x_i} = -1 \text{ for } x_i < 0. \quad (10.14)$$

Equations ???-??? can be combined to give the optimal x^* expressed as the two-sided ReLU function

$$x_i = \text{softmax2}(z_i, \lambda) = \begin{cases} z_i - \lambda & \text{if } z_i \geq \lambda \\ 0 & \text{if } |z_i| < \lambda \\ z_i + \lambda & \text{if } z_i < -\lambda \end{cases}. \quad (10.15)$$

More generally, the iterative-shrinkage-threshold-algorithm (ISTA) that finds \mathbf{x}^*

$$\mathbf{x}^* = \arg \min_{\mathbf{x}} \left[\frac{1}{2} \|\mathbf{z} - \mathbf{W}\mathbf{x}\|_2^2 + \lambda \|\mathbf{x}\|_1 \right], \quad (10.16)$$

is

$$x_i^{(k+1)} = \text{softmax2} \left(\mathbf{x}^{(k)} - \frac{1}{\alpha} \mathbf{W}(\mathbf{W}\mathbf{x}^{(k)} - \mathbf{z}), \frac{\lambda}{\alpha} \right)_i. \quad (10.17)$$

Chapter 11

Sparse Inversion=Neural Networks

We show that a multilayered neural network applied to least squares migration can be recast as a sparse inversion problem. The sparse inversion solution is the one that minimizes the L_1 norm of the reflectivity $\|\mathbf{m}\|_1$ subject to the data misfit function $\|\mathbf{\Gamma}\mathbf{m} - \mathbf{m}^{mig}\|_2^2 \leq \beta$, where β is a specified noise level. This provides a mathematical foundation that can be used to analyze how different neural network architectures can influence the convergence rate and the accuracy of a neural network.

11.1 Introduction

The biological processing of information in a cat's brain can be mathematically approximated as a weighted summation of input values into a vertical layer of neurons, followed by a thresholding operation (Hubel and Wiesel, 1962). Thresholding simplifies the amount of information to be processed by eliminating unimportant input values that fall below a certain threshold. This pair of operations, weighted summation and thresholding of the input values into the first layer of neurons, leads to new inputs inserted into a second layer of neurons. These new inputs are reweighted, summed, and thresholded to inject into the third column of neurons. This process is repeated again and again to form a multi-layered neural network. Such networks are now used in many areas to automatically classify and make decisions about large data sets.

Trial-and-error experimentation with neural networks over several decades generated the architecture known as deep convolutional neural networks (CNNs). The success of the current CNN architectures is evidenced by their practical applications with self-driving cars, image classification and retrieval from digital archives, and medical diagnosis from a combination of body images generated by MRIs, CAT scans, and PET scans.

Until recently, the design of effective CNN architectures was largely based on heuristic experimentation. This shortcoming largely results from the absence of a rigorous mathematical foundation for neural networks in general, and CNN in particular. In 2016, Elad (2018) proposed that CNN could be recast as finding the sparsest model \mathbf{m} under the L_1 norm subject to honoring the data misfit constraint $\|\mathbf{\Gamma}\mathbf{m} - \mathbf{m}^{mig}\|_2 \leq \beta$:

$$\begin{aligned} \text{Given :} \quad & \mathbf{\Gamma}, \mathbf{m}^{mig} \quad \text{and} \quad \mathbf{\Gamma}\mathbf{m} = \mathbf{m}^{mig} + \text{noise}, \\ \text{Find :} \quad & \mathbf{m}^* = \arg \min_{\mathbf{x}} \|\mathbf{x}\|_1 \quad \text{subject to} \quad \|\mathbf{\Gamma}\mathbf{m} - \mathbf{m}^{mig}\|_2^2 \leq \beta \end{aligned} \quad (11.1)$$

where \mathbf{m} is an $N \times 1$ input real-valued vector and $\mathbf{\Gamma}$ is an $M \times N$ matrix of real-valued weights. The scalar β is the specified noise tolerance. The iterative solution to this problem is a series of forward-modeling operations of a neural network, where each layer consists of a concatenation of a weighted summation of input values to give the vector \mathbf{z} followed by a two-sided thresholding operation denoted as $\sigma(\mathbf{z})$.

We now show that the sparse solution to the least squares migration problem reduces to the forward modeling operation of a multi-layered neural network. The final image is denoted as the sparse least squares migration (SLSM) estimate of the reflectivity distribution that honors the L_1 sparsity condition. The next section first defines the least squares migration problem without constraints, and then shows that the sparse LSM problem leads to a single-layer neural network. This is then easily generalized to the equivalence between the multilayer neural network and the multilayer LSM problem.

11.2 Theory of Sparse Least Squares Migration

The theory of standard least squares migration is first presented to establish the benchmark solution under the L_2 norm. This is then followed by the derivation of the SLSM solution for a single-layer network. The final subsection will derive the SLSM solution for a multi-layer network.

11.2.1 Least Squares Migration

The least squares problem (LSM) is defined as finding the reflectivity coefficients m_i in the $N \times 1$ vector \mathbf{m} that minimize the L_2 objective function ϵ :

$$\mathbf{m}^* = \arg \min_{\mathbf{m}} \left\{ \frac{1}{2} \|\mathbf{\Gamma} \mathbf{m} - \mathbf{m}^{mig}\|_2^2 \right\}, \quad (11.2)$$

where \mathbf{L} is the forward modeling operator, \mathbf{L}^T is the migration operator, and $\mathbf{\Gamma} = \mathbf{L}^T \mathbf{L}$ is the Hessian matrix. As discussed in Appendix 1.4, the kernel associated with the Hessian is also known as the point scatterer response of the migration operator or the migration Green's function (Schuster and Hu, 2000).

The formal solution to equation 1.6 is

$$\mathbf{m}^* = \mathbf{\Gamma}^{-1} \mathbf{m}^{mig}, \quad (11.3)$$

where it is too expensive to directly compute the inverse Hessian $\mathbf{\Gamma}^{-1}$. Instead, a gradient method gives the iterative solution

$$\mathbf{m}^{(k+1)} = \mathbf{m}^{(k)} - \alpha \mathbf{L}^T (\mathbf{\Gamma} \mathbf{m}^{(k)} - \mathbf{m}^{mig}), \quad (11.4)$$

where α is the step length, \mathbf{C} is the preconditioning matrix and $\mathbf{m}^{(k)}$ is the solution at the k^{th} iteration.

11.2.2 Sparse Least Squares Migration

The sparse least squares problem (SLSM) is defined as finding the reflectivity coefficients m_i in the $N \times 1$ vector \mathbf{m} that minimize the objective function ϵ :

$$\epsilon = \frac{1}{2} \|\mathbf{\Gamma m} - \mathbf{m}^{mig}\|_2^2 + \lambda S(\mathbf{m}), \quad (11.5)$$

where $\mathbf{\Gamma} = \mathbf{L}^T \mathbf{L}$ represents the migration Green's function (Schuster and Hu, 2000), $\lambda > 0$ is a positive scalar, $\mathbf{m}^{mig} = \mathbf{L}^T \mathbf{d}$ is the migration image computed by migrating the recorded data \mathbf{d} with the migration operator \mathbf{L}^T , and $S(\mathbf{m})$ is a sparseness function. For example, the sparseness function might be $S(\mathbf{m}) = \|\mathbf{m}\|_1$ or $S(\mathbf{m}) = \log(1 + \|\mathbf{m}\|_2^2)$.

11.2.3 Single-Layer Sparse LSM

The solution to equation 1.5 is

$$\mathbf{m}^* = \arg \min_{\mathbf{m}} \left[\frac{1}{2} \|\mathbf{\Gamma m} - \mathbf{m}^{mig}\|_2^2 + \lambda S(\mathbf{m}) \right], \quad (11.6)$$

which can be approximated by an iterative gradient descent method:

$$\begin{aligned} m_i^{(k+1)} &= m_i^{(k)} - \alpha \left[\overbrace{\mathbf{\Gamma}^T (\mathbf{\Gamma m} - \mathbf{m}^{mig})}^{\mathbf{r}=\text{residual}} + \lambda S(\mathbf{m})' \right]_i, \\ &= m_i^{(k)} - \alpha [\mathbf{\Gamma}^T \mathbf{r} + \lambda S(\mathbf{m})']_i. \end{aligned} \quad (11.7)$$

Here, $S(\mathbf{m})'_i$ is the derivative of the sparseness function with respect to the model parameter m_i and the step length is α . Vectors and matrices are, respectively, denoted by boldface lowercase and uppercase letters and Appendix 1.5 derives the gradient of the sparseness function for the special case of $S(\mathbf{x}) = \|\mathbf{x}\|_1$. Therefore, the solution in equation 1.7 can be recast as

$$m_i^{(k+1)} = \text{soft2} \left(\left[\mathbf{m}^{(k)} - \frac{1}{\alpha} \mathbf{\Gamma}^T (\mathbf{\Gamma m}^{(k)} - \mathbf{m}_{mig}) \right]_i, \frac{\lambda}{\alpha} \right), \quad (11.8)$$

which is similar to the forward modeling procedure of the one-layer neural network in Figure 1.1. That is, set $k = 0$, $\mathbf{m}^{(0)} = 0$, and let the input vector be the residual vector $\mathbf{r} = -(\mathbf{\Gamma m}^{(0)} - \mathbf{m}_{mig}) = \mathbf{m}_{mig}$ so that the first-iterate solution can be compactly represented by

$$\mathbf{m}^{(1)} = \text{softmax2}(\mathbf{z} = \mathbf{\Gamma}^T \mathbf{m}^{mig}, \lambda), \quad (11.9)$$

where $\alpha = 1$. Here, the input vector $\mathbf{r} = \mathbf{m}^{mig}$ is multiplied by the matrix $\mathbf{\Gamma}^T$ to give $\mathbf{z} = \mathbf{\Gamma}^T \mathbf{r}$, and \mathbf{z} is then thresholded and shrunk to give the output $\mathbf{a} = \text{softmax2}(\mathbf{z}, \lambda)$. If a non-negative constraint for \mathbf{z} is imposed then the softmax2 becomes that of a one-sided softmax function, also known as the Rectified Linear Unit or ReLU function. To simplify the notation, the $\text{softmax2}(\mathbf{z}, \lambda)$ or $\text{softmax}(\mathbf{z}, \lambda)$ function is replaced by $\sigma_\lambda(\mathbf{z})$ so that equation 1.10 is given by

$$\mathbf{m}^{(1)} = \sigma_\lambda(\mathbf{\Gamma}^T \mathbf{m}^{mig}). \quad (11.10)$$

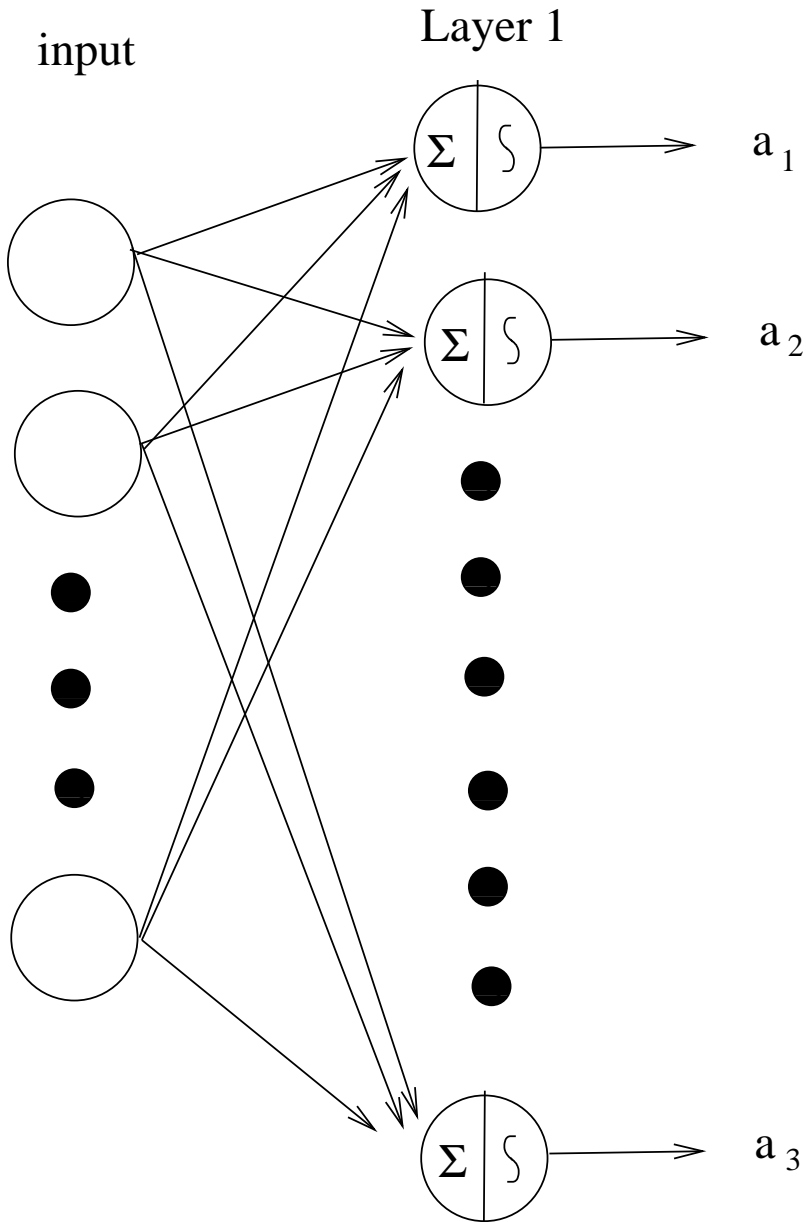


Figure 11.1: The architecture of a single-layer neural network is equivalent to the 1st iterate of the sparse solution of equation 1.6. The Σ and S symbols in the circles correspond to matrix-vector multiplication and thresholding, respectively.

11.2.4 Multilayer Sparse LSM

The multilayer sparse LSM problem is defined as the following.

$$\begin{aligned}
 &\text{Find: } \mathbf{m}_1, \mathbf{m}_2, \dots, \mathbf{m}_N \text{ such that} \\
 &\mathbf{m}_1^* = \arg \min_{\mathbf{m}_1} \left[\frac{1}{2} \|\mathbf{\Gamma}_1 \mathbf{m}_1 - \mathbf{m}^{mig}\|_2^2 + \lambda S(\mathbf{m}_1) \right], \\
 &\mathbf{m}_2^* = \arg \min_{\mathbf{m}_2} \left[\frac{1}{2} \|\mathbf{\Gamma}_2 \mathbf{m}_2 - \mathbf{m}_1\|_2^2 + \lambda S(\mathbf{m}_2) \right], \\
 &\quad \cdot \\
 &\quad \cdot \\
 &\quad \cdot \\
 &\mathbf{m}_N^* = \arg \min_{\mathbf{m}_N} \left[\frac{1}{2} \|\mathbf{\Gamma}_N \mathbf{m}_N - \mathbf{m}_{N-1}^*\|_2^2 + \lambda S(\mathbf{m}_N) \right], \tag{11.11}
 \end{aligned}$$

where $\mathbf{\Gamma}_i$ is the i th Hessian matrix in the i th layer. The first iterate solution to the above system of equations can be cast in a form similar to equation 1.10, except we have

$$\mathbf{m}_N^* \approx \sigma_\lambda (\mathbf{\Gamma}_N^T \sigma_\lambda (\mathbf{\Gamma}_{N-1}^T (\dots \sigma_\lambda (\mathbf{\Gamma}_1^T \mathbf{m}^{mig}) \dots)), \tag{11.12}$$

which is a repeated concatenation of the two forward modeling operations of a layered neural network: matrix-vector multiplies followed by a thresholding operation.

11.3 Discussion

The forward modeling for a multilayered neural network is shown to be equivalent to the first iteration of a multilayered LSM problem. According to Elad (2018), an increase in the number of layers is equivalent to the number of iterations in a gradient descent method. The output of the first layer provides the small scale, i.e. high-wavenumber, features associated with the input data. Elad classifies these features as atoms. The second layer is a weighted sum of the first-layer features, which create lower wavenumber feature maps. Elad classifies these features as molecules. The feature maps of the third layer are a weighted sum of the second-layer's features to produce even lower-wavenumber feature maps. Elad classifies these features as cellular organisms. This process proceeds to eventually reconstruct a recognizable version of the entire organism.

There are some open questions with the sparse inversion model of neural networks.

1. What is the physical meaning of each layer in a multilayered LSM? See Liu and Schuster (2018) for the meaning of feature maps in neural network least squares migration.
2. Elad (2018) points out that the greater number of CNN layers correspond to more iterations in estimating the \mathbf{m} by a gradient descent method. Does this mean faster convergence with deeper neural networks?
3. For standard LSM the Green's functions comprising $\mathbf{\Gamma}$ are not spatially invariant for general velocity models. Therefore CNN might not be appropriate for LSM because the CNN filters must be spatially invariant, i.e. convolution operators. In contrast, Liu and Schuster (2018) show that NNLSM produces useful results, at least for filtering out coherent noise.

4. How does sparse inversion incorporate the maxpooling operators? Is this a form of multiscale sparse inversion?
5. What is the sparse inversion formulation that is equivalent to skip layers used in CNNs? Is this a form of regularization such as Marquardt damping?
6. Do some of the unusual CNN architectures make sense in terms of sparse inversion?
- 7.

11.4 Appendix: Migration Green's Function

Schuster and Hu (2000) show that the poststack migration (Yilmaz, 2000) image $m(\mathbf{x})^{mig}$ in the frequency domain is computed by weighting each reflectivity value $m(\mathbf{z})$ by $\Gamma(\mathbf{x}|\mathbf{z})$ and integrating over the model-space coordinates \mathbf{z} :

$$\text{for } \mathbf{x} \in D_{model} : \quad m(\mathbf{x}) = \int_{D_{model}} d\mathbf{z} \overbrace{\int_{\mathbf{y} \in D_{data}} d\mathbf{y} \omega^4 G(\mathbf{x}|\mathbf{y})^{2*} G(\mathbf{y}|\mathbf{z})^2}^{\Gamma(\mathbf{x}|\mathbf{z})} m(\mathbf{z}) \quad (11.13)$$

where the migration Green's function $\Gamma(\mathbf{x}|\mathbf{z})$ is given by

$$\text{for } \mathbf{x}, \mathbf{z} \in D_{model} : \quad \Gamma(\mathbf{x}|\mathbf{z}) = \int_{\mathbf{y} \in D_{data}} d\mathbf{y} \omega^4 G(\mathbf{x}|\mathbf{y})^{2*} G(\mathbf{y}|\mathbf{z})^2. \quad (11.14)$$

Here we implicitly assume a normalized source wavelet in the frequency domain, and D_{model} and D_{data} represent the sets of coordinates in, respectively, the model and data spaces. The term $G(\mathbf{x}'|\mathbf{x}) = e^{i\omega\tau_{xx'}}/||\mathbf{x} - \mathbf{x}'||$ is the Green's function for a source at \mathbf{x} and a receiver at \mathbf{x}' in a smoothly varying medium¹. The traveltime $\tau_{xx'}$ is for a direct arrival to propagate from \mathbf{x} to \mathbf{x}' .

The physical interpretation of the kernel $\Gamma(\mathbf{x}'|\mathbf{x})$ is that it is the migration operator's² response at \mathbf{x}' to a point scatterer at \mathbf{x} , otherwise known as the MGF or the migration Green's function (Schuster and Hu, 2000). It is analogous to the point spread function (PSF) of an optical lens for a point light source at \mathbf{x} in front of the lens and its optical image at \mathbf{x}' behind the lens on the image plane. In discrete form, the modeling term $[\mathbf{\Gamma m}]_i$ in equation 10.4 can be expressed as

$$[\mathbf{\Gamma m}]_i = \sum_j \Gamma(\mathbf{x}_i|\mathbf{z}_j) m_j. \quad (11.15)$$

with the physical interpretation that $[\mathbf{\Gamma m}]_i$ is the migration Green's function response at \mathbf{x}_i . An alternative interpretation is that $[\mathbf{\Gamma m}]_i$ is the weighted sum of basis functions $\Gamma(\mathbf{x}_i|\mathbf{z}_j)$ where the weights are the reflection coefficients m_j and the summation is over the j index.

¹If the source and receiver are coincident at \mathbf{x} then the zero-offset trace is represented by the squared Green's function $G(\mathbf{x}|\mathbf{x})^2$.

²This assumes that the zero-offset trace is generated with an impulsive point source with a smoothly varying background velocity model, and then migrated by a poststack migration operation. It is always assumed that the direct arrival is muted and there are no multiples.

We will now consider this last interpretation and redefine the problem as finding both the weights m_i and the basis functions $\Gamma(\mathbf{x}_i|\mathbf{z}_j)$. This will be shown to be equivalent to the problem of a fully connected (FC) neural network.

11.5 Appendix: Softmax2 Function

Define the sparse inversion problem as finding the optimal value x^* that minimizes the objective function

$$\epsilon = \frac{1}{2} \|\mathbf{z} - \mathbf{x}\|_2^2 + \lambda \|\mathbf{x}\|_1, \quad (11.16)$$

where the L_1 norm demands sparsity in the solution \mathbf{x} . An example is where \mathbf{z} is a noisy $M \times N$ image such that $\mathbf{z} = \mathbf{x} + \text{noise}$, and we seek the optimal vector \mathbf{x} that satisfies equation 1.16. Here, the noisy $M \times N$ image has been flattened into the tall $MN \times 1$ vector \mathbf{z} .

The stationary condition for equation 1.16 is

$$\begin{aligned} \frac{\partial \epsilon}{\partial x_i} &= (x_i - z_i) + \lambda \frac{\partial \|\mathbf{x}\|_1}{\partial x_i}, \\ &= 0, \end{aligned} \quad (11.17)$$

where

$$\frac{\partial \|\mathbf{x}\|_1}{\partial x_i} = 1 \text{ for } x_i \geq 0; \quad \frac{\partial \|\mathbf{x}\|_1}{\partial x_i} = -1 \text{ for } x_i < 0. \quad (11.18)$$

Equations 1.17-1.18 can be combined to give the optimal x^* expressed as the two-sided ReLu function

$$x_i = \text{softmax2}(z_i, \lambda) = \begin{cases} z_i - \lambda & \text{if } z_i \geq \lambda \\ 0 & \text{if } |z_i| < \lambda \\ z_i + \lambda & \text{if } z_i < -\lambda \end{cases}. \quad (11.19)$$

More generally, the iterative-shrinkage-threshold-algorithm (ISTA) that finds \mathbf{x}^*

$$\mathbf{x}^* = \arg \min_{\mathbf{x}} \left[\frac{1}{2} \|\mathbf{z} - \mathbf{W}\mathbf{x}\|_2^2 + \lambda \|\mathbf{x}\|_1 \right], \quad (11.20)$$

is

$$x_i^{(k+1)} = \text{softmax2} \left(\mathbf{x}^{(k)} - \frac{1}{\alpha} \mathbf{W}(\mathbf{W}\mathbf{x}^{(k)} - \mathbf{z}), \frac{\lambda}{\alpha} \right)_i. \quad (11.21)$$

Chapter 12

Support Vector Machines

A support learning machine (SVM) is a supervised learning method that classifies *binary* data into two classes (Cortes and Vapnik, 1995). It has the same purpose as logistic regression in classifying data, but SVM is sometimes preferred because it is simpler in that there is no need for the design of a complicated network architecture. It can also be generalized to classifying data that has more than two classes (Bishop, 2007) and its popularity has been growing over the last two decades (see Figure 12.1).

12.1 Introduction

In the supervised learning problem of classification we are given a set of training data consisting of N feature vectors

$$(\mathbf{x}^{(i)}, y^{(i)}), \quad (12.1)$$

where $\mathbf{x}^{(i)}$ is the i^{th} feature vector with dimension $D \times 1$ and $y^{(i)} = \pm 1$ is the binary target data value for classification. For a set of two-dimensional feature vectors $\mathbf{x}^{(i)}$, the goal of SVM is to find the *best* line that separates the two classes of data, denoted as +’s and -’s, in Figure 12.2. Here, the *best* line is the dashed black one with the fattest margin width $2d$ and is equidistant between the solid black lines that are parallel to one another. This dashed line, also known as the *decision line* or *decision boundary*, is mathematically characterized by the normal vector \mathbf{w} and intercept value b , where any vector \mathbf{x} on the decision line satisfies $w_1x_1 + w_2x_2 + b = 0$. The black solid lines intersect the circled margin points $\mathbf{x}^{(i)}$ known as *support vectors* for the specified index values i . These support vectors define the points with the closest perpendicular distance to the decision boundary.

A less than optimal *decision line* is represented by the red dashed line in Figure 12.2 that also separates the two classes of data. Here, the margin thickness is skinnier than the one associated with the black lines. The skinnier the margin thickness, the easier it is to misclassify data subject to errors in the training pair $(\mathbf{x}^{(i)}, y^{(i)})$.

Once the \mathbf{w} is found after sufficient training, the SVM classifies new points $\tilde{\mathbf{x}}^{(i)}$ that are out of the training set. Figure 12.2 depicts points in a two-dimensional space, but points in a D -dimensional space can be separated by a $D - 1$ dimensional hyperplane. In this case the point \mathbf{x} on the hyperplane satisfies $\mathbf{w} \cdot \mathbf{x} + b = w_1x_1 + w_2x_2 + \dots + w_Dx_D + b = 0$.

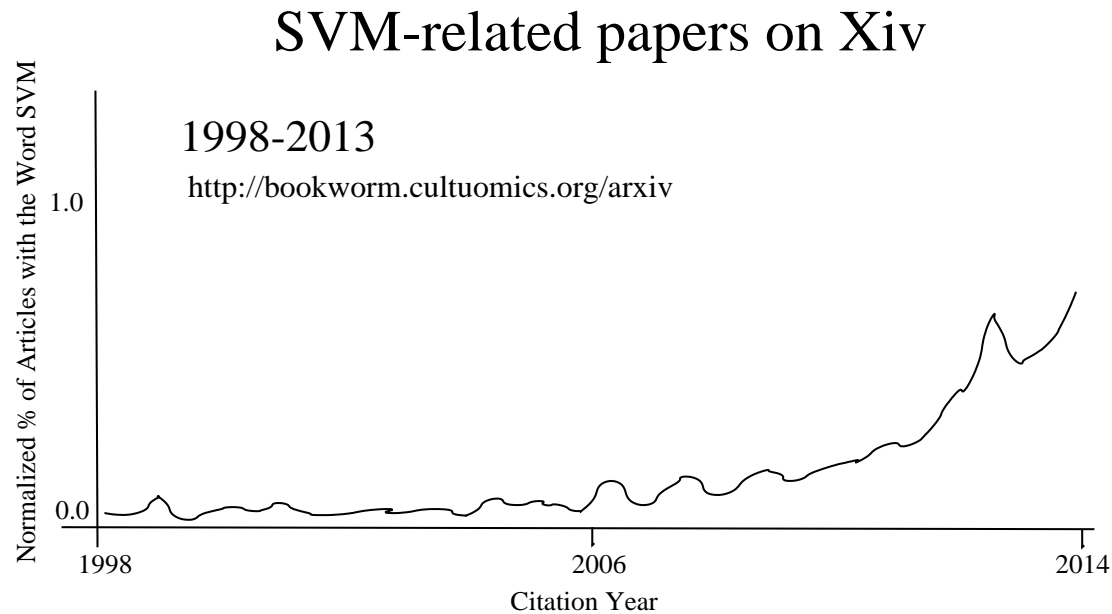


Figure 12.1: Citations in books for the word *support vector machines* plotted against calendar year.

The advantage of SVM over classification by logistic regression is that the optimal SVM line has the thickest margin, which is not necessarily the case with logistic regression when the points are linearly separable. The SVM procedure is very popular as a classification method, as evidenced by its citations in Figure 12.1 and some of the examples shown in this book. It is still one of the most effective classification methods, and can be adapted for non-linear classification.

12.1.1 SVM Applications

Many fields of science and engineering use SVM for classification, which include the following.

1. SVMs are helpful in text and hypertext categorization.
2. Classification of images can also be performed using SVMs. According to Wikipedia (https://en.wikipedia.org/wiki/Support_vector_machine) "experimental results show that SVMs achieve significantly higher search accuracy than traditional query refinement schemes after just three to four rounds of relevance feedback. This is also true of image segmentation systems, including those using a modified version SVM that uses the privileged approach as suggested by Vapnik (DeCoste, 2002).".
3. Hand-written characters can be recognized using SVM (DeCoste, 2002)..
4. According to Wikipedia (https://en.wikipedia.org/wiki/Support_vector_machine) "The SVM algorithm has been widely applied in the biological and other sciences. They have been used to classify proteins with up to 90% of the compounds classified

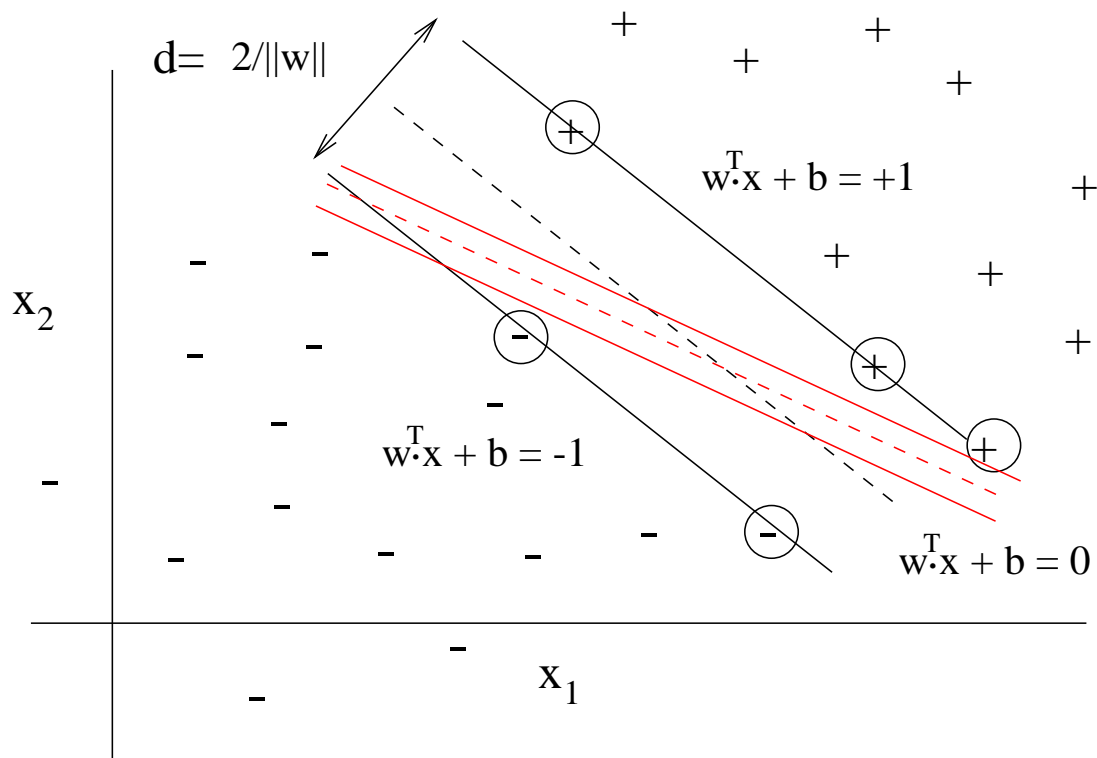


Figure 12.2: The points $\mathbf{x}^{(i)}$ denoted by the class symbols \pm are separable by a decision line. The decision line with the thickest margin is the optimal one estimated by SVM and the circled margin points $\mathbf{x}^{(i)}$ are known as *support vectors*.

correctly. Permutation tests based on SVM weights have been suggested as a mechanism for interpretation of SVM models (Gaonkar and Davatzikos, 2013). Support vector machine models can be used to identify features in the biological sciences.”.

12.2 Linear SVM Theory

Define the N feature vectors $(\mathbf{x}^{(n)}, y^{(n)})$ for $n \in [1, 2 \dots N]$, with the binary classification of $y^{(n)} = \pm 1$. We assume that the set of points $(\mathbf{x}^{(n)}, y^{(n)})$ are linearly separable so that there exists lines that separate the positive and negative classes from one another in Figure 12.2. SVM seeks the decision boundary, i.e. line, with the fattest margin thickness. This margin thickness can be defined by first defining the perpendicular distance \tilde{d} between \mathbf{x} on the decision plane in Figure 12.3 and any other point $\mathbf{x}^{(n)}$ as

$$\begin{aligned} \tilde{d} &= \frac{1}{\|\mathbf{w}\|} |\mathbf{w}^T \cdot (\mathbf{x}^{(n)} - \mathbf{x})|, \\ &= 0 \text{ for } \mathbf{x} \text{ on decision boundary} \\ &= \frac{1}{\|\mathbf{w}\|} |\mathbf{w}^T \cdot \mathbf{x}^{(n)} + b - \overbrace{(\mathbf{w}^T \cdot \mathbf{x} + b)}|, \\ &= \frac{1}{\|\mathbf{w}\|} |\mathbf{w}^T \cdot \mathbf{x}^{(n)} + b|, \end{aligned} \tag{12.2}$$

where $\hat{\mathbf{w}} = \mathbf{w}/\|\mathbf{w}\|$ is the unit vector in Figure 12.3. Note, if $\mathbf{x}^{(n)}$ is on the decision line then $\mathbf{w}^T \cdot \mathbf{x}^{(n)} + b = 0$. If $\mathbf{x}^{(n)}$ is on the same side of the decision plane that \mathbf{w} is pointing towards then $\mathbf{w}^T \cdot \mathbf{x}^{(n)} + b > 0$. If $\mathbf{x}^{(n)}$ is on the other side then $\mathbf{w}^T \cdot \mathbf{x}^{(n)} + b < 0$.

The annoying absolute value operator in equation 12.2 can be eliminated by replacing it with the product of the target value $y^{(n)}$ and $\mathbf{w}^T \cdot \mathbf{x}^{(n)} + b$:

$$\tilde{d} = \frac{1}{\|\mathbf{w}\|} y^{(n)} (\mathbf{w}^T \cdot \mathbf{x}^{(n)} + b), \tag{12.3}$$

which is always positive if $\mathbf{x}^{(n)}$ is correctly classified as the value of $y^{(n)}$. For example, if \mathbf{w} in Figure 12.2 points to the right then the product $y^{(n)} (\mathbf{w}^T \cdot \mathbf{x}^{(n)} + b) > 0$ is positive for $\mathbf{x}^{(n)}$ to the right of the decision line. This is because $y^{(n)} = +1$ and $(\mathbf{w}^T \cdot \mathbf{x}^{(n)} + b) > 0$ are also positive. For points $\mathbf{x}^{(n)}$ to the left of the decision line $y^{(n)} = -1$, then the value $y^{(n)} (\mathbf{w}^T \cdot \mathbf{x}^{(n)} + b) > 0$ is positive because both $(\mathbf{w}^T \cdot \mathbf{x}^{(n)} + b) < 0$ and $y^{(n)} = -1$ are negative.

For a given \mathbf{w} and b that cleanly separates the data, the margin thickness is given by the perpendicular distance between the decision boundary and the closest point in the data set that satisfies the following conditions:

$$\begin{aligned} &\frac{1}{\|\mathbf{w}\|} \min_{\mathbf{x}^{(n)}} [y^{(n)} (\mathbf{w}^T \cdot \mathbf{x}^{(n)} + b)] \\ &\text{subject to } y^{(n)} (\mathbf{w}^T \cdot \mathbf{x}^{(n)} + b) > 0 \quad \forall \mathbf{x}^{(n)}, \end{aligned} \tag{12.4}$$

where the inequality constraint can be described as the *clean-separation* condition.

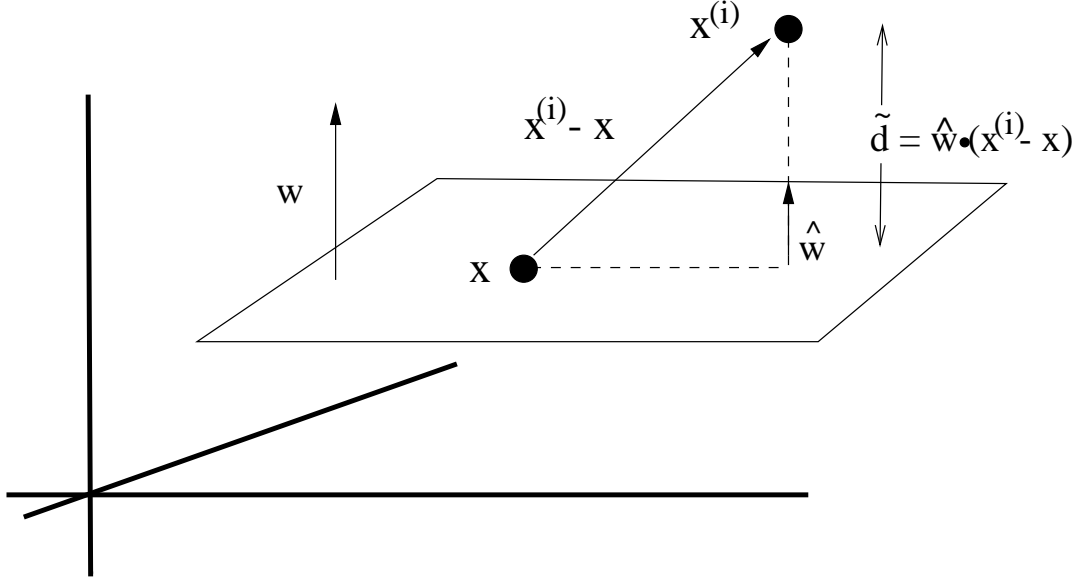


Figure 12.3: The perpendicular distance between \mathbf{x} on the plane defined by $\hat{\mathbf{w}}^T \cdot \mathbf{x} + b = 0$ and $\mathbf{x}^{(i)}$ is given by $\tilde{d} = |\hat{\mathbf{w}}^T \cdot (\mathbf{x}^{(i)} - \mathbf{x})|$, where $\hat{\mathbf{w}}$ is the unit vector perpendicular to the decision plane.

As illustrated in Figure 12.2, there are many different sets of (\mathbf{w}, b) that satisfy the above conditions. However, there is only one set of (\mathbf{w}, b) that satisfies the following conditions:

$$(\mathbf{w}^*, b^*) = \arg \max_{\mathbf{w}, b} \left\{ \frac{1}{\|\mathbf{w}\|} \min_{\mathbf{x}^{(n)}} [y^{(n)}(\mathbf{w}^T \cdot \mathbf{x}^{(n)} + b)] \right\}, \quad (12.5)$$

$$\text{subject to } y^{(n)}(\mathbf{w}^T \cdot \mathbf{x}^{(n)} + b) > 0 \quad \forall \mathbf{x}^{(n)}. \quad (12.6)$$

where the $1/\|\mathbf{w}\|$ term is outside the $\min_{\mathbf{x}^{(n)}}$ operation because it does not depend on the point $\mathbf{x}^{(n)}$. The optimal set (\mathbf{w}^*, b^*) and the support vectors on the margin boundary describe the SVM slab with the thickest width.

The ratio $\frac{1}{\|\mathbf{w}\|} \min_{\mathbf{x}^{(n)}} [y^{(n)}(\mathbf{w}^T \cdot \mathbf{x}^{(n)} + b)]$ in equation 12.5 is the same value if the elements of (\mathbf{w}, b) are rescaled as $\alpha \times (\mathbf{w}, b)$, where α is a scalar. We choose the scalar α so that the transformation $(\mathbf{w}, b) := \alpha(\mathbf{w}, b)$ transforms the inequality constraint in equation 12.6 to be

$$y^{(n)}(\mathbf{w}^T \cdot \mathbf{x}^{(n)} + b) \geq 1 \quad \forall \mathbf{x}^{(n)}, \quad (12.7)$$

where

$$y^{(n)}(\mathbf{w}^T \cdot \mathbf{x}^{(n)} + b) = 1, \quad \forall \mathbf{x}_{supp}^{(n)}, \quad (12.8)$$

for $\mathbf{x}_{supp}^{(n)}$ defined as a support vector on the margin boundary. There will be at least one support vector at each of the two margin boundaries.

The vectors $\mathbf{x}^{(n)}$ in equation 12.5 that minimize the numerator $\min_{\mathbf{x}^{(n)}} [y^{(n)}(\mathbf{w}^T \cdot \mathbf{x}^{(n)} + b)]$ are the support vectors $\mathbf{x}_{supp}^{(n)}$ on the margin boundaries. Therefore, equation 12.8 says that the numerator in equation 12.5 can be replaced by the value 1 so that the optimization problem defined by equations 12.7-12.8 can be redefined as finding (\mathbf{w}, b) such that

$$\begin{aligned} (\mathbf{w}^*, b^*) &= \arg \max_{\mathbf{w}, b} \left\{ \frac{1}{\|\mathbf{w}\|} \right\}, \\ \text{subject to } &y^{(n)}(\mathbf{w}^T \cdot \mathbf{x}^{(n)} + b) \geq 1 \quad \forall \mathbf{x}^{(n)}. \end{aligned} \quad (12.9)$$

It is algorithmically convenient to transform this maximization problem into a minimization problem by replacing $1/\|\mathbf{w}\|$ with $1/2\|\mathbf{w}\|^2$:

$$\begin{aligned} (\mathbf{w}^*, b^*) &= \arg \min_{\mathbf{w}, b} d = \frac{1}{2}\|\mathbf{w}\|^2, \\ \text{subject to } &y^{(n)}(\mathbf{w}^T \cdot \mathbf{x}^{(n)} + b) \geq 1 \quad \forall \mathbf{x}^{(n)}. \end{aligned} \quad (12.10)$$

The inequality demands that (\mathbf{w}, b) cleanly separates the training set $(\mathbf{x}^{(n)}, b)$ and the minimization equation is satisfied by the decision boundary with the shortest inverse thickness $1/d = \|\mathbf{w}\|$ of the margin. Shortest inverse thickness is, of course, equivalent to maximum thickness of the margin. A numerical solution by, e.g. quadratic programming (Nocedal and Wright, 1999; Press et al., 2007), will give the optimal values of (\mathbf{w}, b) that have the fattest margin in Figure 12.2. We can treat quadratic programming as a black box, where the algorithmic details are given in Nocedal and Wright (1999).

12.3 Nonlinear SVM

A set of training data might not be linearly separable, such as the data points shown in Figure 12.4a. In this case, a line cannot separate the different classes of data but higher-order polynomials might be able to describe the separable boundary. To determine this non-linear separation boundary we use a non-linear transformation $z_i = \phi(\mathbf{x})_i$ of the coordinates in \mathbf{x} to add extra dimensions to the solution space, just as we did for the motorcycle model in equation 2.34.

As an example, the two classes of data in Figure 12.4a can be separated by the dashed red circle. This decision boundary can be described by the transformation from 2D feature coordinates (x_1, x_2) to the 3D space of (z_1, z_2, z_3) defined by

$$(x_1, x_2) \rightarrow (z_1, z_2, z_3) = (\underbrace{\phi(\mathbf{x})_1}_{x_1}, \underbrace{\phi(\mathbf{x})_2}_{x_2}, \underbrace{\phi(\mathbf{x})_3}_{\sqrt{x_1^2 + x_2^2}}). \quad (12.11)$$

A hyperplane in the transformed space is described by the 3×1 normal vector $\tilde{\mathbf{w}} = (\tilde{w}_1, \tilde{w}_2, \tilde{w}_3)^T$ and the bias term \tilde{b} . Figure 12.4b depicts the data plotted in this transformed coordinate system, which are now separated by the horizontal plane defined by $z_3 = 3$. Once the coordinates (z_1^b, z_2^b, z_3^b) of the boundary are determined from $(\tilde{\mathbf{w}}, \tilde{b})$, then the associated decision boundary in the original space (x_1, x_2) can be found by the inverse

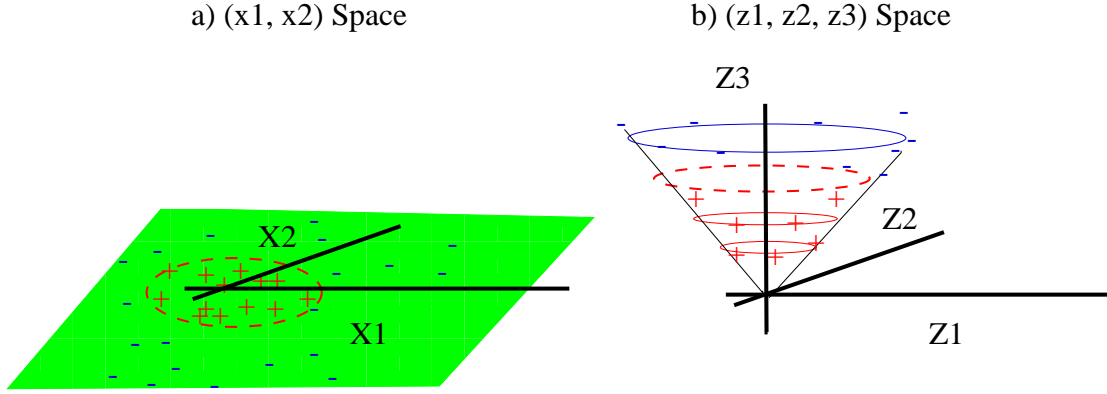


Figure 12.4: Data with a binary classification are plotted in a) the original 2D and b) transformed 3D spaces using equation 12.11. The blue symbols above the plane $z_3 = 3$ in b) are cleanly separated from the red symbols below it.

mapping from \mathbf{z} to \mathbf{x} . For convenience we did not include the affine coordinate in this transformation, but it can easily be included.

Therefore, a non-linear SVM defines a non-linear transformation such that the new feature coordinates are $z_i = \phi(\mathbf{x})_i$ and we seek the solution $(\tilde{\mathbf{w}}, \tilde{b})$ to the following optimization problem with inequality constraints.

Box 12.3.1. Primal Optimization Problem with Inequality Constraints

$$\begin{aligned}
 (\tilde{w}^*, \tilde{b}^*) &= \arg \min_{\tilde{\mathbf{w}}, \tilde{b}} d = \frac{1}{2} \|\tilde{\mathbf{w}}\|^2, \\
 &\text{subject to } y^{(n)}(\tilde{\mathbf{w}}^T \cdot \mathbf{z}^{(n)} + \tilde{b}) \geq 1.
 \end{aligned} \tag{12.12}$$

where the linear inequality constraint is with respect to the z -coordinates and the tilde indicates the parameters associated with the hyperplane in the z -space. The optimal parameters $(\tilde{\mathbf{w}}^*, \tilde{b}^*)$ define the hyperplane with the fattest margin that cleanly separates the transformed training data in z -space.

As in the original problem, a quadratic programming method can be used to find the solution.

For the example described by equation 12.11, the inverse mapping is straightforward because $x_1 = z_1^b$ and $x_2 = z_2^b$ so that the boundary in the \mathbf{x} coordinates is described by the equation $\sqrt{x_1^2 + x_2^2} = 3$ for a circle. In general, the inverse map is more complicated and an iterative gradient-search method can be used to find the mapping $\mathbf{z}^b \rightarrow \mathbf{x}^b$. For example, a steepest descent method can be used to find \mathbf{x}^b from $\mathbf{z}^b = (z_1^b, z_2^b, z_3^b \dots z_I^b)$ where

the objective function ϵ is

$$\epsilon = 1/2 \sum_{b=1}^B \sum_{i=1}^I \|z_i^b - \phi(\mathbf{x}^b)_i\|^2. \quad (12.13)$$

The steepest descent algorithm is then used to find the coordinates of \mathbf{x}^b along the boundary defined by the B boundary points \mathbf{z}^b . Here there are B boundary points and I is the dimension of the coordinates in the z -space.

The penalty in going to a higher dimension is that it can increase the computational cost by a significant amount. For example, if the feature vector is a $D \times 1 = 10^5 \times 1$ vector and the non-linear transform increases the dimension by a factor of four, then the cost of the quadratic programming solution increases from $O(D^3)$ to $O(4^3 D^3)$ algebraic operations. For D very large, this extra cost can be reduced by solving the dual Lagrangian problem as discussed in the next section.

12.4 Primal and Dual Solutions

The constrained optimization problem with inequality constraints in equation 12.10 or equation 12.12 is defined as the primal problem. Its numerical solution requires about $O(D^3)$ algebraic operations, where D is the dimension of the $D \times 1$ vector \mathbf{w} . This can be expensive for $D \gg 1$ so the alternative is to solve the dual problem.

Box 12.4.1. Dual Optimization Problem with Inequality Constraints

The dual problem is defined as finding \mathbf{w} , b and $\boldsymbol{\alpha}$ that maximize the Lagrangian $L(\mathbf{w}, b, \boldsymbol{\alpha})$:

$$L(\mathbf{w}, b, \boldsymbol{\alpha}) = \frac{1}{2} \mathbf{w}^T \cdot \mathbf{w} - \sum_{n=1}^N \alpha_n \overbrace{(y^{(n)}(\mathbf{w}^T \cdot \mathbf{x}^{(n)} + b) - 1)}^{d_n},$$

subject to $\alpha_n \geq 0$ for $n = 1, 2 \dots N$, (12.14)

for $\alpha_n > 0$ and L is the Lagrangian function discussed in Appendix 12.13. Here, N is the number of inequality constraints, α_n is the Lagrange multiplier for the n^{th} inequality equation and $\boldsymbol{\alpha} = (\alpha_1, \alpha_2 \dots \alpha_N)^T$ is the $N \times 1$ Lagrange multiplier vector. We will show that this approach only requires finding N unknowns, the number of inequality constraints in the \mathbf{x} space. For SVM the number of inequality constraints is equal to the number of feature vectors in a mini-batch of data. This can result in a significant reduction in computational costs if N is much less than the number of elements in the $D \times 1$ vector \mathbf{w} .

The starting point for computing the solution to equation 12.14 is to find \mathbf{w} and b in terms of the α_n . The resulting Lagrangian is denoted as the reduced Lagrangian. Once this is done we can pass the problem to a quadratic programming code to solve for the N values of α_i .

We have replaced the primal problem with inequality constraints in equation 12.10 or equation 12.12 with a similar one in equation 12.14, so what have we gained? Nothing is gained until we eliminate the \mathbf{w} and b in terms of the variables α_n . This can be done by setting the gradients of the Lagrangian L w.r.t. to w_i and b to zero:

$$\frac{\partial L}{\partial w_i} = w_i - \sum_{n=1}^N \alpha_n y^{(n)} x_i^{(n)} = 0 \rightarrow \mathbf{w} = \sum_{n=1}^N \alpha_n y^{(n)} \mathbf{x}^{(n)}, \quad (12.15)$$

and

$$\frac{\partial L}{\partial b} = \sum_{n=1}^N \alpha_n y^{(n)} = 0. \quad (12.16)$$

Inserting equation 12.16 into equation 12.14 gives the transformed Lagrangian:

$$\begin{aligned} L(\mathbf{w}, b, \boldsymbol{\alpha}) &= \frac{1}{2} \mathbf{w}^T \cdot \mathbf{w} - \sum_{n=1}^N \alpha_n (y^{(n)} (\mathbf{w}^T \cdot \mathbf{x}^{(n)} + b) - 1), \\ &= \frac{1}{2} \mathbf{w}^T \cdot \mathbf{w} - \sum_{n=1}^N \alpha_n y^{(n)} \mathbf{w}^T \cdot \mathbf{x}^{(n)} + \sum_{n=1}^N \alpha_n - \overbrace{b \sum_{n=1}^N \alpha_n y^{(n)}}^{\boldsymbol{\alpha}^T \mathbf{y} = 0 \text{ by eq. 12.16}}, \\ &= \sum_{n=1}^N \alpha_n + \frac{1}{2} \mathbf{w}^T \cdot \mathbf{w} - \sum_{n=1}^N \alpha_n y^{(n)} \mathbf{w}^T \cdot \mathbf{x}^{(n)}, \end{aligned} \quad (12.17)$$

where b is now eliminated.

Box 12.4.2. Reduced Dual Optimization Problem with Inequality Constraints

The \mathbf{w} in equation 12.17 can be eliminated by plugging $\mathbf{w} = \sum_{n=1}^N \alpha_n y^{(n)} \mathbf{x}^{(n)}$ from equation 12.15 into equation 12.17 to get the *reduced* Lagrangian:

$$\begin{aligned} L(\mathbf{w}, b, \boldsymbol{\alpha}) &= \sum_{n=1}^N \alpha_n - \frac{1}{2} \sum_{n=1}^N \sum_{m=1}^N y^{(n)} y^{(m)} \alpha_n \alpha_m \mathbf{x}^{(n)T} \cdot \mathbf{x}^{(m)}, \\ \alpha_n &\geq 0; \quad \boldsymbol{\alpha}^T \mathbf{y} = 0, \end{aligned} \quad (12.18)$$

where the only unknowns are the N variables α_n that maximize $L(\mathbf{w}, b, \boldsymbol{\alpha})$ subject to the inequality constraints. Here, N is also the number of feature vectors in the training set which can be small if the original training data set is broken up into mini-batches. In this case, solving the reduced dual optimization problem is much more efficient if the dimension of the $D \times 1$ feature vector is huge compared to the number N of feature vectors in a mini-batch. A dramatic SVM example that demands the more efficient dual optimization approach is in medical diagnosis where each input $D \times 1$ vector can be a tomographic scan with millions of pixel per scan (Gaonkar and Davatzikos, 2013).

Multiplying the reduced lagrangian by -1 transforms it to a minimization problem w.r.t. α_i :

$$\min_{\alpha} \frac{1}{2} \alpha^T \overbrace{\begin{bmatrix} y^{(1)}y^{(1)}\mathbf{x}^{(1)T} \cdot \mathbf{x}^{(1)} & y^{(1)}y^{(2)}\mathbf{x}^{(1)T} \cdot \mathbf{x}^{(2)} & \dots & y^{(1)}y^{(N)}\mathbf{x}^{(1)T} \cdot \mathbf{x}^{(N)} \\ y^{(1)}y^{(2)}\mathbf{x}^{(2)T} \cdot \mathbf{x}^{(1)} & y^{(2)}y^{(2)}\mathbf{x}^{(2)T} \cdot \mathbf{x}^{(2)} & \dots & y^{(2)}y^{(N)}\mathbf{x}^{(2)T} \cdot \mathbf{x}^{(N)} \\ \dots & \dots & \dots & \dots \\ y^{(N)}y^{(1)}\mathbf{x}^{(N)T} \cdot \mathbf{x}^{(1)} & y^{(N)}y^{(2)}\mathbf{x}^{(N)T} \cdot \mathbf{x}^{(2)} & \dots & y^{(N)}y^{(N)}\mathbf{x}^{(N)T} \cdot \mathbf{x}^{(N)} \end{bmatrix}}^{\text{quadratic coefficients}} \alpha + (-\mathbf{1}^T)\alpha \quad (12.19)$$

$$\text{subject to} \quad \mathbf{y}^T \cdot \alpha = 0 \quad \text{and} \quad \alpha_n \geq 0 \quad \forall n. \quad (12.20)$$

The $N \times N$ matrix of dot products is known as the Gram matrix, where the optimal solution is found by a quadratic programming method with a computational cost as high as $O(N^3)$ for inverting this matrix.

If the non-linear SVM method is used then we are seeking the $(\tilde{\mathbf{w}}, \tilde{b})$ that gives rise to the same type of Gram matrix seen in equation 12.19, except $\mathbf{x}^{(n)T} \cdot \mathbf{x}^{(m)}$ is replaced by $\mathbf{z}^{(m)T} \cdot \mathbf{z}^{(m)}$:

$$\min_{\alpha} \frac{1}{2} \alpha^T \overbrace{\begin{bmatrix} y^{(1)}y^{(1)}\mathbf{z}^{(1)T} \cdot \mathbf{z}^{(1)} & y^{(1)}y^{(2)}\mathbf{z}^{(1)T} \cdot \mathbf{z}^{(2)} & \dots & y^{(1)}y^{(N)}\mathbf{z}^{(1)T} \cdot \mathbf{z}^{(N)} \\ y^{(1)}y^{(2)}\mathbf{z}^{(2)T} \cdot \mathbf{z}^{(1)} & y^{(2)}y^{(2)}\mathbf{z}^{(2)T} \cdot \mathbf{z}^{(2)} & \dots & y^{(2)}y^{(N)}\mathbf{z}^{(2)T} \cdot \mathbf{z}^{(N)} \\ \dots & \dots & \dots & \dots \\ y^{(N)}y^{(1)}\mathbf{z}^{(N)T} \cdot \mathbf{z}^{(1)} & y^{(N)}y^{(2)}\mathbf{z}^{(N)T} \cdot \mathbf{z}^{(2)} & \dots & y^{(N)}y^{(N)}\mathbf{z}^{(N)T} \cdot \mathbf{z}^{(N)} \end{bmatrix}}^{\text{quadratic coefficients}} \alpha + (-\mathbf{1}^T)\alpha \quad (12.21)$$

$$\text{subject to} \quad \mathbf{y}^T \cdot \alpha = 0 \quad \text{and} \quad \alpha_i \geq 0. \quad (12.22)$$

Here, we have to construct $\mathbf{z}^{(m)} \forall m$ and then use $\mathbf{z}^{(m)}$ to compute the dot products. However, this is impractical if $\mathbf{z}^{(m)}$ is of large or infinite dimension. The remedy is to specify the analytical form of the dot product as a kernel $k(\mathbf{x}, \mathbf{x}') = \mathbf{z}(\mathbf{x})^T \cdot \mathbf{z}(\mathbf{x}')$, as will be discussed in the next section.

12.5 Kernel Methods

The problem with the non-linear SVM method is that the choice of a very high-order transformation $z_i = \phi(\mathbf{x})$ will increase the number of unknowns and therefore increase the computational cost. It also can lead to overfitting of the training data if a highly oscillatory polynomial is selected.

To overcome these two problems we can reformulate the non-linear SVM problem in the dual space by specifying an infinite dimensional kernel function $k(\mathbf{x}, \mathbf{x}') = \mathbf{z}(\mathbf{x})^T \cdot \mathbf{z}(\mathbf{x}')$. In

this case, equation 12.21 becomes the Gram matrix:

$$\min_{\alpha} \frac{1}{2} \alpha^T \begin{bmatrix} y^{(1)}y^{(1)}k(\mathbf{x}^{(1)}, \mathbf{x}^{(1)}) & y^{(1)}y^{(2)}k(\mathbf{x}^{(1)}, \mathbf{x}^{(2)}) & \dots & y^{(1)}y^{(N)}k(\mathbf{x}^{(1)}, \mathbf{x}^{(N)}) \\ y^{(2)}y^{(1)}k(\mathbf{x}^{(2)}, \mathbf{x}^{(1)}) & y^{(2)}y^{(2)}k(\mathbf{x}^{(2)}, \mathbf{x}^{(2)}) & \dots & y^{(2)}y^{(N)}k(\mathbf{x}^{(2)}, \mathbf{x}^{(N)}) \\ \dots & \dots & \dots & \dots \\ y^{(N)}y^{(1)}k(\mathbf{x}^{(N)}, \mathbf{x}^{(1)}) & y^{(N)}y^{(2)}k(\mathbf{x}^{(N)}, \mathbf{x}^{(2)}) & \dots & y^{(N)}y^{(N)}k(\mathbf{x}^{(N)}, \mathbf{x}^{(N)}) \end{bmatrix} \alpha + (-\mathbf{1}^T)\alpha. \quad (12.23)$$

The stationary conditions in equation 12.17 become

$$\frac{\partial L}{\partial \tilde{w}_i} = \tilde{w}_i - \sum_{n=1}^{N_z} \alpha_n y^{(n)} z_i^{(n)} = 0 \rightarrow \quad \tilde{\mathbf{w}} = \sum_{n=1}^{N_z} \alpha_n y^{(n)} \mathbf{z}^{(n)}, \quad (12.24)$$

and

$$\frac{\partial L}{\partial \tilde{b}} = \sum_{n=1}^{N_z} \alpha_n y^{(n)} = 0. \quad (12.25)$$

Here \tilde{b} and $\tilde{\mathbf{w}}$ define, respectively, the bias and $D_z \times 1$ hyperplane normal vector in the z -space.

There is a huge computational savings in explicitly specifying the kernel $k(\mathbf{x}, \mathbf{x}')$ in equation 12.27 rather than computing $\mathbf{z}(\mathbf{x})^T \cdot \mathbf{z}(\mathbf{x}')$ in equation 12.21. If \mathbf{z} is an infinite-dimensional vector \mathbf{z} then its dot product $\mathbf{z}(\mathbf{x})^T \cdot \mathbf{z}(\mathbf{x}')$ cannot be practically computed. In contrast, if $k(\mathbf{x}, \mathbf{x}')$ is analytically specified as a, e.g. Gaussian kernel $k(\mathbf{x}, \mathbf{x}') = e^{-\|\mathbf{x} - \mathbf{x}'\|^2}$, then the kernel $k(\mathbf{x}, \mathbf{x}')$ in equation 12.27 can easily be computed for any specified pair of vectors \mathbf{x} and \mathbf{x}' .

As an example, take the scalar case where

$$\begin{aligned} k(x', x) &= e^{-(x' - x)^2}, \\ &= e^{-x^2} e^{-x'^2} e^{-2xx'}, \\ &= e^{-x^2} e^{-x'^2} \sum_k^{\infty} \frac{2x^k x'^k}{k!}, \\ &= e^{-x^2} e^{-x'^2} \overbrace{(1 + 2xx' + x^2 x'^2 + \dots)}^{Taylor \ series}, \\ &= \overbrace{(e^{-x^2} (1, \sqrt{2}x, x^2, \dots))}^{\mathbf{z}(x)} \overbrace{(e^{-x'^2} (1, \sqrt{2}x', x'^2, \dots))}^{\mathbf{z}(x')} \quad (12.26) \end{aligned}$$

Here, the infinite dimensional vector $\mathbf{z}(x)$ and its inner product with $\mathbf{z}(x')$ cannot be practically computed, but the computation of the kernel $k(\mathbf{x}, \mathbf{x}') = e^{-\|\mathbf{x} - \mathbf{x}'\|^2}$ is trivial.

The kernel $k(\mathbf{x}, \mathbf{x}')$ must satisfy two properties (Press et al., 2007) in order to be used as a substitute for $\mathbf{z}(\mathbf{x}') \cdot \mathbf{z}(\mathbf{x})$ in equation 12.21:

- $k(\mathbf{x}, \mathbf{x}')$ must be symmetric such that $k(\mathbf{x}, \mathbf{x}') = k(\mathbf{x}', \mathbf{x})$.

- The Gram matrix must be positive semi-definite. Symmetry for the Gaussian kernel is proven by inspection and the positive semi-definite property can be empirically tested by using an example matrix.

Box 12.5.1. SVM Algorithm

In summary, the non-linear SVM algorithm with an infinite-dimensional kernel is the following.

1. Specify the functional form of the kernel, e.g. $k(\mathbf{x}^{(n)}, \mathbf{x}^{(m)}) = e^{-\beta \|\mathbf{x}^{(n)} - \mathbf{x}^{(m)}\|^2}$, and compute the $N \times N$ Gram matrix in equation 12.24. Here, β is a constant specified by the user where large values of β indicate that the main influence of this basis function is only around points $\mathbf{x}^{(n)}$ and $\mathbf{x}^{(m)}$ that are close neighbors to one another. Use quadratic programming (QP) or the Lagrangian barrier method (Nocedal and Wright, 1999) method to solve for $\alpha_n \forall n$. If the number of feature vectors is huge, then the entire data set is broken up into small mini-batches and the non-linear optimization method is used to inexpensively invert the mini-batch of data to find (\mathbf{w}, b) ; this is computationally inexpensive because the number of mini-batch feature vectors is small. This solution is then the starting model for inverting the next mini-batch of data, and the procedure is repeated until all the mini-batches are used.
2. Define the feature vector \mathbf{x} so that its predicted classification value y is given by $\text{sign}(\tilde{\mathbf{w}} \cdot \mathbf{z}(\mathbf{x}) + \tilde{b})$. Substituting $\tilde{\mathbf{w}}$ from equation 12.24 gives the predicted classification value:

$$\begin{aligned} y &= \text{sign}\left(\sum_{n=1}^N \alpha_n y^{(n)} \mathbf{z}(\mathbf{x})^T \cdot \mathbf{z}(\mathbf{x})^{(n)} + \tilde{b}\right), \\ &= \text{sign}\left(\sum_{n \in B_{\text{support}}} \alpha_n y^{(n)} k(\mathbf{x}, \mathbf{x}^{(n)}) + \tilde{b}\right), \end{aligned} \quad (12.27)$$

where B_{support} is the set of indices associated with the support vectors where $\alpha_i \neq 0$.

The value of \tilde{b} in equation 12.27 is obtained by noting that the support vector $\mathbf{z}(\mathbf{x}_i)$ for $i \in B_{\text{support}}$ is associated with the non-zero Lagrange multiplier $\alpha_n \neq 0$ that satisfies the constraint equation

$$\begin{aligned} y^{(i)} &= \tilde{\mathbf{w}}^T \cdot \mathbf{z}(\mathbf{x}^{(i)}) + \tilde{b}, \\ &= \sum_{n \in B_{\text{support}}} \alpha_n y^{(n)} \mathbf{z}(\mathbf{x}^{(n)})^T \cdot \mathbf{z}(\mathbf{x}^{(i)}) + \tilde{b} \quad \text{for } i \in B_{\text{support}}, \end{aligned} \quad (12.28)$$

where equation 12.24 is used for $\tilde{\mathbf{w}}$. Substituting $k(\mathbf{x}^{(n)}, \mathbf{x}^{(i)}) = \mathbf{z}(\mathbf{x}^{(n)})^T \cdot \mathbf{z}(\mathbf{x}^{(i)})$ and equation 12.24 for \mathbf{w} gives

$$\sum_{n \in B_{\text{support}}} \alpha_n y^{(n)} k(\mathbf{x}^{(i)}, \mathbf{x}^{(n)}) + \tilde{b} = y^{(i)}. \quad (12.29)$$

This equation is now solved for in terms of \tilde{b} . To get a more robust estimate of \tilde{b} , compute the average of the different support vectors to get \bar{b} :

$$\bar{b} = \frac{1}{N_{\text{support}}} \sum_{i \in B_{\text{support}}} [y^{(i)} - \sum_{n \in B_{\text{support}}} \alpha_n y^{(n)} k(\mathbf{x}^{(i)}, \mathbf{x}^{(n)})], \quad (12.30)$$

where N_{support} is the number of support vectors in the dual space where $\alpha_i \neq 0$.

3. All of the feature vectors in the validation set can now be classified with equations 12.27 and 12.30. An example is given in Figure 12.5.

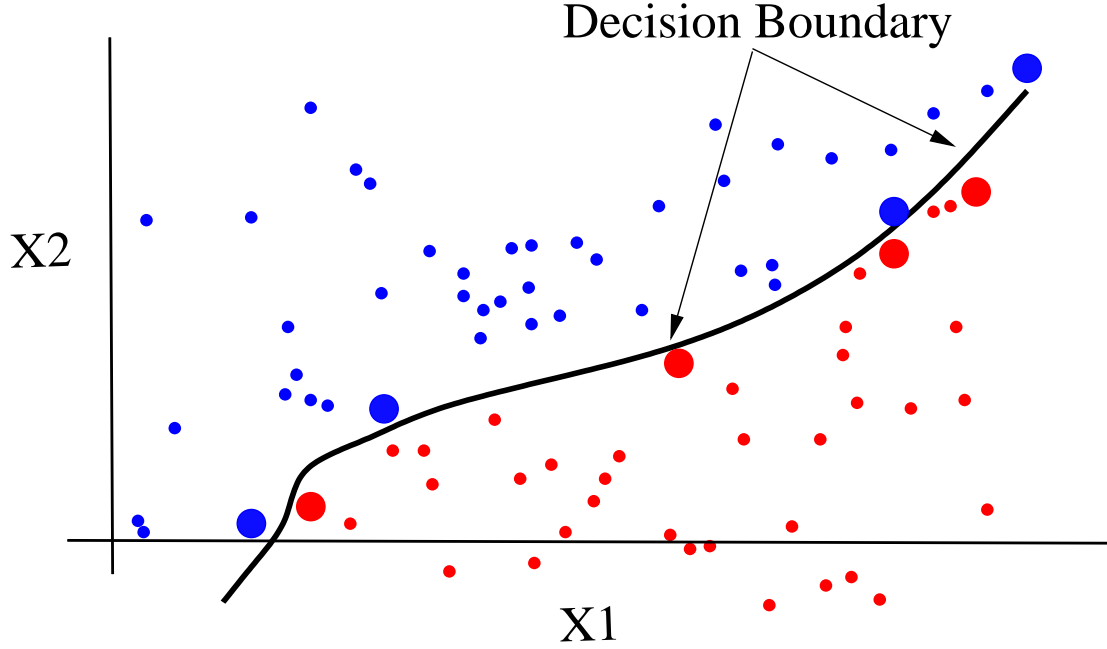


Figure 12.5: Feature points in (x_1, x_2) space with the black-decision boundary computed by the Gaussian-kernel method in the dual space. The support points are the large filled circles and the input examples are classified as either blue or red points. Image redrawn from the Youtube video of Dr. AbuMostafa.

12.6 Numerical Examples

Recall that seismic migration is an imaging method that identifies the geometries and strengths of subsurface reflectors from seismic data; the final result is the migration image $m(\mathbf{x})$. For example, seismic data recorded on the top horizontal surface were migrated to give the large amplitude values of $m(\mathbf{x})$ in Figure 12.6a, which denote the locations of reflecting interfaces. Some of the large amplitude values are artifacts from the migration method and do not indicate an actual reflector. A simple description of seismic migration is in Appendix 12.15 and more details are in Yilmaz (2001). We will now use the SVM method to denoise migration images computed from synthetic seismic data.

The goal is to use SVM to distinguish noise from the yellow signal in the Figure 12.6a migration image. The elliptical features are typically due to aliasing artifacts in the migration image and can be identified as noise by a trained interpreter. The SVM can then be trained to distinguish noise from signal in the classified images, and then it can be used to identify noise in the rest of the data. Once identified, a suitable filtering method can be used to suppress the noisy artifacts in the migration image.

To train the SVM, the first step is to define a small 5×5 window centered at the i^{th} pixel.

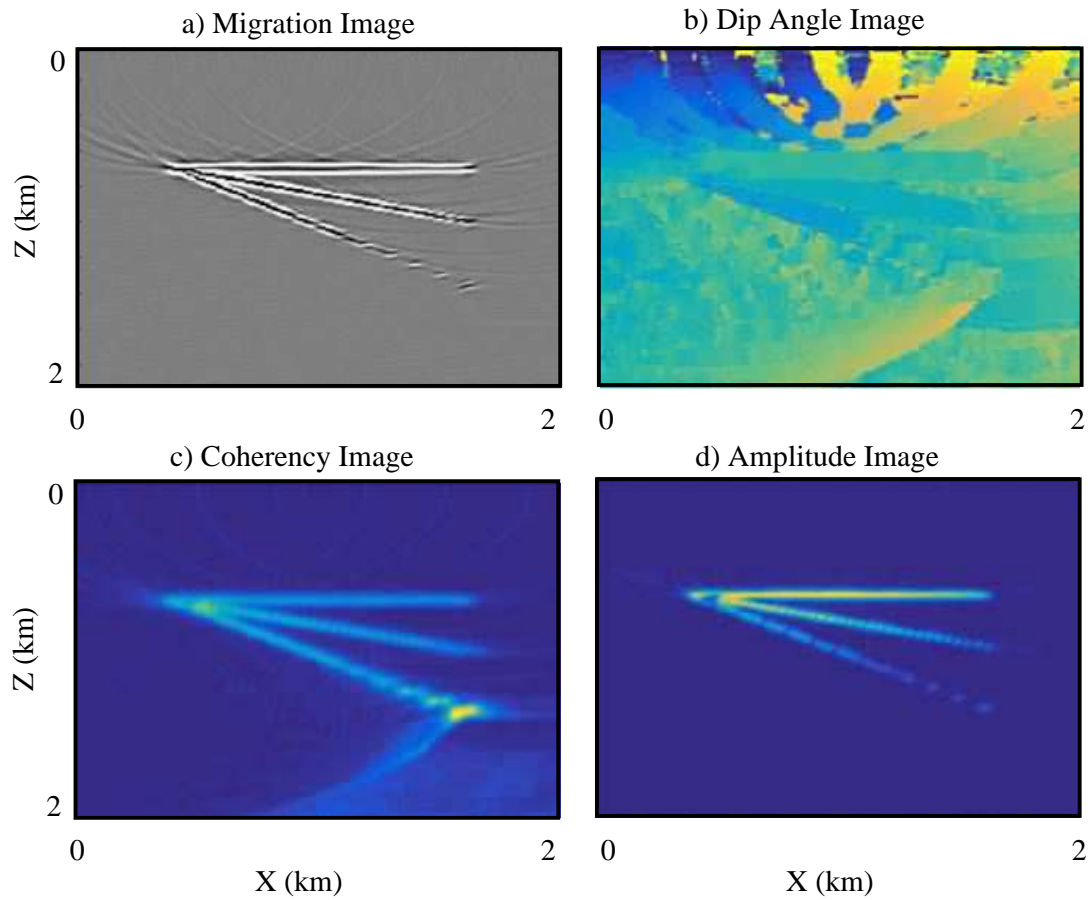


Figure 12.6: Images of the a) raw migration section, b) dominant dip angle at each pixel, c) migration coherency, and d) amplitudes. The yellow areas in the Figure 12.7c migration image a) correspond to the label of signal ($y = 1$) and the other areas are labeled noise ($y = -1$). Images courtesy of Yuqing Chen.

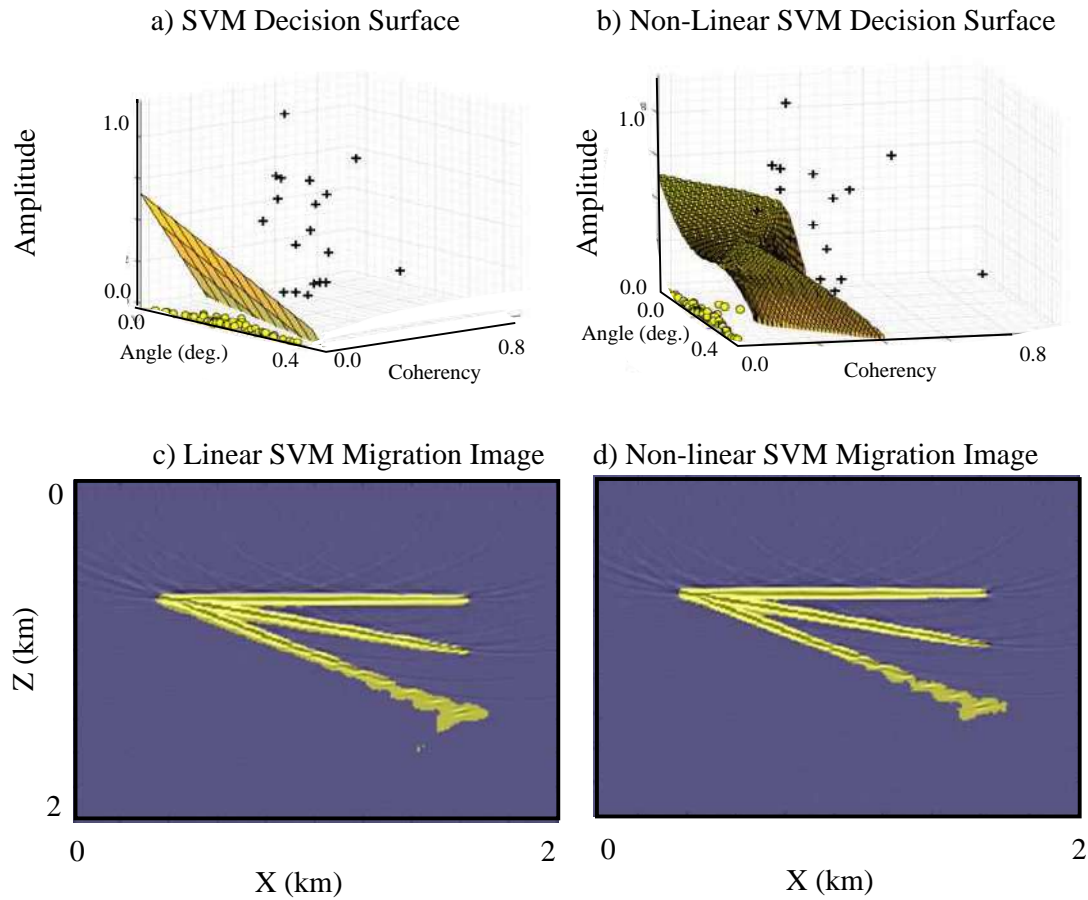
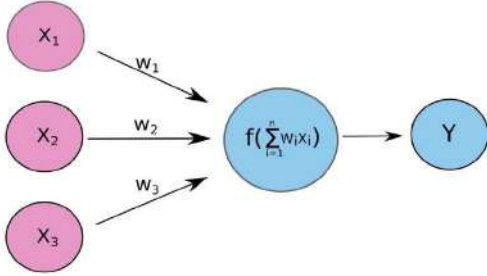


Figure 12.7: Decision boundaries computed by a) linear SVM and b) non-linear SVM with regularization. The corresponding migration images are directly below the feature plots. Here, the yellow colors denote signal and the black colors denote noise. The amplitudes classified as noise are suppressed by muting and the resulting migration images are shown in c) and d).

a) One-Layer Neural Network



b) Two-layer Neural Network

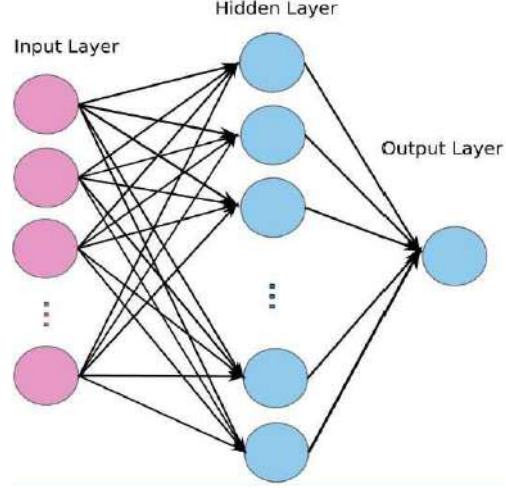


Figure 12.8: Architectural diagrams for a) one- and b) two-layer neural networks. The one-layer one-node network diagram is for the logistic network and the two-layer multi-node architecture is for the neural network used in the examples. Images courtesy of Yuqing Chen.

Three skeletonized characteristics are then computed for the image in this small window: dominant dip angle, coherency and maximum amplitude as described in Appendix 12.15. The user classifies each point in the training migration image as either noise or signal. The computer computes the three skeletal characteristics $(x_1^{(i)}, x_2^{(i)}, x_3^{(i)})$ at each point of $m(\mathbf{x})$ and assigns the classification value $y^{(i)}$. Therefore, the input feature vectors are the 4×1 vectors $(x_1^{(i)}, x_2^{(i)}, x_3^{(i)}, y^{(i)})$. For the migration examples, only 70 image points are selected for training from the 201×201 migration image $m(\mathbf{x})$, which means that only 0.17 % of the original migration image is used for training.

What should we use for the skeletal characteristics of $m(\mathbf{x})$ that can be used to distinguish noise from signal? The answer is to use intuition and experience to identify the most significant characteristics that distinguish noise from signal. For example, we recognize that migration artifacts should have weak coherency ϕ_i , large dip angles θ_i , and weak amplitudes A_i at the i^{th} pixel, while the reflection signal should mostly be characterized by strong coherency, modest dip angles, and strong amplitudes. As an example, Figure 12.6 plots the ϕ_i values at all pixels where weak coherency is indicated by the deep-blue color. Therefore we use $(\theta_i, \phi_i, A_i, y^{(i)})$ as the skeletonized characteristics of the migration image to distinguish noise from signal. Other characteristics might be more effective and should be used if needed for more accuracy.

The input training set is now defined as $(\mathbf{x}^{(i)}, y^{(i)}) = (\theta_i, \phi_i, A_i, y^{(i)})$ for 70 points in the migration image in Figure 12.6a. Each pixel in the training migration images is manually classified as either signal (+1) or noise (−1). The SVM procedure is then used to find the 3×1 vector $\mathbf{w} = (w_1, w_2, w_3)$ and the bias b that cleanly separate the labeled noise and signal. This generates a hyperplane in feature space as shown in Figure 12.7a, where the

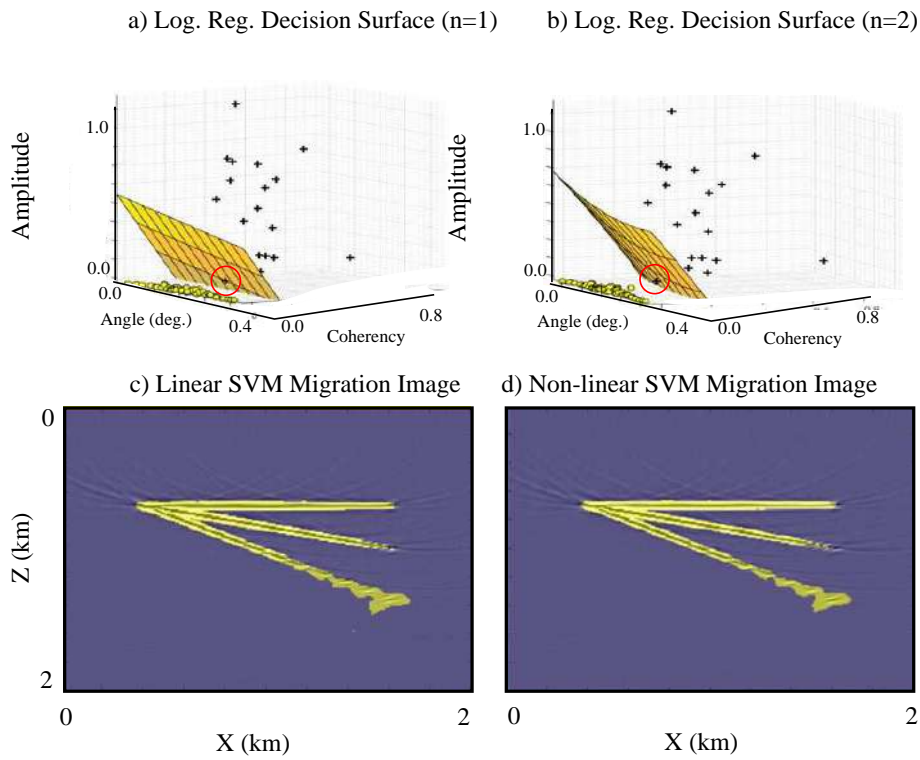


Figure 12.9: Same as Figure 12.7 except logistic regression with a)-c) order $n = 1$ and b)-d) $n = 2$ is used for classification of the features. Notice the misclassified point denoted by a red circle. Images courtesy of Yuqing Chen.

yellow colored plane defines the decision hyperplane in 3D. Once the \mathbf{w} and b are found then the other parts of the migration image (i.e., out-of-the-training-set data) are automatically labeled by determining the sign of $\mathbf{w} \cdot \mathbf{x}^{(n)} + b$. If the amplitude of the automatically labeled image is noise then that amplitude can later be filtered by some method.

The automatically labeled features are shown in Figure 12.7c, where yellow indicates signal and deep blue indicates noise. In comparison, when regularization is included in the SVM method the surface is shown in Figure 12.7b, with the resulting labeled signal denoted by the yellow portions.

As a comparison, logistic regression with orders $n = 1$ and $n = 2$ are used to classify the same training set used with SVM. See the diagram on the left of Figure 12.8 for the architecture of the logistic regression. In this case $n = 1$ means the input is a 3×1 feature vector (x_1, x_2, x_3) while $n = 2$ means that the input is the 9×1 vector: $(x_1, x_2, x_3, x_1^2, x_2^2, x_3^2, x_1x_2, x_1x_3, x_2x_3)$. The results are shown in Figure 12.9, where there is not much of a difference in any of the images.

These results are to be compared to those in Figure 12.10 where the features are classified by a fully connected neural network with two layers and 15 nodes in the hidden layer. The neural network appears to provide a similar classification of image points compared to logistic regression, even though it misclassified a data point.

Finally, a realistic migration image is used as the input data to get the three features of maximum dip angle, coherence, and amplitude for each pixel. The signals in the images are colored yellow in Figure 12.11 as classified by a) two-node logistic regression, b) a two-layer neural network, c) SVM with a Gaussian kernel without regularization, and d) SVM with a Gaussian kernel with regularization. The SVM image w/o regularization in Figure 12.11c is judged to be the best result because it picks out most of the steeply dipping interfaces in the red box. This suggests that the regularization strategy should be improved to not exclude steep dips.

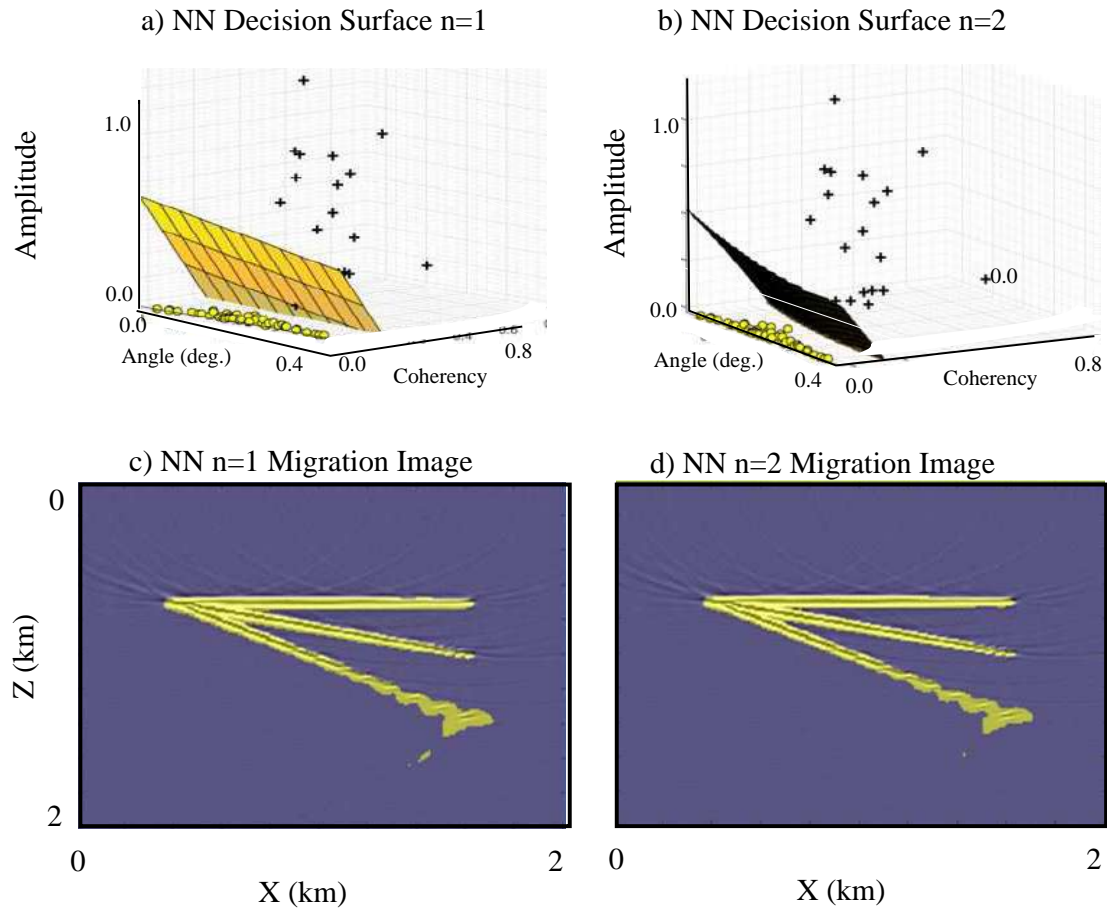
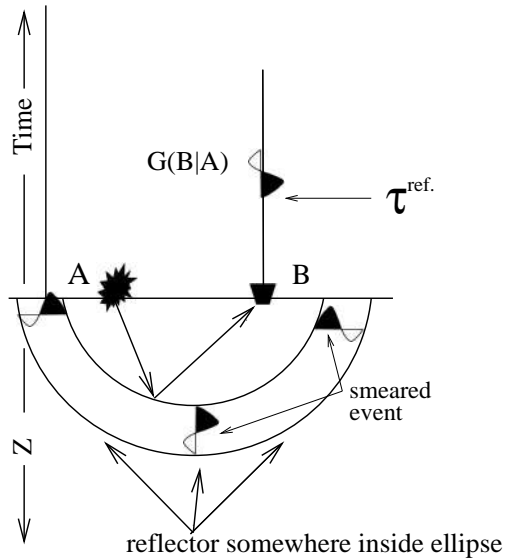


Figure 12.10: Same as Figure 12.7 except a neural network with a)-c) $n=1$ and b)-d) $n=2$ layers are used for classification. Images courtesy of Yuqing Chen.

Migration: Smear and Sum Refl. Amp. Along Ellipses

a) One-trace migration.



b) Two-trace migration.

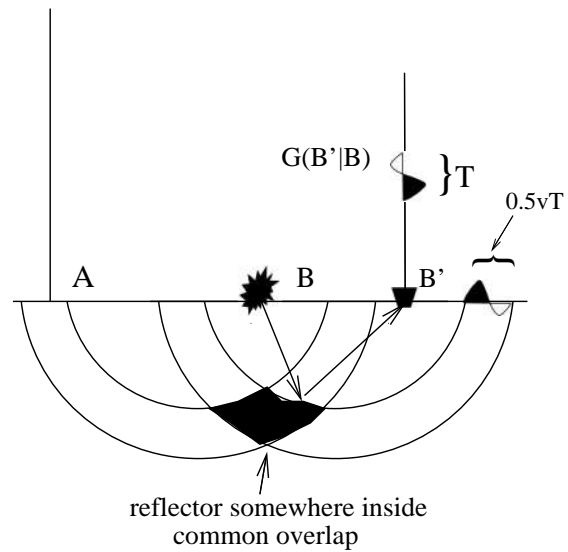


Figure 12.11: Migration images classified as signal (yellow) by a) logistic regression of order two, b) a neural network with 2 layers and 15 nodes in the hidden layer, c) SVM with a Gaussian kernel w/o regularization and d) SVM with a Gaussian kernel with regularization. Images courtesy of Yuqing Chen.

12.6.1 MATLAB Codes

The migration images in Figures 12.6-12.11 were created by MATLAB codes, with the main code fragments given below. Before they are executed the user selects 50 points in the migration image that are migration artifacts and then selects 50 points that are reflectors. These classified points are then used to train the algorithms. This lab is in the Computational labs directory *LAB1/Chapter.Book.SVM/Chapter.SVM1/lab.html*.

The main fragment of the logistic regression code is give below.

```

                                MATLAB Logistic Regression Code (Yuqing Chen)

[m,n]=size(X);    % Get the size of training example
X2=[ones(m,1) X]; % Add intercept term to the training set

disp('Calculating decision boundary')
maxiter=500;      % Iteration numbers
theta=rand(n+1,1)-0.5; % Initialize the model parameters
step=10;          % Set the step length

for iter=1:maxiter
    [cost, grad] = costFunction2(theta, X2, Y); % Compute data misfit (cost) and gradient (grad)
    if(mod(iter,20)==0) % Show the data misfit at every 20 iterations
        fprintf('iter= %d res = %f\n',iter,cost)
    end
    theta2=theta-step.*grad; % Update the model parameters with a
                             % trial step length
    [cost1, grad_temp] = costFunction2(theta2, X2, Y); % Compute the new misfit (cost1)
                                                         % and gradient (grad_temp)
                                                         % fprintf('res1 = %f\n',cost1)

    if(cost1>cost) % If the new misfit (cost1) is larger than the previous misfit (cost),
                  % then we reduce the step length and try again
        step=step*0.8; % Reduce the step length
        theta2=theta-step.*grad; % Update the model parameters with reduced trail step length
        [cost1, grad_temp] = costFunction2(theta2, X2, Y); % Compute the new misfit
        fprintf('step = %f, res1 = %f\n',step,cost1) % Print the step length and data misfit
    end % When the new misfit is smaller than the
        %misfit at the previous iteration (cost1 < cost), we update the model parameter

    theta=theta2;
end
%
%
disp('Display decision boundary')
[X_surf1,Y_surf1]=meshgrid(min(cohe_vec2):0.01:max(cohe_vec2),min(angl_vec2):0.01:max(cohe_vec2));
Z_surf1=-(theta(1)+theta(2).*X_surf1+theta(3).*Y_surf1)./theta(4); % compute the hyperplane
% predicted by the logistic
% regression
hold on
surf(X_surf1,Y_surf1,Z_surf1) % Display the hyperplane

```

The main fragment of the neural network code is give below.

```

MATLAB Neural Network Code (Yuqing Chen)

lamda=0.0; step=10; maxiter=500; % lambda: regularization term (higher lambda can avoid
                                % over-fitting but will lost accuracy)
for iter=1:maxiter
    [cost,grad] = nnCostFunction(nn_params, input_layer_size, hidden_layer_size, ...
                                num_labels, X2, Y, lamda); % nnCostFunction is the kernel used to
                                                            % compute the data misfit and gradient
    if(mod(iter,50)==0||iter==1)
        fprintf('iter= %d, res = %f\n',iter,cost)
    end
    nn_params2=nn_params-step*grad;
    [cost1,grad_temp] = nnCostFunction(nn_params2, input_layer_size, hidden_layer_size, ...
                                      num_labels, X2, Y, lamda);
    while(cost1>cost)
        step=step*0.8;
        nn_params2=nn_params-step*grad;
        [cost1,grad_temp] = nnCostFunction(nn_params2, input_layer_size, hidden_layer_size, ...
                                          num_labels, X2, Y, lamda);
        fprintf('step = %f, res1 = %f\n',step,cost1)
    end
    nn_params=nn_params2;
end

```

The main fragment of the SVM code is give below.

```

MATLAB SVM Kernel Code (Yuqing Chen)

%%%%%%%%%%%% Make decesion boundary by SVM
C = 1; % The C parameter is a positive value that controls the
        % penalty for misclassified training examples. A large
        % C parameter tells the SVM to try to classify all the
        % examples correctly. C plays a role similar to
        % 1/lambda, where lambda is the regularization parameter
sigma = 0.1; % sigma controls the shape of gaussian function. In other
              % words, how fast the similarity metric decrease

% "svmTrain" is the matlab function used for SVM training. Here we choose
% Gaussian as the kernel. If you want to use the linear kernel, please use
% model= svmTrain(X, Y, C, @linearKernel);
model= svmTrain(X, Y, C, @(x1, x2) gaussianKernel(x1, x2, sigma));

```

The above code fragments are documented in the MATLAB codes in *LAB1/Chapter.Book.SVM/Chapter.S*

12.7 Multiclass SVM

Sometimes the data need to be divided into more than two types of data, in which case a multiclass SVM method can be used. In this case the *one-versus-the-rest* approach of Vapnik (1998) is often used. In this method if there are K classes of data, one of the data types, denoted as the $k = 1$ class, is assigned one binary value by the SVM method and the rest of the data are assigned the other one. This procedure is repeated for the $k = 2$ class, and then again one at a time until all the classes are separated.

The problem with this approach is that the data are imbalanced, with fewer data in the specified class than the rest of the data. This can lead to an imbalanced gradient that prefers reducing the residuals for the rest of the class compared to that for the specified class. This can lead to both slow convergence and a large percentage error in the predicted classifications. Balancing the gradient, also known as preconditioning (Schuster, 2017) in full waveform inversion, can be a partial remedy where the weight of the specified class has $+1$ while the other data have a weight of $-1/(K-1)$. If the number of points in each class differs significantly from one another then each point in a class is divided by the number of points in that class.

Sometimes data points are assigned by the *one-versus-the-rest* SVM to more than one class, which is an error in classification. This contradiction is sometimes resolved by assigning the misclassified point to the class with the largest value of the predicted target function y .

A number of other heuristic approaches to multiclass SVM are described in Bishop (2007), but he states that the *all-versus-one* approach is the one that is most widely used today. Research into better multiclass SVM methods is still an ongoing effort.

12.8 Soft-Margin SVM

The linear SVM assumes that the data are linearly separable with the consequence that the QP solution to the dual problem will give a *hard-margin* decision boundary. This is sometimes referred to as *hard-margin* SVM¹. However, data are often polluted with errors in misclassification and/or feature coordinates. To account for these errors *soft-margin* SVM adds a regularization function $\gamma(\mathbf{x}^{(n)})$ to the SVM objective function ϵ , where

$$\gamma(\mathbf{x}^{(n)}) = \max(0, 1 - y^{(n)}(\mathbf{w} \cdot \mathbf{x}^{(n)} - b)). \quad (12.31)$$

This regularization term, also known as a penalty function, is denoted as the hinge-loss function in the ML community.

If the data are properly classified then $1 - y^{(n)}(\mathbf{w} \cdot \mathbf{x}^{(n)} - b) \leq 0$ so that $\gamma(\mathbf{x}^{(n)}) = 0$; hence, ϵ collapses to the hard-margin objective function. However, misclassified data points $\mathbf{x}^{(n)}$ lead to progressively larger penalty functions the farther away they are from the correct side of the margin boundary. For example if $\mathbf{x}^{(n)}$ is on the actual decision boundary then $y^{(n)}(\mathbf{w} \cdot \mathbf{x}^{(n)} - b) = 0$ so that the penalty value is $\gamma(\mathbf{x}^{(n)}) = 1$. Therefore the regularized SVM objective function is

$$\epsilon = \lambda \|\mathbf{w}\|^2 + \frac{1}{N} \sum_{n=1}^N \max(0, 1 - y^{(n)}(\mathbf{w} \cdot \mathbf{x}^{(n)} - b)), \quad (12.32)$$

where the parameter λ determines the tradeoff between maximizing the margin width and ensuring that $\mathbf{x}^{(n)}$ is on the correct side of the margin boundary. For a large enough value

¹When the dimensionality of \mathbf{w} is in the millions while the sample sizes are in the hundreds, one can always find hyperplanes (the high dimensional analogue to lines) that can separate any possible labeling of points. Thus, when using linear SVMs, one can always find a separating hyperplane that perfectly separates the training data (Gaonkar and Davatzikos, 2013). This allows us to use the hard margin SVM formulation from (Vapnik, 1995) instead of the soft-margin SVM described in this section.

of $\lambda > 0$ the decision boundary is the same as that for unregularized SVM. In this case the margin thickness can be quite skinny if there are slight errors in the feature coordinates. However, the margin thickness can get larger in the presence of such errors if λ becomes smaller. A concern is that strong outliers might unduly influence the final solution.

12.9 Practical Issues for Implementing SVM

For migration denoising, the three skeletonized characteristics had different units. Therefore, one feature characteristic might consist of numbers that are much bigger or smaller than the other two feature characteristics. This will lead to a scaling problem so that the resulting matrix for QP can be ill-conditioned. In addition, a wide range of examples should be used in order to characterize any type of example outside the training set. If not enough examples are available for training then data augmentation can be used.

12.9.1 Scaling

Each of the feature values need to be normalized before they are input into the SVM algorithm. This scaling can take the form of dividing each feature x_i at the i^{th} pixel by its standard deviation:

$$\hat{x}_i = \frac{x_i - \bar{x}}{\sigma}, \quad (12.33)$$

where the data are also demeaned by subtracting the mean value \bar{x} from the feature value x_i . An alternative is the mean normalization formula:

$$\hat{x}_i = \frac{x_i - \bar{x}}{\max(x_i) - \min(x_i)}, \quad (12.34)$$

where \max and \min take the maximum and minimum values of the feature values for all examples. This will provide an input data set with feature values varying between 1 and -1 with a zero mean.

12.9.2 Data Augmentation

Data augmentation is used to increase the size the training data. Inexpensive data augmentation methods are the following.

1. Image flip. The images are flipped, i.e. reflected, along different axes to create new images with different orientations. Flipping along the vertical or horizontal axes is the easiest augmentation method.
2. Image rotation. Images are rotated by a rotation transform to create new images.
3. Scaling. Images are either magnified or demagnified to create new images. Care must be taken to not distort images too much.
4. Cropping. Crop images so that the main features are still present but the background is reduced in size.
5. Additive Gaussian noise. Add Gaussian noise to images to emulate actual noise in input images.

12.10 Summary

The linear SVM is a binary classification method that finds (\mathbf{w}, b) which gives the fattest margin distance in a $D - 1$ hyperplane. This defines the optimization problem with linear inequality constraints, also known as the primal problem. The optimal (\mathbf{w}, b) can be computed by a quadratic programming method. If the dimension of the $D \times 1$ feature vector is huge compared to the number N of feature vectors in a mini-batch, then solving the reduced dual problem is the only way to go.

If the data are not separable by a hyperplane, then a higher-order SVM surface can be found by applying a non-linear transformation $\mathbf{z}_i = \phi(\mathbf{x})_i$ to the original feature vectors \mathbf{x} , where the new $D_z \times 1$ feature vector is \mathbf{z} and $D_z > D$. To reduce the computational costs, the primal SVM problem is transformed into the dual Lagrangian problem, where the number of unknowns D is the same as that for original linear problem.

Kernel methods are used to avoid the problems of highly oscillatory basis functions with a non-linear transform. The first step is to specify the functional form of a kernel $k(\mathbf{x}, \mathbf{x}') = \mathbf{z}(\mathbf{x})^T \cdot \mathbf{z}(\mathbf{x}')$, where there is no explicit specification of \mathbf{z} . The solution to the reduced Lagrangian is then obtained by a QP method, and the validation data can now be classified.

12.11 Exercises

1. Form the Lagrangian for the dual problem of soft-margin SVM in equation 12.32. Write down the equations for the stationarity conditions of $L(\boldsymbol{\alpha}, \mathbf{w}, b)$. The derivative of the *max* operator cannot be strictly defined. Replace it with a suitable approximation that can be differentiated.
2. Reformulate the objective to be $\epsilon = 1/2\|\mathbf{w}\|^2 + C \sum_{n=1}^N \eta_n$ with the constraint

$$\mathbf{w} \cdot \mathbf{x}^{(n)} + b - 1 \geq \eta_n, \quad (12.35)$$

where $\eta_n \geq 0$. Here, C is a specified tradeoff parameter. What are the KKT conditions? See Appendix 12.14 for the definition of the Karush-Kuhn-Tucker (KKT) conditions.

3. Derive the reduced Lagrangian for the above problem and state the constraints. See page 333 in Bishop (2007).
4. Derive the gradient for the misfit function in equation 12.13. Write a pseudo-MATLAB code for finding \mathbf{x}^b from \mathbf{z}^b by a steepest descent method.

12.12 Computational Labs

Go to the SVM lab in *LAB1/Chapter.Book.SVM/Chapter.SVM1/lab.html* and run the SVM lab. This MATLAB code computes the decision boundaries that separate signal from noise in migration images, and then mutes the noise in the migration image. The performance of the SVM is compared to that of the neural network and logistic regression algorithms.

12.13 Appendix: Defining the Dual Problem with a Lagrangian

Finding the optimal \mathbf{x} that minimizes or maximizes a quadratic functional $f(\mathbf{x})$ subject to N inequality constraints $g(\mathbf{x})^{(n)} \geq 0$ can be recast as the solution to the dual problem. The objective function for the dual problem is formed by adding N weighted inequality constraints onto $f(\mathbf{x})$ to form what is known as the Lagrangian: $L = 1/2f(\mathbf{x}) - \sum_n \alpha_n g(\mathbf{x})^{(n)}$ subject to the simpler inequality constraints $\alpha_n \geq 0$. There is an unknown weight α_n , also known as the Lagrange multiplier, for each constraint so that there are N more unknowns to be determined. This dual problem is sometimes computationally less expensive to solve than the *primal* problem, as discussed in section 12.4. We now give a heuristic and intuitive derivation of a Lagrangian function for one inequality constraint, i.e. $n = 1$.

Consider the following minimization problem with one inequality constraint:

$$\begin{aligned} & \underset{\mathbf{x}}{\text{minimize}} && f(\mathbf{x}) \\ & \text{subject to} && g(\mathbf{x}) \geq 0, \end{aligned} \quad (12.36)$$

Figure 12.12a shows a 2D example where $f(\mathbf{x})$ describes the red elliptical contours and $g(\mathbf{x}) = \sqrt{x_1^2 + x_2^2}$ describes a circle for the inequality constraint. In this case all points in the infinitely-extended green region in Figure 12.12a satisfy the inequality constraint $g(\mathbf{x}) \geq 0$ so that the solution to equation 12.36 is at the center point \mathbf{x}^* of the red ellipse. An unconstrained steepest descent method can then be used to search for \mathbf{x} that satisfies $\nabla f(\mathbf{x}) = 0$.

If $g(\mathbf{x}) = -\sqrt{x_1^2 + x_2^2} + 3 \geq 0$ then the feasible points \mathbf{x} are only in the small green disk in Figure 12.12b. Which of these feasible points minimizes $f(\mathbf{x})$? It is geometrically clear that the dashed red ellipse with the contour value $f(\mathbf{x}) = 4$ just *kisses* the boundary of the green disk at \mathbf{x}^* . No other ellipse contour with a *smaller* value intersects the green region. Therefore, \mathbf{x}^* must be the solution that minimizes $f(\mathbf{x})$ and also satisfies the inequality constraint in equation 12.36. As discussed below, L achieves a maximum at this stationary point.

Notice that the circular contour at \mathbf{x}^* in Figure 12.12b is tangent to the red dashed contour of the ellipse. This means that the normal vectors $\nabla g(\mathbf{x})$ and $\nabla f(\mathbf{x})$ at \mathbf{x}^* are parallel² to one another at the minimization point \mathbf{x}^* . This suggests that we can define a new function L that is the weighted sum

$$L(\mathbf{x}, \alpha) = f(\mathbf{x}) - \alpha g(\mathbf{x}), \quad (12.37)$$

which has the property of being stationary at the *kissing* point \mathbf{x}^* :

$$\begin{aligned} \nabla L(\mathbf{x}, \alpha)|_{\mathbf{x}=\mathbf{x}^*} &= [\nabla f(\mathbf{x}) - \alpha \nabla g(\mathbf{x})]|_{\mathbf{x}=\mathbf{x}^*}, \\ &= 0, \end{aligned} \quad (12.38)$$

if $\alpha = |\nabla f|/|\nabla g| \geq 0$. The weight $\alpha \geq 0$ because the gradients of both functions are parallel and have the same sign at \mathbf{x}^* , so $\alpha \geq 0$ to satisfy equation 12.38. In the third quadrant of

²The values of the ellipse and circle are both increasing to the left at \mathbf{x}^* . Hence, the gradients are parallel to one another, not anti-parallel.

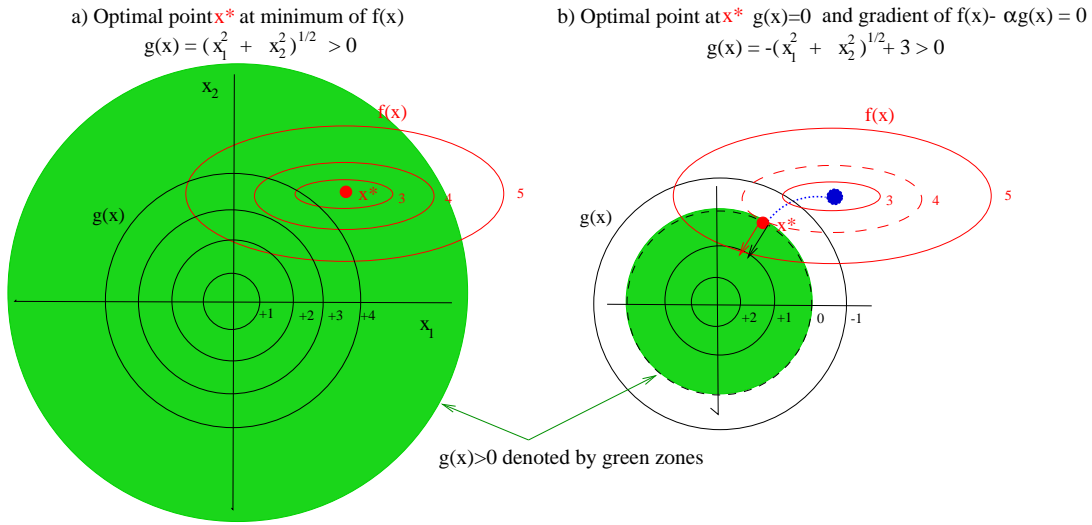


Figure 12.12: Red and black contours for the functions $f(\mathbf{x})$ and $g(\mathbf{x})$, respectively; the green areas define the points $\mathbf{x} \in V_o$ that satisfy the inequality constraint $g(\mathbf{x}) \geq 0$. In a) the constraint $g(\mathbf{x}) = \sqrt{x_1^2 + x_2^2} \geq 0$ is satisfied everywhere so the minimum of $f(\mathbf{x})$ is at the origin. In b), $g(\mathbf{x}) = -\sqrt{x_1^2 + x_2^2} + 3 \geq 0$ so the feasible solution points \mathbf{x} are inside the small green disk. The points $\mathbf{x} \in B_o$ on the dashed circular boundary satisfy $g(\mathbf{x}) = 0$, and the optimal point where L is stationary and a maximum is at the "kiss" point \mathbf{x}^* on B_o where $\nabla L(\mathbf{x}, \alpha) = \nabla f(\mathbf{x}) - \alpha \nabla g(\mathbf{x}) = 0$. The points along the dashed blue line are defined to be the ones where the elliptical and circular contours "kiss" each other, i.e. they satisfy the stationary condition $\nabla f(\mathbf{x}) - \alpha \nabla g(\mathbf{x}) = 0$ where $\alpha = |\nabla f(\mathbf{x})|/|\nabla g(\mathbf{x})|$.

b), the gradients ∇f and ∇g at their kissing points are *anti-parallel* so $\alpha \geq 0$ excludes the stationarity condition in equation 12.38.

Equation 12.38 is a necessary but not sufficient condition for \mathbf{x}^* to be a minimizer of $f(\mathbf{x})$. For example, the dashed blue curve in Figure 12.12b is denoted as the *kiss* curve where the circular and elliptical contours just *kiss* one another so that $\nabla L(\mathbf{x}, \alpha)|_{\mathbf{x}=kiss\ pts} = 0$ for $\alpha = |\nabla f|/|\nabla g|$. These *kiss* points along the blue curve can be continued into the green disk.

So we need another mathematical condition in addition to equation 12.38 to pick out the optimal *kiss* point \mathbf{x}^* at the dashed black boundary. This new condition is that, for all the kiss points on the blue *kiss* curve³ (and its extension into the green zone), the optimal \mathbf{x}^* is where $L(\mathbf{x}, \alpha)$ is maximum. This can be proven by noting that the values of $\alpha = |\nabla f|/|\nabla g|$ vary continuously on the "kiss" curve, so that differentiating equation 12.37 w/r to α gives

$$\frac{\partial L}{\partial \alpha} = -g(\mathbf{x}). \quad (12.39)$$

At the boundary point \mathbf{x}^* we have $\frac{\partial L}{\partial \alpha}|_{\mathbf{x}=\mathbf{x}^*} = -g(\mathbf{x}^*) = 0$, and at points just to the left of \mathbf{x}^* the slope is negative and to the right the slope is positive. This is the condition for $L(\mathbf{x}, \alpha)$ to be a maximum at \mathbf{x}^* along the kiss curve. Therefore, the two conditions that are necessary and sufficient for \mathbf{x}^* to minimize $f(\mathbf{x})$ subject to the inequality constraint are

$$\begin{aligned} & \underset{\mathbf{x}, \alpha}{\text{maximize}} && f(\mathbf{x}) - \alpha g(\mathbf{x}), \\ & \text{subject to} && \nabla f(\mathbf{x}) - \alpha \nabla g(\mathbf{x}) = 0 \\ & && \alpha \geq 0, \end{aligned} \quad (12.40)$$

The next section shows a 1D example for solving the Lagrangian dual problem.

12.13.1 Simple Example of a Dual Solution

For a simple 1D convex minimization problem with inequality constraints, the optimization problem is defined as

$$\begin{aligned} & \underset{x}{\text{minimize}} && f(x) \\ & \text{subject to} && g(x) \geq 0, \end{aligned} \quad (12.41)$$

For the example $f(x) = x^2$ and one inequality constraint, equation 12.41 becomes

$$\begin{aligned} & \underset{x}{\text{minimize}} && f(x) = x^2 \\ & \text{subject to} && g(x) = 0.7x - 0.14 \geq 0, \end{aligned} \quad (12.42)$$

where $f(x) = x^2$, $g(x) = 0.7x - 0.14$, and $h(x) = f(x) - \alpha g(x)$ are plotted in Figure 12.13. The inequality constraint is $g(x) = 0.7x - 0.14 \geq 0$ so that the feasible points are for $x \geq 0.2$. It is obvious that $x^* = 0.2$ at the green star minimizes $f(x)$ for the feasible points $x \geq 0.2$. In contrast, the global minimum of $f(x)$ is at $x = 0$ to the left of x^* , but $x = 0$ will violate the inequality constraint $x \geq 0.2$.

³The blue kiss curve is defined by the *kissing* points where $\nabla L = 0$ for $\alpha = |\nabla f|/|\nabla g|$

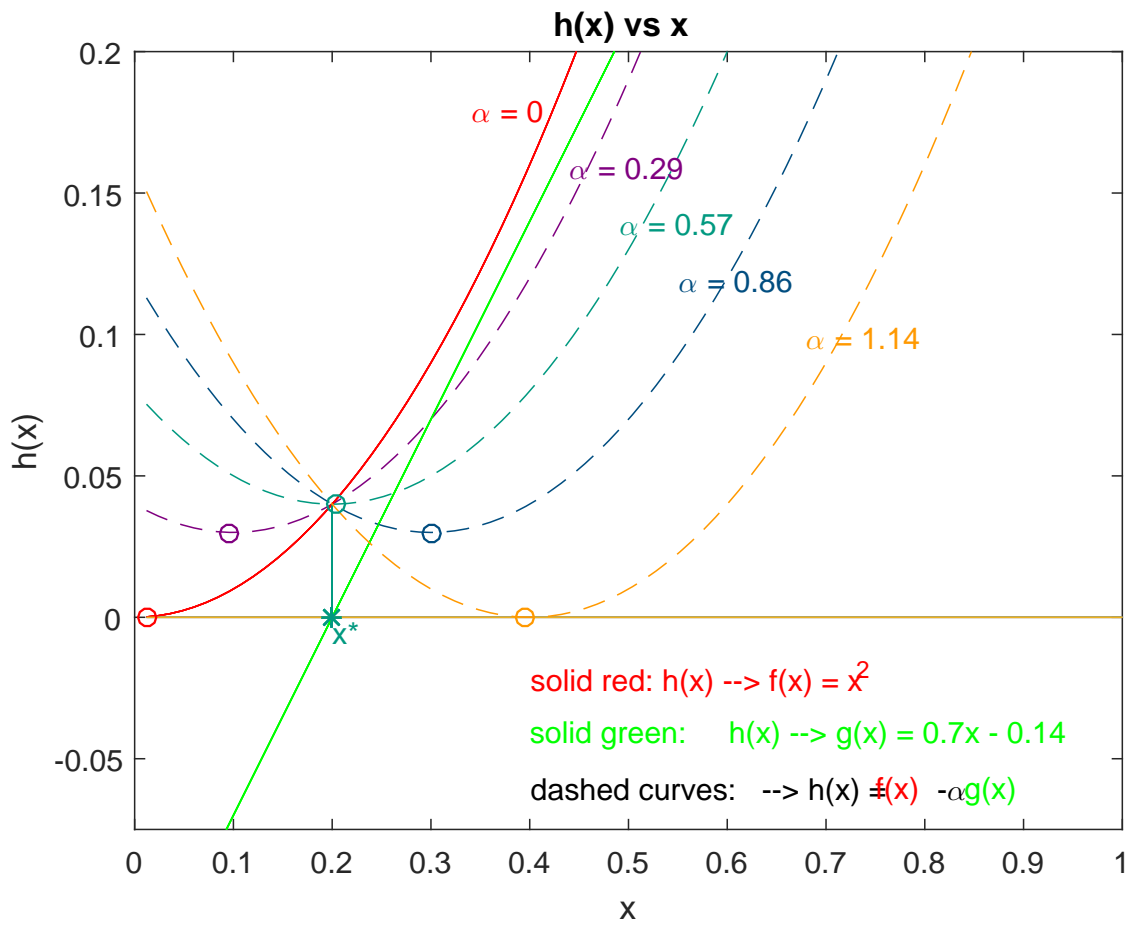


Figure 12.13: Plots of $f(x) = x^2$, $g(x) = 0.7x - 0.14$, and $f(x) - \alpha g(x)$, where x^* is the optimal solution that minimizes L subject to the inequality constraint. The Lagrangian $L(x, \alpha) = f(x) - \alpha g(x)$ is plotted as dashed lines for various values of α .

An alternative to the above optimization problem is to find x that minimizes the Lagrangian

$$\begin{aligned} \underset{x}{\text{minimize}} \quad & L(x, \alpha) = f(x) - \alpha g(x), \\ \text{subject to} \quad & \alpha > 0, \end{aligned} \quad (12.43)$$

and also maximizes $L(x, \alpha)$ w.r.t. α , where α is the Lagrange multiplier. These two stationarity conditions are expressed as

$$\begin{aligned} \frac{\partial L}{\partial x} &= \frac{\partial f}{\partial x} - \alpha \frac{\partial g}{\partial x} = 0 \\ \frac{\partial L}{\partial \alpha} &= -g(x) = 0 \quad \text{subject to } \alpha > 0. \end{aligned} \quad (12.44)$$

For the equation 12.42 example,

$$L(x, \alpha) = x^2 - \alpha(0.7x - 0.14), \quad (12.45)$$

so that equation 12.44 becomes

$$\frac{\partial L}{\partial x} = \frac{\partial x^2}{\partial x} - \alpha \frac{\partial(0.7x - 0.14)}{\partial x} = 2x - 0.7\alpha = 0 \rightarrow \alpha = x/0.35, \quad (12.46)$$

$$\frac{\partial L}{\partial \alpha} = -0.7x + 0.14 = 0 \rightarrow x = 0.2. \quad (12.47)$$

Plugging equation 12.47 into equation 12.46 gives $\alpha = 0.2/0.35 = 0.57$, which is associated with the dashed blue curve $L(x, \alpha = 0.57)$ plotted in Figure 12.13. This value of $\alpha = 0.57 > 0$ satisfies the positivity constraint and also balances out the gradients of df/dx and dg/dx so that the sum $\partial L/\partial x = \partial f/\partial x - \alpha \partial g/\partial x = 0$ is stationary at $x^* = 0.2$.

At each value of x there is a unique value of $\alpha = x/0.35$ (see equation 12.46) that allows $\partial L/\partial x = 0$. Setting $\alpha \rightarrow \alpha(x) = x/0.35$ from equation 12.46 says that $L(x, \alpha(x))$ is a maximum at $x^* = 0.2$ because it satisfies the maximality conditions: $\partial L/\partial \alpha = 0$ for $x = 0.2$ and its second derivative

$$\begin{aligned} \frac{\partial^2 L(x = 0.35 * \alpha, \alpha)}{\partial \alpha^2} &= \frac{\partial^2(0.1225\alpha^2 - 0.245\alpha^2 + 0.049\alpha)}{\partial \alpha^2}, \\ &= -.245 \end{aligned} \quad (12.48)$$

is negative⁴ Thus, the values of $L(x, \alpha(x))$ plotted against x intersect the circled points in Figure 12.13 where $L(x, \alpha(x))$ is a maximum at $x^* = 0.2$.

⁴The negative second-derivative is an alternative to the first-derivative maximum conditions we used earlier.

12.14 Appendix: Karush-Kuhn-Tucker Conditions

We now define the Karush-Kuhn-Tucker conditions for the optimization problem with inequality constraints discussed in Appendix 12.13. If \mathbf{x} is in the *inactive* region where $g(\mathbf{x}) > 0$ then the inequality constraint $g(\mathbf{x}) \geq 0$ is denoted as inactive and $\alpha = 0$ for the solution to the Lagrangian problem. This constraint is not needed when \mathbf{x} is in the inactive region so it makes sense to set $\lambda = 0$ because it leads to a smaller Lagrangian, i.e.

$$\mathbf{x} \in \text{inactive region}; \quad [f(\mathbf{x}) - \alpha g(\mathbf{x})]_{\alpha > 0} > [f(\mathbf{x}) - \alpha g(\mathbf{x})]_{\alpha = 0}. \quad (12.49)$$

However, if \mathbf{x} is on the boundary defined by $g(\mathbf{x}) = 0$ then the constraint is active and $\lambda > 0$.

Assigning α to be either 0 or > 0 is compactly summarized by the condition $\alpha g(\mathbf{x}) = 0$, where $\alpha > 0$ for \mathbf{x} on the boundary or $\alpha = 0$ for \mathbf{x} in an inactive region where $g(\mathbf{x}) > 0$. Thus, this leads to three constraints for the Lagrangian problem known as the Karush-Kuhn-Tucker (KKT) conditions:

$$\begin{aligned} g(\mathbf{x}) &\geq 0, \\ \alpha &\geq 0, \\ \alpha g(\mathbf{x}) &= 0. \end{aligned} \quad (12.50)$$

If there are N inequality constraint such that $g(\mathbf{x})^{(n)} \geq 0$ for $n = [1, 2, \dots, N]$ then there are N Lagrange multipliers with $\alpha_n \geq 0$ and $g(\mathbf{x})^{(n)} \alpha_n = 0$ for $n = [1, 2, \dots, N]$. See Nocedal and Wright (1999) for more details.

12.15 Appendix: Diffraction Stack Migration

Integral equation migration is a popular seismic imaging method (Yilmaz, 2001) used in the oil industry. It can be described as summing the weighted reflection data along pseudo-hyperbolas associated with each trial image point at \mathbf{x} and placing that summation number at \mathbf{x} to give the migration image $m(\mathbf{x})$. This summation is described by the diffraction-stack migration formula

$$\begin{aligned} m(\mathbf{x}) &= \sum_A \sum_B \sum_{\omega} [i\omega D(\mathbf{B}|\mathbf{A}) e^{-i\omega(\tau_{Ax} + \tau_{xB})}], \\ &= \sum_A \sum_B d(\mathbf{B}, \tau_{Ax} + \tau_{xB} | \mathbf{A}), \end{aligned} \quad (12.51)$$

where $D(\mathbf{B}|\mathbf{A})$ is the frequency-domain representation of the trace in Figure 12.14, its inverse Fourier transform is given by $d(\mathbf{B}, t | \mathbf{A})$, and the summations run over the indices for the source at A and the receiver at \mathbf{B} . For a homogeneous medium having velocity c the time for waves to propagate from the source at \mathbf{A} down to the scatterer at \mathbf{x}_0 and back up to the receiver at \mathbf{B} is given by

$$\tau_{Ax} + \tau_{xB} = \frac{\sqrt{(x_A - x_0)^2 + (z_A - z_0)^2} + \sqrt{(x_B - x_0)^2 + (z_B - z_0)^2}}{c}, \quad (12.52)$$

where $z_A = z_B = 0$ for sources and receivers on a horizontal datum. This two-way traveltimes equation describes a hyperbola in $x_B - \text{time}$ coordinates for any image point at \mathbf{x} and a source fixed at \mathbf{A} ; the apex of the hyperbola is centered over the point scatterer at \mathbf{x}_o . If the reflection time on the leftside of equation 12.52 is fixed at a specific time then the values of \mathbf{x} that satisfy this traveltimes equation form an ellipse with the foci at \mathbf{A} and \mathbf{B} , as depicted in Figure 12.14.

The observed data for a single scatterer can be approximated by

$$D(\mathbf{B}|\mathbf{A}) = e^{-i\omega(\tau_{Ax_o} + \tau_{x_oB})}, \quad (12.53)$$

where geometric spreading and the reflection coefficient are conveniently ignored. Substituting equation 12.53 into equation 12.51 gives

$$m(\mathbf{x}) = \sum_A \sum_B \sum_\omega [i\omega e^{-i\omega(\tau_{Ax} + \tau_{xB} - \tau_{Ax_o} - \tau_{x_oB})}]. \quad (12.54)$$

If the trial image point at \mathbf{x} coincides with the actual scatterer at \mathbf{x}_o then the phases cancel one another exactly and the summation over the sources at \mathbf{A} and receivers at \mathbf{B} is completely coherent and sums to a very large number to be placed at \mathbf{x}_o . On the other hand, if \mathbf{x} is far from the actual scatterer then the predicted hyperbola will not match the actual hyperbola of recorded events. The consequence is that the summation in equation 12.54 will be largely incoherent and sum to a small number to be placed at the trial image point at $\mathbf{x} \neq \mathbf{x}_o$. data along.

This type of imaging is also known as diffraction-stack migration (Yilmaz, 2001). For a single source and single receiver the above equation becomes

$$m(\mathbf{x}) = \dot{d}(B, \tau_{Ax} + \tau_{xB}|A). \quad (12.55)$$

In a 2D homogeneous medium, the reflection traveltimes $\tau^{ref.} = \tau_{Ax} + \tau_{xB}$ associated with the trial scattering point at \mathbf{x} can be expressed as

$$\tau^{ref.} = [\sqrt{(x_A - x)^2 + (z_A - z)^2} + \sqrt{(x_B - x)^2 + (z_B - z)^2}]/v, \quad (12.56)$$

which, for $\tau^{ref.} = \text{const}$, describes an ellipse in model-space coordinates (x, z) with the foci at $\mathbf{A} = (x_A, z_A)$ and $\mathbf{B} = (x_B, z_B)$. It follows from equation 12.55 that the reflectivity image $m(\mathbf{x})$ is approximated by smearing the trace amplitude at time $\tau^{ref.}$ over the ellipse described by equation 12.56 in model space.

Smearing the seismic amplitude over an ellipse is shown in Figure 12.14a; here, the temporal interval T of the trace's source wavelet determines the thickness c/T of the fat ellipse in (x, z) space. Somewhere along this ellipse is a scatterer that gave rise to the event at time $\tau^{ref.}$ for the receiver at \mathbf{d} . The scatterer's location can be better estimated by stacking (see equation 12.51) the "smears" from other traces into the model, as illustrated in Figure 12.14b. Figure 12.15 gives an example of migration of poststack data (where the source is at the receiver) for a homogeneous velocity model with 6 scattering points. The lateral spatial resolution of the image becomes worse with increasing depth.

Migration: Smear and Sum Refl. Amp. Along Ellipses

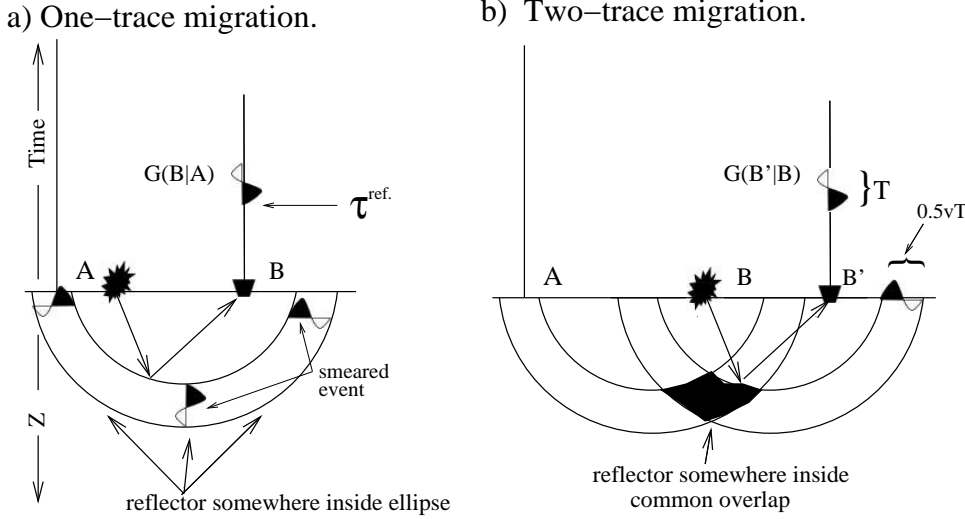


Figure 12.14: Migration is the smearing of trace amplitudes along the appropriate fat ellipses in (x, z) for each source-receiver pair **A – B** (Claerbout, 1992). Migration of two traces in b) has better spatial resolution than migrating just one trace in a), and the thickness of each fat ellipse is c/T , where T is the dominant period of the source wavelet.

12.15.1 Dip Angles, Coherency and Amplitudes of a Migration Image

Dip angle, coherency and amplitude of a migration image are skeletonized characteristics that can be used to possibly distinguish noise from signal. We now describe the computation of each feature.

To compute these three skeletonized characteristics we first define a 5×5 window centered at the i^{th} pixel in the migration image. A 5×5 window is used because it is about one wavelength in size. To compute the dip angle in this window we apply a local slant stack (Yilmaz, 2001) to the windowed data centered at the i^{th} pixel to get the dip angle that has the dominant energy; this dip angle θ_i is assigned to the i^{th} pixel. Slant stacking consists of summing the amplitudes of the data that intercept a line with a specified dip angle. This dip angle is iteratively incremented by about 15 degrees and the dip angle with the largest summed amplitude is assigned to be θ_i .

The window is shifted over by one pixel to the $i+1$ pixel and the slant stack procedure is repeated to give θ_{i+1} . Repeating this procedure for all the training set pixels in Figure 12.6a gives the dip angle image shown in Figure 12.6b. In practice, only 70 pixels are in the actual training set.

The coherency ϕ_i at the i^{th} pixel of Figure 12.6a is computed by forming a common image gather (CIG) or a common angle gather (CAG) from the prestack migration images (Yilmaz, 2001). If the migration velocity is accurate then summing along the offset axis (or angle axis if the CAG is used) should give a strong coherency value ϕ_i at the i^{th} pixel. Repeating this procedure for all the pixels in Figure 12.6a gives the coherency image shown

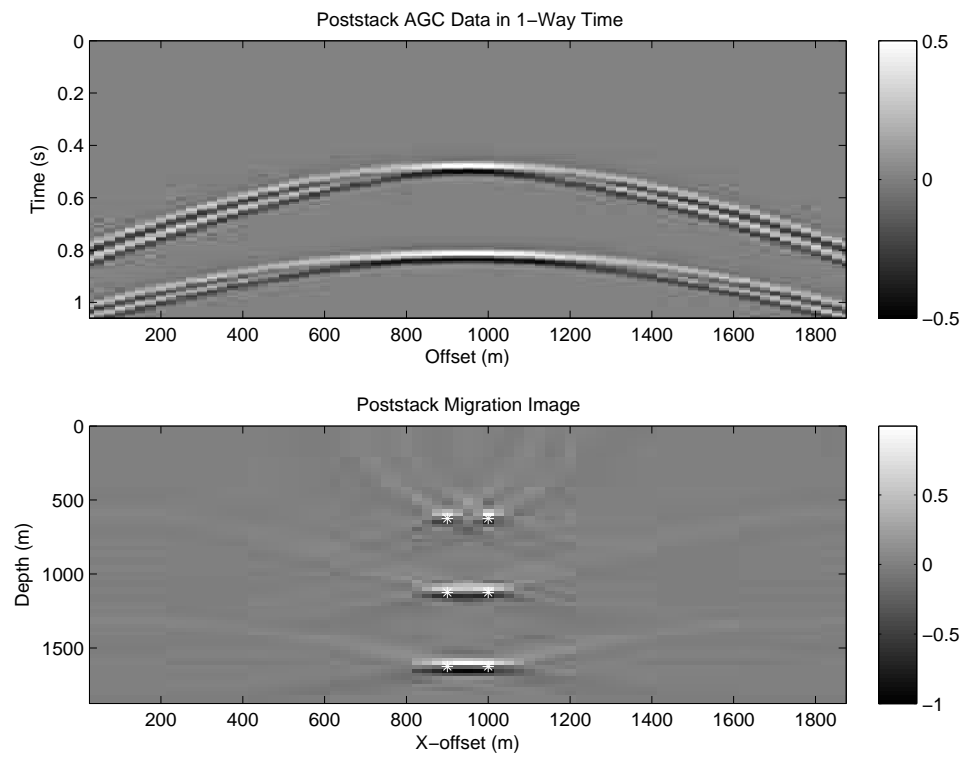


Figure 12.15: (Top) Poststack data and (bottom) migration image where there are 6 point scatterers indicated by the white stars. Note, the spatial resolution of the image becomes better with decreasing depth of the scatterers.

in Figure 12.6c.

The amplitude image in Figure 12.6d is obtained by computing the Hilbert transform of a trace in the migration image (Yilmaz, 2001). Then the envelope of the migration trace is computed in the window centered at the i^{th} pixel and its maximum amplitude gives A_i .

Chapter 13

Clustering Algorithms

Cluster analysis is the formal study of methods and algorithms for grouping, or clustering, objects according to measured or perceived intrinsic characteristics or similarity (Jain, 2010). It is similar to logistic regression in grouping data into different classes, except the training data do not have to be labeled and there can be many different clusters. Thus, a cluster algorithm is an unsupervised learning method that avoids the cost of supervised labeling of large data sets. One of the most widely used clustering algorithms (see Figure ??) is the K-means cluster method proposed more than 50 years ago (Steinhaus, 1956; Lloyd, 1982; Ball and Hall, 1965; and MacQueen, 1965). It is simple and very effective in machine learning studies, and will be the main focus of this chapter.

13.1 Introduction

According to Jain (2010) there are thousands of different cluster algorithms, many of them tailored to a different scientific algorithm. They differ in the choice of their definition of distance between points, the objective function, the assignment of probability properties and heuristics. Many of them are unsupervised, although some assign labeling to a small number of points to assist in the final assignment of clusters. In this case this would be a semi- or weakly-supervised learning algorithm.

What is the definition of a cluster of points? According to Jain (2010), we start with a set of N points, each being an D -dimensional feature vector, and there are K groups of these points. The points in any group have a measure of high similarity to one another, but have a low similarity to members outside that group. Similarity is an arbitrarily defined quantity, but the points in a specified group in Figure 13.2 are similar in their close distance to one another.

The labeling of points was first introduced in early chapters on supervised learning. In this case, a learning algorithm was used, such as SVM or logistic regression, to classify the points in Figure 13.2a. A semi-supervised learning algorithm for the data in Figure 13.2b could be devised so that a few points in each cluster are already labeled so they can be used to automatically classify the unlabeled points. For example, the unlabeled point is assigned the group identity of the nearest labeled point. A partially constrained clustering algorithm is depicted in Figure 13.2c. Here, some points are known not to belong to

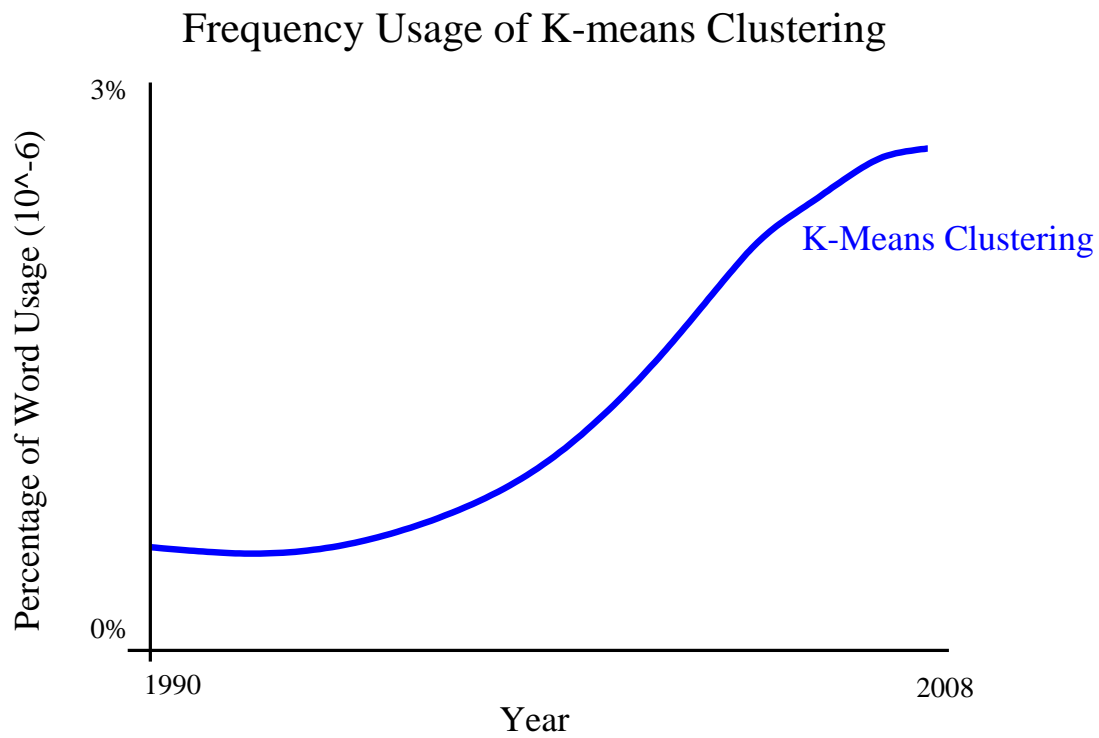


Figure 13.1: Percentage of citations in books for the phrase *K-means clustering* plotted against calendar year. Courtesy of <https://books.google.com/ngrams/>.

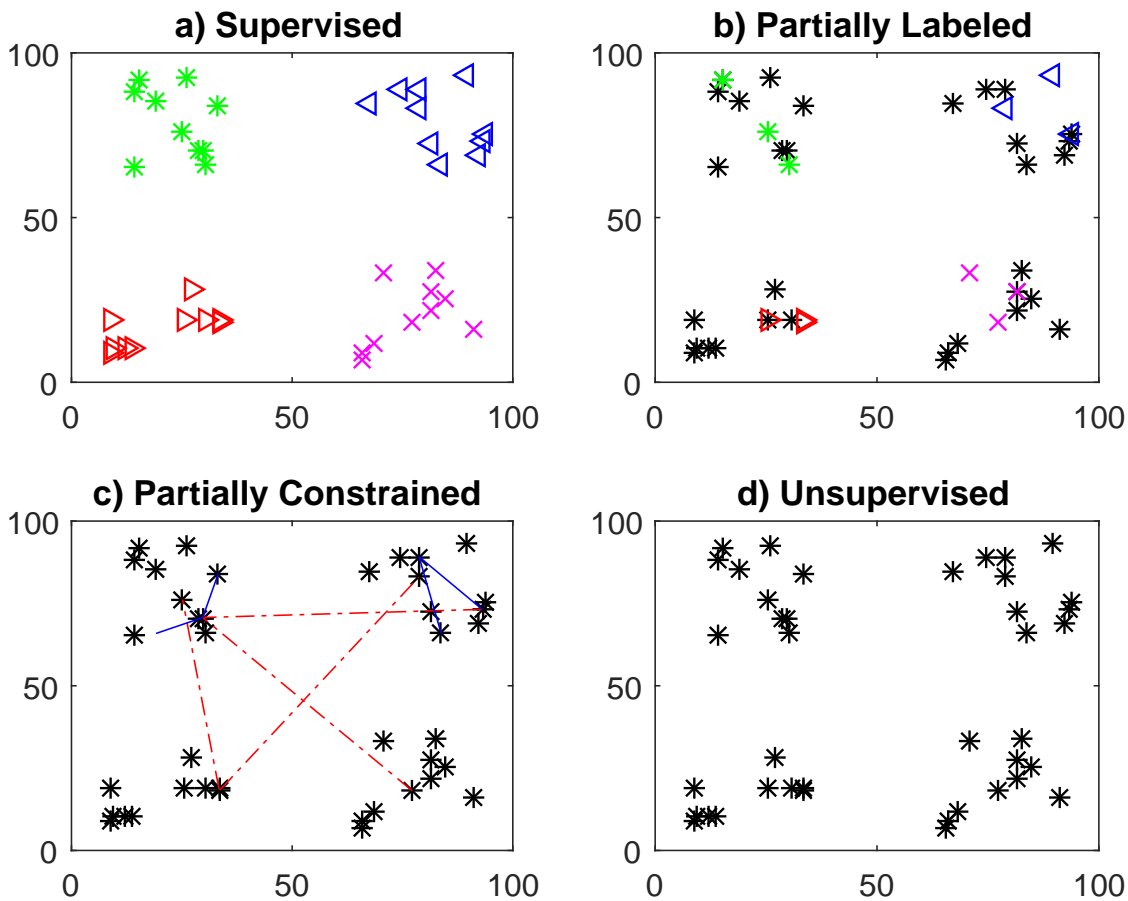


Figure 13.2: Different groups of points: a) Supervised learning where each points in different clusters are labeled with different colored symbols, b) partially labeled where only a few non-black points are labeled, c) partially constrained where the dashed red (solid blue) lines forbid (enforce) the points to be in the same cluster, and d) completely unlabeled or constrained points. Figure modified from Jain (2010).

certain groups so a constraint is imposed that is honored by the clustering algorithm. For example, the distance between the points in the dissimilar groups can be used as a soft threshold such that the distance between two points in the same group should not exceed this soft threshold, otherwise its candidacy is assigned a lower grade. Finally, we have the completely unsupervised clustering problem illustrated in Figure 13.2d. In this case, the weighted distance between one point and another is used as a criterion for eligibility in a separate cluster.

The problem shown in in Figure 13.2d is the one that is largely addressed in this chapter: clustering unlabeled points by unsupervised learning. Due to its simplicity, empirical success and its widespread use in the Machine Learning community, this chapter focuses on the K-means clustering algorithm.

13.2 Theory of K-means Clustering

Let \mathbf{x}_{ij} be j^{th} $D \times 1$ feature vector associated with the i^{th} cluster, where there are I clusters. The mean centroid point \mathbf{C}_i of the i^{th} cluster is defined as

$$\mathbf{C}_i = \frac{1}{m_i} \sum_{j=1}^{m_i} \mathbf{x}_{ij}, \quad (13.1)$$

where m_i is the number of points in the i^{th} cluster. The points \mathbf{x}_{ij} in the i^{th} cluster are defined as having the smallest distance $\|\mathbf{C}_i - \mathbf{x}_{ij}\|$ between that point and \mathbf{C}_i compared to any other centroid point \mathbf{C}_j for $j \neq i$.

The averaged sum of the weighted squared distances between the i^{th} centroid point \mathbf{C}_i and the points in the i cluster is given as

$$d_i = \frac{1}{m_i} \sum_{j=1}^{m_i} \|\mathbf{C}_i - \mathbf{x}_{ij}\|^2. \quad (13.2)$$

The goal is to find the optimal distribution of cluster points \mathbf{C}_k such that the objective function ϵ is minimized:

$$\epsilon = \frac{1}{2} \sum_{i=1}^I \frac{1}{m_i} \sum_{j=1}^{m_i} \|\mathbf{C}_i - \mathbf{x}_{ij}\|^2. \quad (13.3)$$

There are two groups of clustering algorithms: hierarchical and partitional. For the hierarchical algorithm, there are two strategies.

- The bottom-up approach starts with each point being a its own distinct cluster, and iteratively finds a smaller number of clusters that contain the closest points to that cluster's centroid.
- The top-down approach, where all points belong to one super cluster, and smaller clusters are iteratively computed.

The partitioning clustering sets the number of clusters and finds the optimal arrangement of points that minimize the misfit function. For the semblance example below, we use a top-down hierarchical approach where the number of clusters increase and we choose the cluster where the residual reduction becomes small.

There are four steps to the K-means clustering algorithm where the number of clusters is specified.

1. Select an initial configuration of I clusters. Compute the centroid point \mathbf{C}_i for each cluster.
2. Compute the distances $\|\mathbf{C}_i - \mathbf{x}_{ij}\|$, and reassign points to the cluster of the centroid point they are closest to. If the elements in each vector have different units then they should be normalized by their standard deviations.
3. Compute the new centroid points from the newly assigned points.

4. Repeat steps 2 and 3 until convergence. This procedure can be adapted to the hierarchical approach where an outer loop can be added where the number of clusters is either increased or decreased.

A problem with the above approach is that it can get stuck in a local minimum. Sometimes this difficulty is remedied by using different starting configurations to determine if they converge to the same answer. This same procedure is used to test for local minima problems with many non-linear optimization methods. Another way to mitigate this problem is to specify different numbers of clusters and choose the final cluster configuration that best suits our goal. This approach will be used in a geoscience application involving velocity analysis.

13.3 Information Weighted Clustering

The clustering algorithm can be recast as an iterative optimization problem where the regularized objective function is given by

$$\epsilon = \frac{1}{2} \sum_{i=1}^I \frac{1}{m_i} \sum_{j=1}^{m_i} \|\mathbf{C}_i - \mathbf{x}_{ij}\|^2 + \frac{\lambda}{2} \sum_{i=1}^I \|\mathbf{C}_i - \bar{\mathbf{C}}_i\|^2 \quad (13.4)$$

where $\lambda > 0$ is the damping parameter and $\bar{\mathbf{C}}_i$ is a desired centroid point that should be near our final cluster point \mathbf{C}_i . The gradient of this objective function is

$$\begin{aligned} \frac{\partial \epsilon}{\partial \mathbf{C}_i} &= \frac{1}{m_i^{(k)}} \sum_{j=1}^{m_i} (\mathbf{C}_i - \mathbf{x}_{ij}) + \lambda (\mathbf{C}_i^{(k)} - \bar{\mathbf{C}}_i), \\ &= \mathbf{C}_i - \frac{1}{m_i^{(k)}} \sum_{j=1}^{m_i} \mathbf{x}_{ij} + \lambda (\mathbf{C}_i^{(k)} - \bar{\mathbf{C}}_i), \end{aligned} \quad (13.5)$$

where

$$\frac{\partial \epsilon}{\partial \mathbf{C}_i} = \left(\frac{\partial \epsilon}{\partial C_{i1}}, \frac{\partial \epsilon}{\partial C_{i2}}, \dots, \frac{\partial \epsilon}{\partial C_{iD}} \right)^T, \quad (13.6)$$

and C_{il} is the l^{th} component of the i^{th} cluster vector \mathbf{C}_i . The corresponding steepest descent formula for updating \mathbf{C}_i is given by

$$\begin{aligned} \mathbf{C}_i^{(k+1)} &= \mathbf{C}_i^{(k)} - \alpha \frac{\partial \epsilon}{\partial \mathbf{C}_i}, \\ &= \mathbf{C}_i^{(k)} - \alpha \frac{1}{m_i^{(k)}} \sum_{j=1}^{m_i^{(k)}} (\mathbf{C}_i^{(k)} - \mathbf{x}_{ij}^{(k)}) - \alpha \lambda (\mathbf{C}_i^{(k)} - \bar{\mathbf{C}}_i), \\ &\quad \text{Average of Points in } i^{th} \text{ Cluster} \\ &= \alpha \underbrace{\frac{1}{m_i^{(k)}} \sum_{j=1}^{m_i^{(k)}} \mathbf{x}_{ij}^{(k)}}_{\text{Average of Points in } i^{th} \text{ Cluster}} - \alpha \lambda (\mathbf{C}_i^{(k)} - \bar{\mathbf{C}}_i), \end{aligned} \quad (13.7)$$

where k is the iteration index in the superscripts of $(\mathbf{C}_i^{(k)}, \mathbf{x}_{ij}^{(k)}, m_i^{(k)})$.

The iterative cluster algorithm described by equation 13.7 can be made more robust by applying a weight w_{ij} to each point in the i^{th} cluster (Chen, 2018a-2018b). The weight w_{ij} can be based on the information content of that point, e.g., points with a large-amplitude value in an image contain more important information than low-amplitude points in a migration image. The importance of points based on their amplitude values A_{ij} can be given a soft-max weighting such that

$$w_{ij} = \frac{e^{A_{ij}}}{\sum_{j=1}^{m_j} e^{A_{ij}}} \quad \text{where} \quad \sum_{j=1}^{m_j} w_{ij} = 1. \quad (13.8)$$

Therefore the information-weighted clustering (IWC) formula is

$$\mathbf{C}_i^{(k+1)} = \alpha \underbrace{\frac{1}{m_i^{(k)}} \sum_{j=1}^{m_i^{(k)}} w_{ij} \mathbf{x}_{ij}^{(k)}}_{\text{Weighted Average of Points in } i^{th} \text{ Cluster}} - \alpha \lambda (\mathbf{C}_i^{(k)} - \bar{\mathbf{C}}_i). \quad (13.9)$$

The Numerical Examples section tests the effectiveness of both the standard and regularized cluster algorithms on synthetic data and field data from the Gulf of Mexico.

13.3.1 Elbow Method for Determining the Number of Clusters

The number of clusters is sometimes determined by using the elbow method (Thorndike, 1953; Goutte et al., 1999).

1. Define the initial number of clusters as $i = 2$ and the initial two centroid points.
2. Use equation 13.9 to recompute the new cluster centroids $\mathbf{C}(i)$ from the old centroids. Determine the number of points $m(i)$ in the i^{th} cluster. Then find the sum of the squared distances $SSD(i)$ between the centroid of the i^{th} cluster and the $m(i)$ points in that cluster. Compute the average of the variances $SSD(i)$ as $ASSD(i) = SSD(i)/m(i)$ for all i .
3. Plot $ASSD(i)$ against i as shown in Figure ??.
4. Increase the number of centroids by one and repeat steps 2-3 until enough points are computed to show an elbow in the curve. The choice of the new centroid is up to the user, but setting it to be the average point of the computed centroids is one strategy. *The first few clusters are proportional to the average variance and show a large change with respect to a change in the number of clusters. Thus, these first clusters will add much information (explain a lot of variance). At some point the marginal gain will drop, giving an angle in the graph. The number of clusters is chosen at this point, hence the "elbow criterion". Instead of plotting average variance one can plot the percentage of variance.*

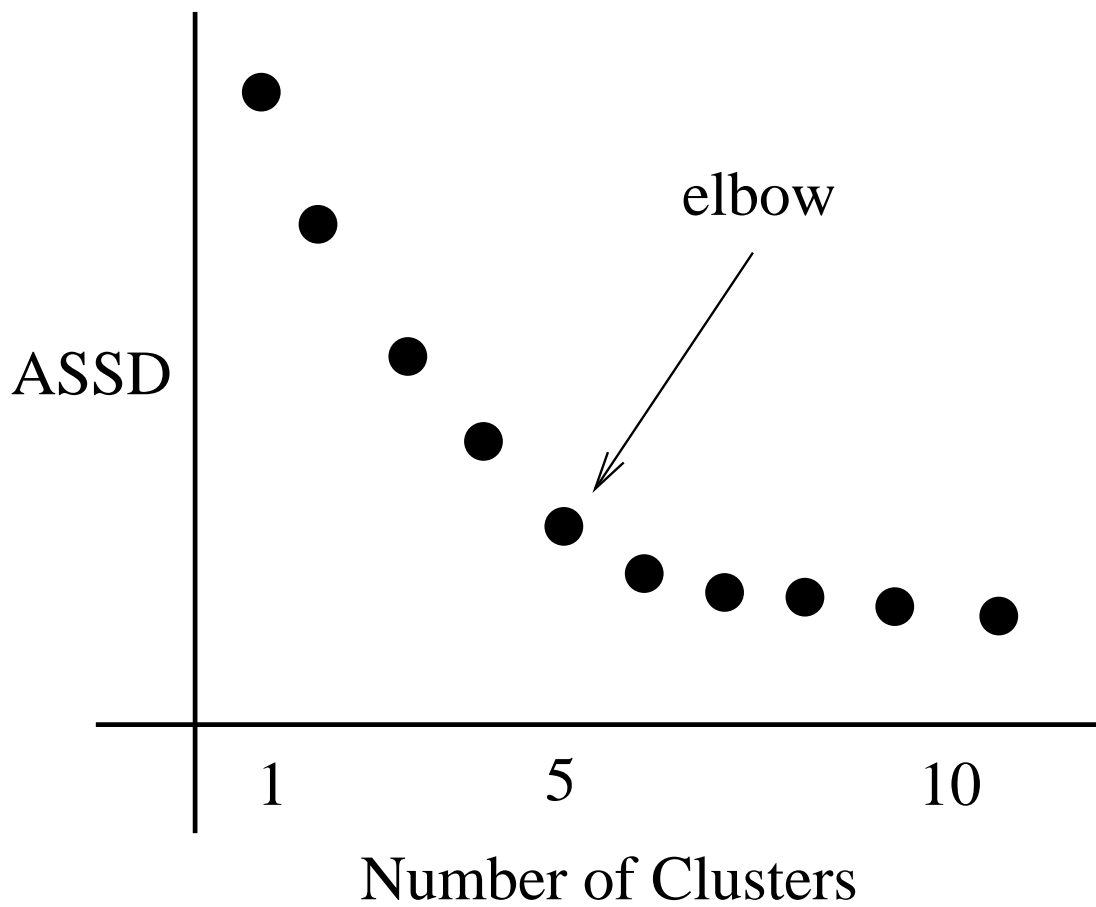


Figure 13.3: Average sum of squared distances ($ASSD(i)$) plotted against the number of clusters. The *elbow* cannot always be determined unambiguously ([https://en.wikipedia.org/wiki/Elbow_method_\(clustering\)](https://en.wikipedia.org/wiki/Elbow_method_(clustering))).

13.4 Numerical Examples

K-means clustering will now be used for automatically picking of the stacking velocity from semblance panels (Yilmaz, 2001). Hierarchical cluster analysis is used to identify different clusters of stacking velocities with high semblance values in the semblance panel. The centroids of each cluster are then connected to form the stacking velocity curve.

13.4.1 Picking Stacking Velocities by K-means Cluster Analysis

Seismic data generated by a single shot (see Figure 13.4a) are most often too noisy to be used for imaging the subsurface properties. In particular, the primary reflections are degraded by both random and coherent noise. To increase the SNR level of the primaries, primary reflections from the same subsurface reflection point at $\mathbf{x} = (x_o, z)$ are generated by shots at different locations. The traces where the midpoints of the sources and receivers have the same midpoint coordinate¹ x_o are assembled into a *common midpoint gather* (CMG) as illustrated in Figure 13.4b. The *common midpoint* reflections from the same reflector are shifted in time so they all align with one another (see Figure 13.4c), and then they are stacked together to get the stacked trace in Figure 13.4d with an increased SNR. This alignment time is the two-way zero-offset time T_o of a zero-offset primary reflection reflecting at \mathbf{x} ; here, zero-offset refers to the fact that the separation between the source and receiver has zero offset and both are located at $(x_o, 0)$ on the horizontal free surface. This assumes a layered medium and we use semblance analysis (Yilmaz, 2001) to find the best way to time shift and stack the traces to get the primary reflection with the best SNR. As illustrated in Figure 13.5, the goal of semblance analysis is to find the stacking velocity V_{stack} as a function of two-way zero-offset traveltimes T_o such that the hyperbola

$$t(x, V_{stack}) = \sqrt{\frac{x^2}{V_{stack}^2} + T_o^2}, \quad (13.10)$$

best fits the reflections in a common midpoint gather. Here, the midpoint coordinate is $x_o = (x_r - x_s)/2$ and the offset between the source and receiver is $x = x_r - x_s$. The primary reflections in each trace $d(x, t)$ approximately follow the traveltimes in equation 13.10 for the correct values of V_o and T_o , so the stacking procedure uses the semblance equation given by

$$S(V_{stack}, T_o) = \frac{\sum_x d(x, t(x, V_{stack}))}{\sum_x d(x, t(x, V_{stack}))^2}, \quad (13.11)$$

where $S(V_{stack}, T_o)$ is the semblance panel associated with the midpoint coordinate $x_o = (x_r - x_s)/2$. To generate a smooth semblance panel, the trace amplitudes are typically stacked together along a half-period wide strip centered about the moveout curve described in equation 13.10. The black curve in Figure 13.5 joining the peak values of the semblance energy are picked as the best estimate of the stacking velocity $V_{stack}(T_o)$ as a function of zero-offset traveltimes T_o . This optimal stacking velocity produces the optimal "stacked" trace at zero-offset, where optimal corresponds to reflection events with the highest signal-to-noise ratio.

¹For pedagogical convenience, we assume a 2D survey geometry and a layered medium where the sources and receivers are along a line on a horizontal free surface.

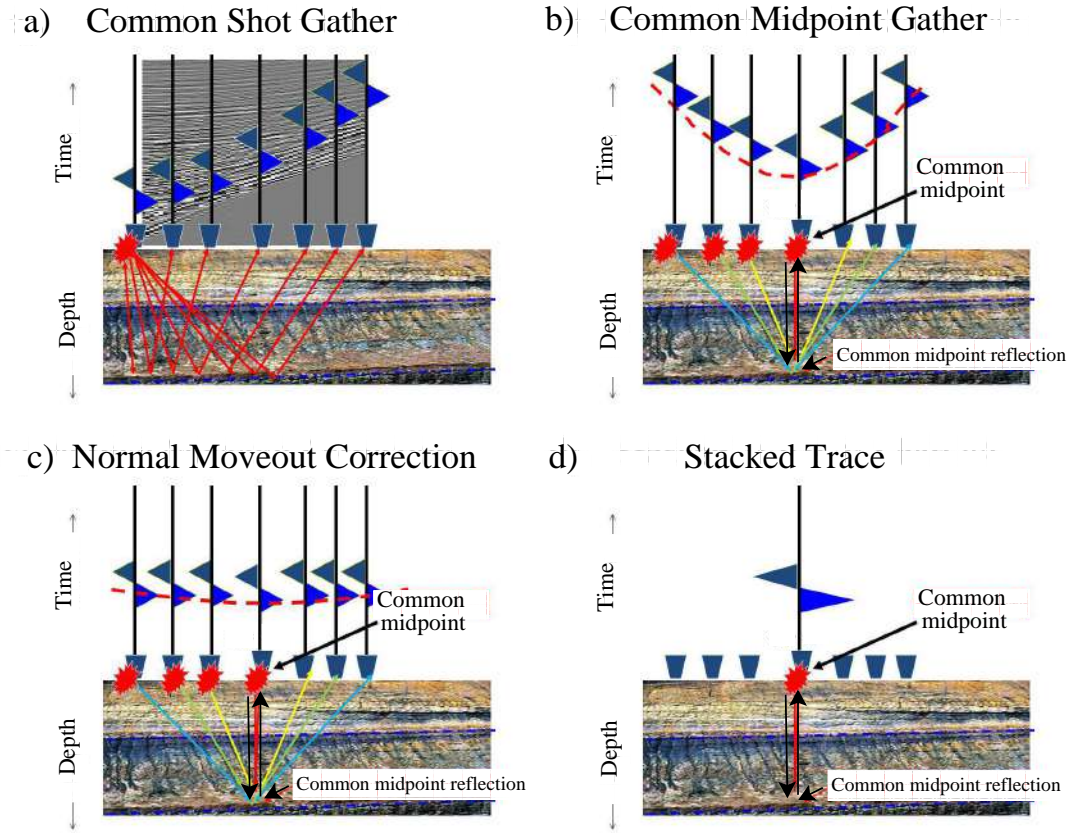


Figure 13.4: Simple processing steps for seismic data recorded over a layered medium, where the layers are mostly horizontal. a) common shot gather where a single source is recorded by all of the geophones to form a common shot gather (CSG) of traces. b) The traces from many CSGs can be reassembled to form a common midpoint gather (CMG) where a trace associated with each source-receiver pair has the same midpoint position on the surface. The common subsurface reflection point is known as the common reflection point; if the interface is dipping then rays associated with traces in the same CMG do not share a common reflection point. c) Traces after time shifting the CMG traces to align with the zero-offset trace. d) The stacked trace is formed by adding the normal moveout (NMO) corrected traces. In this case the fold is 7 and the signal/noise is enhanced by a factor of $\sqrt{7}$ if there is only additive white noise in the traces. This stacked trace approximates a zero-offset (ZO) trace where the source and geophone are coincident with one another.

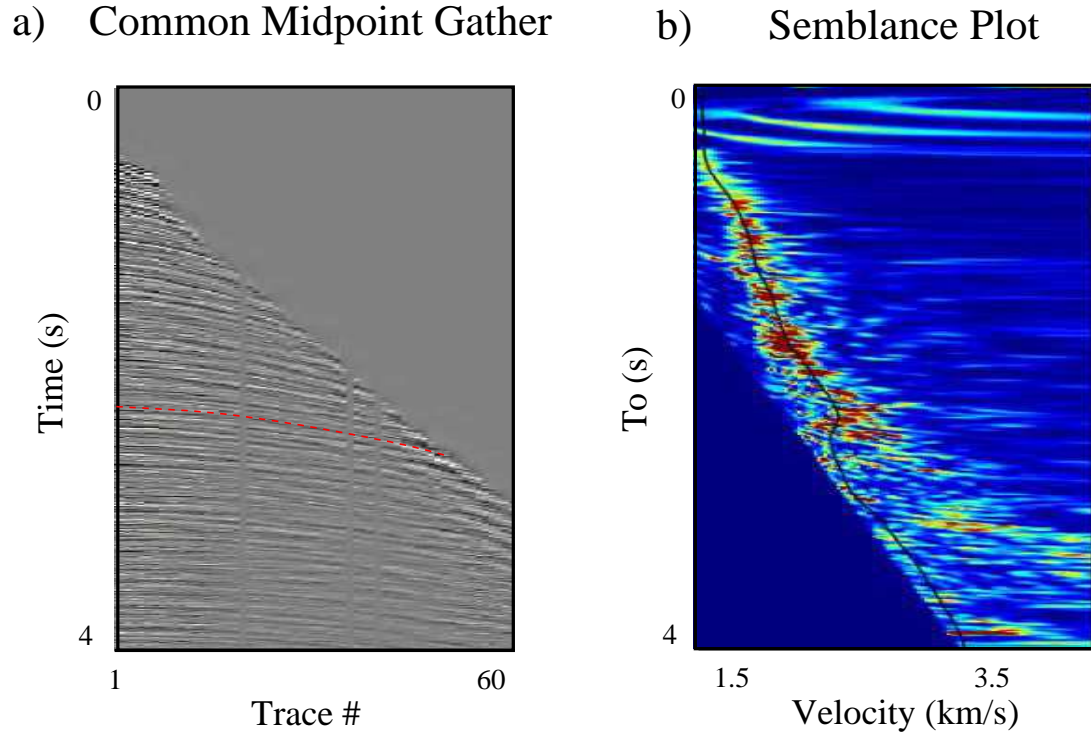


Figure 13.5: a) Common midpoint gather of traces assembled from traces recorded by a seismic reflection survey. For a dense survey, a shot can be located at each source position. The traces in a) are summed and weighted along different hyperbolas (e.g., the red dashed curve) described by equation 13.3 for different values of V_{stack} and T_o to get the semblance plot shown in b). The black line in b) describes the stacking velocity curve that is used to estimate the velocity as a function of depth. Images extracted from <http://www.ahay.org/RSF/book/geo384s/hw3/nmo/Fig/cmp700.png>.

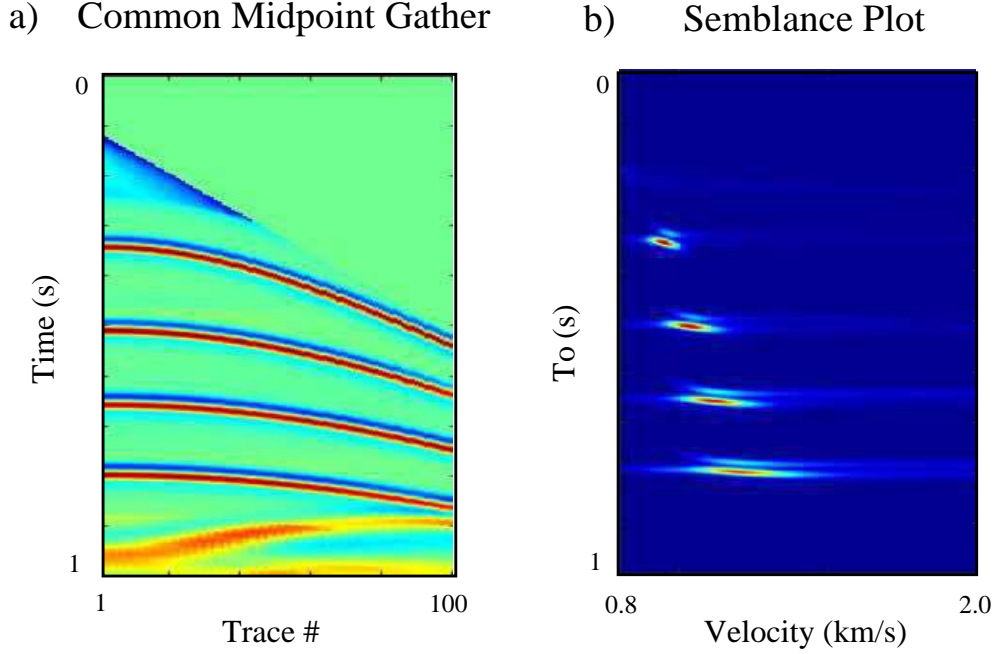


Figure 13.6: a) Common midpoint gather (CMG) for a 5-layer velocity model and b) semblance spectrum, Plots courtesy of Yuqing Chen (2018a-2018b).

The problem with picking the semblance curve in Figure 13.5 is that it can easily get confused by strong noise or by free-surface multiples that stack in coherently. In this case, semblance curves must be manually picked by hand which can be extremely time consuming for large 3D data sets. To mitigate this expense, Chen (2018a-2018b) proposed a bottom-up method for K-means clustering to automatically group the large energy events in $S(V_{stack}, T_o)$ into different clusters.

He proposed the following algorithm.

1. Set the initial number of clusters $K=4$. Assign the centroid point of the k cluster to be $(V_o^{(k)}, T_o^{(k)})$. These K points are selected at equi-spaced T_o intervals along an initial semblance curve.
2. Apply K-means clustering for several iterations until a stable group of K clusters has emerged.
3. Increment the value of K by 1 and repeat step 2. The value of K is incrementally increased until the residual misfit in equation 13.3 does not decrease by a significant amount.
4. The centroids of the final cluster are used to form the final semblance curve.

As an example, the bottom-up K-means algorithm is applied to the common midpoint gather (CMG) in Figure 13.6a. Here, the data are computed for a five-layer velocity model and the semblance spectrum is shown in Figure 13.6b. The bottom-up K-means clustering

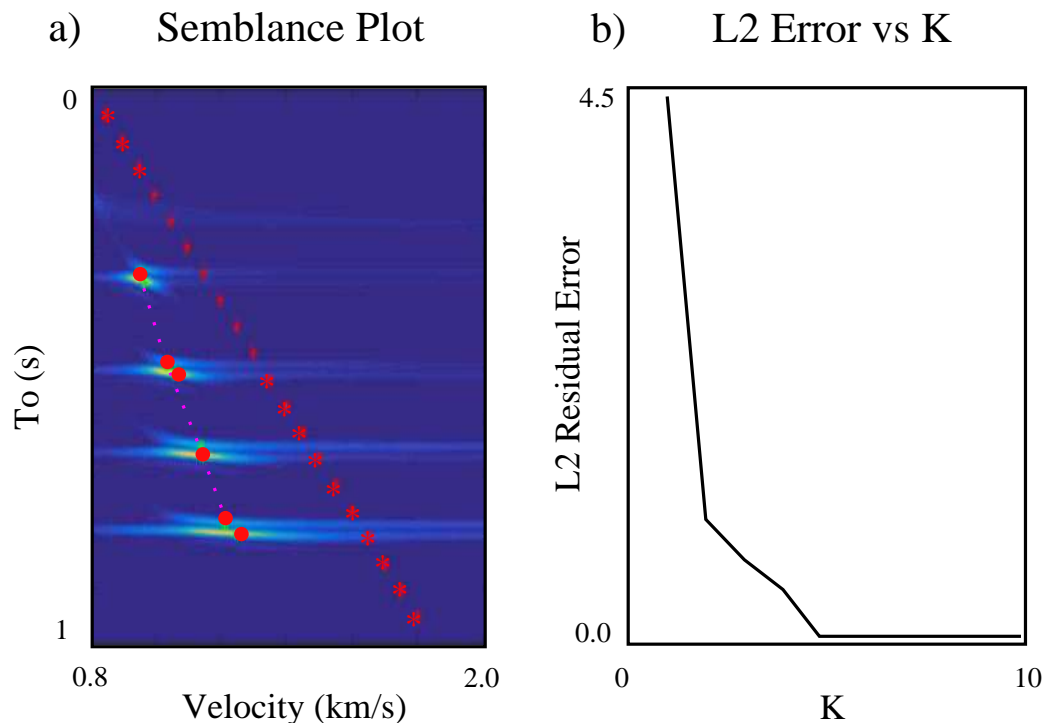


Figure 13.7: a) Final cluster configuration where the centroid of each cluster is marked by a red dot. The red stars are the initial starting model and b) denotes the sum of the squared residuals plotted against the number of clusters K . Plots courtesy of Yuqing Chen (2018a-2018b).

algorithm is used to pick the clusters for $1 \leq K \leq 10$. curve using the K-means clustering algorithm. Six clusters, with centroids denoted by the red dots in Figure 13.7a, were found to be optimal before the decrease in the L_2 residual became negligible in b). These centroids are connected by the dashed magenta line, which agrees with the one manually picked from the semblance plot.

A more challenging example is to estimate the semblance curve from data generated from the Marmousi model in Figure 13.8a. In this case, there are 100 traces in most of the common midpoint gathers, and the semblance curve is shown in Figure 13.8b. Here, the number of clusters was selected to be $K = 12$ because this represented the largest cluster number before the error decrease became small. A plot of misfit values against cluster numbers is shown in Figure 13.8c.

A final example is the field data shown in Figure 13.9a. The semblance spectrum by the K-means algorithm is shown in Figure 13.9b and agrees well with the one estimated by a human interpreter. The misfit error plotted against K in Figure 13.9c suggests that $K = 12$ is the optimal number of clusters.

One of the problems with semblance analysis for marine data is that free-surface multiples can contribute to strong semblance energy at stacking velocities near that of the water velocity. In this case constraints should be imposed to steer the K-means picking algorithm

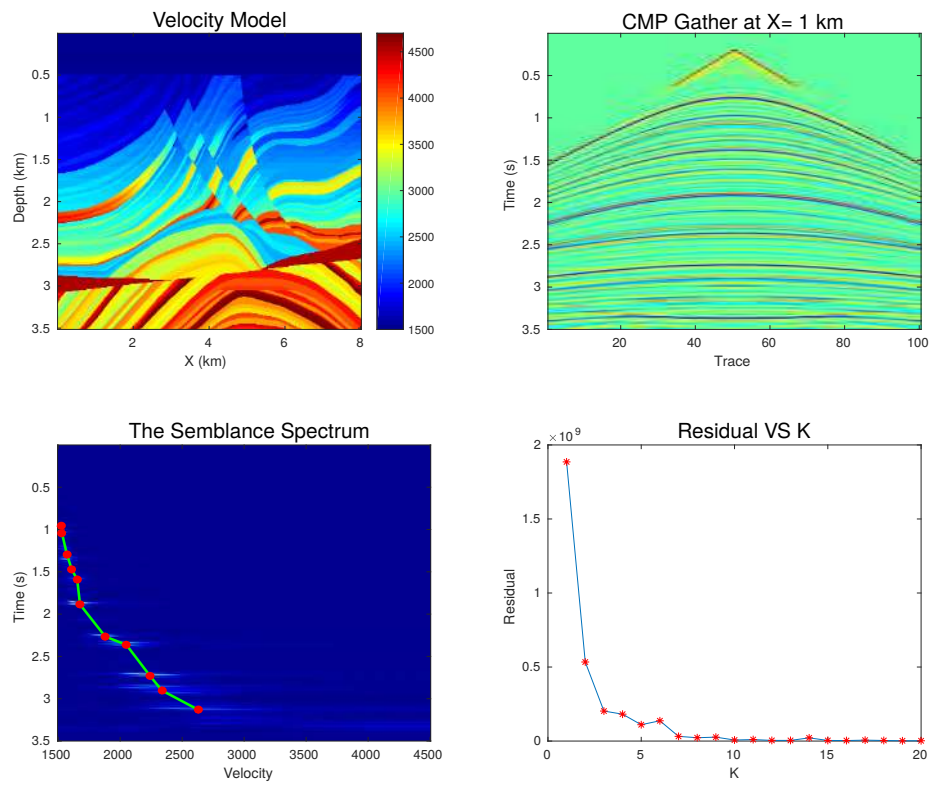


Figure 13.8: a) Marmousi model, b) common-midpoint gather, c) semblance spectrum with centroids picked by the K-means algorithm, and d) plot of L_2 norm of residuals vs K (Chen, 2018a).

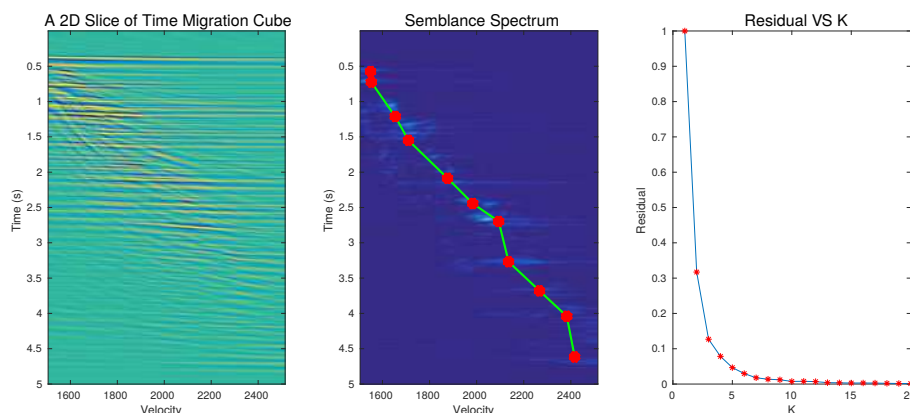


Figure 13.9: a) A 2D slice of the time migration cube of Gulf of Mexico (GOM) data at $X = 1$ km and b) semblance spectrum with the semblance curve picked from the centroids of the final cluster configuration. c) Misfit error plotted against K , the number of clusters (Chen, 2018a).

away from choosing the semblance curve associated with multiples. See Exercises 4-5.

The IWC algorithm described in equation 13.9 is now applied to the GOM data. The starting cluster points are shown as 15 red dots along the lines in Figures 13.10b and 13.10d. The IWC algorithm converged to the red dots intersecting the black curves in Figures 13.10a and 13.10c. These auto-picked curves ignored the multiples at the lower semblance velocity because the IWC algorithm weighted the clusters points with the amplitude of the semblance values in Figures 13.10b and 13.10d. The semblance values for the primaries appear to be much larger than those for the perceived multiples.

13.5 Summary

The advantage of unsupervised clustering is there is no manual labeling of the data prior to clustering. As demonstrated by the semblance examples, this approach can avoid manual labor in estimating the initial velocity model from semblance panels. For semblance analysis, any final choice of stacking velocity curves should be vetted by a skilled interpreter.

If the data have strong coherent noise then the clustering algorithm can erroneously pick the wrong velocity models. In this case constraints can be imposed to avoid the characteristic low velocities of free-surface multiples. In this case, the constrained clustering algorithm illustrated in Figure 13.2c would be appropriate. Another possibility is a semi-supervised clustering algorithm because a few labeled data serve as groundtruth anchors that can steer the algorithm away from incorrect cluster memberships. Another alternative is the IWC algorithm which weights each cluster point with a weight that is proportional to the information content of that point.

A different geoscience problem might require a clustering algorithm tuned to that problem. In that case, studying some of the many other variations of cluster algorithm might provide the right algorithm or ideas for solving your problem.

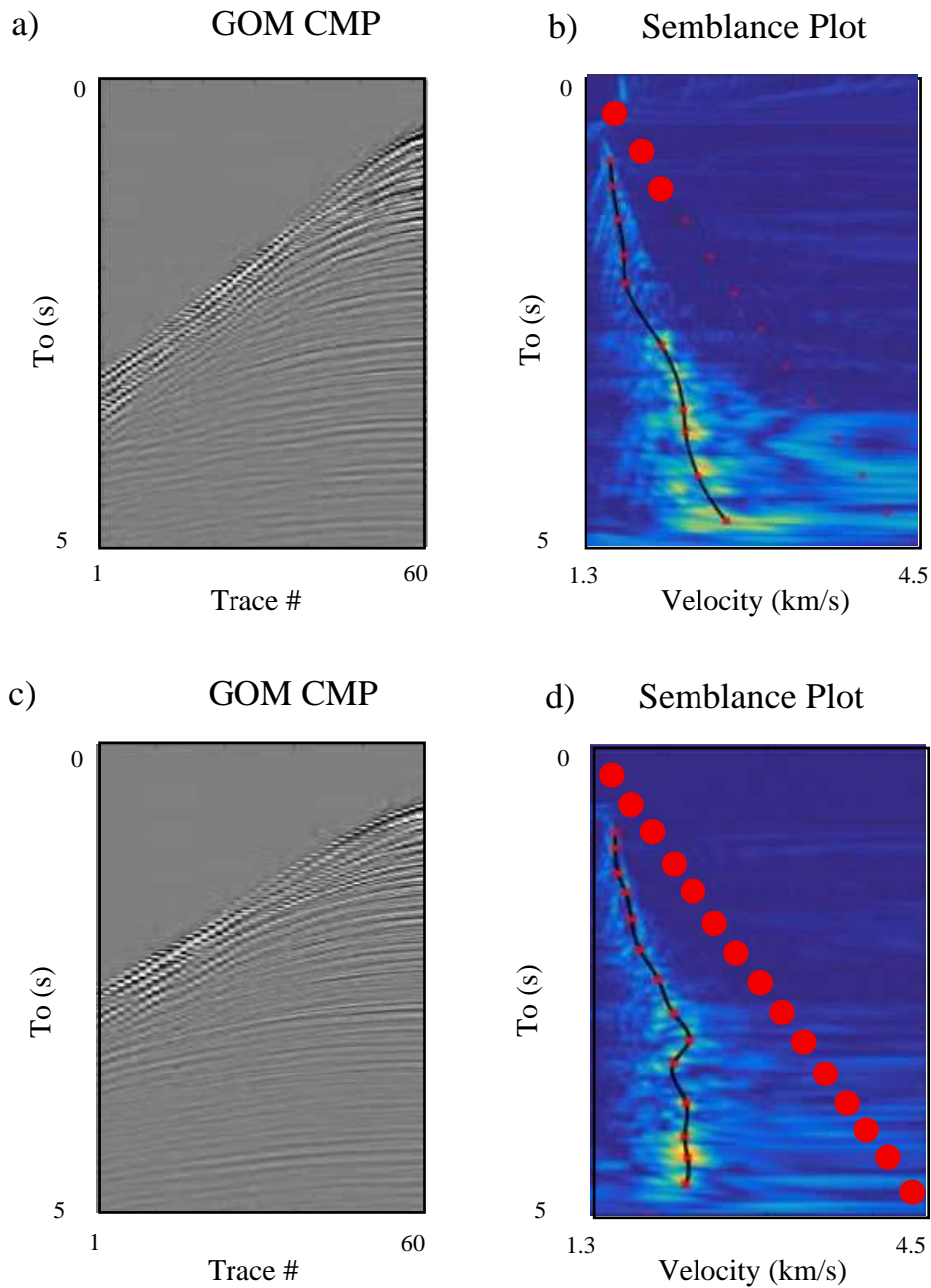


Figure 13.10: Common midpoint gathers and (right column) semblance images picked by the IWC algorithm where the large red points along a line are the initial cluster points and the black line is through the final red cluster points (Chen, 2018b). Note, there are 15 initial cluster points and the final number is 14.

13.6 Exercises

1. Create a Ricker wavelet with the MATLAB commands:

```
% dt = time sampling interval
% np = # of points in Ricker wavelet
% fr = peak frequency of Ricker wavelet in Hz
npt=np*dt;
t=(-npt/2):dt:npt/2;
rick1=(1-t.*t*fr^2*pi^2).*exp(-t.^2*pi^2*fr^2);
rick=rick1(round(np/2)-round(1/fr/dt)+1:np);
l=length(rick);plot([0:l-1]*dt,rick);
xlabel('Time (s)');
title([num2str(fr),' Hz Ricker Wavelet']);
```

Your task will be to examine the seismograms in Figure 13.6a and determine the values of dt and fr from the CMG traces. This CMG is in the 2001×101 matrix "seis". The "seis" file can be obtained by downloading Labs\Cluster\Yuqing\csg_2001_101.bin and typing `fp=fopen('csg_2001_101.bin','rb');` `seis=fread(fp,[2001,101],'float');`. Type `imagesc(seis)` to view this trace.

Create a new 2001×101 matrix "seis1" where the each trace has one event that honors the moveout traveltime in equation 13.10 with velocity $V = 0.6 \text{ km/s}$ and $T_o = 0.5\text{s}$. Each trace has 2001 samples can be created by forming a 2001×1 vector of zeros, and adding onto it the Ricker wavelet shifted by the number of time samples for that offset x .

2. Download

```
Labs\Cluster\Yuqing\K_means,
Labs\Cluster\Yuqing\agc.m,
Labs\Cluster\Yuqing\csg_2001_101.bin,
Labs\Cluster\Yuqing\data_3500_100.bin,
Labs\Cluster\Yuqing\dist_1_101.bin,
Labs\Cluster\Yuqing\dist_100_1.bin,
Labs\Cluster\Yuqing\main_cluster.m,
Labs\Cluster\Yuqing\Normalize.m,
and Labs\Cluster\Yuqing\ricker.m.
```

and type the command `K_means.m`. This will iteratively generate the sequence of clusters from $K = 1$ to $K = 10$ for the semblance plot in Figure 13.6b. After running "K-means.m", type the command `imagesc(seis)` and you will get the CMG seen in Figure 13.6a. Add onto the CMG matrix "seis" the matrix "seis1" you created in the previous exercise.

Now run "K-means.m" again and determine if this new set of events becomes its own cluster. Does it have the correct moveout velocity and zero-offset traveltime in the semblance panel?

3. Now generate 5 sets of reflection events, each with a moveout velocity $V = 0.6$ km/s but with $T_0 = [0.2, 0.4, 0.6, 0.8, 0.9]$. The events in each trace have the same Ricker wavelet that can be associated with a free-surface multiple with much lower velocity than the primaries. Add the CMG corresponding to these new events to the "seis" matrix. Rerun `K_means.m` with both the multiples and primaries in "seis". Do the multiples have their own cluster? If they do then the picked stacking velocity curve jumps between the primary and multiples velocities, which is undesirable. Your desire is to only stack in the primaries.
4. Devise different constrained clustering algorithms that can be used to exclusively cluster the primaries and ignore the multiples. Can you use a supervised SVM or neural network to exclude multiples clusters?
5. Implement your best clustering algorithm that ignores multiples.

Chapter 14

Principal Component Analysis

Principal component analysis (PCA) is an unsupervised machine learning method that finds an orthogonal coordinate system that maximizes the variability of the components along one axis. The demeaned data points \mathbf{x} are used to compute a data covariance matrix $\mathbf{X}^T \mathbf{X}$ and its eigenvectors and eigenvalues. The eigenvector associated with the largest eigenvalue is parallel to the principal component axis. This procedure is used to automatically separate correlated data points so different classes are more easily identified and separated from one another.

14.1 Introduction

Principal component analysis (PCA) is an unsupervised machine learning method that finds an orthogonal coordinate system that maximizes the variability of the components along one axis. For example, if the points (x_1, x_2) correlated along the 45° line in Figure 14.1 are plotted over the range $-1 < x < 1$, then both their x-components and y-components vary by a range of 2 units. If the coordinate system is rotated by 45° then the variation of the components along the slanted line, denoted as the principal axis, has the maximum range of $\sqrt{1^2 + 1^2} = 2\sqrt{2} > 2$ units. In contrast, there is a much smaller variation of the point projections along the orthogonal axis tilted at 135° . Information spread out over a wider range of units are often easier to separate from one another compared to tightly bunched points. Hence, PCA is an unsupervised ML method that can more easily separate correlated data into different classes based on their locations along the principal axis. Therefore the two key ideas with PCA is that it finds a coordinate system which maximizes the variability of the components of the points along the *principal component axis*, and therefore enhances the ability to automatically separate and filter them from one another.

PCA was introduced by Pearson (1901) and independently developed by Hotelling (1936). For different fields of science and engineering, the PCA goes by different names such as the KLT transform in signal processing, the Hotelling transform in multivariate quality control, and the singular value decomposition that is used in many different fields (Golub and Van Loan, 1996). The Machine Learning community uses PCA as an unsupervised learning method that, combined with a clustering algorithm, can classify unlabeled data into different classes if the data have distinct correlations in the different classes.

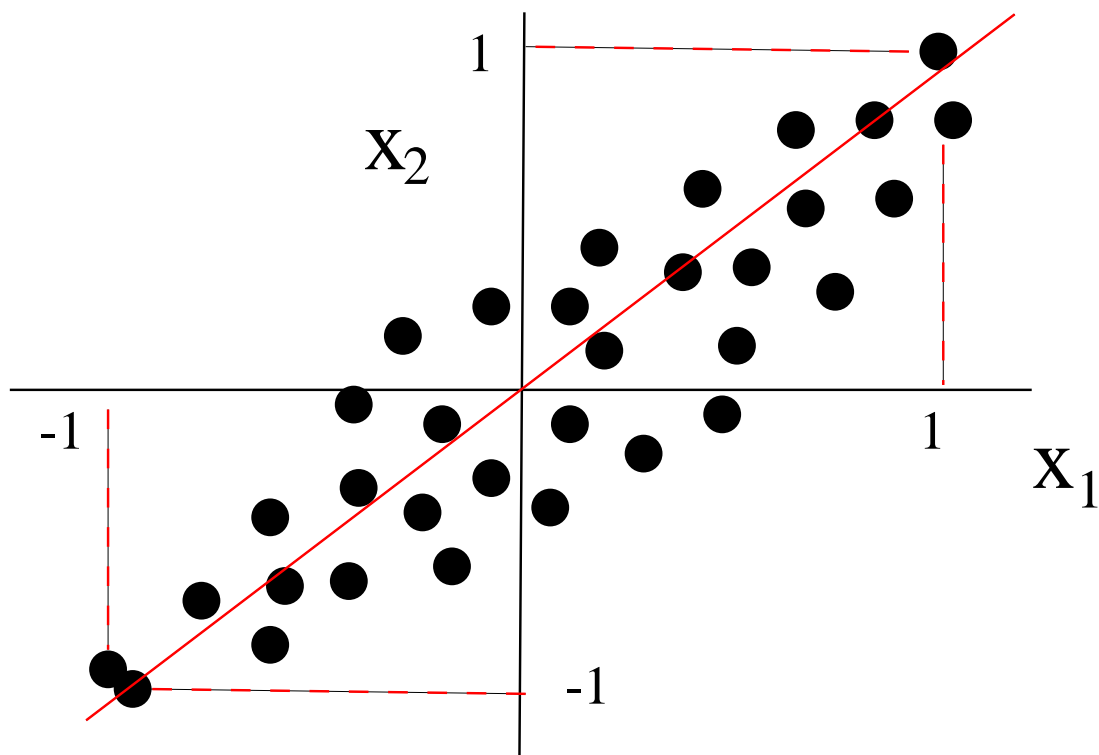


Figure 14.1: Elliptical cloud of points where the projections on the horizontal and vertical axis vary over the range $-1 \geq x, y \geq 1$.

Figure 14.2: Two 2×2 migration images, denoted as Mig1 and Mig2, are used to form the data covariance matrix $\mathbf{X}^T \mathbf{X}$.

The following sections describe the theory of PCA, and then demonstrates it with a simple example. This is followed by some applications to geoscience problems. Finally we show how PCA can be used with a clustering algorithm for automatic classification of points.

14.2 Theory of Principal Component Analysis

Assume \mathbf{x} is an $N \times 1$ vector where each component x_n is a random variable governed by a Gaussian probability distribution with mean value $\mu_n = 0$. This means that the data \mathbf{x} should be demeaned before applying PCA. The data covariance matrix $\langle \mathbf{x}^T \cdot \mathbf{x} \rangle$ for zero-mean data is then defined as

$$\begin{aligned} \langle \mathbf{x}^T \cdot \mathbf{x} \rangle &= \left\langle \begin{pmatrix} x_1 \\ x_2 \\ \vdots \\ x_N \end{pmatrix} \begin{pmatrix} x_1 & x_2 & \dots & x_N \end{pmatrix} \right\rangle \\ &= \begin{bmatrix} \langle x_1 x_1 \rangle & \langle x_1 x_2 \rangle & \dots & \langle x_1 x_N \rangle \\ \langle x_2 x_1 \rangle & \langle x_2 x_2 \rangle & \dots & \langle x_2 x_N \rangle \\ \vdots & \vdots & \ddots & \vdots \\ \langle x_N x_1 \rangle & \langle x_N x_2 \rangle & \dots & \langle x_N x_N \rangle \end{bmatrix}, \end{aligned} \quad (14.1)$$

where $\langle \rangle$ indicates averaging of the random variable x_i over the infinite set of experimental outcomes, which we call an ensemble.

Unfortunately we only have a finite set of experimental outcomes where $x_n^{(i)}$ is denoted as the outcome of the i^{th} experiment for the n^{th} random variable. The covariance can then be approximated $\langle x_n x_m \rangle \approx \frac{1}{I-1} \sum_{i=1}^N x_n^{(i)} x_m^{(i)}$ where I is the number of experiments. As an example, consider the $i = 1$ and $i = 2$ migration images in Figure 14.2 where the 2×2 matrices of migration intensity values have been *vectorized* into the 4×1 vector $\mathbf{x}^{(i)}$ for $i = 1, 2$. These idealized migration images depict the subsurface reflectivity distribution for two different source locations on the surface. The migration intensity value $x_n^{(i)}$ at the n^{th} pixel can be considered as a random variable with values $1 \geq x_n \geq 256$.

The mean value of the x_n random variable in the n^{th} pixel can be approximated as

$$\mu_n \approx \frac{1}{I} \sum_{i=1}^I x_n^{(i)}, \quad (14.2)$$

This mean value is used to demean the migration image at each pixel so that covariances in Figure 14.1 can be approximated as

$$\langle x_n x_m \rangle \approx \frac{1}{I-1} \sum_{i=1}^I (x_n^{(i)} - \mu_n)(x_m^{(i)} - \mu_m). \quad (14.3)$$

In all further discussion we assume that the random variables in \mathbf{x} have been demeaned so $\mu_n = 0$. Sometimes the feature vector is composed of elements with different units, which can be accounted for by dividing the elements by the appropriate standard deviation (Coates et al., 2011).

The goal of PCA is to find the $N \times 1$ principal axis vector \mathbf{a} that maximizes the variability of the projection of the $N \times 1$ vector \mathbf{x} onto \mathbf{a} . This projection $\mathbf{x}^T \cdot \mathbf{a}$ is interpreted as the length between the origin and the projected point along \mathbf{a} , denoted as x_1 in Figure 14.1 for \mathbf{a} taken as the horizontal axis. Mathematically this principal axis vector is found by finding the unit vector \mathbf{a} that maximizes the sum of the squared lengths $(\mathbf{x}^{(i)T} \cdot \mathbf{a})^2$:

$$\begin{aligned} \epsilon &= \frac{1}{N-1} \overbrace{\sum_{i=1}^N (\mathbf{a}^T \cdot \mathbf{x}^{(i)}) (\mathbf{x}^{(i)T} \cdot \mathbf{a})}^{\text{sum of squared lengths of } \mathbf{x}^{(i)} \text{ projected onto } \mathbf{a}} + \lambda(1 - \mathbf{a}^T \cdot \mathbf{a}), \\ &= \mathbf{a}^T \left(\frac{1}{N-1} \sum_{i=1}^N [\mathbf{x}^{(i)} \mathbf{x}^{(i)T}] \right) \mathbf{a} + \lambda(1 - \mathbf{a}^T \cdot \mathbf{a}), \end{aligned} \quad (14.4)$$

where $[\mathbf{x}^{(i)} \mathbf{x}^{(i)T}]$ is the $N \times N$ outer product matrix and $\lambda > 0$ is the Lagrange multiplier condition that insures that \mathbf{a} is a unit vector. The data covariance matrix approximated from two migration images is depicted in Figure 14.2.

The stationary condition $\partial\epsilon/\partial a_i = 0 \forall i$ for equation 14.4 leads to

$$\mathbf{X}^T \mathbf{X} \mathbf{a} = \lambda \mathbf{a}, \quad (14.5)$$

where $\|\mathbf{a}\| = 1$ and $\mathbf{X}^T \mathbf{X} = \frac{1}{N-1} \sum_{i=1}^N [\mathbf{x}^{(i)} \mathbf{x}^{(i)T}]$ is the numerical data covariance matrix that approximates the actual one in equation 14.1. The solution to equation 14.5 solves the eigenvalue problem, and the unit eigenvector \mathbf{a}_n with the largest eigenvalue λ_n maximizes the objective function ϵ in equation 14.4.

Since the $N \times N$ matrix $\mathbf{X}^T \mathbf{X}$ is real and symmetric then there are N real eigenvalues λ_n where the N eigenvectors \mathbf{a}_n are orthogonal and have unit length. Each eigenvector \mathbf{a}_n defines one of the principal axes of the system. The physical interpretation of λ_n is that it is equal to the sum of the squared lengths of the projections of the points $\mathbf{x}^{(i)}$ along the n^{th} principal axis. Therefore, the eigenvector with the largest eigenvalue λ_n defines the maximum principal axis vector \mathbf{a}_n with the largest variation of projections $\mathbf{x}^{(i)}$ onto this axis.

14.2.1 Simple Example

As a simple example, apply PCA to the two points $\mathbf{x}^{(1)} = (1, 1)^T$ and $\mathbf{x}^{(2)} = (-1, -1)^T$ plotted in Figure 14.3. In this case

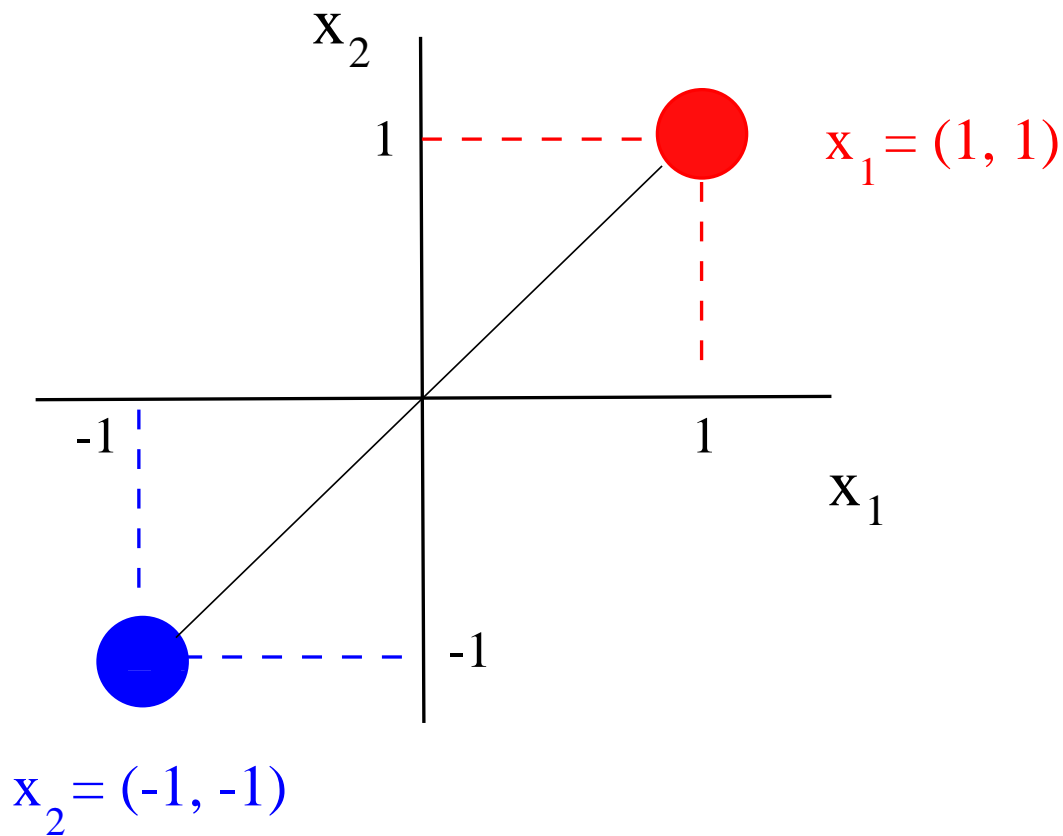


Figure 14.3: The sum of the squared projections $|(1, 0)^T \cdot \mathbf{x}^{(1)}|^2 + |(1, 0)^T \cdot \mathbf{x}^{(2)}|^2 = (1)^2 + (-1)^2$ on the x -axis is equal to 2. The sum of the squared projections of $\mathbf{x}^{(1)}$ and $\mathbf{x}^{(2)}$ on the slanted red unit vector $(1, 1)/\sqrt{2}$ is even larger at $|\left(\frac{1}{\sqrt{2}}, \frac{1}{\sqrt{2}}\right)^T \cdot \mathbf{x}^{(1)}|^2 + |\left(\frac{1}{\sqrt{2}}, \frac{1}{\sqrt{2}}\right)^T \cdot \mathbf{x}^{(2)}|^2 = 4$.

$$\begin{aligned}
\mathbf{X}^T \mathbf{X} &= \begin{pmatrix} x_1^{(1)} \\ x_2^{(1)} \end{pmatrix} \begin{pmatrix} x_1^{(1)} & x_2^{(1)} \end{pmatrix} + \begin{pmatrix} x_1^{(2)} \\ x_2^{(2)} \end{pmatrix} \begin{pmatrix} x_1^{(2)} & x_2^{(2)} \end{pmatrix}, \\
&= \begin{bmatrix} x_1^{(1)} & x_1^{(2)} \\ x_2^{(1)} & x_2^{(2)} \end{bmatrix} \begin{bmatrix} x_1^{(1)} & x_2^{(1)} \\ x_1^{(2)} & x_2^{(2)} \end{bmatrix}, \\
&= \begin{bmatrix} 1 & -1 \\ 1 & -1 \end{bmatrix} \begin{bmatrix} 1 & 1 \\ -1 & -1 \end{bmatrix}, \\
&= \begin{bmatrix} 2 & 2 \\ 2 & 2 \end{bmatrix}.
\end{aligned} \tag{14.6}$$

The eigenvalues of this matrix can be found by setting the determinant $|\mathbf{X}^T \mathbf{X} - \lambda \mathbf{I}|$ to zero:

$$\begin{aligned}
|\mathbf{X}^T \mathbf{X} - \lambda \mathbf{I}| &= \left| \begin{bmatrix} 2 - \lambda & 2 \\ 2 & 2 - \lambda \end{bmatrix} \right|, \\
&= (2 - \lambda)^2 - 4 = 0,
\end{aligned} \tag{14.7}$$

where the two eigenvalues are $\lambda_1 = 4$ and $\lambda_2 = 0$ and their normalized eigenvectors are, respectively, $\mathbf{a}_1 = (1, 1)/\sqrt{2}$ and $\mathbf{a}_2 = (1, -1)/\sqrt{2}$.

The first eigenvector \mathbf{a}_1 is parallel to the maximum principal axis and is slanted at 45° to the horizontal as shown in Figure 14.3. It is obvious that the projections $\mathbf{a}_1^{(T)} \cdot \mathbf{x}^{(1)} = \sqrt{2}$ and $\mathbf{a}_1^{(T)} \cdot \mathbf{x}^{(2)} = -\sqrt{2}$ on the principal axis now have their maximum variation along this line. That is, the sum of the squared lengths of these projections is equal to the eigenvalue $\lambda_1 = 4$. The two points have zero projection along the other principle axis vector \mathbf{a}_2 , which is consistent with the nil eigenvalue $\lambda_2 = 0$.

14.2.2 Filtering the PCA Components

The original image $\mathbf{x}^{(i)}$ can be expressed as a weighted sum of eigenvectors:

$$\mathbf{x}^{(i)} = \sum_{n=1}^N (\mathbf{a}_n^T \cdot \mathbf{x}^{(i)}) \mathbf{a}_n, \tag{14.8}$$

where $\mathbf{a}_n^T \cdot \mathbf{x}^{(i)}$ is the projection of the i^{th} migration image onto the n^{th} principal component vector. Here, the increasing value of the eigenvector index $n \in [1, 2 \dots n]$ is associated with the decreasing magnitude of the eigenvalue. The goal now is to filter the migration image to retain coherent signal and reduce the random additive noise.

The random noise in the migration image is often uncorrelated with itself (and assumed to be uncorrelated with the signal) so it does not contribute much to the element values of the data covariance matrix. This suggests that the eigenvectors associated with small eigenvalues are largely due to the additive noise, while the larger eigenvalues are associated with the coherent reflection image. To filter out this noise, a rule-of-thumb is to only keep the eigenvector components from $n = 1 \dots N_{cutoff}$ in equation 14.8 that contribute about 70% of the energy. Thus we take the upper limit in the sum to be $N_{cutoff} \ll N$, where

$$\frac{\sum_{n=1}^{N_{cutoff}} |\lambda_n|}{\sum_{n=1}^N |\lambda_n|} \approx 0.7. \tag{14.9}$$

14.2.3 Clustering the PCA Components

Chapter 15

Sparse Coding

Chapter 16

Generative Adversarial Networks

Chapter 17

Compressive Sensing and Neural Networks

References

- Aki, K. and P. Richards, 2002, *Quantitative Seismology*: University Science Books.
- AlRegib, G., M. Deriche, Z. Long, H. Di, Z. Wang, Y. Alaudah, M. A. Shaq, and M. Alfarraj, 2018, Subsurface structure analysis using computational interpretation and learning: A visual signal processing perspective: *IEEE Signal Processing Magazine*, **35**, 82-98.
- Ball, G. and Hall, D., 1965, ISODATA, a novel method of data analysis and pattern classification: Technical report NTIS, AD 699616. Stanford Research Institute, Stanford, CA.
- Barala, S. and P. Mohanty, 2016, Enhancement of geologic interpretation using a new post-stack seismic attribute: 2016 SEG International Exposition and Annual Meeting, Society of Exploration Geophysicists, 1677-1681.
- Barghout, L., 2015, Spatial-Taxon information granules as used in iterative fuzzy-decision-making for image segmentation: *Granular Computing and Decision-Making*, Springer International Publishing, 285-318.
- Bishop, C., 2006, *Pattern Recognition and Machine Learning*: Springer Press.
- Boonyasiriwat, C., P. Valasek, P. Routh, B. Macy, W. Cao, and G. T. Schuster, 2009, A multiscale method for time-domain waveform tomography: *Geophysics* **74**, WCC59-WCC68.
- Boyd, S. and L. Vandenberghe, 2004, *Convex Optimization*, Cambridge University Press. p. 216.
- Bunks, C., F. Saleck, S. Zaleski, and G. Chavent, 1995, Multiscale seismic waveform inversion: *Geophysics*, **60**, 1457-1473.
- Chen, Q., and S. Sidney, 1997, Seismic attribute technology for reservoir forecasting and monitoring: *The Leading Edge*, **16**, 445-448.
- Chen, Y., 2018a, K-means clustering for picking stacking velocity curves in semblance panels: CSIM midyear report.
- Chen, Y., 2018b, Automatic Semblance Picking by a Bottom-up Clustering Method workshop: October, 2018 SEG Maximizing Asset Value through Artificial Intelligence and Machine Learning Workshop in Beijing.
- Chopra, S., and K. Marfurt, 2006, Seismic attributes-a promising aid for geologic prediction: *CSEG Recorder*, **31**, 110-120.

Ciresan, D. C., A. Giusti, L. M. Gambardella, and J. Schmidhuber, 2013, Mitosis detection in breast cancer histology images with deep neural networks: International Conference on Medical Image Computing and Computer-assisted Intervention, Springer, 411-418.

Claerbout, J. F., 1992, Earth Soundings Analysis: Processing vs Inversion: Blackwell Scientific Inc.

Coates, A., H. Lee, and A. Ng, 2011, An analysis of single-layer networks in unsupervised feature learning: Proceedings of the Fourteenth International Conference on Artificial Intelligence and Statistics, PMLR, 215–223.

Cortes, C., and V. Vapnik, 1995, Support-vector networks: Machine Learning, 20, 273–297. Artificial Intelligence and Statistics, PMLR, 215–223.

Elad, A, 2018, Sparse modeling in image processing and deep learning:

"<https://www.youtube.com/playlist?list=PL0H3pMD88m8W39EbuArGLa9yXk8q6QGip>"

DeCoste, D., 2002, Training invariant support vector machines: Machine Learning. 46, 161–190.

Gaonkar, B. and Davatzikos, C., 2013, Analytic estimation of statistical significance maps for support vector machine based multi-variate image analysis and classification: Neuroimage, 78, 270-283.

Geoffrion, A. M., 1971, Duality in nonlinear programming: A simplified applications-oriented development: SIAM Review, **13**, 1–37.

Fukushima, K., 1980, Neocognitron: A self-organizing neural network model for a mechanism of pattern recognition unaffected by shift in position: Biol. Cybernetics, **36**, 193–202.

Gaonkar, B. and Davatzikos, C., 2013, Analytic estimation of statistical significance maps for support vector machine based multi-variate image analysis and classification: NeuroImage, **78**, 270–83.

Gill, P., W. Murray, and M. Wright, 1981, Practical Optimization: Academic Press Inc.

Golub, G. and C. van Loan, 1996, Matrix Computations (4th edition): John Hopkins University Press.

Golub, G. and U. von Matt, 1997, Generalized cross-validation for large-scale problems: Journal of Computational and Graphical Statistics, **6**, 1–34.

Goodfellow, I., Y. Benigo, and A. Courville, 2016, Deep Learning, MIT Press.

Google, 2017, Tensorflow tutorials: convolutional neural networks, <https://www.tensorflow.org/tutorials/deep-cnn>, August 2017.

Goutte, C., P. Toft, E. Rostrup, F. Arup Nielsen, L.Hansen, 1999, On Clustering fMRI time series: *NeuroImage*, **9-3**, 298-310.

He, K., X. Zhang, S. Ren and J. Sun, 2016, Deep residual learning for image recognition: 2016 IEEE Conference on Computer Vision and Pattern Recognition (CVPR), DOI : 10.1109/CVPR.2016.90.

Hotelling, H., 1936,. Relations between two sets of variates: *Biometrika*, **28**, 321–377.

Hornik, K., 1991, Approximation capabilities of multilayer feedforward networks: *Neural Networks*, **4(2)**, 251-257.

Hornik, K., M. Stinchcombe, and H. White, 1989, Multilayer feedforward networks are universal approximators: *Neural Networks*, **2(5)**, 359-366.

Hubel, D. and T. Wiesel, 1962, Receptive fields, binocular interaction and functional architecture in cat's visual cortex: *J. Physiol.*, **160**, 106–154.

Jain, A., 2010, Data clustering: 50 years beyond K-means: *Pattern Recognition*, **31**, 651–666.

Jolliffe I.T., 2002, *Principal Component Analysis*: Springer Series in Statistics, 2nd ed., Springer, NY, 428 pages.

Kivinen, J., C. Williams, and N. Heess, 2014, Visual boundary prediction: A deep neural prediction network and quality dissection: *Artificial Intelligence and Statistics*, 512-521.

Krizhevsky, A., and G. Hinton, 2009, Learning multiple layers of features from tiny images: M.S. thesis, University of Toronto.

Krizhevsky, A., I. Sutskever, and G. E. Hinton, 2012, Imagenet classification with deep convolutional neural networks: *Advances in neural information processing systems*, 25, no. 2, 1097–1105.

Li, J., S. Hanafy and G.T. Schuster, 2018, Wave equation dispersion inversion of guided P waves in a waveguide of arbitrary geometry: *J. of Geophys. Research: Solid Earth*, **123**, 10.1029/2018JB016127.

Lines, L. R. and S. Treitel, 1984, Tutorial, review of least-squares inversion and its application to geophysical problems: *Geophysical Prospecting*, **32**, 159–186.

Liu, Z. and G.T. Schuster, 2018, Neural network least squares migration: 2018 Annual CSIM report.

LeCun, Y., L. Bottou, Y. Bengio, and P. Haffner, 1998, Gradient-based learning applied to document recognition: Proceedings of the IEEE.

LeCun, Y., Y. Bengio, and G. Hinton, 2015, Deep learning: Nature, **521**, 436.

Liu, Z., and K. Lu, 2018, Convolutional sparse coding for noise attenuation of seismic data, CSIM midyear report.

Lloyd, S., 1982. Least squares quantization in PCM: IEEE Trans. Inform. Theory 28, 129–137. Originally as an unpublished Bell laboratories Technical Note (1957).

Lu, K., J. Li, B. Guo, L. Fu, and G. Schuster, 2017, Tutorial for wave-equation inversion of skeletonized data: Interpretation, SO1–SO10.

Luo, Y., and G. T. Schuster, 1991a, Wave equation inversion of skeletonized geophysical data: Geophysical Journal International, 105, 289–294.

Luo, Y. and G. T. Schuster, 1991b, Wave equation traveltime inversion: Geophysics, **56**, 645–653.

MacQueen, J., 1967. Some methods for classification and analysis of multivariate observations: In *Fifth Berkeley Symposium on Mathematics. Statistics and Probability*, University of California Press, 281–297.

Menke, W., 1984, Geophysical Data Analysis: Discrete Inverse Theory: Academic Press Inc., NY, NY.

Nitish, N., C. G. Hinton, A. Krizhevsky, I. Sutskever, R. Salakhutdinov, 2014, Dropout: A Simple Way to Prevent Neural Networks from overfitting: Journal of Machine Learning Research, **15**, 1929–1958.

Nocedal, J. and S. Wright, 1999, Numerical Optimization: Springer Verlag Inc.

Olshausen, B. and D. Field, 1996, Emergence of simple-cell receptive field properties by learning a sparse code for natural images, Letters to Nature: **381**, 607–609.

Patel, A. B., T. Nguyen, R. Baraniuk, 2016, A probabilistic framework for deep learning: 2016, arXiv:1612.01936P.

Patel, A. and S. Chatterjee, 2016, Computer vision-based limestone rock-type classification using probabilistic neural network: Geoscience Frontiers, 7, 53–60.

- Pearson, K., 1901, On lines and planes of closest fit to systems of points in space: *Philosophical Magazine*, **2** (11), 559–572.
- Perez, C., 2013, Regularization of neural networks using DropConnect: ICML and JMLR, W and CP., jmlr.org.
- Press, W., S. Teukolsky, W. Vetterling, and B. Flannery, 2007, *Numerical Recipes: The Art of Scientific Computing*: Cambridge University Press Inc.
- Qi, J., G. Machado, and K. Marfurt, 2017, A workflow to skeletonize faults and stratigraphic features: *Geophysics*, **82**, no. 4, O57–O70.
- Roth, H. R., L. Lu, J. Liu, J. Yao, A. Seff, K. Cherry, L. Kim, and R. M. Summers, 2016, Improving computer- aided detection using convolutional neural networks and random view aggregation: *IEEE transactions on Medical Imaging*, **35**, 1170–1181.
- Rickett, J., 2003, Illumination-based normalization for wave-equation depth migration: *Geophysics*, **68**, 1371–1379.
- Ripley, B. D., 1996, *Pattern Recognition and Neural Networks*: Cambridge University Press.
- Rosenblatt, F., 1958, The Perceptron: A probabilistic model for information storage and organization in the brain: *Cornell Aeronautical Laboratory, Psychological Review*, v65, No. 6, 386–408. doi:10.1037/h0042519.
- Rosenblatt, F., 1962, *Principles of Neurodynamics*: Washington, DC:Spartan Books.
- Schuster, G. T. and J. Hu, 2000, Green’s functions for migration: continuous recording geometry: *Geophysics*, **65**, 167–175.
- Schuster, 2017, *Seismic Inversion*: SEG, Tulsa, Ok..
- Schuster, G., 2018, Machine learning and wave equation inversion of skeletonized data: EAGE Copenhagen workshop ”Seismic Imaging with Ray and Waves - Where do we stand? Part I: Velocity Estimation”.
- Steinhaus, H., 1956, Sur la division des corp materiels en parties: *Bull. Acad. Polon. Sci. IV* (C1.III), 801–804.
- Sun, Y. and G. T. Schuster, 1992, Hierarchic optimizations for smoothing and cooperative inversion: *SEG Technical Program Expanded Abstracts*, 745–748.
- Taner, M. T., 2001, Seismic attributes: *CSEG Recorder*, **26**, 49–56.

Tarantola, A., 1987, Inverse Problem Theory Methods for Data Fitting and Model Parameter Estimation: Elsevier Science Publication.

Wiener, N., 1948, Cybernetics, or Control and Communication in the Animal and the Machine. Cambridge: MIT Press.

Thorndike, R., 1953, Who Belongs in the Family?: Psychometrika. **18** (4): 267-276.

Vapnik, V. N., 1995, The Nature of Statistical Learning Theory: New York, NY, USA: Springer-Verlag New York, Inc..

Vapnik, V. N., 1998, Statistical Learning Theory: Wiley.

Xiong, W., X. Ji, Y. Ma¹, Y. Wang, N. Ben-Hassan and Y. Luo, 2018, Seismic fault detection with convolutional neural network: Geophysics (in press).

Yilmaz, O., 2001, Seismic Data Analysis: SEG Press Book.

Zhang, C., C. Frogner, M. Araya-Polo, and D. Hohl, 2014, Machine-learning based automated fault detection in seismic traces: 76th Conference and Exhibition, EAGE, Extended Abstract. doi: 10.3997/2214-4609.20141500.

Zhang, L., F. Yang, Y. D. Zhang, and Y. J. Zhu, 2016, Road crack detection using deep convolutional neural network: Image Processing (ICIP), 2016 IEEE International Conference on Image Processing (ICIP), 3708-3712.

Zhang, Y., K. Sohn, R. Villegas, G. Pan, and H. Lee, 2015, Improving object detection with deep convolutional networks via Bayesian optimization and structured prediction: Proceedings of the IEEE Conference on Computer Vision and Pattern Recognition, 249-258.